

---

# Noninvasive Measurements of Electron Bunch Current Profiles with Few-Femtosecond Resolution at MHz Repetition Rates

---

DISSERTATION

*zur Erlangung des Doktorgrades*

*an der Fakultät für Mathematik, Informatik und Naturwissenschaften*

*Fachbereich Physik*

*der Universität Hamburg*

*vorgelegt von*

Nils Maris Alexander LOCKMANN

Hamburg

2021

Gutachter der Dissertation:	PD Dr. Bernhard Schmidt Prof. Dr. Wolfgang Hillert
Zusammensetzung der Prüfungskommission:	PD Dr. Bernhard Schmidt Prof. Dr. Wolfgang Hillert Prof Dr. Gudrid Moortgat-Pick Prof. Dr. Daniela Pfannkuche Dr. Torsten Limberg
Vorsitzende der Prüfungskommission:	Prof. Dr. Daniela Pfannkuche
Datum der Disputation:	24.09.2021
Vorsitzender Fach-Promotionsausschusses PHYSIK:	Prof. Dr. Wolfgang Hansen
Leiter des Fachbereichs PHYSIK:	Prof. Dr. Günter H. W. Sigl
Dekan der Fakultät MIN:	Prof. Dr. Heinrich Graener

## *Abstract*

The upcoming generation of hard X-ray free-electron lasers (XFEL) delivers X-ray pulses with unmatched brilliance at megahertz repetition rates based on superconducting linear accelerators. The European XFEL, the first XFEL of this generation, accelerates bursts of up to 2700 electron bunches every tenth of a second over a distance of 1.7 km to energies as high as 17.5 GeV. The bunches are distributed individually at a maximum of 4.5 MHz to three FEL beamlines, where they generate ultrashort radiation pulses in the soft and hard X-ray regime. The electron bunch current profile is of fundamental importance for the generation of these XFEL pulses and is required to have kilo-Ampere peak currents. However, diagnosis is challenging because bunch durations as short as a few femtoseconds have to be measured bunch-resolved at MHz repetition rates. In the scope of this thesis, the single-shot spectrometer CRISP has been installed and commissioned at European XFEL. Monitoring of coherent diffraction radiation (CDR) enables for the first time noninvasive and bunch-resolved form factor measurements in two frequency bands: 0.7 THz – 6.6 THz (438  $\mu\text{m}$  – 45  $\mu\text{m}$ ) and 6.9 THz – 58.4 THz (44  $\mu\text{m}$  – 5.1  $\mu\text{m}$ ). The detector electronics and signal processing of the CRISP spectrometer have been modified for MHz repetition rates and exhibit in combination sufficient sensitivity for the range of bunch charges at European XFEL from 50 pC to 1 nC. The current profiles are reconstructed from the measured form factors with a further developed iterative procedure. Using a transverse deflecting structure and a bunch compression monitor, the current profiles have been confirmed by established comparative diagnostic measurements. The measurements presented in this thesis cover rms bunch durations from 6 fs to 100 fs and peak currents up to 10 kA. Variations of bunch duration and peak current within the bursts of electron bunches have been identified with a relative rms bunch duration resolution of less than 1 fs.



## *Kurzfassung*

Eine neue Generation von Freien-Elektronenlasern im harten Röntgenbereich (XFEL) erzeugt Röntgenstrahlungspulse von unerreichter Brillianz mit Wiederholraten im Megahertzbereich, basierend auf supraleitenden Linearbeschleunigern. Der European XFEL, der erste XFEL dieser Generation, beschleunigt jede Zehntelsekunde einen Pulszug von bis zu 2700 Elektronenpaketen über eine 1.7 km lange Strecke auf maximal 17.5 GeV Strahlenergie. Die Elektronenpakete werden dabei mit bis zu 4.5 MHz einzeln auf drei FEL Strahllinien verteilt, in denen sie ultrakurze Strahlungspulse im harten und weichen Röntgenbereich erzeugen. Das Stromprofil ist dabei von fundamentaler Bedeutung für die Erzeugung dieser XFEL-Pulse und benötigt Spitzenströme im Kiloamperebereich. Allerdings gestaltet sich seine Diagnose, bei der Elektronenpaketdauern runter bis zu wenigen Femtosekunden mit MHz-Wiederholraten vermessen werden müssen, schwierig. Im Rahmen der vorliegenden Dissertation wurde das Einzelschussspektrometer CRISP am European XFEL installiert und in Betrieb genommen. Die Aufnahme des Spektrums kohärenter Diffraktionsstrahlung (CDR) ermöglicht zum ersten Mal Messungen des Formfaktors der einzelnen Elektronenpakete in zwei Frequenzbändern von 0.7 THz – 6.6 THz (438  $\mu\text{m}$  – 45  $\mu\text{m}$ ) und 6.9 THz – 58.4 THz (44  $\mu\text{m}$  – 5.1  $\mu\text{m}$ ), ohne die Elektronenpakete dabei für den FEL Betrieb untauglich zu machen. Die Detektorelektronik sowie Signalverarbeitung des Spektrometers wurden speziell für MHz-Wiederholraten angepasst und verfügen in ihrer Kombination über genügend Sensitivität für Paketladungen im Bereich von 50 pC bis 1 nC am European XFEL. Die Stromprofile werden mit einem weiterentwickeltem iterativem Verfahren zur Phasenrückgewinnung aus den gemessenen Formfaktoren rekonstruiert. Mittels einer transversal ablenkenden Struktur sowie eines Kompressionsmonitors wurden die Stromprofile durch Vergleichsmessungen etablierter Diagnostik bestätigt. Die in dieser Arbeit gezeigten Messungen decken eine Bunchdauer von 6 fs bis 100 fs (rms) sowie Spitzenströme bis zu 10 kA ab. Veränderungen der Paketdauer und des Spitzenstroms innerhalb eines Pulszuges wurden mit einer relativen Auflösung der Bunchdauer (rms) von weniger als 1 fs ausgemacht.



# Contents

<b>1</b>	<b>Introduction</b>	<b>1</b>
1.1	Free-Electron Lasers . . . . .	1
1.2	Motivation . . . . .	4
<b>2</b>	<b>Linear Accelerators for XFELs</b>	<b>7</b>
2.1	Acceleration and Compression . . . . .	7
2.2	Collective Effects . . . . .	11
2.3	European XFEL . . . . .	13
2.4	Longitudinal Diagnostics . . . . .	18
<b>3</b>	<b>Coherent Radiation Diagnostics</b>	<b>23</b>
3.1	Coherent Emission . . . . .	24
3.2	Form Factor and Current Profile . . . . .	26
3.3	Current Profile Reconstructions . . . . .	28
3.4	Transition and Diffraction Radiation . . . . .	33
<b>4</b>	<b>Experimental Setup</b>	<b>41</b>
4.1	Screen Station . . . . .	41
4.2	THz Beamline . . . . .	46
4.3	CRISP Spectrometer . . . . .	50
<b>5</b>	<b>Spectrometer Sensitivity</b>	<b>57</b>
5.1	Modeling . . . . .	58
5.2	In-Situ Identification . . . . .	62
5.3	Saturation . . . . .	68
5.4	TR/DR Comparison . . . . .	69
5.5	Orbit Dependencies . . . . .	71
<b>6</b>	<b>Benchmarking Based on Complementary Diagnostics</b>	<b>75</b>
6.1	Data Processing . . . . .	75
6.2	Comparative Measurements with TDS . . . . .	79
6.3	Comparative Measurements with BCM . . . . .	84
6.4	Conclusion . . . . .	89
<b>7</b>	<b>Megahertz Operation</b>	<b>93</b>
7.1	Pileup . . . . .	93
7.2	Comparative Measurements . . . . .	100
7.3	Results during FEL Operation . . . . .	105
7.4	Outlook . . . . .	110
<b>8</b>	<b>Summary</b>	<b>113</b>

<b>A Radiation Propagation Based on Fourier Transform</b>	<b>115</b>
A.1 Principle of Radiation Propagation . . . . .	115
A.2 Optical Elements . . . . .	116
A.3 Numerical Implementation . . . . .	117
<b>B Resolution</b>	<b>119</b>
B.1 Overall Bunch Shape . . . . .	119
B.2 Pronounced Peaks with High Current . . . . .	123
<b>C Online Measurements</b>	<b>125</b>
C.1 Single Grating Set Operation . . . . .	125
C.2 Single Shot Operation . . . . .	128
<b>Bibliography</b>	<b>131</b>
<b>List of Publications</b>	<b>139</b>
<b>Acknowledgements/Danksagung</b>	<b>141</b>

## Chapter 1

# Introduction

Since the discovery of X-rays in 1895 by W. C. Röntgen [Rön98], this part of the electromagnetic radiation spectrum has played a major role in science and research. In addition to their applications in medicine, X-rays have also enabled studies of smallest structures using diffraction patterns of crystals, which was pioneered by the work of Max von Laue [Eck12] in 1912. A famous example is the structure of DNA, that was decoded with the help of X-ray diffraction patterns in 1953 [WC53]. Another example, which is currently of utmost importance for people's life around the globe, is research carried out within the scope of the COVID-19 pandemic. X-rays have been used to characterize the virus' properties and helped to identify possible drugs and vaccines in the fight against it (e.g. [Cus+20; Sie+20]). The potential of synchrotron radiation for X-ray applications has been realized very soon after it has first been discovered at a circular accelerator [Eld+47].

A key parameter for the classification of X-ray sources and their applicability in experiments is the brilliance  $B$ , which is defined as number of photons  $\Delta N_p$  per time  $t$ , area  $A$  and solid angle  $\Delta\Omega$  within a certain spectral bandwidth  $\Delta\lambda/\lambda$  [AM11]:

$$B = \frac{\Delta N_p}{t \cdot A \cdot \Delta\Omega \cdot \frac{\Delta\lambda}{\lambda}}. \quad (1.1)$$

The historical overview in Fig. 1.1 demonstrates that advantages in accelerator physics led to an enormous increase of the achievable X-ray brilliance starting from Röntgen's X-ray tube. In the beginning, scientists took advantage of synchrotron radiation generated as a byproduct of accelerators built for nuclear and particle physics. This is now called the first generation of synchrotron light sources [Wil00]. Today, synchrotron light sources of the fourth generation, which generate highly brilliant X-ray radiation, are being built or already in operation. This generation is not only characterized by transversely diffraction limited radiation properties due to a tremendous electron bunch quality [Tav+18; CJ18] but also by coherent and ultra-short radiation pulses. X-rays with the latter properties are a product of free-electron lasers (FEL). They are able to produce X-ray pulses with full transverse and partial temporal coherence. Pulse lengths down to a few femtoseconds and below render the exploration of ultra-fast phenomena on the atomic scale, which is a reason for the fast growing scientific interest in these light sources [Dun18].

### 1.1 Free-Electron Lasers

The development of FELs started in 1971 when John Madey first published the fundamental principle [Mad71]. It is based on stimulated emission of radiation, which is caused by the interaction of electrons with a radiation field while they are moving along the periodically alternating magnetic field of an undulator. The process of stimulated emission can be understood as follows (see e.g. [Sch+14]):

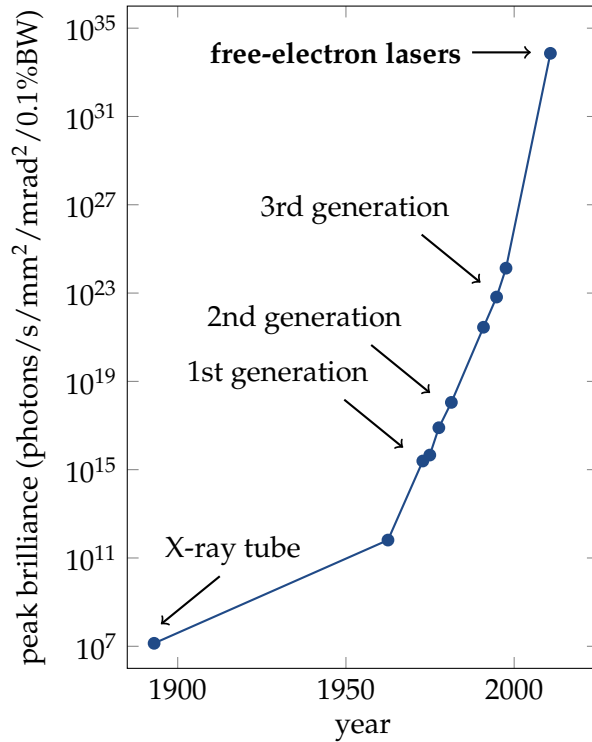


FIGURE 1.1: Historical evolution of the exponentially growing peak brilliance of X-ray sources. The developments of synchrotron light sources are summarized in different generations and form clusters of similar peak brilliance. Free-electron lasers as part of the 4th generation are on top. Data taken from [Shi07].

Inside the undulators with period length  $\lambda_u$  and undulator parameter  $K$ , relativistic electrons with Lorentz factor  $\gamma$  emit radiation at the wavelength

$$\lambda_L = \frac{\lambda_u}{2\gamma^2} \left( 1 + \frac{K^2}{2} \right) \quad (1.2)$$

due to their sinusoidal trajectory. At the same time, radiation at this wavelength sustains an energy exchange with the individual electrons as electric field and electron movement are in phase. Hereby, electrons gain or lose energy depending on the phase relation between their transverse motion and the radiation field. This phase relation depends on the longitudinal position of the electron inside the electron bunch that spans along many radiation wavelengths. Additionally, an energy-dependent path length inside the undulator causes the formation of a region with electron surplus and a region with electron deficit within each radiation wavelength. This phenomenon is called microbunching. In order to avoid a balance between gain and loss, the microbunches must be properly positioned with respect to the radiation field. If this is the case, stimulated emission (electrons losing energy to the radiation field) predominates over absorption (electrons gaining energy from the radiation field) such that the radiation field is amplified.

Two ways to generate the required relation between electron density and radiation field are established. The first method is a so-called low-gain FEL. The radiation field is stored in an optical cavity consisting of high reflectivity mirrors. An electron beam with an energy  $\gamma$  slightly above the resonance condition of Eq. (1.2) is repetitively passed through the undulator. The energy transfer of each passage amounts only to a few percent of the radiation field and the corresponding amount

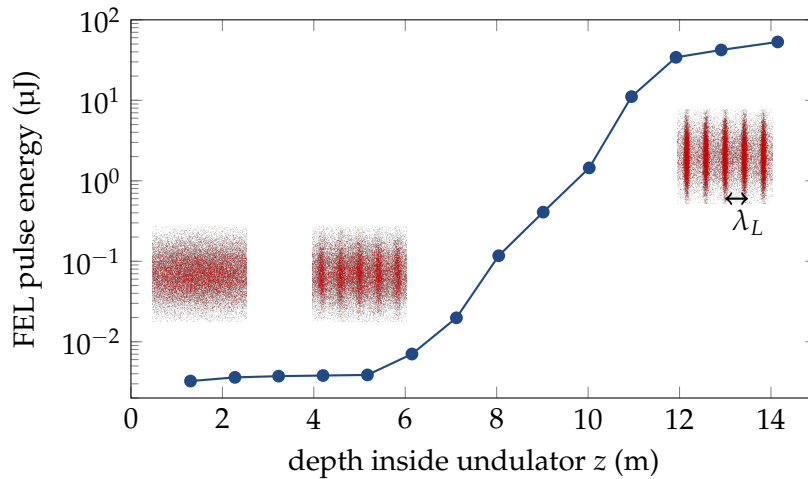


FIGURE 1.2: Measured FEL pulse energy as function of the used undulator length, which is often referred to as gain-curve, at the SASE FEL of the TESLA Test Facility. Data taken from [Ayv+02]. As illustrated in red, the FEL amplification process is driven by the formation of microbunches, which are separated by the FEL wavelength  $\lambda_L$ . At the final undulator length, the FEL process has reached saturation.

of intensity exits the cavity, where it is guided to an experiment. Beforehand, the continuous grow of the radiation intensity inside the cavity with each passage of the electron beam has led to an equilibrium between intensity increase and cavity loss. The amount of energy stored in the cavity is thus sufficient to generate FEL pulses of high brilliance even though the energy transfer amounts only to a few percent. This method is mainly limited to wavelengths in the infrared and optical regime as building optical resonators for shorter wavelengths becomes a difficult task [KSR08]. For wavelengths in the X-ray regime, the amplification has to take place in a single passage of a long undulator, which is called a high-gain FEL. The emerging density modulation leads to an alteration of the phase velocity of the electric field. Intrinsically, the microbunches start to position themselves at proper phases with respect to the radiation field. The intensity of the radiation field grows, which leads to even more stimulated emission caused by the formation of microbunches. This self-amplification results in an exponentially growing intensity of the X-ray pulse.

The high-gain amplification process is either started by an initial radiation field or density modulation, which is externally generated (seeding [Rei13]), or it is made use of the Self-Amplified Spontaneous Emission (SASE) process [KS80]. In the SASE case, the initial spontaneous undulator radiation is amplified, which has the advantage of being applicable at any wavelength. Due to the stochastic behaviour of the spontaneous radiation, SASE exhibits drawbacks compared to seeding, such as decreased temporal coherence or shot-to-shot stability. However, in the X-ray regime robust – but at the same time versatile – seeding techniques are not yet established such that SASE is currently the most popular method for so-called XFELs.

An illustration of the exponential growing SASE FEL pulse energy while the electron bunch is propagating through the undulator is presented in Fig. 1.2. In the beginning, there is not much energy gain (lethargy regime), but microbunches (illustrated in red) start to form. A key parameter for a successful FEL operation is the FEL parameter  $\rho_{\text{FEL}}$ . It determines the slope of the exponential growing region in

Fig. 1.2, but also the FEL pulse energy at the finally occurring saturation. The FEL parameter scales with the beam's current density  $j_0$  as [BPN84]

$$\rho_{\text{FEL}} \propto \left( \frac{\lambda_u^2 K^2 j_0}{\gamma^3} \right)^{\frac{1}{3}} \quad (1.3)$$

and must be maximized. Besides the slope of the exponential increase (gain length), the FEL parameter also determines many other fundamental aspects, like e.g. bandwidth and coherence time.

Technical restrictions limit the feasible undulator period  $\lambda_u$  to a few centimeters [Bah11] with an undulator parameter near one. Consequently, hard X-ray FEL radiation with wavelengths below  $\leq 0.1$  nm (photon energies above 10 keV) demands several GeV electron beam energy to provide a sufficient Lorentz factor  $\gamma$  (see Eq. (1.2)). The small FEL wavelengths require a very high beam current density (see Eq. (1.3)) and thereby put strict limits on the 6-dimensional phase space distribution of the electron bunch. The required peak currents in the kilo-Ampere regime can only be generated in linear accelerators (linac) while maintaining small energy spreads and high transverse beam quality. Repelling Coulomb forces between the electrons deny highly-dense bunches at low beam energies and they must be gradually compressed during acceleration. Nonetheless, Coulomb forces and collective emission of radiation may still strongly influence the 6-dimensional phase space distribution of the electron bunch. Thus, diagnostics monitoring the current profile of the electron bunch are of fundamental importance for successful FEL operation.

Fourth generation synchrotron light sources based on storage rings do not generate X-ray pulses with the coherence properties and short-time scales of XFELs, but profit from high pulse repetition rates ( $\sim$ GHz). Because, in contrast to circular accelerators, the particles in linear accelerators are only accelerated once inside each rf cavity, these machines require substantially more rf power to reach the required beam energies within available distances. As a consequence of the rf power dissipation, the accelerating field inside normal conducting cavities is only present for short fractions of time such that acceleration is limited to a few hundred bunches per second. Using superconductive cavities, the rf power dissipation is strongly reduced and longer rf flat-tops or even continuous-wave (cw) operation is possible [Sch02]. In this case, more than several thousand electron bunches can be accelerated per second and the gap between the overall photon flux at storage rings and linac-driven FELs is strongly reduced.

## 1.2 Motivation

Because of the strong dependency of the SASE FEL pulse on the current density  $j_0$  (see Eq. (1.3)), the current profile of the electron bunches influences decisively the intensity and temporal structure of the X-ray pulses. The electron bunches must be compressed to current densities that are easily affected by collective effects and instabilities. Diagnostics for the longitudinal electron bunch properties are indispensable. Studies of coherently emitted radiation are a powerful method to monitor the longitudinal electron bunch structure.

Coherent emission of radiation is achieved by a fixed phase relation between the individual emitters (electrons) of wavefronts. This leads to many orders of magnitude more intense radiation than in the incoherent (randomly distributed phase relations) case. As the spatial structure of the electron bunch and the coherent radiation

spectrum are connected via Fourier transform, spectral measurements of the emitted radiation can be used to retrieve information about the longitudinal current profile [Sch+18]. The underlying radiation process must yield sufficiently broadband radiation in order to cover the entire frequency range of the longitudinal electron bunch structure. In order to cope with the stochastic nature of possible current profile instabilities, the spectral properties of the coherent radiation must be detected on single-shot basis. As a consequence of the frequency range of interest, which lies in the THz/FIR regime, and the need to cover frequencies orders of magnitude apart, suitable commercial spectrometers are rare. Instead, a novel single-shot spectrometer covering an order of magnitude in frequency in THz and FIR regime has been developed in a collaboration of DESY and the University of Hamburg solely for this purpose [Wes+11].

The Coherent Radiation Intensity Spectrometer (CRISP) has been deployed at the soft X-ray FEL FLASH [Ack+07]. Using invasive transition radiation [GF45], CRISP at FLASH has been used for research on current profile reconstruction from measured coherent radiation spectra. Recent results – also profiting from work within the scope of this thesis – have demonstrated robust and accurate current profile measurements with few-femtosecond resolution [Sch+20].

At European XFEL [Dec+20], the CRISP spectrometer has the potential to be operated with noninvasive diffraction radiation due to roughly 10-times higher beam energy compared to FLASH. The single-shot capabilities, together with modifications of pulse-shaping and readout electronics, open up the possibility to diagnose all 2700 bunches within one rf pulse of European XFEL. The rf pulse is divided in different regions for the parallel operation of three SASE FEL beamlines, such that the longitudinal properties of the electron bunches are individually optimized.

In this thesis, noninvasive current profile measurement of bunches with rms durations to below 10 fs are carried out at megahertz (MHz) bunch repetition rates. The following chapter explains how electron bunches with durations in the femtosecond regime and the required peak currents are generated at European XFEL and the facility itself is introduced. In the next chapter, the principle of coherent radiation diagnostics is explained. The connection between coherent radiation spectrum and current profile by the form factor is in detail examined. Transition and diffraction radiation as invasive and noninvasive radiation sources are compared.

Chapter 4 describes the experimental setup that realizes current profile measurements based on coherent diffraction radiation with MHz bunch repetition rates for European XFEL. The design of radiation source, radiation transport to the CRISP spectrometer, as well as modifications of the spectrometer itself are motivated and presented. The spectrometer sensitivity, which is mandatory for an accurate determination of the coherent radiation spectrum, is investigated in the next chapter. As the sensitivity depends on radiation source and transport, while possibilities for an external calibration of the spectrometer are limited, the sensitivity must be determined in-situ. Besides a modeled sensitivity, this thesis also presents a systematic procedure to obtain the in-situ sensitivity. In chapter 6, the current profile reconstruction at European XFEL is presented. In single bunch operation (i.e. 10 Hz bunch repetition rate), the results of the CRISP spectrometer are benchmarked with comparative diagnostics. Finally, current profile reconstructions along the bunch train (MHz repetition rates) of European XFEL are presented in chapter 7 and an outlook to possible applications of the spectrometer is given. The thesis ends with a summary and appendices include studies of the temporal resolution and online current profile measurements of single bunches.



## Chapter 2

# Linear Accelerators for XFELs

Electron bunches with peak currents of several kA, small transverse diameters and low energy spread, which is required for the high-gain FEL process in the X-ray regime, are generated by linear accelerators (linac). The repelling Coulomb force between the individual electrons denies acceleration of initially ultrashort ( $\lesssim 100$  fs) electron bunches. Instead, the high peak currents are achieved by exploiting the decrease of the Coulomb force with the Lorentz factor  $\gamma$  and gradually compressing the electron bunch at increasing beam energies. The FEL pulse duration limits the temporal resolution of pump-probe experiments [MR15]. As the pulse duration is determined to a large extent by the electron bunch duration [Beh+12], experiments request for ever shorter bunches in order to develop higher resolution. This chapter demonstrates the demands for the noninvasive current profile diagnostic for fully compressed electron bunches at European XFEL. The fundamental relations introduced here are required to comprehend the experimental results presented in this thesis.

The first section deals with the acceleration of electron bunches to the required beam energies above several GeV and their longitudinal compression to shortest possible bunch durations. Depending on bunch charge, bunch durations down to a few femtoseconds can be reached. The high electron densities modify the electron bunch properties, which will be described in the second section, and it will be shown that longitudinal diagnostics are indispensable. The layout and operation of the X-ray free-electron laser facility European XFEL, at which the experiments presented in this thesis are carried out, is described to the required extent. Finally, the longitudinal diagnostics at European XFEL for bunches with  $\lesssim 100$  fs rms duration are shortly discussed and serve as a typical example for current profile monitoring at XFELs. Fundamental expressions from the field of accelerator physics that are not explicitly introduced can be found in [Wie15].

## 2.1 Acceleration and Compression

The description of electron bunch acceleration above several GeV and their compression to the femtosecond scale in this section follows closely [DLE05] as well as sections 1.3 and 1.4 in [Wes12]. High-quality electron bunches for XFELs are generated either by the photoelectric or thermionic effect. In the first case, a short laser pulse of typically a few picosecond duration penetrates a photocathode and the emitted electrons are immediately accelerated by a strong electric field to several megaelectronvolt beam energies [Dwe+97; Zho+19]. In case of thermionic emission, the emitted electron pulse is first several microsecond long but is chopped and bunched to several picosecond long bunches while being accelerated to beam energies of several megaelectronvolt. At these energies, the electrons are already relativistic with a Lorentz factor  $\gamma > 10$  and travel approximately with the speed of light  $c$ . They

enter radio-frequency (rf) cavities, where they are accelerated using the TM01 mode [Wil00] of the electromagnetic field. Hereby, standing-wave cavities are designed such that the time needed by the electrons to pass a single cell equals half of the rf oscillation time. The field direction has inverted when the electrons arrive at the next cell and thus they are continuously accelerated. The energy gain of an electron with elementary charge  $e$  and longitudinal intra-bunch coordinate  $\zeta$  after passing through a resonator of length  $L$  is

$$\Delta W = e E_0 L \cos \left( \frac{2\pi f_{\text{ACC}}}{c} \zeta + \phi_{\text{ACC}} \right). \quad (2.1)$$

The center of the electron bunch is injected at phase  $\phi_{\text{ACC}}$  with respect to the accelerating rf field with average amplitude  $E_0$  along the cavity and frequency  $f_{\text{ACC}}$ . The overall accelerating voltage is  $V = E_0 L$ . The electron bunch is much shorter than the rf wavelength ( $\zeta \ll c/f_{\text{ACC}}$ ) and maximum mean beam energies are reached using on-crest acceleration ( $\phi_{\text{ACC}} = 0$ ).

The slope of the electric field along the accelerating phase will be transferred onto the energy distribution of the bunch. Electrons in the front of the bunch sample different electric field strengths than electrons in the back of the bunch. A Taylor expansion of Eq. (2.1) around  $\zeta = 0$  yields:

$$\Delta W(\zeta) \approx \Delta W_0 \left( 1 + h\zeta + \frac{1}{2}h'\zeta^2 + \frac{1}{6}h''\zeta^3 + \mathcal{O}(\zeta^4) \right), \quad (2.2)$$

where  $\Delta W_0 = eV \cos \phi_{\text{ACC}}$  is the energy gain of the bunch center. The parameter

$$h = -\frac{eV}{\Delta W_0} \frac{2\pi f_{\text{ACC}}}{c} \sin \left( \frac{2\pi f_{\text{ACC}}}{c} \zeta + \phi_{\text{ACC}} \right) \Big|_{\zeta=0} \quad (2.3)$$

and its derivatives  $h'$ ,  $h''$  describe the variation of the relative electron energy deviation  $\delta = (\Delta W - \Delta W_0)/\Delta W_0$  along the intra-bunch coordinate  $\zeta$

$$\frac{d\delta}{d\zeta} \approx h + h'\zeta + \frac{1}{2}h''\zeta^2. \quad (2.4)$$

As the parameter  $h$  defines the linear dependency of the energy along the bunch it is in analogy to optics called chirp.

The dependency of the electron energy along the bunch is exploited for bunch compression. This is not done by different velocities (as the electrons are highly relativistic, the differences are negligible) but by a magnetic chicane consisting of several dipoles. An example of such a bunch compressor is a widely-used C-chicane shown in Fig. 2.1. The Lorentz force inside the dipole magnets will deflect electrons with negative relative energy deviation ( $\delta < 0$ ) stronger than electrons with positive energy deviation ( $\delta > 0$ ). As a consequence, electrons with less energy travel a longer path and fall back while electrons with higher energy move ahead. For now, the change of the intra-bunch coordinate will be considered only in first order of the relative energy deviation [DLE05]:

$$\Delta \zeta = - (R_{56} \delta + \mathcal{O}(\delta^2)). \quad (2.5)$$

The parameter  $R_{56}$  is given by the magnetic structure of the bunch compressor. Higher orders are neglected at this point because the first order dominates strongly, which is caused by small relative energy deviations in the order of  $\delta \approx 10^{-3}$ . The first order is sufficient to describe the fundamental principle of bunch compression.

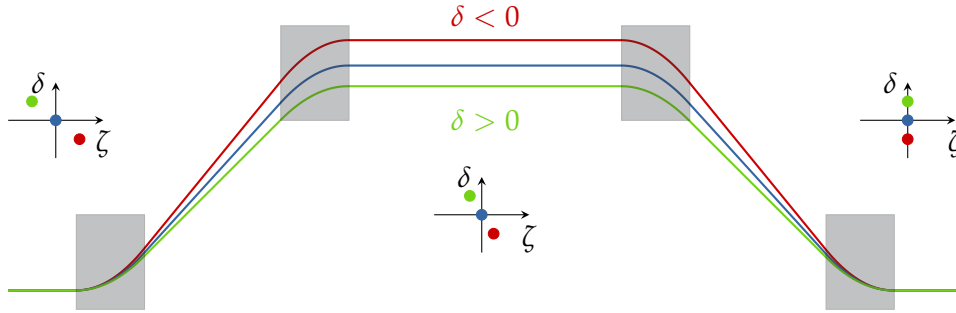


FIGURE 2.1: Principle of a magnetic bunch compressor. Particles with different relative energy deviations  $\delta$  with respect to the bunch center experience different bending radii in the dipole magnets (gray rectangles) which leads to path length differences. Electrons with higher energy (green) travel a shorter path than electrons with less energy (red). For relativistic electrons the difference in velocity is negligible, and particles with higher energy move up ( $+\Delta\zeta$ ) while particles with less energy fall back ( $-\Delta\zeta$ ) with respect to the bunch center (blue).

Considering a perfectly linear energy-position relationship ( $h' = 0, h'' = 0, \dots$ ) of the bunch, the relative energy deviations of the electrons with individual intrinsic energy deviation  $\delta_i$  are

$$\delta = h \cdot \zeta + \delta_i. \quad (2.6)$$

The magnetic chicane will transform the intra-bunch coordinate as

$$\zeta \mapsto \zeta - R_{56}\delta = (1 - hR_{56})\zeta - R_{56}\delta_i. \quad (2.7)$$

Consequently, the length of the bunch with energy spread  $\sigma_\delta$  and initial bunch length  $\sigma_\zeta$  will be

$$\sigma_\zeta^* = \sqrt{(1 - hR_{56})^2 \sigma_\zeta^2 + R_{56}^2 \sigma_\delta^2}. \quad (2.8)$$

As the intrinsic energy spread  $\sigma_\delta$  from the gun is small, the first term dominates, which allows to define the compression factor as

$$C = \frac{\sigma_\zeta}{\sigma_\zeta^*} \approx \frac{1}{1 - hR_{56}}. \quad (2.9)$$

For the most common types of bunch compressors the  $R_{56}$  parameter is negative, and thus a negative relation between energy and intra-bunch coordinate is needed ( $d\delta/d\zeta < 0$ ) to compress the bunch. This is achieved by injecting the electron bunch off-crest ( $\phi_{\text{ACC}} > 0$ ). Chirp  $h$  and beam energy  $\Delta W_0$  are strongly coupled. Therefore, if the chirp shall be increased at the same beam energy, it is required to inject the bunch further off-crest and increase the rf amplitude (see Eq. (2.3)). This limits the available chirp range because of limited rf power. In addition, the derivatives of the chirp contribute significantly to the energy-position relation, which is not linear as assumed in Eq. (2.6) and leads to an inhomogeneous compression along the bunch. A linear relation can be achieved by introducing a cavity module operating at the  $n$ -th harmonic of the fundamental accelerating frequency, which adds more flexibility to the bunch compression scheme. The longitudinal energy distribution in terms of Eq. (2.4) is then given by [DLE05]

$$\Delta W_0 \begin{pmatrix} 1 \\ h \\ h' \\ h'' \end{pmatrix} = \begin{pmatrix} 1 & 0 & 1 & 0 \\ 0 & -k & 0 & -(nk) \\ -k^2 & 0 & -(nk)^2 & 0 \\ 0 & k^3 & 0 & (nk)^3 \end{pmatrix} \begin{pmatrix} eV_1 \cos \phi_1 \\ eV_1 \sin \phi_1 \\ eV_n \cos \phi_n \\ eV_n \sin \phi_n \end{pmatrix}, \quad (2.10)$$

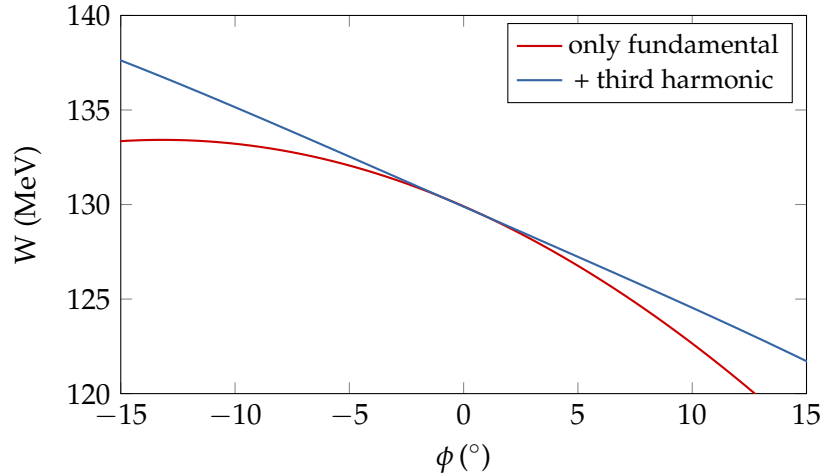


FIGURE 2.2: Linearization of the overall accelerating voltage by introducing third harmonic cavities. The higher order parameters  $h'$ ,  $h''$  of the chirp can be completely removed at the position of the bunch center  $\phi = 0$ . The longitudinal phase space (i.e. the energy-position relation) of the bunch is linearized.

where  $k = 2\pi f_{\text{ACC}}/c$  is the wave number of the fundamental accelerating frequency. The accelerating voltages and phases for the fundamental ( $V_1, \phi_1$ ) and the higher harmonic ( $V_n, \phi_n$ ) can be calculated analytically from the desired beam energy  $\Delta W_0$  and parameters  $h, h', h''$ . As demonstrated in Fig. 2.2, the removal of curvature  $h'$  and third derivative  $h''$  leads to a more linear energy position relation compared to the solely fundamental case while maintaining beam energy and chirp.

This linear relation between intra-bunch coordinate  $\zeta$  and relative energy deviation  $\delta$  is required for a homogeneous compression inside the magnetic chicane along the entire bunch for different compression settings as shown in Fig. 2.3. The off-crest acceleration leads to an increased overall energy spread. Only the energy spread  $\sigma_{\delta,s}$  within short slices along the temporal axis (slice energy spread) before the bunch compressor is still defined by the intrinsic energy spread  $\sigma_\delta$ . The longitudinal phase space of the electron bunch is sheared by the magnetic chicane. Thus, the initial chirp determines the strength of the compression and the resulting bunch duration as given by Eqs. (2.8,2.9). The minimal achievable bunch duration is determined by the intrinsic energy spread  $\sigma_\delta$ . For a very strong chirp (red), the compression factor turns negative and the shearing exceeds the optimum point of compression. The energy chirp is reversed, which is called over-compression. For FEL operation, this is generally not a desirable state as the bunch passes the delicate point of maximum density (see Sec. 2.2). It should also be noted that the slice energy spread, which is of fundamental importance for the FEL performance, increases as  $\sigma_{\delta,s}^* = C \cdot \sigma_{\delta,s}$  because the phase space density must be preserved.

In reality, higher order chicane parameters in Eq. (2.5) as well as nonlinearities of the relative energy deviation are not negligible, especially when approaching full compression ( $hR_{56} \rightarrow 1$ ). Moreover, the compression is subject to effects that cannot be sufficiently described analytically (see Sec. 2.2). Thus, the compression is empirically optimized starting from the results of numerical simulations to achieve best possible conditions for the users of the FEL pulses. The four parameters ( $\Delta W_0, h, h', h''$ ) of Eq. (2.10) allow a well manageable change of the compression, which are then converted to voltages and phases of the rf by the accelerator control system. Additionally, compression of the electron bunch to kiloampere peak currents with just one

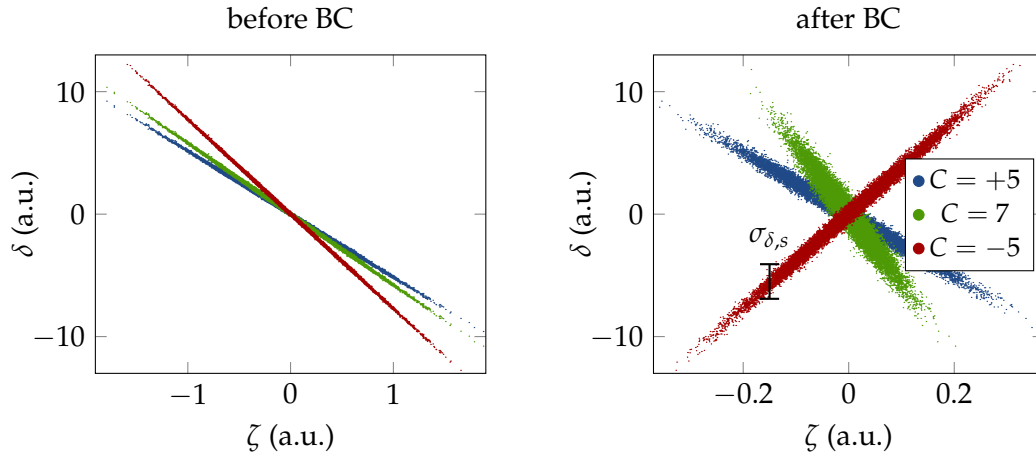


FIGURE 2.3: Linearized longitudinal phase space before (left) and after (right) a perfectly linear (see Eq. (2.7)) bunch compressor. The strength of the chirp determines the compression factor for a given chicane as it shears the longitudinal phase space along the  $\zeta$ -axis. If the compression factor is negative, the distribution is sheared above the point of shortest electron bunch duration and the slope reversed. Besides increasing the peak current, the shearing also increases the energy spread  $\sigma_{\delta,s}$  within one longitudinal slice.

bunch compressor would lead into complications. At low energies, the beam quality would degrade because of Coulomb repulsion. At high energies, the required chirp results in a large slice energy spread after the bunch compressor. Therefore, the bunch compression is usually carried out in a multi-stage setup. Another advantage is that the requirements on rf phase stability for a steady compression are decreased (see e. g. [DL05]). Figure 2.4 illustrates qualitatively how different orders of the nonlinear energy position relation effect the shape of the current density  $\rho_L$  downstream of the bunch compressor because of inhomogeneous compression. For the operation of the FEL, these higher orders are of fundamental importance. They are used to generate specific current profiles for an optimized operation. In Chap. 6, the parameters of the accelerating rf are varied to characterize the spectrometer with a variety of current profiles. The measurements in Chap. 7 show the influence of empirical bunch compression optimization for individual FEL beamlines.

## 2.2 Collective Effects

While the previously neglected nonlinear terms of the rf slope as well as higher order terms of the chicane still allow to clearly calculate the electron bunch compression, other effects that depend strongly on the charge distribution of the bunch itself do not. Because of high charge densities, interactions of the electrons with each other and their surroundings become very important. These effects that change the momentum of the electrons are usually combined under the keyword collective effects. As the parameters of the six-dimensional phase space are coupled (e. g. by the  $R_{56}$  of the bunch compressors), they influence the entire electron bunch phase space.

In the following, the most important collective effects and their influence on the electron bunch will be introduced. The discussion is oriented on the stated effects in [Sch+14]. In general, the influence of these effects cannot be calculated analytically and one has to rely on numerical simulations as for example described in [Fen+]. The nonlinear behaviour of these effects can lead to drastically varying results even for small changes of the electron bunch properties. As the FEL intensity depends

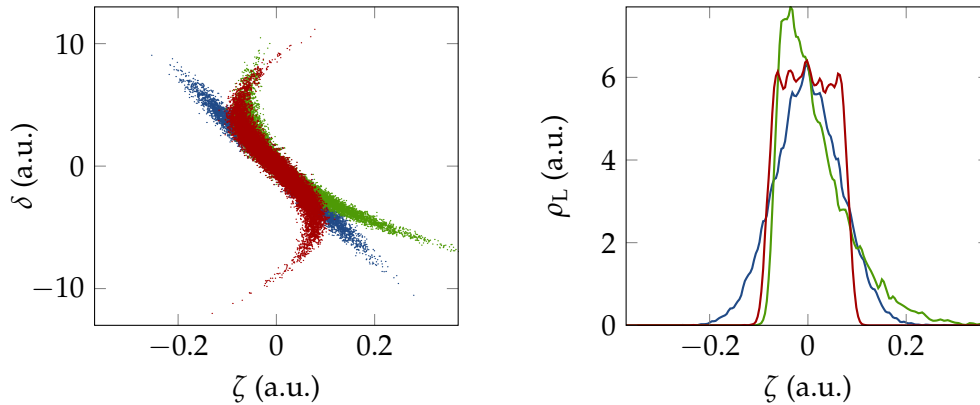


FIGURE 2.4: The shape of the longitudinal density profile  $\rho_L$  changes after the compression depending on the nonlinear orders of the energy-position relation. If the energy-position relation is not purely linear, the bunch is not homogeneously compressed. Here, the chirp is the same for all settings and only  $h'$  and  $h''$  vary. Blue:  $h' = 0, h'' = 0$ ; Green:  $h' \neq 0, h'' = 0$ ; Red:  $h' = 0, h'' \neq 0$ .

strongly on the peak current, diagnostics monitoring the current profile of the electron bunch are indispensable for successful operation of linear accelerators driving XFELs.

### Longitudinal space charge

The Coulomb forces of dense electron distributions lead to a repulsive force acting back on the electrons. A discussion of the resulting forces inside the bunch can be found in [FMP13]. The longitudinal force pushing the electrons apart scales inversely with the relativistic factor as  $\gamma^{-2}$  and is thus especially problematic for low energy electron beams. As mentioned earlier, this is the reason why the electron bunches cannot be compressed to several kiloampere peak currents at beam energies below the GeV-regime. Nevertheless, even at high beam energies ( $> \text{GeV}$ ) this effect cannot be neglected if the electron bunch density is extremely high and can have a severe influence [SSY04]. Moderate longitudinal space charge forces result in a positive energy chirp as electrons in the front gain momentum and electrons in the back lose momentum. It can be utilized to remove the negative chirp remaining close to full compression downstream of the final compression stage (see e.g. [ZDT19]).

### Coherent synchrotron radiation

In the dipoles of a magnetic chicane, electrons emit broadband synchrotron radiation. For wavelengths with the same length as the electron bunch or larger, this radiation will be emitted coherently (see Sec. 3.1). In this case, the radiation is called coherent synchrotron radiation (CSR) and its intensity as well as the energy loss of the electrons scales quadratically with the number of electrons involved  $I_{\text{CSR}} \sim N_e^2$  [Der+95]. Consequently, small variations of the electron density along the bunch result in a strongly varying energy loss. This increases the energy spread of the bunch and, due to energy dependent path lengths in the bunch compressors, also the slice energy spread. In addition, the coherent synchrotron radiation emitted at the tail of the electron bunch overtakes the electrons in the magnetic chicanes and may interact with electrons further up in front [SSY97]. This can lead to significant modifications of the relative energy distribution as was observed in e.g. [Beu+06].

### Wake fields

The Coulomb field generated by an electron bunch is modified by the boundary conditions of the accelerator beam pipe. The fields may act back on the bunch or following bunches and are called wake fields [Cha93]. In accelerators, considerable wake fields are excited by the beam pipe having only a finite conductivity (resistive wakes) and variations of the beam pipe cross sections (geometric wakes). Influences on the operation of linacs for FELs are studied in e.g. [DL97].

### Microbunching instability

The combination of collective effects and bunch compressors can lead to another severe phenomenon of longitudinal electron beam dynamics. Even immediately after its generation, the electron bunch will always contain some statistical density granularity and energy modulation. By collective effects like CSR and energy dependent path length as e.g. in the bunch compressor, density and energy modulations are strongly linked and may amplify each other. As a consequence, the initial granularity can evolve and vary highly in modulation scale and depth during a multi-stage bunch compression scheme which impedes the microbunching process of the FEL. This build-up of charge-driven current modulations is called microbunching instability [SSY04] and has been observed for example in [Wes+09; Rat+15]. It has to be taken into account while designing the bunch compression scheme of a XFEL facility and may be countered by artificially increasing the energy spread of the bunch. This can be achieved with a device called laser heater [Hua+10].

## 2.3 European XFEL

European XFEL is the first hard X-ray free-electron laser facility driven by a superconducting linear accelerator. With a length of 1.7 km it is also the longest and most powerful superconducting accelerator. The whole 3.4 km long facility is located in 5.2 m diameter tunnels, which are 25 m to 6 m underground and run from the DESY campus in Hamburg to Schenefeld in Schleswig-Holstein [DW17]. Since its inauguration in September 2017, the world's largest X-ray laser delivers X-ray pulses of extremely high brilliance to a large variety of scientists and industrial users worldwide [Eur].

A schematic overview of the layout of European XFEL with its four accelerating sections (yellow rectangles), which in total contain more than 7000 rf cavity cells, and three self-amplified spontaneous emission (SASE) [KS80] FEL undulator beamlines (SASE1, SASE2, SASE3) is given in Fig. 2.5. An overview paper of the setup and operation of European XFEL can be found in [Dec+20]. General parameters of the European XFEL facility are listed in Tab. 2.1.

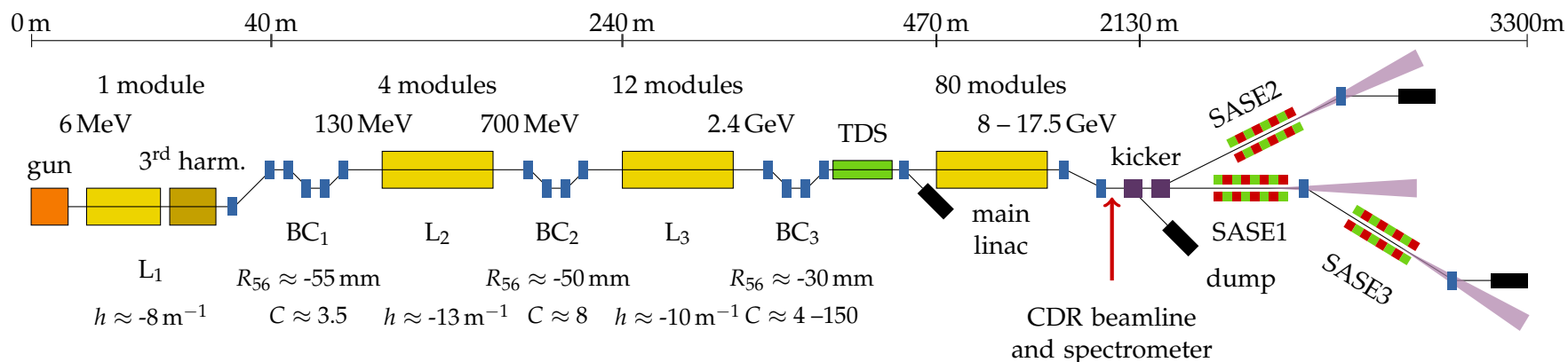


FIGURE 2.5: Layout of European XFEL with its superconducting accelerating sections ( $L_1$ ,  $L_2$ ,  $L_3$ , main linac) separated by three bunch compressors ( $BC_1$ ,  $BC_2$ ,  $BC_3$ ) at the stated beam energies. The third harmonic module in the  $L_1$ -section linearizes the longitudinal phase space for the threefold compression. A transverse deflecting structure (TDS) allows longitudinal beam characterization at final compression but not at full beam energy. This is only possible by using the CRD beamline in front of the undulator switchyard (see Chap. 4). A combination of fast kicker magnets and septa allows to distribute the bunches inside the bunch train as requested by the users of the XFEL pulses to the three SASE undulator beamlines (SASE1, SASE2, SASE3). The stated chirps  $h$ , compression factors  $C$  and  $R_{56}$ -values only indicate typical estimates as they vary depending on FEL operation and optimization [ZDT19; Fen+].

TABLE 2.1: General parameters of European XFEL [DW17; Dec+20].

norm. slice emittance	0.4–1.0 mm mrad
accelerating frequency	1.3 GHz
rf pulse rep. rate	10 Hz
rf pulse length	$\leq 600 \mu\text{s}$
# bunches per rf pulse	1 – 2700
max. rep. rate	4.5 MHz
SASE1/2 photon energy	4–24 keV
SASE3 photon energy	0.25–3 keV

TABLE 2.2: Simulated rms bunch durations inside the different accelerating sections for the range of bunch charges at European XFEL. For better comparison, the rms bunch durations are estimated from the fwhm values in [Fen+] under assumption of Gaussian profiles.

charge	L1	L2	L3	main linac
20 pC	4.5 ps	1.5 ps	190 fs	5 fs
100 pC	4.8 ps	1.6 ps	200 fs	12 fs
250 pC	5.3 ps	1.7 ps	220 fs	25 fs
500 pC	6.0 ps	2.0 ps	260 fs	43 fs
1 nC	6.8 ps	2.2 ps	300 fs	84 fs

Electron bunches with a charge of up to 1 nC are generated by photoelectric emission from an ultraviolet laser pulse hitting a Cs<sub>2</sub>Te photocathode inside the rf gun [Dwe+97]. The laser pulse has a length of around 3 ps rms [CZD20] and transfers its longitudinal and transverse properties to the electron bunch. The gun itself is a normal conducting 1.5-cell cavity operated at 1.3 GHz which allows field amplitudes up to 60 MV/m. Exiting the gun with an energy of roughly 6 MeV the electrons are further accelerated by the first accelerating section L<sub>1</sub> to 130 MeV. In total, the accelerating sections host 97 modules based on TESLA design. Each module consists of eight 9-cell cavities made out of niobium, which are assembled together in a cryostat and cooled down to around 2 K by superfluid helium reaching the state of superconductivity. The cavities are operated at 1.3 GHz with an average acceleration gradient of around 25 MV/m [Wal+16]. Four modules are fed by one rf station, which results in a total of 25 rf stations. The L<sub>1</sub>-section also hosts a module operated at the third harmonic (3.9 GHz) for the linearization of the longitudinal phase space (see Sec. 2.1), as well as a laser heater to counteract microbunching instabilities [Ham+17]. Following the first bunch compressor BC<sub>1</sub>, four modules increase the electron beam energy to 700 MeV until they are further compressed by BC<sub>2</sub>. Another combination of bunch compressor (BC<sub>3</sub>) and 12 modules leads to an energy of 2.4 GeV with which the electrons enter the main linac. Typical compression factors for the three bunch compressors are  $C_1 \approx 3.5$ ,  $C_2 \approx 8$  and  $C_3 \approx 16$  [ZDT19]. The main linac with a length of roughly 1 km consists of 80 modules and is able to reach final beam energies of 17.5 GeV. In order to protect the sensitive permanent magnets of the undulators, the electron beam is bent in the collimator section and an aperture removes particles with unsuited energies and beam halo. In the end, the electron bunches are distributed to the three FEL undulator beamlines where they generate hard X-ray (4 keV to 24 keV in SASE1 and SASE2) or soft X-ray (0.25 keV to 3 keV in SASE3) FEL radiation before being dumped [Dec+20]. More details on the operation of European XFEL are given in Sec. 2.3.1.

As mentioned in Sec. 2.2, the strong dynamics of collective effects make numerical start-to-end simulations of the whole accelerator indispensable. In this way, suitable operation points for the bunch compression can be found. The results of such an optimization for European XFEL and 250 pC bunch charge are presented in Fig. 2.6. The collective and nonlinear effects play a major role and indicate the sensitivity of the entire bunch compression scheme. Nonlinearities of the accelerating rf and the chicane setups are visible at all compression stages of the off-crest acceleration in L<sub>1</sub> to L<sub>3</sub>. The main linac is operated on-crest, but space charge forces remove the negative chirp in the center of the bunch. Resistive wake fields imprint the current profile onto the longitudinal phase space in the collimator section. These simulations model the operation mode which has been mainly used during the measurements in Chaps. 6, 7 and serve as a reference. An overview of the simulated bunch durations for 5 kA peak current with different charges is listed for the four compression stages of European XFEL in Tab. 2.2. Due to the decreasing influence of collective effects, shorter bunch durations can be reached with lower bunch charge. Longitudinal diagnostics are indispensable to set up the accelerator in a way that its bunch properties match those desired from simulations. Small uncertainties in combination with the nonlinearities of collective effects can lead to strong differences of longitudinal beam properties.

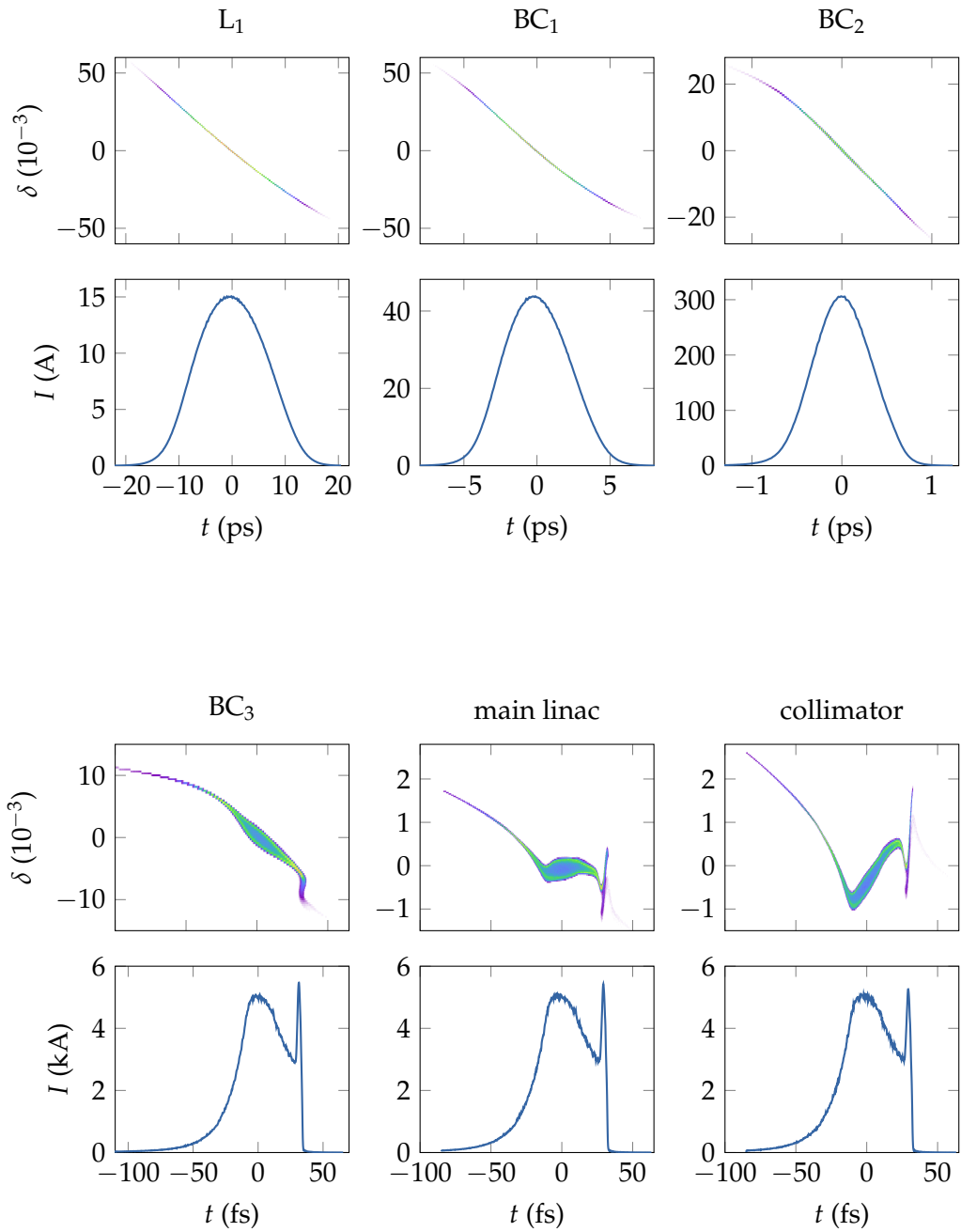


FIGURE 2.6: Simulated longitudinal phase space and resulting current profile of European XFEL at the end of the respective sections for optimized operation at 250 pC with 5 kA peak current. The simulation includes all collective and nonlinear effects, and its data is taken from [Zag20]. Starting from the last bunch compressor BC<sub>3</sub>, the influence of collective effects is clearly visible. In the end, the electron bunch is compressed and the peak current increased by a factor of almost 400. Positive times mark the head of the bunch and negative times the tail.

### 2.3.1 Megahertz XFEL operation

The X-ray properties of FELs are of crucial importance for many experiments in photon science and immensely in demand [O’S01; Dun18; BFH18]. However, the complexity of a XFEL along with enormous construction and operational costs limits the number of available facilities, and the available beam time for user experiments is highly overbooked. At this point, the main advantage of superconducting accelerator technology comes into play: Whereas normal conducting cavities can only accelerate up to a few hundred electron bunches per second with reasonable electric field strengths, the many orders of magnitude reduced rf power dissipation of superconducting cavities [Sch02] allows to accelerate over one million bunches per second [Gal18; Gen+14]. The increased integrated photon flux shortens the time required by each experiment to collect sufficient data and increases the availability of the limited number of XFELs. Besides European XFEL and the soft X-ray FEL FLASH [Ack+07], LCLS-II [Gal18] as well as SHINE [YD19] are now being build as XFELs based on superconducting technology.

The superconducting accelerator of European XFEL is operated in pulsed mode and accelerates up to 2700 bunches at a maximum repetition rate of 4.5 MHz every tenth of a second (burst mode). In addition, not only one but three FEL beamlines (SASE1, SASE2, SASE3, see Fig. 2.5) are supplied with bunches during one rf pulse. A typical structure of bunch destinations along one rf pulse is shown in Fig. 2.7. Electron bunches are injected with a fixed temporal spacing and, in order to assure stable conditions for each FEL experiment, a fast kicker-septum arrangement guides bunches not requested by the FEL experiments to the dump upstream of the FEL beamlines (see Fig. 2.5) [Frö+19]. This way the bunch patterns in the individual FEL beamlines can be independently set without changing the accelerator bunch pattern. Also, bunches that are injected during rise or fall time of the flat-top magnetic kicker for the SASE2 beamline are sent to the dump upstream of the FEL beamlines. The rf pulse has a duration of up to 600  $\mu\text{s}$  and can be split into different flat-tops. These flat-tops allow to individually optimize the rf properties for SASE1/3 and SASE2 bunches within certain limits. By shifting the timing of the SASE2 flat-top kicker, the position of the SASE1/3 and SASE2 bunches may also be reversed.

As discussed in Sec. 2.2, the high electron beam densities for XFELs make longitudinal beam diagnostics indispensable. Additionally, many FEL experiments profit

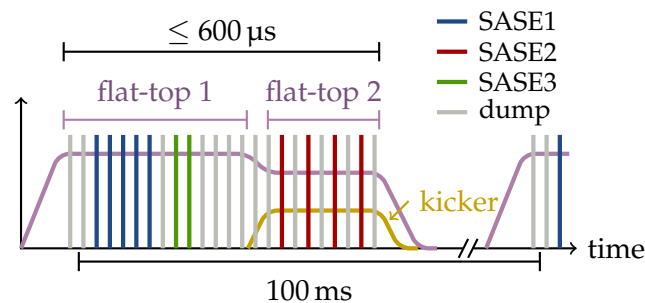


FIGURE 2.7: Schematic of a possible bunch pattern along one rf pulse of European XFEL. Electron bunches (vertical lines) are sent by magnetic kickers to their respective destinations as indicated by the different colours. Bunches during rise or fall time of the SASE2 kicker (yellow) are sent to the dump upstream of the FEL beamlines. For independent optimization of the different FEL beamlines, the rf (purple) amplitude and phase can be individually optimized by dividing it in up to three rf flat-tops.

from the knowledge of the photon pulse duration which is determined by the electron bunch profile to a great part [Beh+12]. Hence, the following section deals with typical implementations of longitudinal beam diagnostics at XFELs using the example of European XFEL.

## 2.4 Longitudinal Diagnostics

Longitudinal current profile monitors are essential to understand the physical processes during acceleration and compression as well as to optimize and stabilize the FEL radiation pulses. They are a prerequisite for feedback systems on bunch compression and beam energy. However, the FEL radiation pulses that are generated by the electron bunches are used to study shortest processes on the molecular level and belong to the shortest events that have ever been directly created by mankind. Thus it is clear that well-known reference processes, which could be used to sample the electron bunch itself, are not yet available. Instead, the characterization of the current profile relies on creative solutions to translate the temporal profile of the bunch to another measurable distribution. For diagnostics at XFELs, spatial and spectral domain are employed to monitor the current profile. An overview of applied diagnostics is given in e. g. [Sch16]. This section however is restricted to methods implemented at European XFEL, which enable bunch duration monitoring down to the femtosecond level. These diagnostics are used in Chaps. 6, 7 as references for the noninvasive current profile monitor installed within the scope of this thesis.

### 2.4.1 Transverse deflective structure

A technique utilizing the spatial dimension for longitudinal bunch profile measurements at linacs with few-femtosecond resolution is based on a so-called transverse deflecting structure (TDS). It was first introduced at SLAC [EFK00; Akr+01] and is currently used at many existing FEL facilities worldwide (see e.g. [Mae+12; Kre+13]). Ongoing research and development yielding new possibilities (see e.g. [Cra+20]) underline the versatility of this method. The basic principle is to deflect the electrons in transverse direction while the strength of the kick depends on their longitudinal position inside the bunch. In this way, the longitudinal distribution is transferred to a transverse distribution and can be monitored on e.g. a scintillation screen. The derivation here follows closely the detailed description in [Yan15], where also the TDS setups at European XFEL are presented. European XFEL hosts a TDS in the  $L_1$  section and after the  $BC_3$  section. However, the TDS principle will be explained using the setup downstream of the  $BC_3$  section (see Fig. 2.5) and the TDS setup is illustrated in Fig. 2.8. In this section, the current profile is monitored at final compression. It will be of importance for the determination of the spectrometer sensitivity (Chap. 5) as well as for benchmarking the reconstructed current profiles (Chaps. 6, 7).

The electron bunch (gray) enters the  $L_{\text{TDS}} = 3.6$  m long TDS, which is operated at  $f_{\text{TDS}} = 2.997$  GHz and is designed to mainly contain a horizontal electric field mode with a phase velocity close to the speed of light  $c$  [Zav16]. While the electrons with momentum  $p$  pass the structure their phase with the electric field (orange line) of amplitude  $E_0$  remains constant and they obtain a horizontal kick given by

$$\Delta x'(\zeta) = \frac{eE_0 L_{\text{TDS}}}{c p} \sin\left(\frac{2\pi}{c} f_{\text{TDS}} \zeta + \phi_{\text{TDS}}\right). \quad (2.11)$$

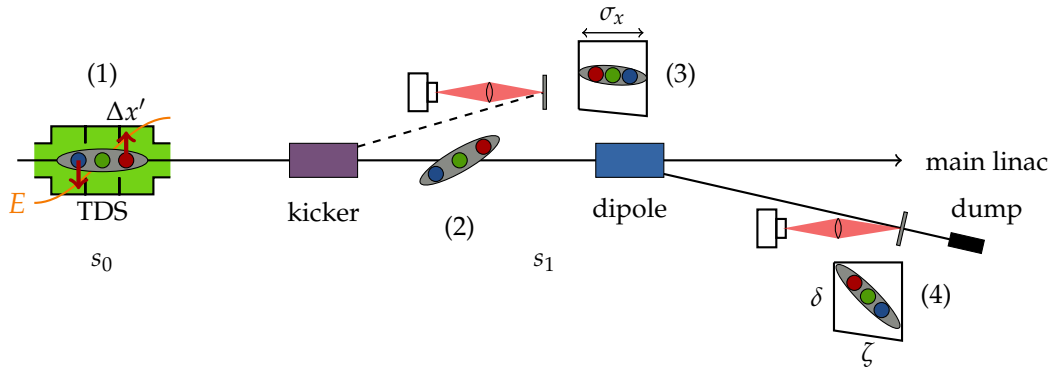


FIGURE 2.8: Schematic overview of the TDS section after last bunch compressor  $BC_3$ . Inside the TDS, the electrons experience a horizontal kick depending on their longitudinal intra-bunch coordinate. This kick results downstream in horizontal offset and the longitudinal bunch profile can be monitored on an off-axis scintillation screen onto which a magnetic kicker deflects the bunch. In combination with a vertical deflecting dipole further downstream, the energy distribution is simultaneously mapped to the vertical axis. This allows measurements of the longitudinal phase space with high temporal resolution ( $\geq 5$  fs) in the local dump section.

Depending on their longitudinal position  $\zeta$  inside the bunch the electrons experience different kick strengths (1). The maximum effective voltage is hereby 27 MV. For diagnostics purposes, it makes sense to operate the TDS at  $\phi_{\text{TDS}} = 0, \pi, \dots$  as this results in the largest kick slope along the bunch and no deflection of the bunch centroid. The bunch length is small compared to the wavelength of the rf field and Eq. (2.11) can be approximated by

$$\Delta x' \approx \pm 2\pi \frac{eE_0 L_{\text{TDS}} f_{\text{TDS}}}{c^2 p} \zeta. \quad (2.12)$$

At position  $s_1$  downstream of the central TDS position  $s_0$ , the kick results in an offset of the horizontal centroid position  $x_0$  for each temporal slice within the bunch (2). The offset is determined by the parameter  $R_{12}$  of the magnetic transfer lattice:

$$x(s_1) = x_0(s_1) + R_{12} \Delta x' = x_0(s_1) + S \cdot \zeta. \quad (2.13)$$

The dimensionless streak parameter  $S$  of the TDS represents the mapping of the longitudinal intra-bunch  $\zeta$  to the horizontal coordinate  $x$ , which allows to characterize the longitudinal current profile using the horizontal axis of a scintillation screen (3). From Eq. (2.13) it is obvious that observations on the longitudinal current profile can only be made if the offset due to the TDS is larger than the unstreaked ( $S = 0$ ) beam size at the screen. As a consequence the intrinsic beam size  $\sigma_{x0} = \sqrt{\beta_x(s_1) \varepsilon_{n,x} \gamma^{-1}}$  in combination with the streak parameter yields the achievable resolution of a TDS measurement

$$\mathcal{R}_t = \frac{1}{c} \left| \frac{\sigma_{x0}}{S} \right| = \left| \frac{c}{2\pi e} \frac{p}{E_0 L_{\text{TDS}} f_{\text{TDS}}} \sqrt{\frac{\varepsilon_{n,x}}{\gamma \beta_x(s_0)}} \frac{1}{\sin \Delta\psi_x} \right|, \quad (2.14)$$

which is obtained after replacing the parameter  $R_{12} = \sqrt{\beta_x(s_1) \beta_x(s_0)} \sin \Delta\psi_x$  of the magnetic lattice with the horizontal  $\beta$ -functions and the phase advance  $\Delta\psi_x$  between TDS and screen. Optimizing the resolution requires a magnetic lattice that maximizes the horizontal beam size inside the TDS  $\beta_x(s_0)$  and a phase advance  $\Delta\psi_x$  between TDS and screen close to  $\pi/2$ .

By inserting a dipole magnet, that bends the electron beam in vertical direction, the energy distribution can be characterized as well. This electron beam spectrometer (4) will result in a vertical offset of the electrons depending on their energy (blue, red, green). Thus, the longitudinal phase space distribution  $(\zeta, \gamma)$  is mapped to the observable transverse dimensions.

For measurements of the longitudinal phase space at European XFEL, a dipole magnet deflects the beam into a diagnostics dump (see Fig. 2.8). The temporal resolution can be as high as  $\sim 5$  fs with a relative energy resolution around  $10^{-4}$  [Yan15]. These resolutions are achieved with a special electron beam optic that is not compatible with FEL operation. This high resolution mode is used for the calibration of the spectrometer (Chap. 5) as well as for comparative measurements in single bunch operation (Chap. 6). During FEL operation, the TDS can be used in combination with a kicker for current profile measurements. Depending on the bunch repetition rate, the TDS is able to streak one to four consecutive bunches out of the bunch train without disturbing the remaining bunches inside the train due to its filling time below 1  $\mu$ s. The fast kicker deflects one of the streaked bunches onto an off-axis screen (see Fig. 2.8). In this so-called pulse-stealing mode, current profile measurements of a selected bunch of the train are possible without disturbing the FEL operation of the remaining bunches. It is used in Chap. 7 for comparative measurements of the current profile along the bunch train. The energy axis of the longitudinal phase space is not accessible and the temporal resolution suffers from the compatibility with FEL operation. The resolution is limited to  $\sim 15$  fs [Yan15].

## 2.4.2 Bunch compression monitors

Another possibility for longitudinal diagnostic at XFELs is to monitor the bunch duration in the spectral and not spatial domain as in the case of a TDS. As time and frequency domain are linked by Fourier transform, shorter bunches yield a wider frequency spectrum (see Chap. 3). This effect is exploited at European XFEL by the bunch compression monitors (BCM) [PDG14]. Downstream of each bunch compressor, they measure the total radiation intensity emitted by the electron bunch within a certain frequency range. As the bunch duration decreases with each compression stage, the frequency range to be measured shifts to higher frequencies. This is realized by the setup of the BCM stations shown in Fig. 2.9.

After the first compression stage the frequency range to be detected is in the microwave regime (see Tab. 2.2). Therefore the first BCM station hosts rf detector antennas<sup>1</sup> with central detection frequencies around 100 GHz. All following stations are equipped with pyroelectric detectors<sup>2</sup> to detect the intensity in the infrared (IR) regime. Each BCM station hosts two detectors D1/D2. The spectral sensitivity of each detector can be independently optimized to serve different purposes such as coarse and fine channel. The spectral intensity of the radiation transmitted through the beam splitter (BS) can be altered by inserting optical filters (F1/F2) into the beam path. Another possibility is to remotely change the position of the detectors with respect to the focal point of the radiation by the focusing mirrors (transverse) and the linear-motion stages (longitudinal) on which the detectors are mounted. The combination of detectors and pulse-shaping electronics is fast enough to resolve single bunches during MHz operation of European XFEL.

As the BCM detectors carry out an integral measurement of the electron bunches frequency spectrum multiplied with their spectral sensitivity, they do not yield

<sup>1</sup>Millitech DET-08, Virginia Diodes WR5.1R6

<sup>2</sup>InfraTec LIE-301-X004 (custom made)

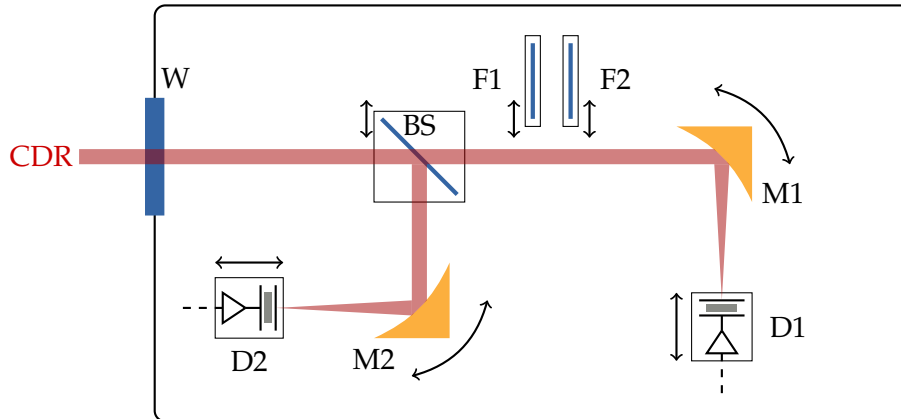


FIGURE 2.9: Schematic overview of the setup for the bunch compressor monitors at European XFEL. Coherent diffraction radiation (CDR) enters the aluminum tank through a vacuum window (W) separating the BCM setup from the accelerator vacuum. For the BCM after the last bunch compressor  $BC_3$ , the aluminum tank is evacuated and a diamond window instead of a z-cut quartz window is used. If the beamsplitter (BS) is inserted, the radiation is focused by gold-coated parabolic mirrors M1/M2 in each path onto the detectors D1/D2. The transmitted beam path hosts the opportunity to insert up to two filters (F1/F2) with different spectral transmissions into the beam path.

any information about the shape of the longitudinal electron bunch distribution. The detected signal only allows a determination of the overall bunch duration. However, as will be studied in Sec. 6.3.2, different bunch durations with different shapes can lead to the same signal at the BCM.

Nonetheless, as the BCs are served by noninvasive coherent diffraction radiation (see Sec. 3.4) they enable an online monitoring of the longitudinal bunch properties for all bunches inside the train. This opens up the possibility to correlate experimental data obtained with the X-ray FEL pulse with the longitudinal electron bunch properties. Additionally, this information can be used to stabilize the accelerator operation along the bunch train [Din18].

If the complete frequency spectrum of the electron bunch is known, the shape of the current profile can be characterized as well. This requires spectral measurements over large frequency ranges with a large variation of intensity. The work of this thesis enables these measurements on single-shot basis at European XFEL using coherent diffraction radiation. Thus, the following chapter deals with the fundamental properties of transition/diffraction radiation as well as the connection between current profile and coherent radiation spectrum.



## Chapter 3

# Coherent Radiation Diagnostics

The technique used in this thesis to characterize the electron current profile is based on coherent radiation diagnostic (CRD). CRD makes use of the fact that the spectral distribution of radiation emitted by a short electron bunch depends on its longitudinal structure. In the introduction of this chapter, the underlying fundamental process of coherent emission of radiation is shortly motivated before it will be studied in detail in the following sections.

In case of a radiation wavelength much shorter than the electron bunch itself, the phase relation of wavefronts from individual electrons is randomly distributed (see Fig. 3.1 left). This stochastic superposition leads to an overall amplitude of the electric field scaling with the square root of the individual emitters. Thus, the intensity of the radiation scales linearly with the number of electrons  $N_e$  inside the bunch. This process is called incoherent emission. However, if the wavelength of the radiation is much longer than the electron bunch, the phase difference between the individual wavefronts is small and the whole bunch radiates like a single particle (see Fig. 3.1 right). In this case, the field amplitude increases linearly with the number of electrons – constructive interference – and the intensity consequently scales quadratically with the number of electrons involved. This process is called coherent emission.

An electron bunch used in XFELs has typically a charge of a few ten picocoulomb up to one nanocoulomb. Thus, the ratio of radiated intensity in the fully coherent to the incoherent regime is  $N_e \sim 10^8$ – $10^9$ . The radiation intensity of short bunches is higher at short wavelengths (high frequencies) than those of long bunches. Of peculiar interest for CRD is hereby the frequency range in which the transition from the fully incoherent to the fully coherent regime takes place. Here, the spectral distribution is described by the specific details of the longitudinal structure and not only the overall length of the electron bunch.

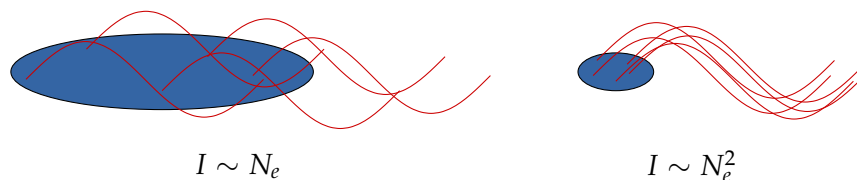


FIGURE 3.1: Incoherent (left) and coherent (right) emission of radiation from an electron bunch. For incoherent radiation, there is no fixed phase relation. If the wavelength of the radiation is longer than the electron bunch, the wavefronts add up coherently due to the fixed phase relation which leads to a quadratic increase of the intensity  $I$  with the number of electrons  $N_e$ .

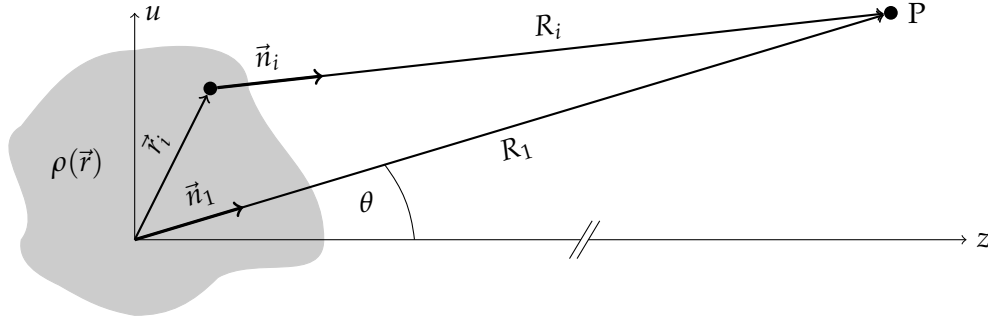


FIGURE 3.2: Geometry of vectors and positions for the mathematical derivation of coherent emission. Within the ensemble of density  $\rho(\vec{r})$ , electrons are distributed with position  $\vec{r}_i$  along transverse ( $u$ ) and longitudinal axis ( $z$ ). The observer of the emitted radiation is located at point P. The distance to the observer is assumed to be much larger than the dimensions of the bunch as indicated by the discontinuity on the  $z$ -axis.  $\vec{n}_1$  and  $\vec{n}_i$  are normalized vectors.

In the following section, the mathematical description of coherent emission from an electron bunch will be derived and lead to the definition of the form factor. The connection between current profile and form factor are studied thereafter, before transition and diffraction radiation as source for coherently emitted radiation are investigated.

### 3.1 Coherent Emission

This section follows closely the elaboration in [GS06]. Figure 3.2 illustrates the geometrical setup with a spatial distribution of electrons described by the density  $\rho(\vec{r})$  and an observation point P. The distance to the observer is assumed to be much larger than the dimensions of the electron ensemble. This results in the far-field condition  $\vec{n}_1 \vec{n}_i \approx 1$  and each electron  $i$  emits the same electric field  $\vec{E}_i$  only with a time offset  $\Delta t_i$  to a reference electron at the origin

$$\vec{E}(t) = \sum_{i=1}^{N_e} \vec{E}_i(t) = \sum_{i=1}^{N_e} \vec{E}_1(t + \Delta t_i). \quad (3.1)$$

The spectral energy density  $dU/d\omega$  per solid angle  $\Omega$  in the far field regime is proportional to the square of the absolute electric field (see e.g. the appendix of [GS06])

$$\frac{d^2U}{d\omega d\Omega}(\omega) \propto |\vec{E}(\omega)|^2. \quad (3.2)$$

The electric field  $\vec{E}(\omega)$  in the frequency domain can be retrieved by applying a Fourier transform to the total electric field  $\vec{E}(t)$  in time domain. The Fourier transform can be decomposed into the product of the electric field of a single electron and the sum over all phase terms after substituting the integration variable  $t = \tau - \Delta t_i$ :

$$\begin{aligned} \vec{E}(\omega) &= \frac{1}{\sqrt{2\pi}} \int_{-\infty}^{+\infty} \sum_{i=1}^{N_e} \vec{E}_1(t + \Delta t_i) e^{-i\omega t} dt = \frac{1}{\sqrt{2\pi}} \sum_{i=1}^{N_e} \int_{-\infty}^{+\infty} \vec{E}_1(\tau) e^{-i\omega(\tau - \Delta t_i)} d\tau \\ &= \vec{E}_1(\omega) \sum_{i=1}^{N_e} e^{i\omega \Delta t_i}. \end{aligned} \quad (3.3)$$

The time shift induced by the path length difference can be expressed by using the far field condition  $\vec{n}_1 \vec{n}_i \approx 1$  and  $\vec{r}_i + R_i \vec{n}_i = R_1 \vec{n}_1$  as

$$\Delta t_i = \frac{R_i - R_1}{c} = -\frac{\vec{n}_1 \vec{r}_i}{c} = -\frac{\vec{k} \vec{r}_i}{ck}. \quad (3.4)$$

Here, the wave vector  $\vec{k} = \vec{n}_1 \omega / c$  has been introduced. The spectral energy density becomes

$$\frac{d^2 U}{d\omega d\Omega} \propto \left| E_1(\omega) \sum_{i=1}^{N_e} e^{-i\vec{r}_i \vec{k}} \right|^2 = \left[ \frac{d^2 U}{d\omega d\Omega} \right]_1 \left| \sum_{i=1}^{N_e} e^{-i\vec{r}_i \vec{k}} \right|^2 \quad (3.5)$$

with the spectral energy density of a single electron  $[d^2 U / d\omega d\Omega]_1$ . The quadratic absolute value of the sum can be segmented into the two complex conjugates

$$\left| \sum_{i=1}^{N_e} e^{-i\vec{k} \vec{r}_i} \right|^2 = \sum_{i=1}^{N_e} e^{-i\vec{k} \vec{r}_i} \sum_{j=1}^{N_e} e^{+i\vec{k} \vec{r}_j} = N_e + \sum_{i=1}^{N_e} e^{-i\vec{k} \vec{r}_i} \sum_{\substack{j=1 \\ j \neq i}}^{N_e} e^{i\vec{k} \vec{r}_j}. \quad (3.6)$$

After inserting the Dirac function  $\delta(x)$ , integration and sum can be reversed

$$\sum_{i=1}^{N_e} e^{-i\vec{k} \vec{r}_i} = \sum_{i=1}^{N_e} \int_{-\infty}^{+\infty} \delta(\vec{r} - \vec{r}_i) e^{-i\vec{k} \vec{r}_i} d\vec{r} = \int_{-\infty}^{+\infty} \sum_{i=1}^{N_e} \delta(\vec{r} - \vec{r}_i) e^{-i\vec{k} \vec{r}} d\vec{r}. \quad (3.7)$$

This allows to change from the microscopical positions of the electrons to the normalized density function of the ensemble average

$$\rho(\vec{r}) = \frac{1}{N_e} \left\langle \sum_{i=1}^{N_e} \delta(\vec{r} - \vec{r}_i) \right\rangle, \quad (3.8)$$

such that Eq. (3.6) becomes

$$\left| \sum_{i=1}^{N_e} e^{-i\vec{k} \vec{r}_i} \right|^2 = N_e + N_e \int_{-\infty}^{+\infty} \rho(\vec{r}) e^{-i\vec{k} \vec{r}} d\vec{r} \cdot (N_e - 1) \int_{-\infty}^{\infty} \rho(\vec{r}) e^{i\vec{k} \vec{r}} d\vec{r}. \quad (3.9)$$

With the definition of the form factor

$$F_{3D}(\vec{k}) = \int_{-\infty}^{\infty} \rho(\vec{r}) e^{-i\vec{k} \vec{r}} d\vec{r}, \quad (3.10)$$

as the Fourier transform of the bunch density function, the spectral energy density according to Eqs. (3.5), (3.9) finally reads

$$\frac{d^2 U}{d\omega d\Omega}(\vec{k}) = \left[ \frac{d^2 U}{d\omega d\Omega} \right]_1(\vec{k}) \left( N_e + N_e(N_e - 1) |F_{3D}(\vec{k})|^2 \right). \quad (3.11)$$

The overall spectral energy density is a superposition of incoherent and coherent part. As mentioned in this chapter's introduction, the spectral intensity of the incoherent part increases only linearly with the number of electrons inside the bunch and is independent of the bunch structure. In contrast, the coherent part scales quadratically and depends on the form factor  $|F_{3D}(\vec{k})|$  of the electron bunch.

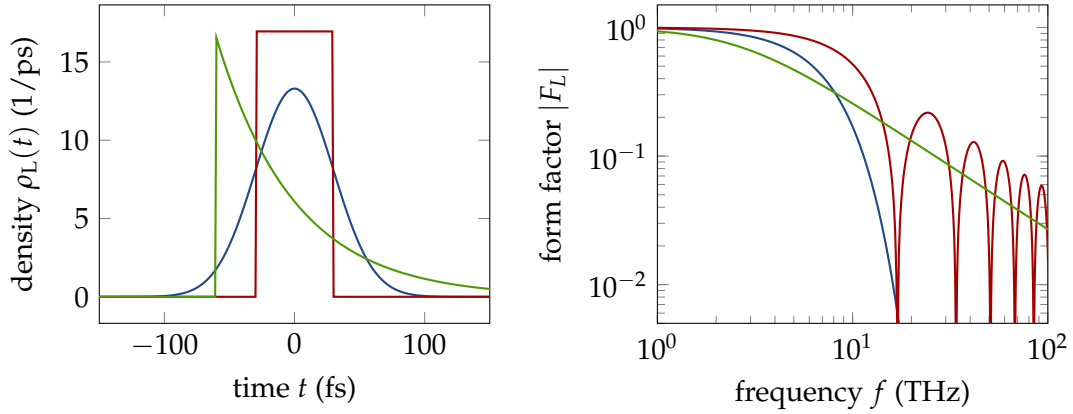


FIGURE 3.3: Different longitudinal electron bunch distributions (left) and the corresponding form factor modulus (right). The Gaussian, rectangular and exponential-step like profiles exhibit a distinct and characteristic form factor modulus.

### 3.2 Form Factor and Current Profile

As seen in Sec. 3.1, the form factor depends generally on the full three dimensional distribution of the electron bunch. Radiation emitted by highly-relativistic electrons with Lorentz factor  $\gamma$  is mainly concentrated in a small cone with opening angles in the vicinity of  $1/\gamma$  (see e.g. Sec. 3.4). Thus, radiation is usually emitted within a few milliradian, and the time difference of the individual emitters is mainly given by the longitudinal distribution. This suppresses the influence of the transverse electron distribution, such that it is appropriate to decompose the form factor into a transverse and longitudinal component as a function of  $\vec{k} = (k_x, k_y, k_z)$  by neglecting transverse-longitudinal correlations [GS06]:

$$F_{3D}(\vec{k}) = \iint \rho_{\text{trans}}(x, y) e^{-i(k_x x + k_y y)} dx dy \int \rho_L(z) e^{-ik_z z} dz = F_T(k_x, k_y) \cdot F_L(k_z). \quad (3.12)$$

It will be shown in Sec. 3.4, that it is also appropriate to neglect the influence of the transverse form factor for the experimental methods applied in this thesis and assume  $|\vec{k}| \approx k_z$  such that  $f = k_z c / 2\pi$  as well as  $|F_T(f)| = 1$ . The measured spectral energy density according to Eq. (3.11) becomes consequently for the large number of electrons inside the bunches of XFELs:

$$\frac{dU}{df}(f) \approx \left[ \frac{dU}{df}(f) \right]_1 \left( N_e + N_e^2 |F_L(f)|^2 \right). \quad (3.13)$$

Figure 3.3 shows the relation of three different density profiles on the form factor modulus  $|F_L(f)|$  which defines the spectral distribution of the coherently emitted radiation. For all profiles, the depicted form factor modulus approaches  $|F_L(0)| = 1$  as a consequence of the normalized density function  $\int \rho(t) dt = 1$  and the definition of the form factor in Eq. (3.10). The form factor decreases towards high frequencies with different behaviour depending on the density profile. While the form factor of a Gaussian profile exhibits a steep and continuous drop, interference due to the edges of the rectangular profile leads to an oscillating behaviour with pronounced minima. The sharp edge of the exponential-step function leads to high frequency components and a slowly decreasing form factor.

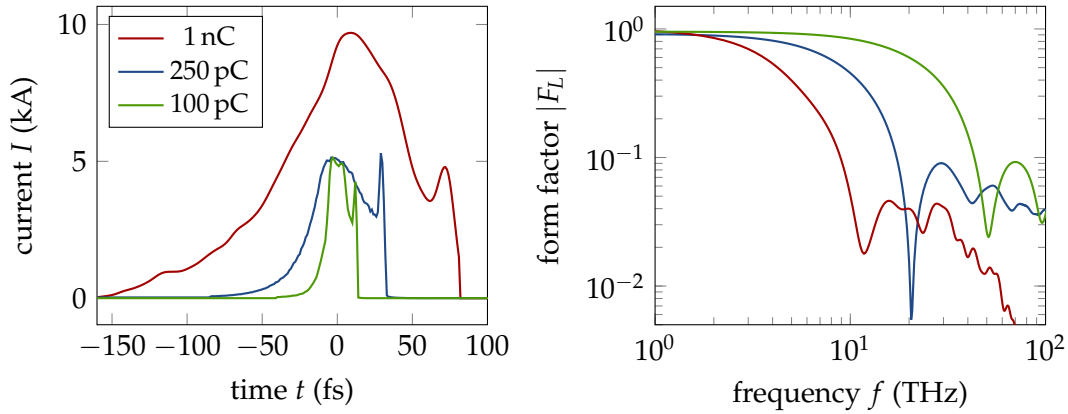


FIGURE 3.4: Current profiles (left) from start-to-end simulations for different operation modes (1 nC, 250 pC, 100 pC bunch charge) of European XFEL [Zag20] and their corresponding form factors (right). The transition between coherent and incoherent emission described by the form factor takes place in the THz and infrared regime, which is thus the frequency range for current profile diagnostics.

Current profiles and resulting form factors of start-to-end-simulations of European XFEL are presented in Fig. 3.4. The current profiles (left) of different operation modes vary strongly in duration (see Tab. 2.2) and show a complex temporal structure. The structure also results in a complex behaviour of the form factors (right) compared to the model functions shown in Fig. 3.3. The form factor of shorter profiles extends to higher frequencies. For all three operation modes, the form factor decreases within the frequency region 1 THz to 100 THz by more than an order of magnitude, which indicates the frequency region of interest for CRD.

Experimentally, the form factor modulus can be determined by

$$\frac{dU}{df}(f) \approx \left[ \frac{dU}{df}(f) \right]_1 N_e^2 |F_L(f)|^2, \quad (3.14)$$

if the coherent part of Eq. (3.13) is much more intense than the incoherent background. This approximation allows form factor measurements down to  $|F_L| \gtrsim 10/\sqrt{N_e}$ . For XFELs, this results in a well tolerable limit of roughly  $|F_L| > 10^{-4} - 10^{-3}$ . High frequency structures resulting in even smaller form factors are anyway only due to negligible nuances of the current profile. If both, the ratio of the spectral energy density of the coherent radiation to the spectral energy density of a single electron and the number of electrons inside the bunch, are known, the longitudinal form factor modulus can easily be identified. Spectroscopic measurements yielding the ratio of the spectral energy density are the main subject of this thesis and require a good knowledge of the expected signal from a single electron, i.e. the incoherent radiation (see Chap. 5).

### 3.2.1 Ambiguities

Only the form factor modulus is experimentally accessible by spectral measurements according to Eq. (3.14). The phase  $\phi(f)$  of the complex form factor

$$F_L(f) = |F_L(f)| e^{i\phi(f)}, \quad (3.15)$$

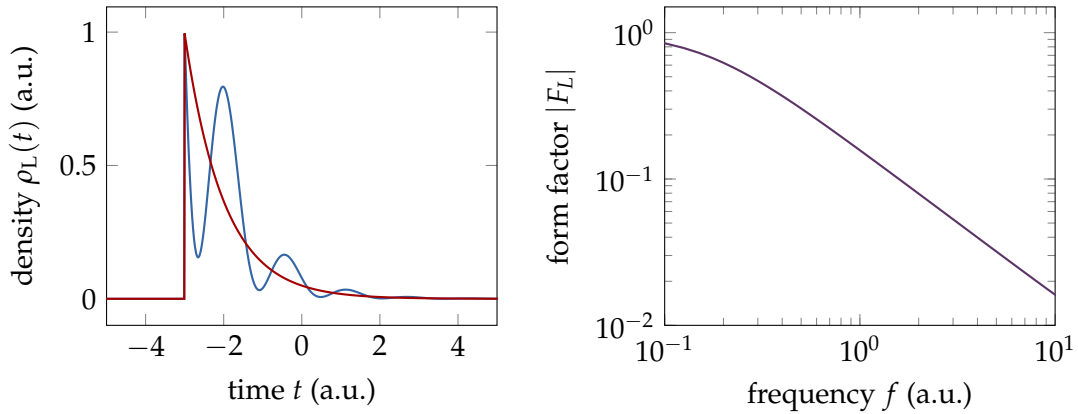


FIGURE 3.5: Example of different density profiles (left) yielding different phases but the same modulus of the form factor (right).

which is needed to obtain the density profile  $\rho_L(t)$  based on Fourier transform

$$\rho_L(t) = \frac{1}{2\pi} \int F_L(f) e^{i2\pi ft} df, \quad (3.16)$$

remains unknown. This leads in general to inevitable ambiguities between current profile and spectral energy density [Sch+18]:

- Inverting the temporal density profile  $\rho_L(t) \mapsto \rho_L(-t)$  leads to the same spectrum.
- A time shift of the temporal density profile  $\rho_L(t) \mapsto \rho_L(t + \Delta t)$  results in the same form factor modulus.
- Different current profiles may lead to the same form factor modulus and only the form factor phase is different.

A time shift is of no importance for longitudinal current profile measurements and the time direction may already be expected from simulation results or once identified by a comparative diagnostic. The ambiguity of the associated current profile however requires adequate considerations. A famous example is given by the functions considered by Akutowicz [Aku56] which are presented in Fig. 3.5. Even though the blue current profile on the left shows large modulations which are not present for the red current profile, the form factor modulus on the right is identical. In order to calculate a current profile using the Fourier transformation of Eq. (3.16) the phase  $\phi(f)$  is mandatory. Retrieval methods that yield adequate phases of the form factor from its modulus alone are studied in the following section for realistic electron bunch current profiles.

### 3.3 Current Profile Reconstructions

For reconstructions of the current profile from the form factor modulus, the following very important fact must be considered: It is mathematically impossible in the one dimensional case (see [BN85] for a detailed discussion) to retrieve an unambiguous phase from the form factor modulus. Thus, also a mathematically exact and unique density profile cannot be calculated by applying Eq. (3.16) to the results

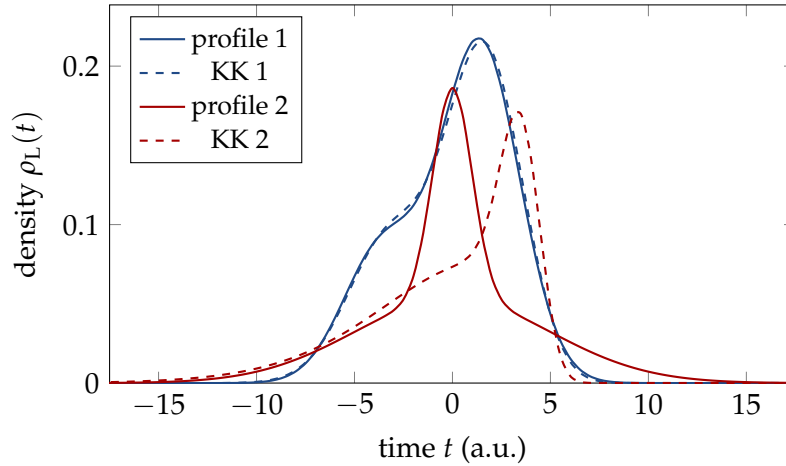


FIGURE 3.6: Example for a failure of the Kramers-Kronig phase. For profile 1 the current profile can be well reconstructed. This is not the case for profile 2 due to zeros of the form factor in the upper half of the complex  $\omega$  plane (see [Sch+18]).

of spectroscopic measurements, i.e. Eq. (3.14). Nonetheless, it will be shown that for applications as longitudinal diagnostics it is possible to specify an associated current profile with sufficient significance. In order to empower online measurements, this reconstruction method must not only yield a trustworthy and well-defined density profile, but must also be fast and reliable. This section will introduce methods based on analytical and iterative approaches and study them with respect to the above requirements. This will finally lead to the reconstruction algorithm that has been developed for current profile measurements as presented in this thesis.

The Kramers-Kronig dispersion relation [de 26; Kra27] links real and imaginary part of the Fourier transform of causal functions. It has been adapted to retrieve the phase from the modulus alone [Woo72], which – applied to form factor of electron bunches – yields the principle-value integral [LHS94]

$$\phi_{\text{KK}}(f) = \frac{2f}{\pi} \mathcal{P} \int_0^{\infty} \frac{\ln |F(f')| - \ln |F(f)|}{f^2 - f'^2} df'. \quad (3.17)$$

The Kramers-Kronig phase  $\phi_{\text{KK}}$  is derived by an expansion to the complex  $\omega$  plane and using a fundamental assumption: The complex form factor does not have any zeros in the upper half of the complex  $\omega$  plane. For a mathematical derivation and rigorous description of this problem please refer to [Sch+18]. At this point it is only important to know that this assumption cannot be considered to be true for all possible current profiles. It also cannot be determined from the form factor modulus whether this requirement is fulfilled or not. An example for the violation of this assumption is given in Fig. 3.6. The form factor of profile 1 has no zeros in the upper half of the complex  $\omega$  plane. The Kramers-Kronig phase is calculated from the form factor based on Eq. (3.17). The resulting Kramers-Kronig profile (dashed line) reconstructs the actual profile well. The form factor of profile 2 exhibits zeros in the upper half of the complex  $\omega$  plane and thus violates the assumption. Here, the Kramers-Kronig phase leads to significant differences between the density profile reconstructed from the form factor modulus and the actual density profile. It should be noted that independently of fulfilling the assumption or not, the profiles do not exhibit inconceivable structures for bunches at XFELs. Nevertheless, also for profile 2 peak current, bunch duration and overall structure are still satisfactorily reproduced. With respect

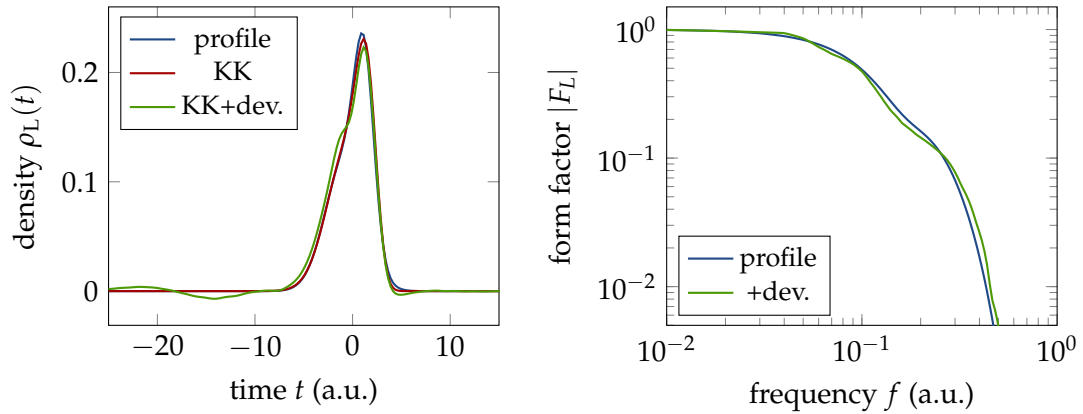


FIGURE 3.7: Density profile reconstruction using the Kramers-Kronig phase retrieval. Form factors (right) without any deviation (blue) and with small deviations (green) yield different reconstructions to the actual current profile (left, blue). While without noise the density profile is almost perfectly reconstructed (red), the form factor deviations lead to an unphysical density function with negative values (green).

to an application as an online monitor, the analytic Kramers-Kronig phase enables fast reconstructions with an unique current profile for each form factor.

However, the analytical evaluation of Eq. (3.17) requires an exact specification of the form factor and does not consider any uncertainties. In reality, this cannot be fulfilled as uncertainties on the measured form factor are always present. As a consequence, even a minor misconduct of the form factor may yield a density profile with negative currents as is shown in Fig. 3.7. These form factor deviations often lead to an unphysical density profile with long tails and negative undershoots. For trustworthy current profile reconstructions, the spectrometer sensitivity must be precisely known to avoid misconducts in form factor measurements. For the spectroscopic measurements in this thesis, a systematic procedure to identify the sensitivity is given in Chap. 5.

The Gerchberg-Saxton algorithm has been initially developed to retrieve the phase of two-dimensional problems, e.g. to retrieve the complex wavefront from image and diffraction pattern [GS72], for which a quasi-unambiguous solution exists [Kli06]. It was the first iterative method to be introduced to the one-dimensional problem of longitudinal beam diagnostics [Baj+13] and other algorithms have followed (see e.g. [Hei+15]). The principle of the Gerchberg-Saxton algorithm is illustrated in Fig. 3.8. The algorithm starts with any initial phase function  $\phi_0(f)$  to form the initial complex form factor together with measured modulus  $|F_L(f)|$ . The respective density profile  $\rho_n^*$  is obtained by an inverse fast Fourier transform (IFFT) and is inspected to fulfill the fundamental constraints in the time domain (e.g.  $\rho(t) \not\leq 0$ ). If the constraints are violated the density profile is adjusted accordingly to  $\rho_n(t)$ . A fast Fourier transform (FFT) yields a new complex form factor with modulus  $|E_n(f)|$  and phase  $\phi_n(f)$ . The modulus is replaced with the measured modulus  $|F_L(f)|$ . The phase  $\phi_n(f)$  based on the adapted time domain profile  $\rho_n(t)$  is kept and used as the input for the next loop  $n \mapsto n + 1$  of the algorithm. The algorithm is executed until the time domain constraints are fulfilled or  $|E_n(f)|$  converges.

The final current profile of the Gerchberg-Saxton algorithm depends on the initial start phase as is depicted in Fig. 3.9. As a consequence of the ambiguity (see Sec. 3.2), the same form factor measurement results in a variety of current profiles. Hereby not all of them reproduce the actual current profile precisely. The solution can be

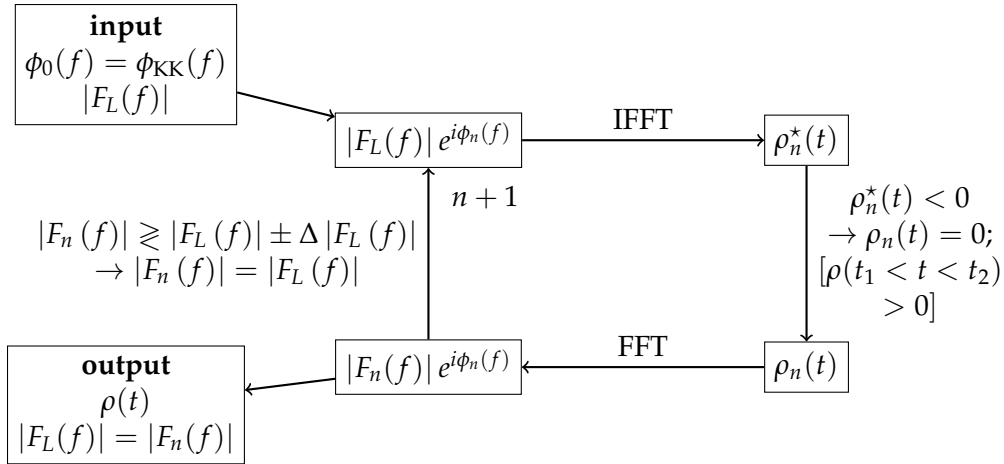


FIGURE 3.8: Block-diagram of the Gerchberg-Saxton algorithm implemented in this thesis which utilizes the Kramers-Kronig phase as start phase. In each loop, a density profile  $\rho_n^*(t)$  is calculated by fast inverse Fourier transform (IFFT) of the measured form factor modulus  $|F_L(f)|$  combined with the phase of the previous loop  $\phi_n(f)$ . The density profile is adapted such that it does not contain negative currents. For the results in this thesis, the constraint on intermediate zeros has been added with respect to [Sch+20]. From the complex form factor of the adapted density profile  $\rho_n(t)$  the phase is taken as input for the next loop while the modulus is replaced by the measurement where it does not agree within its uncertainty  $\Delta |F_L(f)|$ .

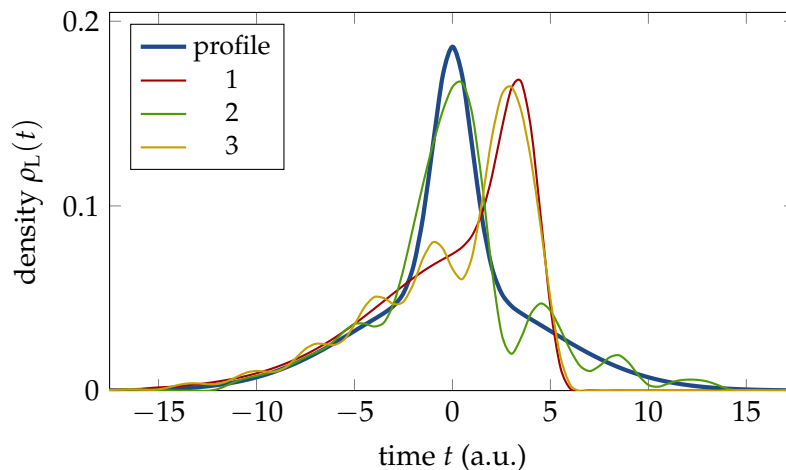


FIGURE 3.9: Three solutions (1,2,3) of the iterative Gerchberg-Saxton algorithm starting with random phases. Using random phases, the density profiles of the iterative algorithm often result in complex structures which are much less likely to present current profiles at XFELs.

arranged in clusters, defining a possible parameter space of the longitudinal current profile [Has18]. However, for this the algorithm has to be executed numerous times while each execution needs many iterations. Thus, this method is not desirable for online current profile measurements. Furthermore, the individual solutions of the algorithm do not necessarily reflect compact bunch shapes as expected at XFELs.

The convergence of the algorithm can be sped up if it is not started with completely random phases, but with phases already having some connection to a reasonable density profile [Fie78]. Additionally, a unique result can be retrieved if the Gerchberg-Saxton algorithm is started with the Kramers-Kronig phase  $\phi_{\text{KK}}$  as was introduced in [Sch+20]. By this implementation of the Gerchberg-Saxton algorithm, which has been illustrated in Fig. 3.8, the start phase of the algorithm is always clearly defined and leads to a unique solution for each form factor. The algorithm quickly removes the tails and negative undershoots of the current profile reconstructed with the Kramers-Kronig phase  $\phi_{\text{KK}}$  for small misconducts of the measured form factor (see Fig. 3.7). Because this requires mostly only small modifications of the initial density profile, the algorithm converges extremely fast (see Fig. 6.3). The result is still subject to the assumption that there are no zeros of the complex form factor in the upper half of the complex  $\omega$  plane. Nevertheless, the iterative reevaluation of the current profile leads to a highly improved robustness and trustworthiness. In addition, even if the fundamental assumption of the Kramers-Kronig phase is violated, bunch duration, peak current and characteristic properties may still be correctly retrieved as illustrated in Fig. 3.6. In studies, which have been also based on work carried out in this thesis, this method has enabled accurate current profile measurements at FLASH. These results were confirmed using a transverse deflecting structure and compared to other phase retrieval methods [Sch+20]. Another important feature of this method is that it allows small variations of the form factor within the measurement uncertainties  $|\Delta F_L(f)|$  (see Fig. 3.8). A detailed discussion of the general aspects of analytical and iterative phase retrieval algorithm can be found in [Sch+18].

The current profile reconstruction procedure of [Sch+20] has been further developed for the results of this thesis. A constraint that denies intermediate zeros in the current profile, i.e.  $\rho(t_1 < t < t_2) > 0$  while  $\rho(t < t_1) = 0$  and  $\rho(t > t_2) = 0$ , has been added (see Fig. 3.8). This results in an even faster convergence of the algorithm and compact current profiles. The constraints in the frequency domain  $|\Delta F_L(f)|$  have been optimized and represent the measurement uncertainties of the form factor in an accurate way. Now a successful convergence towards only positive density profiles is guaranteed. An example showing the individual steps of the algorithm for data preparation and current profile reconstruction is given with data of an actual measurement in Sec. 6.1. With this procedure, a fast (<100 ms), unique and trustworthy current profile reconstruction is implemented, which is perfectly suited for online monitoring.

The numerical evaluation of the density profile from the complex form factor based on the fast Fourier transform algorithm (FFT) requires not only knowledge about modulus and phase of the complex form factor on a linear grid, but also links this spectral grid of the form factor to a temporal grid of the density profile. As a consequence, the highest frequency  $f_{\text{max}}$  of the form factor determines the temporal spacing  $\Delta t = 1/2f_{\text{max}}$ <sup>1</sup> and thereby the smallest resolvable features of the density profile (see e.g. [RG75]). Additionally, the form factor must be known all the way

<sup>1</sup>The factor 2 appears because the total frequency and time window is given by  $(-f_{\text{max}}, f_{\text{max}})$  and respectively  $(-t_{\text{max}}, t_{\text{max}})$ .

down to  $|F_L(0)| = 1$ , and the frequency grid spacing  $\Delta f$  (and by this the smallest frequency  $f > 0$  Hz) results in the time window  $t_{\max} = 1/2\Delta f$  of the density profile. At European XFEL, this requires to monitor the form factor from frequencies around 1 THz, where it has reached its asymptotic limit of 1 (see Fig. 3.4), up to any frequency which results in the temporal resolution of the measurement (see Sec. 6.1.1, App. B). Above frequencies of 100 THz however, the form factor has usually decreased to small values and any significant contribution is due to small substructures of the current profile and not its overall shape.

### 3.4 Transition and Diffraction Radiation

As seen in the previous sections, the form factor must be determined over a wide frequency range for reliable reconstructions of the longitudinal electron bunch structure. In consequence, the single electron radiation process has to support the required spectral interval (see Eq. (3.14)). For this purpose, several radiation sources have been utilized. A widely used technique (e.g. [LHS94; Shi+94; Max+13]) is transition radiation (TR), which is – as will be shown in this section – very broadband and easily accessible, but invasive to the electron beam. Typical noninvasive radiation sources are diffraction radiation (DR) (e.g. [Cas+01]), synchrotron radiation (e.g. [LHS94]), edge radiation (e.g. [And+09]), Smith-Purcell (e.g. [And+14]) and Cherenkov diffraction radiation (e.g. [Cur+20]). At European XFEL, the closely related transition and diffraction radiation are employed for longitudinal electron bunch diagnostics.

TR occurs when a relativistic charged particle crosses the boundary between vacuum and a medium [GF45]. The difference of the dielectric constants requires a reconfiguration of the electric field which leads to the emission of backward directed radiation when the particle enters the medium. The same fundamental process leads to the emission of diffraction radiation when the particle does not impinge on the medium but passes within the extension of the particle's Coulomb field. However, while TR has enabled current profile characterization of bunches with rms durations below 100 fs [Sch+20], DR has been restricted to sub picosecond bunch durations due to lack of intensity in the infrared region [CSS05]. In this section, it will be demonstrated that the beam energies of XFELs overcome this limitation and DR empowers similar conditions as TR while being noninvasive.

Due to field retardation, the electric field of relativistic single electrons is essentially transverse, which allows to utilize the Weizsäcker-Williams method of virtual quanta [Jac03] for the computation of the radiation field. The virtual photons of the Coulomb field are converted to real photons at the surface of a metallic screen and the electric field is thus reflected. This method is explained in [CSS05] and the description here follows this reference. At the screen in transverse distance  $\rho$  from the electron, the created radiation field is described by the radial Coulomb field of the electron with charge  $e$

$$E_0(t, \rho) = -\frac{e}{4\pi\epsilon_0} \frac{\gamma\rho}{(\rho^2 + \gamma^2 c^2 \beta^2 t^2)^{3/2}} \quad (3.18)$$

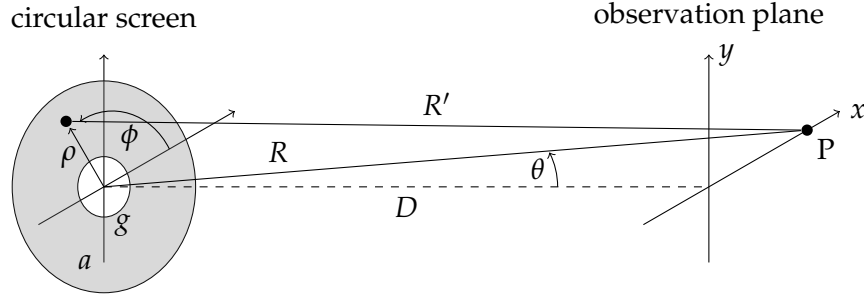


FIGURE 3.10: Geometric definitions for the calculation of transition and diffraction radiation in distance  $D$  from a circular screen with radius  $a$  and aperture  $g$ .

with the electron's velocity  $v = \beta c$  normalized to the speed of light  $c$  and the vacuum permittivity  $\epsilon_0$ . The calculation of the spectral energy density requires as in Sec. 3.1 the Fourier transformed electric field as a function of circular frequency  $\omega$

$$E_0(\omega, \rho) = \frac{1}{2\pi} \int_{-\infty}^{\infty} E_0(t, \rho) e^{-i\omega t} dt = \frac{-e\omega}{(2\pi)^{3/2} \epsilon_0 \beta^2 \gamma c^2} K_1 \left( \frac{\omega \rho}{c\beta\gamma} \right). \quad (3.19)$$

As the Bessel function  $K_1$  is small for arguments bigger than one, the size of the Coulomb field is characterized by the effective radius [CSS05]

$$\rho_{\text{eff}} = \frac{\gamma c \beta}{\omega} \approx \frac{c\gamma}{2\pi f}. \quad (3.20)$$

The effective source size increases with electron beam energy  $\gamma$  and decreases with radiation frequency  $f$ . This sets two very important requirements for the screen design at fixed electron energy: (1) A sufficiently large screen to efficiently generate low frequency radiation. (2) An aperture size that is small enough for the highest frequency of interest.

The geometrical setup for the calculation of the electric field at an observation point  $P$  is shown in Fig. 3.10. The circular screen has radius  $a$  and aperture size  $g$ . Due to radial symmetry, the observation point can be positioned on the  $x$ -axis without any restrictions to the result. According to the Huygens-Fresnel principle, each point of the electromagnetic wave at the source can be considered as the origin of a spherical wave. These wavefronts emitted at the screen interfere at the observation point and create a new wavefront

$$E_x(P, \omega) = -\frac{ik}{2\pi} \int_0^{2\pi} \int_g^a E_0(\omega, \rho) \cos \phi \frac{e^{ikR'}}{R'} \rho d\rho d\theta. \quad (3.21)$$

As the distance to the observer is usually much larger than the transverse dimensions of the screen, the distance  $R'$  is expanded up to second order using  $R^2 = D^2 + x^2$  and the binomial approximation:

$$R' = \sqrt{D^2 + (x - \rho \cos \phi)^2 + \rho^2 \sin^2 \phi} = R \sqrt{1 + \frac{\rho^2}{R^2} - \frac{2x\rho}{R^2} \cos \phi} \quad (3.22)$$

$$\approx R + \frac{\rho^2}{2R} - \frac{x\rho}{R} \cos \phi. \quad (3.23)$$

The  $R'$  in the denominator of Eq. (3.21) only changes the amplitude and can be approximated by  $R$ , whereas for the phase the complete approximation has to be considered in order to properly account for interference. The field at the observer becomes by inserting  $x = R \sin \theta$

$$E_x(P, \omega) = \frac{e\omega}{(2\pi)^{3/2}\varepsilon_0\beta^2\gamma c^2} \frac{ik}{2\pi R} e^{ikR} \iint K_1\left(\frac{\omega\rho}{c\beta\gamma}\right) \cos\phi e^{i\frac{k\rho^2}{2R}} e^{-ik\rho \cos\phi \sin\theta} \rho d\rho d\phi. \quad (3.24)$$

The integration over the azimuthal angle can be carried out analytically and yields the modified Bessel function  $J_1$

$$\int_0^{2\pi} \cos\phi e^{-ik\rho \cos\phi \sin\theta} d\phi = -2\pi i J_1(k\rho \sin\theta). \quad (3.25)$$

With this the spectral energy per solid angle  $d\Omega = dA/R^2$  (see [CSS05]) results in

$$\frac{d^2U}{d\omega d\Omega} = \frac{e^2\omega^4}{4\pi^3\varepsilon_0 c^5 \beta^4 \gamma^2} \left| \int_g^a J_1(k\rho \sin\theta) K_1\left(\frac{k\rho}{\beta\gamma}\right) \exp\left(\frac{ik\rho^2}{2R}\right) \rho d\rho \right|^2. \quad (3.26)$$

In general, the integration along the radial dimension of the screen can only be carried out numerically.

In the far-field approximation, which means not considering the second order of the  $R'$  approximation and thus the phase factor  $e^{ik\rho^2/2R}$ , Eq. (3.26) can be solved analytically. The phase factor can be neglected for distances  $D$  from the screen that hold (see [CSS05])

$$D > \gamma\rho_{\text{eff}} = \frac{c\gamma^2}{2\pi f}. \quad (3.27)$$

For a screen with infinite radius  $a \rightarrow \infty$  and no aperture  $g = 0$ , the result is the famous Ginzburg-Frank formula

$$\frac{d^2U_{\text{GF}}}{d\omega d\Omega} = \frac{e^2}{4\pi^3\varepsilon_0 c} \frac{\beta^2 \sin^2\theta}{(1 - \beta^2 \cos^2\theta)^2}. \quad (3.28)$$

The resulting one and two dimensional intensity profiles of the transition radiation are shown in Fig. 3.11. The spectral intensity does not depend on the frequency. The vanishing intensity on-axis results from the radial polarization and for highly relativistic electrons the radiation is emitted in a narrow cone with maximum intensity at  $\theta_{\text{max}} \approx 1/\gamma$ . The total radiated spectral energy density of Eq. (3.28) is approximated by [CSS05]

$$\frac{dU}{d\omega} = \frac{e^2}{2\pi^2\varepsilon_0 c} \cdot (\ln\gamma + \ln 2 - 0.5), \quad (3.29)$$

which shows that the intensity increases only weakly with the electron beam energy  $\gamma$ .

For finite screens with radius  $a$  and aperture  $g$ , Eq. (3.26) results in [CSS05]

$$\begin{aligned} \frac{d^2U}{d\omega d\Omega} &= \frac{d^2U_{\text{GF}}}{d\omega d\Omega} \cdot [T_g(\theta, \omega) - T_a(\theta, \omega)]^2 \\ T_a(\theta, \omega) &= \frac{\omega a}{c\beta\gamma} J_0\left(\frac{\omega a \sin\theta}{c}\right) K_1\left(\frac{\omega a}{c\beta\gamma}\right) + \frac{\omega a}{c\beta^2\gamma^2 \sin\theta} J_1\left(\frac{\omega a \sin\theta}{c}\right) K_0\left(\frac{\omega a}{c\beta\gamma}\right) \\ T_g(\theta, \omega) &= \frac{\omega g}{c\beta\gamma} J_0\left(\frac{\omega g \sin\theta}{c}\right) K_1\left(\frac{\omega g}{c\beta\gamma}\right) + \frac{\omega g}{c\beta^2\gamma^2 \sin\theta} J_1\left(\frac{\omega g \sin\theta}{c}\right) K_0\left(\frac{\omega g}{c\beta\gamma}\right) \end{aligned} \quad (3.30)$$

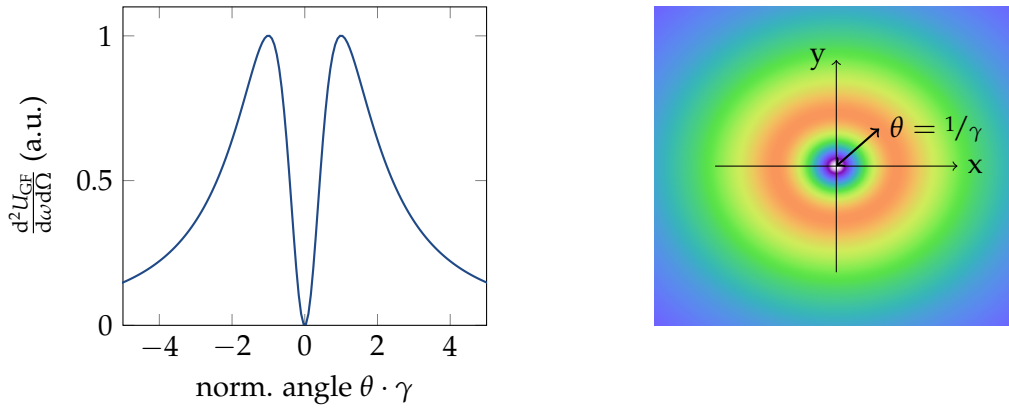


FIGURE 3.11: Intensity distribution of transition radiation according to the Ginzburg-Frank formula shown as one and two dimensional illustration. The characteristic ‘doughnut’-shape results from the vanishing intensity on-axis and the maximum intensity at the opening angle  $\theta_{\max} \approx 1/\gamma$  for highly relativistic electrons.

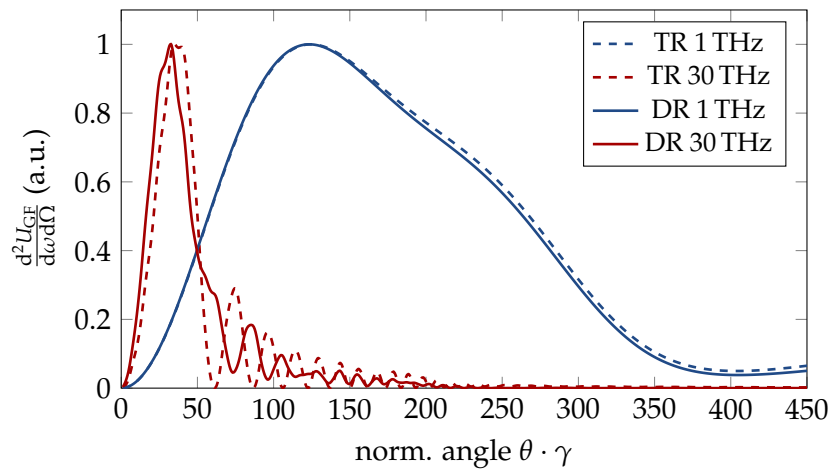


FIGURE 3.12: Normalized transverse TR and DR profiles for two different frequencies at 1 m distance from a 16 mm wide screen (with 1 mm aperture) emitted by an electron beam of 7 GeV. The profiles have been obtained by numerical evaluation of Eq. (3.26).

which in the limit of  $g \rightarrow 0$  and  $a \rightarrow \infty$  resembles the Ginzburg-Frank formula.

At hard XFELs, the TR source size in the THz regime is much larger than the dimension of the screen ( $\sim$  cm) due to the high beam energy ( $\gamma > 5000$ ), but most importantly, the far field condition is not fulfilled. It would require not realizable distances from the screen for a few GeV electron beam energies ( $D > 1$  km) in the THz regime. Thus in these cases, neither Eq. (3.28) nor Eq. (3.30) can be utilized to calculate the spatial distribution of the spectral energy density and Eq. (3.26) has to be numerically integrated over the screen. In App. A, an efficient numerical method based on Fourier transforms, which was introduced in [CSS05], is described to solve this equation for arbitrary screen dimensions also in the near-field regime.

The unfulfilled far-field condition as well as interference effects coming from the screen edges and aperture lead to significantly different transverse distributions than the idealized Ginzburg-Frank formula would predict. Examples of transverse spectral energy profiles at a beam energy of 7 GeV – the smallest expected beam energy at European XFEL – are shown in Fig. 3.12 for TR and DR in the THz (1 THz) and FIR (30 THz) regime. The simple relation of  $\theta \cdot \gamma = 1$  from the Ginzburg-Frank

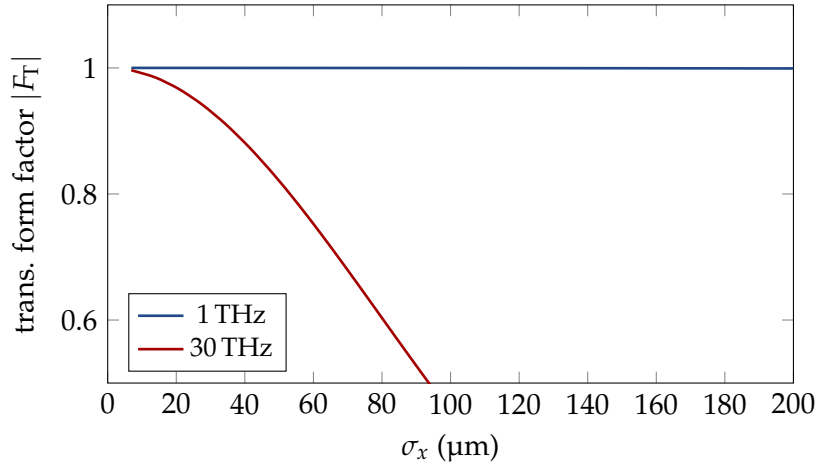


FIGURE 3.13: Transverse form factor at an observation angle of 10 mrad as function of the rms width of a transverse Gaussian distribution of the electron bunch. To avoid unwanted influences of the transverse form factor especially at high frequencies, the electron bunch should be sufficiently focused.

formula for the angle of maximum intensity is strongly violated, and the radiation properties can only be adequately described by numerical simulations. Especially at low frequencies (blue), the profile is much wider than in the Ginzburg-Frank case due to diffraction. At higher frequencies (red), the profile becomes narrower but near field diffraction leads to significant modulations on the profile. At typical beam energies of XFELs and within the required frequency range for current profile measurements, the differences between the profiles of TR (dashed) and DR (solid) at only few mm-wide apertures are small. Additional interference effects by the aperture result in slightly different modulations.

In the previous section 3.2, the decomposition of the form factor into transverse and longitudinal component has been justified by the dominating time difference of the longitudinal distribution due to small opening angles. Even the opening angle of the 1 THz profile in Fig. 3.12 results in roughly 10 mrad, which confirms the small angles. The influence of the transverse form factor at this observation angle is plotted as a function of the width of a Gaussian transverse density profile in Fig. 3.13. At high frequencies, the transverse form factor can have a significant influence if the beam is not sufficiently focused. Especially at low beam energies ( $< 1$  GeV) (for example at soft X-ray FELs) with larger emittances<sup>2</sup>, the transverse beam size has to be considered and may limit the frequency region of coherent emission. It may also be required to determine the transverse electron distribution for accurate longitudinal form factor measurements, which is not a trivial task (see e.g. [Yan11]). For diffraction radiation, the influence of the transverse beam size is suppressed as according to Gauss's law the electric field of a charge density, which only depends on the distance to its center, is given by the enclosed charge alone. Monitoring the transverse beam size is not required.

An advantage at XFELs is that small emittances lead to generally small beam sizes. Yet the screen should be placed at a position with reasonable small  $\beta$ -functions. At European XFEL, the beam size at the position of the screen for the spectrometer (see Sec. 4.1) is dominated by the horizontal plane with a design  $\beta$ -function of  $\approx 50$  m. For a normalized emittance of  $\epsilon_n = 1 \mu\text{m}$  [Dec+20], the largest expected beam size

<sup>2</sup>The emittance  $\epsilon$  is a fundamental property of the transverse beam quality. Together with the  $\beta$ -function for example, it determines the transverse beam size. See [Wie15] for a detailed discussion.

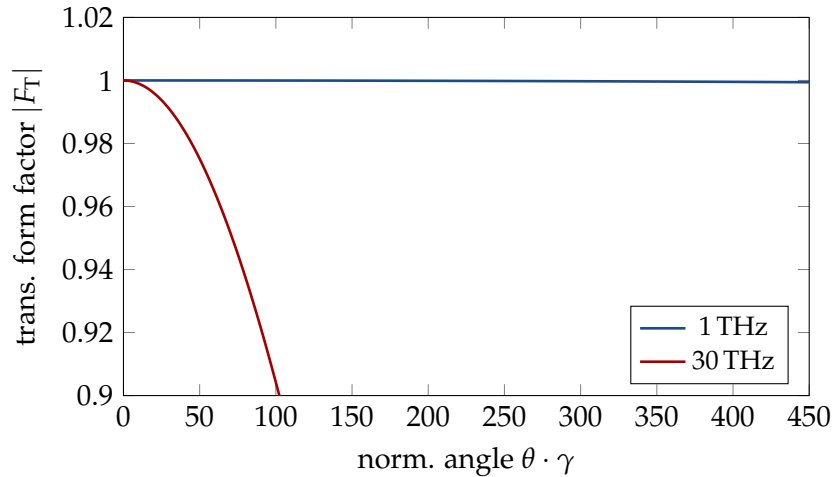


FIGURE 3.14: Transverse form factor of a Gaussian distribution with  $50 \mu\text{m}$  rms width as function of the normalized angle for a direct comparison with Fig. 3.12. The influence of the transverse form factor can be neglected within the opening angles in the THz and FIR regime.

amounts to roughly  $\sigma_x = \sqrt{\beta\epsilon_n/\gamma} \approx 50 \mu\text{m}$  at the lowest expected beam energy of 7 GeV. The influence of the transverse form factor of a corresponding Gaussian distribution is plotted in Fig. 3.14 as a function of the normalized emission angle  $\theta \cdot \gamma$ . For direct comparison, the scale is identical to Fig. 3.12. In the THz and FIR regime, the opening angles of the radiation containing the most part of the intensity are too small to be significantly influenced by the transverse form factor  $|F_T|$  at this beam size. Its influence ( $|F_T| \gtrsim 0.95$ ) on the spectral distribution of the coherent radiation can thus be neglected.

The total emitted spectral energy density of TR and DR can be determined based on Eq. (3.30) and a numerical integration along the solid angle  $\Omega$ . The total spectral energy density does not change at the transition from near-field to far-field regime. Nevertheless, the exact spectral distribution at any detector in the near-field regime can only be determined by numerical simulations which include the actual screen geometry and the acceptance angle of the detector (see Sec. 4.1). An example for the total emitted spectral energy density from typical screen geometries is shown in Fig. 3.15 for 1 GeV and 7 GeV beam energy. The screen has a radius of  $a = 16 \text{ mm}$  with (in the DR case) a  $g = 1 \text{ mm}$  aperture in the center. The influence of the limited screen size is visible for both beam energies. At 1 GeV beam energy, the plateau of the Ginzburg-Frank formula (dashed) is reached at frequencies of around 10 THz, whereas the increased effective source size (Eq. (3.20)) at 7 GeV shifts the beginning of the slightly higher plateau to 70 THz. As mentioned in [CSS05], the plateau is already reached at frequencies that hold  $\rho_{\text{eff}} < 3a$ .

The dotted lines mark the diffraction radiation spectrum for an infinite screen, i.e.  $a \rightarrow \infty$ . Due to the aperture, the intensity decreases towards higher frequencies. The effective source size gets smaller with frequency. The Coulomb field outside the aperture contains less high frequency components which could be converted to real photons. Because the source size increases with beam energy, the DR spectrum shifts to higher frequencies for larger beam energies. Additionally, the influence of effective source size on the limited screen flattens the spectrum.

At 1 GeV, the combination of these two effects lead to a strong drop of DR intensity in the IR regime ( $>10 \text{ THz}$ ), whereas at 7 GeV this cut-off shifts to much higher

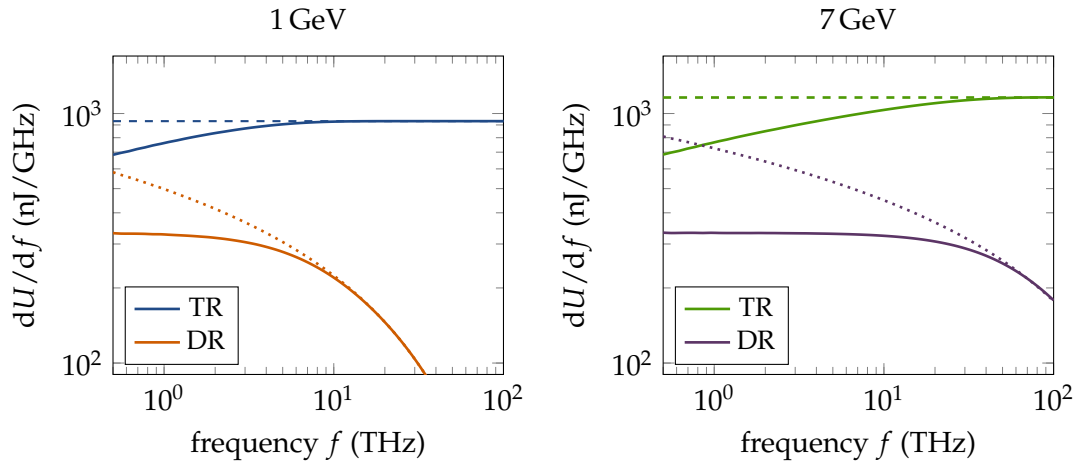


FIGURE 3.15: Total spectral energy densities of TR and DR for two different beam energies emitted by a point-like electron bunch of 1 nC charge at a screen with  $a = 16$  mm radius. The aperture radius for DR is  $g = 1$  mm. The dashed and dotted lines mark the respective spectral energy density for an infinite screen.

frequencies ( $>100$  THz). DR at beam energies below 1 GeV is not well suited for longitudinal form factor measurements of femtosecond bunches because of weak spectral energy density in the IR regime and an overall uneven spectrum which complicates the construction of a single-shot spectrometer. For multi-GeV beam energies however, the cut-off shifts to frequencies which are above the frequency region linked to the overall current profile of the electron bunch. Consequently, DR can be utilized for longitudinal form factor measurements (compare with Fig. 3.4) of bunches with a few femtoseconds duration at hard X-ray FELs.

At the beam energies of hard XFELs, diffraction radiation offers a fairly flat single electron radiation spectrum over a wide frequency range and requires only a comparatively simple setup, which consists only of a screen as illustrated in Fig. 3.16. Besides the spectral, also the spatial properties of DR are in this case very similar to those of TR (see Figs. 3.12, 3.15) and can be utilized in the same manner for longitudinal diagnostics. In addition, DR has the benefit of a clear separation between the applied spectral diagnostic and generation of radiation. DR and TR are easily accessible if the screen is tilted by  $45^\circ$  with respect to the electron beam path. The radiation is then emitted under an angle of  $90^\circ$  with respect to the electron beam axis which has only a minor influence on the emitted radiation by an inclination factor  $\cos \theta$  [CSS05]. The DR spectrum is also not affected by the transverse beam size. This makes DR an ideal source for noninvasive longitudinal electron bunch diagnostics at hard X-ray FELs.

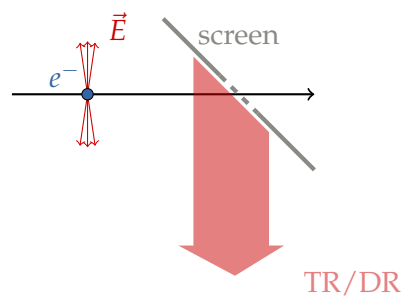


FIGURE 3.16: Simplified illustration of TR and DR at a screen enclosing an angle of  $45^\circ$  with respect to the electron beam axis. The transversely concentrated electric field of a highly relativistic electron bunch is reflected at the surface of a metallic screen and produces transition radiation. In case of diffraction radiation, the electron bunch does not impinge on the screen but passes through an aperture (dashed).

## Chapter 4

# Experimental Setup

The experimental setup for longitudinal bunch profile characterization at European XFEL shall fulfill several requirements in order to provide potent diagnostics for accelerator operation and FEL experiments. The setup should be

- able to resolve bunch profiles down to 10 fs rms bunch duration,
- noninvasive,
- capable of characterizing all bunches at MHz bunch repetition rates.

In order to reconstruct the temporal profile of the electron bunches and their substructures of only a few femtoseconds from the frequency domain, a broadband spectrometer is mandatory (see Sec. 3.2). At DESY, a single-shot spectrometer called CRISP, which fulfills this requirement by covering the frequency range 0.7 THz to 60 THz, has been developed and successfully operated at FLASH with transition radiation (TR) at 10 Hz repetition rate [Wes12; Sch+20]. In this work, the spectrometer has been adapted to achieve operation compatible with the MHz repetition rates of European XFEL using a noninvasive radiation source and modified readout electronics. The experimental setup at European XFEL is shown in Fig. 4.1, and the individual parts of the setup, i.e. the screen station for the generation of coherent radiation, THz beamline, spectrometer and readout electronics, are described and explained.

### 4.1 Screen Station

As elaborated in Sec. 3.4, the spectral and spatial properties of noninvasive DR are similar to those of invasive TR at multi-GeV beam energies. Therefore, the intensity level of noninvasive DR at European XFEL is suitable for the CRISP spectrometer as it can be expected to be comparable to TR intensity at FLASH. The experimental setup for DR does neither put extraordinary restrictions on electron beam optics nor require a complicated setup. Nevertheless, it enables to monitor all bunches inside the bunch train. This is of huge advantage for superconducting FELs with respect to accelerator operation and FEL experiments. Thus, European XFEL, the first superconducting XFEL with multi-GeV beam energy and MHz repetition rates, has been equipped in this work with a diagnostics based on coherent DR spectroscopy for noninvasive current profile reconstructions with femtosecond resolution.

The design of the diffraction radiator for the CRISP spectrometer has been adopted from the bunch compression monitors (BCMs) at European XFEL. These screens [PDG14] are mounted inside a special component of the evacuated accelerator beam pipe called screen station. A technical drawing of the screen station for BCMs and the CRISP spectrometer is shown in Fig. 4.2. The screen itself consists of 1 mm-thick

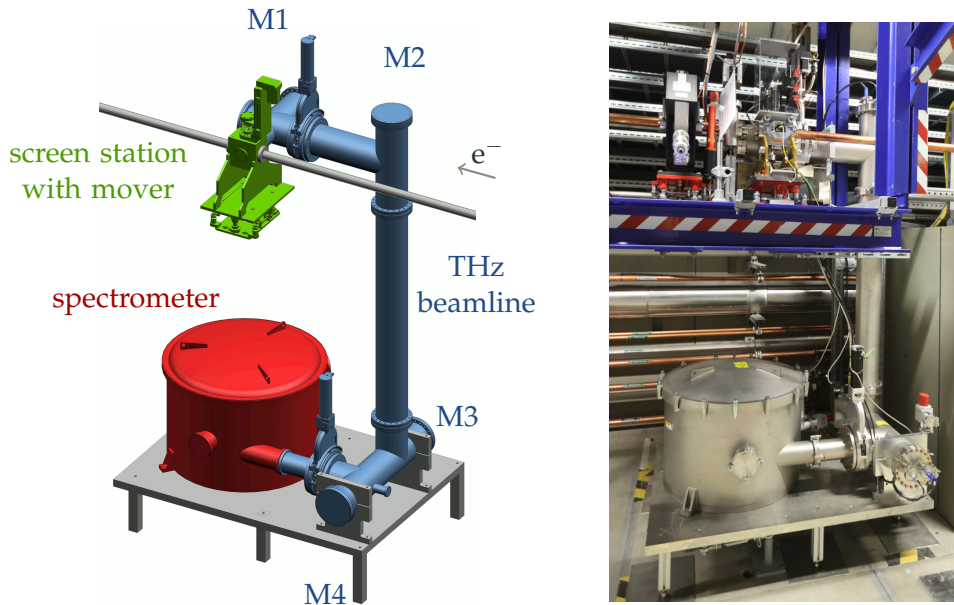


FIGURE 4.1: 3D model (left) and photograph (right, Courtesy of D. Nölle) of the experimental setup for noninvasive longitudinal bunch profile diagnostics at MHz repetition rates based on CDR. In both cases the electron beam is coming from the right. CDR (or CTR if desired) is emitted at the screen inside the screen station (green). Four focusing mirrors (M1-M4) inside the THz beamline (blue) guide the radiation down to the spectrometer (red). The spectrometer is placed on an adjustable support-structure which is attached to the floor.

solid body aluminum and has an area of  $32 \text{ mm} \times 80 \text{ mm}$ . The surface of the screen has been machined with a diamond milling cutter and has a roughness  $< 1 \mu\text{m}$ . It comprises 5 mm and 7 mm apertures in bottom and top section of the screen (see right part of Fig. 4.2). The aperture sizes have been chosen such that also at the BCM stations with low beam energy and thus larger beam sizes the electron beam is ensured to pass without beam loss. The screen is mounted on a remotely-controllable linear motion vacuum feed-through (screen mover) to move either the central part or the apertures vertically onto the nominal beam path. The screen can thus be operated as a transition or diffraction radiator with two different apertures. The screen normal encloses an angle of  $45^\circ$  with respect to the electron beam axis. Backward TR or DR is emitted in the horizontal plane perpendicular to the electron beam axis where it enters the THz beamline through a diamond window<sup>1</sup> with 20 mm circular aperture. The diamond window has a  $1^\circ$  wedge shape in the vertical direction to suppress etalon oscillations (see Fig. 4.6) and is 0.5 mm thick.

In order to maximize the effective source size of the radiation, the screen station for the CRISP spectrometer is positioned after the main linac at full beam energy of up to 17.5 GeV. The location downstream of the collimator section and upstream of the undulator switchyard (see Fig. 2.5) has several advantages:

- The collimator removes dark current and beam halo as well as any other off-energy particles what significantly reduces the beam losses at the diffraction radiator aperture.

<sup>1</sup>Diamond Materials GmbH

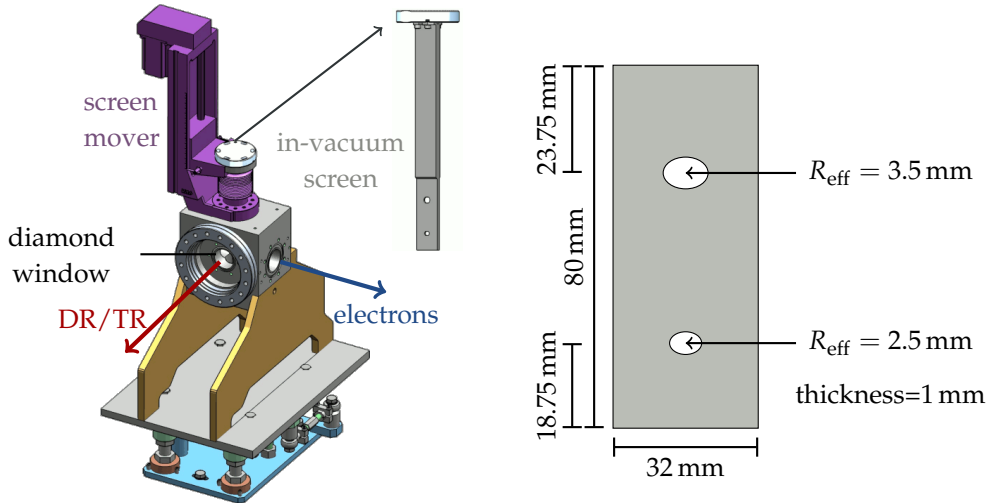


FIGURE 4.2: Screen station to produce coherent diffraction or transition radiation (left) and a schematic view of the aluminum screen itself (right) for the CRISP spectrometer and the BCMS. The screen consists of two diffraction radiator sections (top/bottom) and a transition radiator section (middle), which can be moved into the electron beam path depending on demand by the screen mover (linear motion vacuum feed-through). The elliptical holes result in circular apertures when seen under  $45^\circ$  on the electron beam axis.

- In front of the undulator switchyard all bunches can be monitored even if they are sent to different destinations (i.e. dump, SASE1/3, SASE2).
- It is located downstream of the fast transverse orbit feedback. Thereby it is ensured that all bunches inside the train have almost the same orbit and position dependent effects are eliminated.
- It enables longitudinal profile diagnostics at full compression. This can also be done with a TDS after the last bunch compressor  $BC_3$ , however there the bunches have not yet reached final beam energies and still have to pass the main linac and roughly two kilometers before they reach the FEL undulators.
- The bunches have reached their final beam energies and the spectral energy density of DR is maximized.

To validate the applicability of the screen station for longitudinal current profile measurements, the emission curves of the different screen sections are studied. They are obtained by integrating the spectral energy density over the vacuum window in 55 mm distance to the beam axis for the lowest beam energy to be expected (7 GeV during a possible CW operation [Bri+14]) and the highest beam energy (17.5 GeV). To account for the actual screen geometry and the window aperture, the spectral energy densities are calculated based on the Fourier transform method described in App. A. The results are shown in Fig. 4.3 as solid lines for a bunch with 1 nC charge. They are compared to the results and discussions of Sec. 3.4. For this, the total emitted radiation of a circular screen is calculated by integrating Eq. (3.30) numerically over the entire half sphere in the far-field. These spectra are depicted as dashed lines. The frequency range of the CRISP spectrometer is marked by vertical lines.

The spectral energy density of transition radiation on the diamond window continuously increases for all expected beam energies towards high frequencies due to the limited source size as was already discussed in Sec. 3.4. For 7 GeV, the plateau of

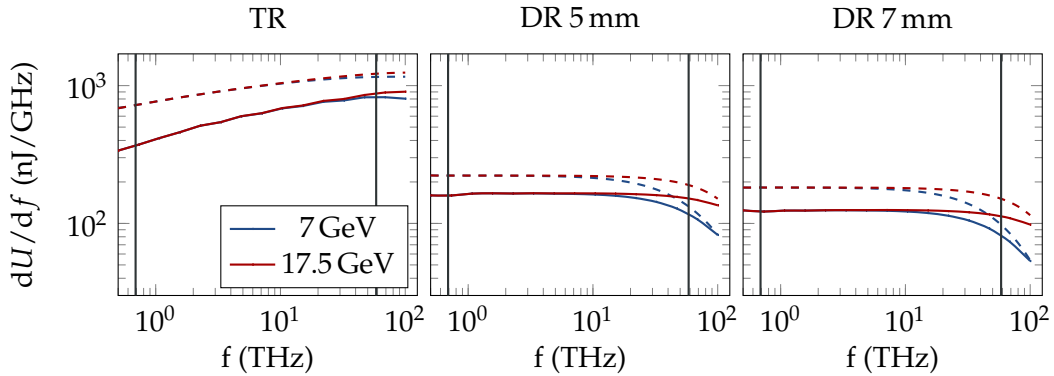


FIGURE 4.3: Spectral energy density of transition and diffraction radiation integrated over the window aperture at lowest and highest expected electron beam energies and illustrated as solid lines. These calculations are based on the numerical method described in App. A. The dashed lines present the results of the entire emission using Eq. (3.30) for a circular screen. The vertical lines mark the frequency range of the CRISP spectrometer. Deviations between the total emitted spectral energy density and the spectral energy density on the window are due to near-field diffraction at the window aperture.

the intensity on the diamond window is reached around 70 THz just like in the idealized far-field case (see also Fig. 3.15). At 17.5 GeV, the plateau is reached outside of the shown frequency range. Advantages of a larger screen, which would shift the plateau to slightly lower frequency are inessential. Anyway, the focus at European XFEL lies on noninvasive operation using diffraction radiation.

Diffraction radiation holds – in comparison to TR – a very flat spectrum along the entire frequency range of the CRISP spectrometer for both screen apertures at 17.5 GeV. At 7 GeV, the decreased source size leads to a small drop of the DR spectral energy density for frequencies above 30 THz. The drop of the spectral energy density at the high frequency end of the CRISP spectrometer is negligible for 17.5 GeV beam energies. At the lowest expected beam energy of 7 GeV, the spectral energy density decreases towards the highest frequencies of the CRISP spectrometer only by roughly one third for both apertures. Overall, DR exhibits a radiation spectrum 3 to 5 times less intense than TR along the CRISP spectrometer’s frequency range.

For all settings, there is a noticeable offset between the total emitted spectral energy density according to Eq. (3.30) and the actual spectral energy density passing the window. This is due to near-field diffraction, which leads to a beam profile with an extended region of low intensity. The transverse TR and DR beam profiles at the window plane are depicted in Fig. 4.4 for a frequency at the low and high frequency end of the spectrometer. The window aperture (red circle) of 20 mm is sufficient for the main radiation spot at all frequencies and the overall evolution of the spectrum is thus similar to the entire emitted radiation. As can be seen in Fig. 4.3, the maximum achievable increase by a larger window results – in an idealized case – to 30 % for DR. In reality however, the additional radiation intensity inside the extended region of low intensity can neither be completely covered by any feasible window aperture nor efficiently transported by a beamline. It should be noted that even at 7 GeV beam energy and radiation frequencies of 100 THz, the far-field is only reached for distances around 100 m from the screen. At frequencies above the spectrometer range, the influence of near-field diffraction decreases and the DR spectral energy density on the window approaches the spectral energy density of the total emitted radiation (see Fig. 4.3).

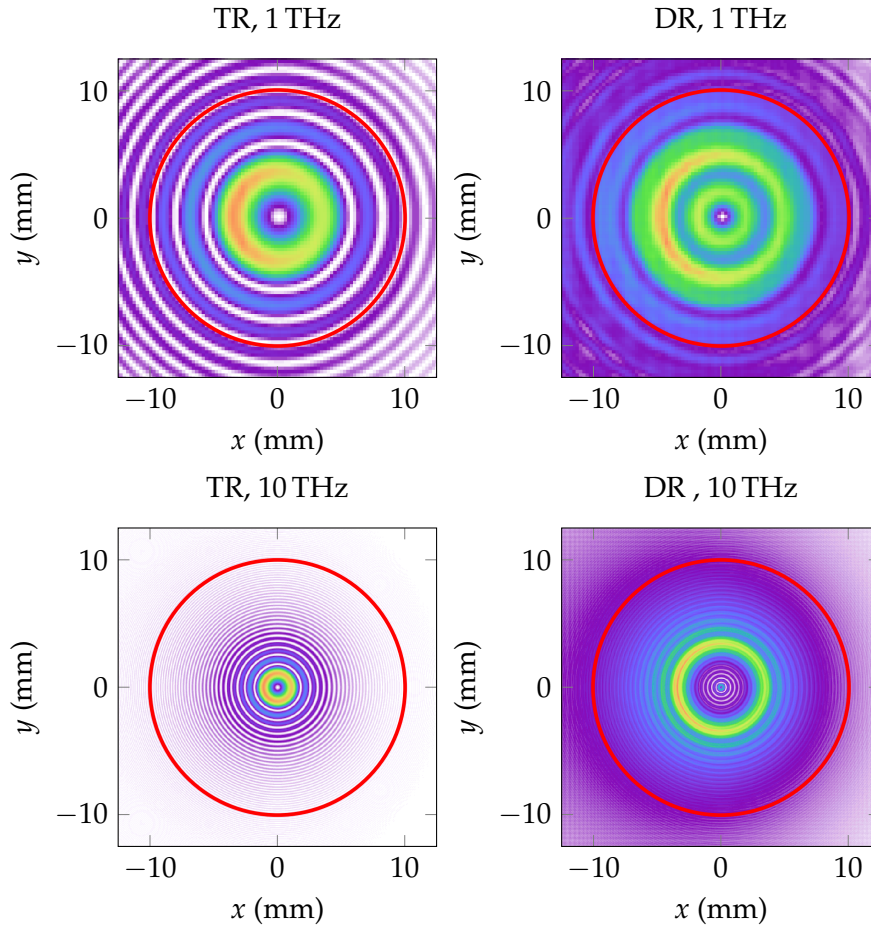


FIGURE 4.4: Simulated intensity profiles at the window plane for TR and DR at the 5 mm aperture for 1 THz and 10 THz and 17.5 GeV beam energy. The red circle indicates the aperture of the diamond window. Near-field diffraction leads to transverse intensity distributions with extended regions of low intensity. Nevertheless, the main radiation spot is well transmitted through the window aperture for all screen settings and frequencies. Thus, the overall evolution of the radiation spectrum on the window is similar to the entire emitted radiation calculated in the far-field regime (see Fig. 4.3).

From experience with THz spectroscopy at FLASH, it is known that TR at beam energies of about 1 GeV generates sufficient intensity along the whole frequency range of the CRISP spectrometer for bunch profile reconstructions with a few femtoseconds resolution [Wes12; Sch+20]. Due to weak scaling of TR with beam energy (see Sec. 3.4), the TR spectral energy densities at FLASH are comparable to those in Fig. 4.3. In this regard, the intensity decrease of DR at the screen station of European XFEL is acceptable especially under consideration of the large influence of current profile and bunch charge on the coherent radiation intensity (see Sec. 3.1). For the entire range of beam energies expected during FEL operation, the high frequency cut-off of DR does not lead to a drastic drop of spectral energy density within the spectrometer range. The diffraction radiation screen stations of European XFEL are a promising noninvasive source for coherent radiation for the CRISP spectrometer. The following sections of this chapter study beam transport and detection.

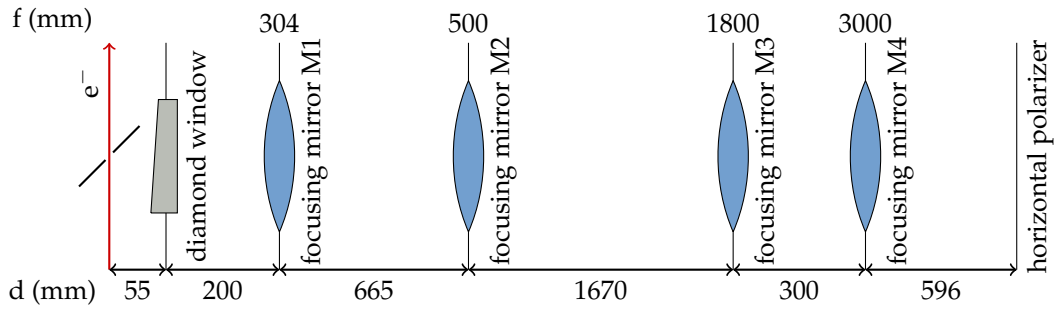


FIGURE 4.5: Schematic of the optical components inside the THz beamline with distances  $d$  (bottom) between the elements and their focusing lengths  $f$  (top). The wedge-shaped diamond window separates the accelerator vacuum from the THz beamline vacuum. Four focusing mirrors (M1-M4) guide the radiation through the THz beamline and collimate it inside the spectrometer. The polarizer marks the first optical element inside the spectrometer (see Sec. 4.3). Not to scale.

## 4.2 THz Beamline

The 3D model and photograph of the experimental setup at European XFEL in Fig. 4.1 illustrates the layout of the THz beamline that connects the screen station with the spectrometer. The THz beamline serves three main aspects: First of all, the optical layout of the THz beamline has to ensure an efficient transport of coherent radiation to the spectrometer over the entire frequency range. In order to properly focus the radiation onto the detectors, the radiation must be sufficiently collimated at the THz beamline exit. This is achieved by four focusing mirrors (M1-M4). Secondly, if the radiation transport would take place in air, the frequency spectrum would be distorted by water vapor absorption lines [Cas+06]. To prevent this, the THz beamline is evacuated by vacuum pipes of 150 mm inner diameter. Last but not least, the sensitive electronics of the spectrometer should not be exposed to ionizing radiation in order to prevent damage. The THz beamline separates the spectrometer from the accelerator beam axis by sufficient distance to minimize the level of harming ionizing radiation. In addition, the spectrometer is placed directly downstream of a rack housing made out of concrete, which shields the spectrometer from Bremsstrahlung in case of beam loss in the collimator section. The spectrometer is attached to a table-like support-structure mounted onto the floor, which provides easy access to the spectrometer.

The four focusing mirrors (M1-M4) are custom made by an industrial company<sup>2</sup> with a projected diameter of 100 mm onto the THz beamline axis. They have toroidal shape for focusing and are mounted on remotely controllable mirror holders for alignment. The optical design of the THz beamline has been carried out by P. Peier before the start of this thesis, but its realization has been part of this thesis. The focusing lengths and distances between the optical elements are given in Fig. 4.5. Besides collimating the beam, the gold-coating of the mirrors also provides an efficient transport of radiation from the THz to the visible regime. The THz beamline transmission is defined as the ratio of the spectral energy density entering the spectrometer to the density on the diamond window. It is shown for DR at the 5 mm aperture as a function of frequency for both polarizations in Fig. 4.6. The transport of the radiation through the THz beamline has been simulated under consideration

<sup>2</sup>LT Ultra-Precision Technology GmbH

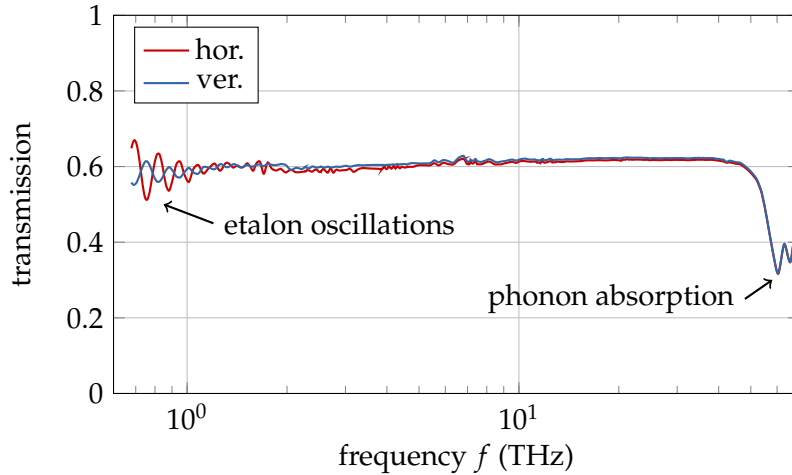


FIGURE 4.6: Transmission of the THz beamline for both polarizations with respect to the screen. Only the vertical polarization is detected due to a polarizer inside the spectrometer (see Sec. 4.3).

of all diffraction effects by using the Fourier transform method described in App. A. Absorption due to the diamond window, its induced kick due to the wedge-shape as well as the focusing mirror reflectivity of 0.97[Cas+09] at the frequencies of interest have been included. The transmission is a flat function of frequency with an overall transmission of 0.6 mainly given by the diamond window [Dia] and the reflectivity of the four focusing mirrors  $0.97^4 = 0.89$ . Only at frequencies below 1 THz, the diamond window leads to a modulation of the THz beamline transmission. Without the wedge shape, the diamond window transmission would vary between 50 % and 100 % [Cas+09] due to etalon oscillations. The wedge shape suppresses these oscillations due to the different time offsets between the internal reflections along the transverse radiation profile. Especially for the vertical polarization, whose radiation profile spans along the wedge axis, the modulation of the transmission is strongly reduced. At 50 THz to 60 THz phonon absorption in the diamond window leads to a dip with transmissions below 0.4.

The simulated beamsizes of the different radiations along the THz beamline and the region of the spectrometer (pol – G4, see Sec. 4.3) are illustrated in Fig. 4.7 for a set of representative frequencies. Hereby the rms beam size is calculated considering both polarizations of the radiation and the position of the optical elements is indicated by the gray vertical lines. As the beam sizes in the horizontal and vertical plane are almost identical, Fig. 4.7 presents only the results of the horizontal beam size. The influence of the beam energy above 10 GeV is negligible, however it shall be stated that the results have been obtained with 15 GeV beam energy. This energy has been chosen, because it represents roughly the central beam energy of European XFEL during this thesis (11 GeV – 17.5 GeV). For all radiation types, the beam size along the beamline is sufficiently small even for frequencies below 1 THz and ensures no significant intensity loss at the aperture of the focusing mirrors. The focusing mirrors M2 and M3 form a periscope which translates vertical polarization at the screen to horizontal polarization inside the spectrometer. As the spectrometer is only sensitive to horizontal polarization (see Sec. 4.3), the detected radiation corresponds to vertical polarization at the screen. The focusing properties of the spectrometer result in a collimated and sufficiently small DR beam along the path inside the spectrometer for its entire frequency range (see Sec. 4.3). Because the THz

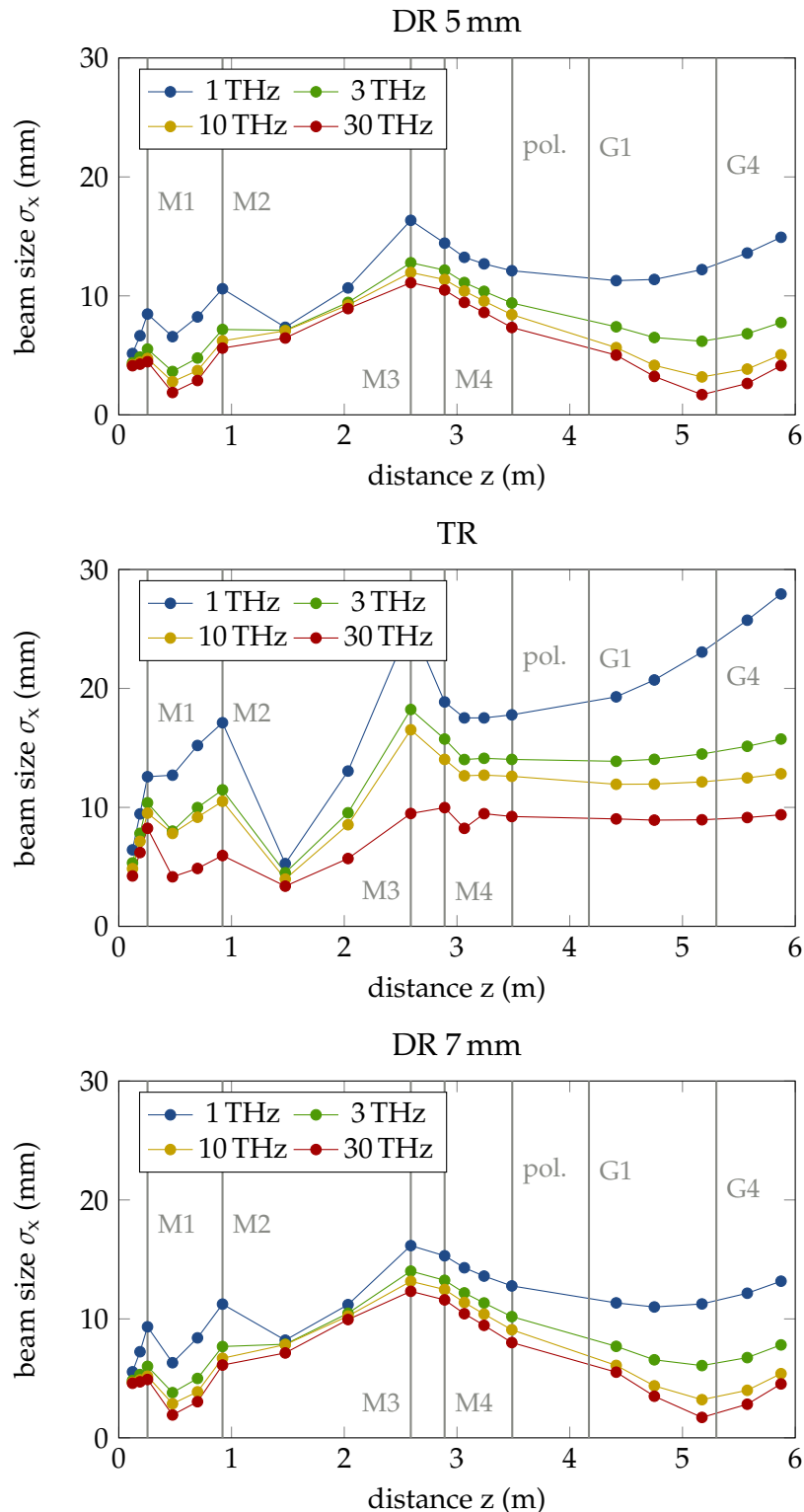


FIGURE 4.7: Simulated beam sizes along the THz beamline and CRISP spectrometer (see Sec. 4.3) for different radiation frequencies in the THz and FIR regime and the three radiation types at 15 GeV beam energy. The radiation is well contained within the 100 mm limiting aperture of the focusing mirrors (M1 – M4) such that a loss free radiation transport is ensured. Inside the spectrometer (pol – G4), the radiation is sufficiently collimated.

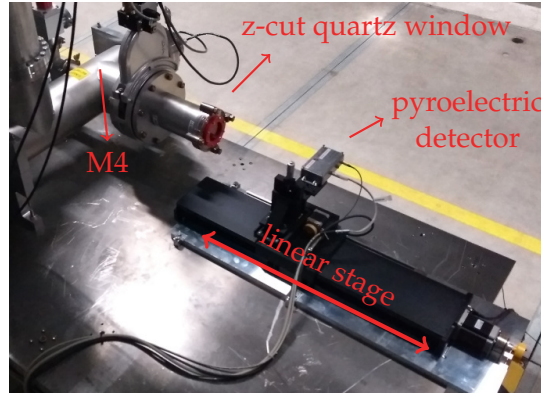


FIGURE 4.8: Single pyroelectric detector setup for the measurement of the focusing property of the THz beamline. The pyroelectric detector is mounted on a linear motion stage, which allows to change the distance to the z-cut quartz window. Transverse scans of the intensity profile are carried out by tilting the last focusing mirror M4.

beamline is optimized for DR, the beam size of TR is slightly larger and less collimated inside the spectrometer for low frequencies. However, this has no significant influences on the operation of the spectrometer (see Sec. 5.4). Higher frequencies are in general focused to smaller beam diameters as the effective source size of the emitted radiation and the influence of diffraction decreases.

#### 4.2.1 Beamline commissioning

Before the spectrometer was attached to the THz beamline, the properties of the collimated radiation have been measured and compared with the results of simulations. A pyroelectric detector has been mounted on a linear stage after the THz beamline which was sealed with a z-cut quartz window. An image of this setup is shown in Fig. 4.8. The used pyroelectric detector system is similar to the detector system of the spectrometer, which is described in Sec. 4.3.1. The setup allows to vary the distance between the pyroelectric detector and the last THz beamline mirror along the optical beam path. In addition, as all THz beamline mirrors are remotely controllable by in-vacuum linear actuators, the last focusing mirror is able to scan the diffraction radiation over the detector measuring the transverse distribution.

An example of a measured transverse profile of the diffraction radiation at the 5 mm aperture is shown in Fig. 4.9, where the obtained profile is compared to the simulation results. The beam energy amounts to 14 GeV. For the simulation, the electron bunch current profile was assumed to be Gaussian with a rms duration of 25 fs. The simulated transverse profile is generated by multiplication of the transverse profiles of each radiation frequency with the form factor as well as the transmission of the z-cut quartz window and the sensitivity of the detector. The transverse dimensions of the detector have hereby explicitly not been considered to visualize even fine structures of the radiation profile. Both profiles agree in size of the diffraction radiation spot and exhibit the characteristic low-intensity center. The asymmetry visible in both profiles is due to the toroidal mirrors and the  $45^\circ$  angle between electron beam axis and DR screen.

The measured and simulated evolution of the transverse beam size after the THz beamline is shown in Fig. 4.10. The measured transverse rms beam size of collimated beam after the last THz beamline mirror agrees within 10% to the results of

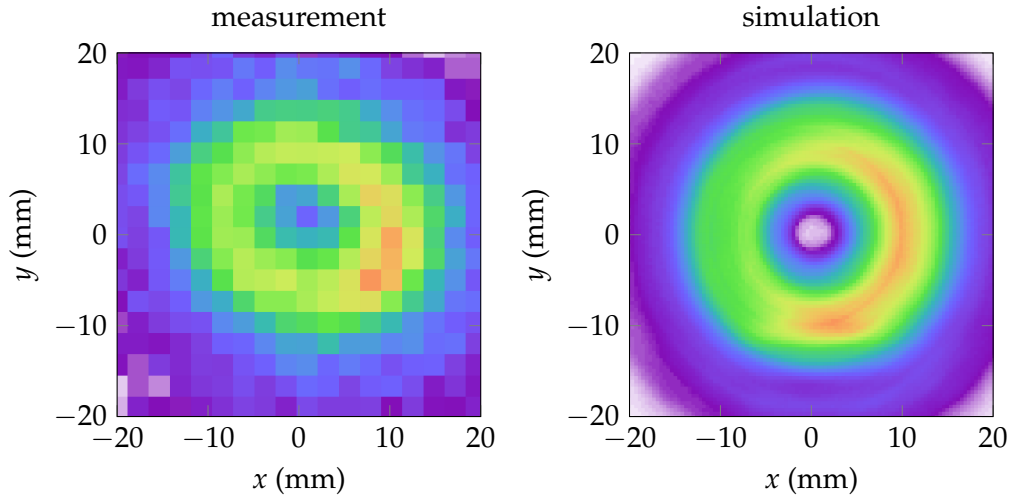


FIGURE 4.9: The measured transverse profile of diffraction radiation (left) in comparison to simulations (right). Measurement and simulation (not considering detector size) agree even within fine details like the slight asymmetry. Both profiles show the characteristic low intensity center for diffraction radiation.

the simulation. These small deviations can be understood by the sensitivity of the experimental rms beam width to fluctuations of the measured profile on the finite measurement grid.

The commissioning results demonstrate that radiation emission, transport and detection are well understood and that the spectrometer provides suitable radiation properties along the frequency range of the CRISP spectrometer.

### 4.3 CRISP Spectrometer

As mentioned in the beginning of this chapter, a single-shot spectrometer for longitudinal bunch profile measurements is operated at FLASH. This Coherent Radiation Intensity SPectrometer (CRISP) is installed in a modified version at the THz beamline of European XFEL. A detailed description of the spectrometer is given in [Wes+11; Wes12] and latest experimental results from FLASH are presented in [Sch+20]. Here, the main aspects of the spectrometer will be discussed.

For single-shot spectroscopy, optical reflection gratings are useful to disperse polychromatic radiation into its spectral components. For radiation wavelength  $\lambda$ , the dispersion angle  $\beta$  with respect to the normal of the grating is given by the grating equation

$$m \frac{\lambda}{d} = \sin \alpha + \sin \beta \text{ with } m \in \mathbb{Z}, \quad (4.1)$$

where  $\alpha$  is the angle of incidence,  $d$  the grating period and  $m$  the dispersion order. A fundamental limitation of reflection gratings for broadband radiation follows directly from Eq. (4.1). It is possible that higher orders ( $m > 1$ ) of smaller wavelengths are dispersed into the same angle  $\beta$  as the first order ( $m = 1$ ) of the frequency of interest. Thus, the influence of higher orders must be sufficiently reduced in order to allow broadband spectroscopic measurements. The efficiencies of higher orders and reflective mode ( $m = 0$ ) depend strongly on the actual grating geometry and the angle of incidence  $\alpha$ .

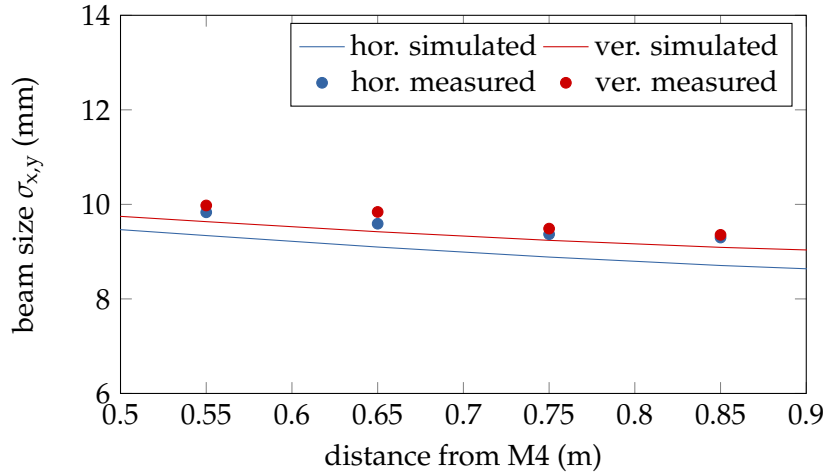


FIGURE 4.10: Simulation and measurement of the transverse beam size after the THz beamline detected by scanning a single pyroelectric detector. The evolution with distance agrees very well with the simulations and the beam sizes deviate by less than 10% from the simulation. The measured rms beam width is sensitive to fluctuations of the low intensity part of the beam profile on the measurement grid, and an estimation of systematic errors therefore omitted at this point.

In [DH08], a grating configuration with the efficiencies shown in Fig. 4.11 for the horizontal polarization has been found. Wavelengths between  $0.72d$  and  $1.32d$  are efficiently dispersed in first order ( $m = 1$ ) into a large angle interval  $\beta = [27.0^\circ, 79.9^\circ]$  for detection of the spectral intensity. Simultaneously, the grating acts like a mirror for wavelengths above  $\lambda_0 = 1.32d$  as they are efficiently reflected ( $m = 0$ ). Due to the sharp transition from dispersive to reflective behaviour, the grating can be understood to operate like band-pass and low-pass. Radiation within the band-pass is dispersed, while radiation with wavelengths above the low-pass threshold is reflected. The angle of incidence hereby accounts to  $\alpha = 19^\circ$ .

The spectral properties of the grating configuration allow to overcome the limitations of a single reflection grating by cascading several gratings with different grating periods  $d$ . Hereby, the low-pass properties of each grating act like a filter for the higher orders at the next grating. The application of this principle at the CRISP spectrometer is illustrated in Fig. 4.12. Each grating disperses a certain wavelength interval and guides longer wavelengths (smaller frequencies) onto the next grating. The grating period  $d$  hereby increases from grating to grating by roughly 1.7, which is determined by matching the lower edge of the dispersion region to the higher edge of the previous grating. The first grating G0 is not used to disperse the radiation onto the detectors but to remove higher orders of the grating stage G1.

The polarizer shown in Fig. 4.12 transmits only the horizontal polarization for which the gratings were designed. With a free aperture of 40 mm the polarizer is the smallest optical component inside the spectrometer. According to Fig. 4.7, the aperture is at least 4-times larger than the rms beam width except for low frequency radiation – especially at TR – where a small fraction of intensity may be cut. This however has no significant influence on the spectrometer sensitivity (see Sec. 5.4). Two mirrors A1 and A2 are used to align the incoming radiation and ensure  $\alpha = 19^\circ$  within a sufficiently small margin ( $< 1^\circ$ ) to neglect deviations [Wes12]. Two different sets of five cascaded gratings are installed inside the spectrometer such that the spectrometer can be operated in THz and far infrared (FIR) regime. The grating constants and frequency ranges of each grating for these two sets are summarized in

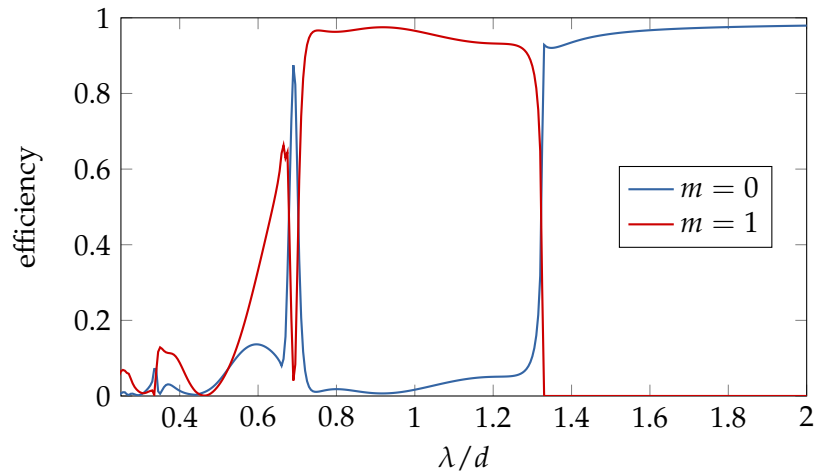


FIGURE 4.11: Computed efficiency of the reflective ( $m = 0$ ) and first dispersive order of the gratings ( $m = 1$ ) as a function of wavelength normalized to the grating period  $d$  for a horizontal polarization of the electric field. Wavelengths above  $1.32d$  are efficiently reflective (low-pass) while wavelengths below are dispersed in first order down to  $0.72d$ . Adapted from [Sch+18].

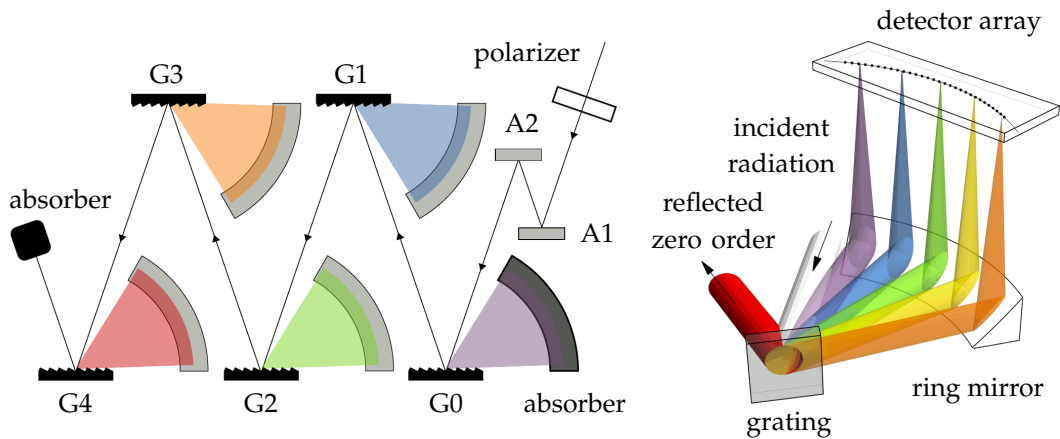


FIGURE 4.12: Layout of the CRISP spectrometer with five cascaded gratings (left). The polarizer transmits only the horizontal polarization for which the spectrometer is designed. The mirrors A1 and A2 are used to align the radiation inside the spectrometer. The first grating filters out high frequencies that would otherwise lead to higher order dispersion effects. For gratings G1-G4, a parabolic ring mirror focuses the radiation on a pyroelectric detector array above (right). Adapted from [Wes12].

TABLE 4.1: Grating period  $d$  and resulting characteristic frequency  $f_0$ , which marks the transition between low-pass and dispersive behaviour. For both grating sets, the detectable frequency range of each grating is given by  $f_{\max}$  and  $f_{\min}$ .

	THz				FIR			
	$d/\mu\text{m}$	$f_{\max}/\text{THz}$	$f_{\min}/\text{THz}$	$f_0/\text{THz}$	$d/\mu\text{m}$	$f_{\max}/\text{THz}$	$f_{\min}/\text{THz}$	$f_0/\text{THz}$
G0	33.33			6.82	4.17			54.54
G1	58.82	6.62	3.88	3.86	6.67	58.48	34.21	34.09
G2	100.0	3.90	2.28	2.27	11.11	35.05	20.55	20.41
G3	181.8	2.14	1.25	1.25	20.0	19.48	11.41	11.36
G4	333.3	1.17	0.69	0.68	33.33	10.91	6.90	

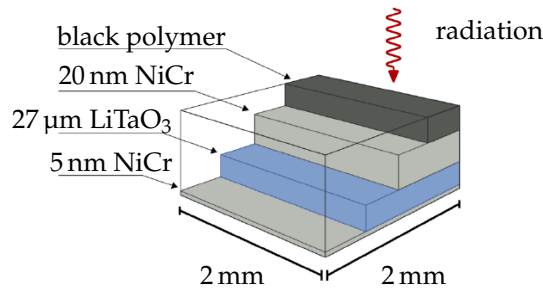


FIGURE 4.13: Layout of the used pyroelectric detector LIM-107-X005 made by InfraTec. The pyroelectric LiTaO<sub>3</sub> crystal is embedded by NiCr electrodes and a black polymer coating increases the sensitivity for frequencies above 3 THz. Adapted from [Wes+11].

Tab. 4.1. The two grating sets are mounted on top of each other on a vertical linear-motion stage and can thereby be remotely interchanged.

An illustration of the setup focusing the dispersed radiation onto detectors is depicted on the right of Fig. 4.12. The dispersed radiation of each grating is reflected upwards and focused by ring-shaped parabolic mirrors covering the dispersion angle interval of  $[25.5^\circ, 85.5^\circ]$ . Above each ring mirror an array of thirty pyroelectric detectors is placed inside the focus to detect the dispersed radiation. The detectors are arranged in a circular arc that covers the dispersion angle interval  $[26.4^\circ, 81.8^\circ]$ .

### 4.3.1 Detection and pulse shaping electronics

The pyroelectric detectors have been developed by an industrial company to have a fast thermal response and sufficient sensitivity for the detection of coherent transition and diffraction radiation. The layout of the used detectors with  $2 \times 2 \text{ mm}^2$  active area is shown in Fig. 4.13. The  $27 \mu\text{m}$  thick pyroelectric lithium tantalate (LiTaO<sub>3</sub>) [RB73] crystal is embedded in  $20 \text{ nm}$  respectively  $5 \text{ nm}$  thick NiCr electrodes. With this configuration, the usual strong frequency-dependent sensitivity oscillations of pyroelectric detectors are suppressed [Wes+11]. A black polymer coating on the front side increases the absorption above 3 THz. The considered response of the detector is shown in Fig. 4.14 (line), which has been obtained by extrapolating measurements (dots) using a suitable model [Beh08]. The spectral sensitivity however depends on the actual layer thicknesses which vary due to fabrication tolerances and are one error source for the modeled sensitivity of the spectrometer (see Sec. 5.1).

Upon absorption of radiation the pyroelectric crystal undergoes a thermal expansion which creates surface charge. As depicted in the schematic illustration of the

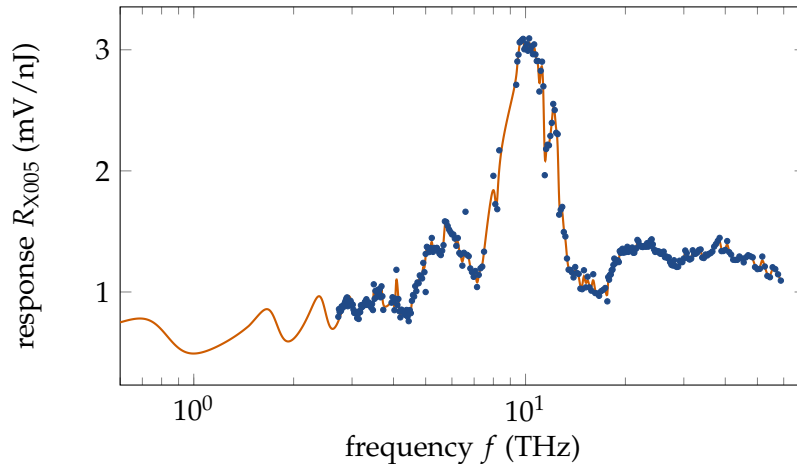


FIGURE 4.14: Considered response of the LIM-107-X005 detector which is obtained by fitting a model to available experimental data (dots) [Beh08]. The detector response also depends on the actual thickness of the different layers, which varies due to limited manufacturing precision [Wes12].

readout electronics in Fig. 4.15, a charge-sensitive preamplifier<sup>3</sup> converts the charge to a voltage signal. The preamplifier has been exchanged with a faster version compared to the spectrometer at FLASH. Here, the preamplifier generates an exponential step-like function with a decay time of only 1.4  $\mu\text{s}$  compared to 140  $\mu\text{s}$  at FLASH. During bunch train operation with the highest possible repetition rate of 4.5 MHz, the signal of the preamplifier reaches a steady state after about 25 bunches as illustrated in Fig. 4.16. At this time, the influence of the first bunch is not significant anymore and the signal reaches values around 7-times the signal amplitude of a single bunch. Smaller time constants decrease the signal-to-noise ratio, but for larger time constants, the steady state occurs later with higher signal level, which potentially is in the saturation regime of the electronic pulse-shaping and readout chain (see Sec. 5.3). The signals are guided outside the spectrometer via shielded twisted-pair cables and RJ-45 connectors to a MicroTCA.4 crate for signal shaping and digitization by a combination of rear transition module (RTM) and advanced mezzanine card (AMC).

The shaping takes place on four Tews RTM TAMC532-TM<sup>4</sup> each with 32 channels which are organized in four blocks. For each block, the input gain can be set to 1, 2, 5 or 10. A differentiator and two 2nd order low-pass filter form the shaping amplifier, which converts the step-like voltage signals to Gaussian-like signals. For each block, the rms width of the shaping can be selected to 0.1  $\mu\text{s}$ , 1  $\mu\text{s}$  or 10  $\mu\text{s}$ . In order to obtain well-separated Gaussian signals for each bunch at MHz repetition rates, the shaping width is set to 0.1  $\mu\text{s}$ . The input buffer gain is set to 1 as no improved signal-to-noise ratio was observed and this minimizes the saturation threshold in single-bunch operation (see Sec. 5.3). Each channel exhibits an adjustable pole-zero compensation to restore the baseline after the bunch induced signal and an adjustable baseline shift at the output buffer.

The signals are digitized by four Tews AMC TAMC532-10R<sup>5</sup>, which are synchronized with the timing system of the European XFEL accelerator. The ADCs are capable of running with a sampling rate up to 75 MHz and have 12-bit resolution. In

<sup>3</sup>custom CR110 rev.2 ( $R = 1 \text{ M}\Omega$ ,  $C = 1.4 \text{ pF}$ ) by Cremat Inc.

<sup>4</sup>[www.tews.com/Products/ArticleGroup/TAMC/TAMC532-TM.html](http://www.tews.com/Products/ArticleGroup/TAMC/TAMC532-TM.html)

<sup>5</sup>[www.tews.com/Products/ArticleGroup/TAMC/TAMC532.html](http://www.tews.com/Products/ArticleGroup/TAMC/TAMC532.html)

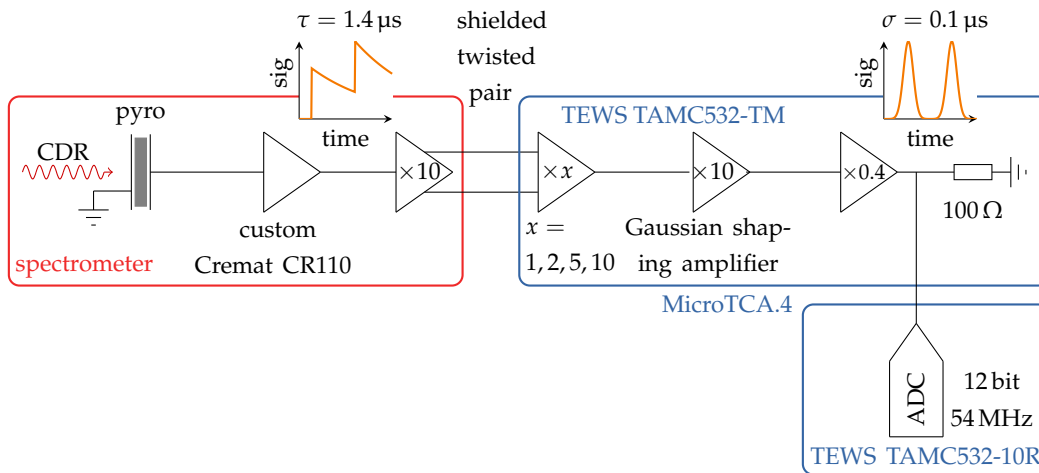


FIGURE 4.15: Schematic illustration of the spectrometer readout electronics. For each channel a charge sensitive preamplifier converts the surface charges at the pyroelectric crystal to an exponential step-like function inside the spectrometer. Gaussian shaping amplifiers on a MicroTCA.4-crate RTM card generate Gaussian-like signals for each bunch which are then digitized by ADC cards inside the crate.

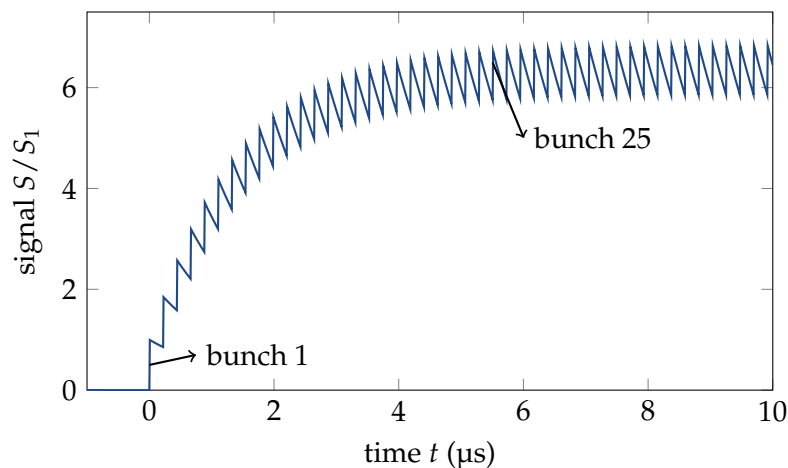


FIGURE 4.16: Illustration of the steady state of the signal after the preamplifier at a repetition rate of 4.5 MHz. The signal  $S$  is normalized to the amplitude  $S_1$  of a single bunch.

interest of the same sample position for each bunch, the ADC sampling rate is set to a multiple of the maximum 4.5 MHz bunch repetition rate. The sampling rate of 54 MHz (12th multiple) yields a good compromise between manageable data size and resolution of the 0.1  $\mu$ s wide Gaussian signals.

Pyroelectric detectors suffer from mechanical crystal oscillations which result in a ringing after the bunch induced signal by the piezoelectric effect [GA70]. The characteristic modulation frequency of the ringing is in the MHz regime and – as this is near the bunch repetition rate – not removed by the pulse shaping electronics. This ringing influences the signal of preceding bunches during MHz operation (pileup), but can be removed by signal processing as will be shown in Sec. 7.1. However, the current status of the readout electronics denies operation with the maximum bunch repetition rate of 4.5 MHz at European XFEL and is currently limited to repetition rates of 2.2 MHz and below. Anyway, the repetition rate within FEL operation has been mostly limited to 2.2 MHz or smaller during the time of this thesis.

## Chapter 5

# Spectrometer Sensitivity

The longitudinal form factor can be determined based on spectroscopic measurements by rearranging Eq. (3.14) to

$$|F_L(f)| \approx \sqrt{\frac{dU}{df}(f) / \left[ \frac{dU}{df}(f) \right]_1} \cdot \frac{1}{N_e}, \quad (5.1)$$

if the ratio of the emitted coherent spectral energy density  $\frac{dU}{df}(f)$  and the single electron spectral energy density  $\left[ \frac{dU}{df}(f) \right]_1$  – together with the number of electrons  $N_e$  inside the bunch – are known. Each detector channel  $m$  covers a certain frequency range with central frequency  $f_m$ . The detector voltage signal  $v_m$  is proportional (linear) to the spectral energy density, such that Eq. (5.1) is for measurements reformulated as

$$|F_L(f_m)| = \sqrt{\frac{v_m}{v_{m,1}}} \cdot \frac{1}{N_e} = \sqrt{\frac{v_m}{R_m}} \cdot \frac{1}{Q}. \quad (5.2)$$

Introducing the bunch charge  $Q$ , the single electron signal  $v_{m,1}$  is replaced by spectrometer sensitivity  $R_m = v_{m,1}/e^2$  normalized to the elementary charge  $e$ .

The application of Eq. (5.2) in order to convert the ADC signals  $v_m$  of the CRISP spectrometer to a form factor requires the following:

- A measurement of the bunch charge, which can be carried out by well-established methods, e. g. toroids [Nöl09].
- A mapping from spectrometer channel  $m$  to frequency  $f_m$ .
- The spectrometer sensitivity  $R_m$  to convert the voltage signal  $v_m$  to a form factor value  $|F_L(f_m)|$ .

The latter is especially difficult to obtain because the single particle, i.e. the incoherent, spectrum is much less intense (see Sec. 3.1) and thus too weak to be detected by the CRISP spectrometer. Furthermore, missing well-characterized sources and detectors in the THz regime [Kle07] prevent an absolute calibration of the spectrometer along its entire range in the frequency domain. The spectral energy density entering the spectrometer depends strongly on radiation emission and transport (see Chap. 4). Therefore, even if an external absolute calibration was accessible, the sensitivity of the CRISP spectrometer would have to be determined anew for every experimental setup. This is also true for different beam energies as the radiation properties change.

For the setup at European XFEL, the spectrometer sensitivity is identified in two ways. First, the sensitivity of the spectrometer is modeled based on numerical simulations and – as far as available – external calibrations of its individual components

[Beh08; Wes12; Köv16]. This sensitivity has been the basis for the design of the experimental setup (e.g. detector electronics). However, the spectrometer is very sensitive to its internal alignment such that an in-situ identification of the spectrometer sensitivity is mandatory for accurate current profile reconstructions. Thus, the second approach to identify the spectrometer sensitivity at European XFEL is based on an in-situ calibration using time domain measurements of a transverse deflecting structure (TDS) as well as beam-based methods. Within the scope of this thesis, such a systematic procedure for the identification of the in-situ sensitivity of the CRISP spectrometer has been carried out for the first time. It is studied whether a possible saturation of the spectrometer signals influences form factor measurements and if the use of noninvasive DR leads to considerable drawbacks compared to invasive TR. As the CRISP spectrometer has not been operated with DR before, it must be clarified how electron beam orbit variations influence the radiation emission and thereby the spectrometer sensitivity.

## 5.1 Modeling

Both, assignment of spectrometer channels to frequencies and spectrometer sensitivity, are modeled based on the Fourier transform method (see App. A). In Chap. 4, the radiation emission of a point-like particle and the radiation transport through the THz beamline is described. Now, the radiation is also tracked through the spectrometer itself. The spectrometer is modeled in the same way as described in [Wes12] such that the structure of this section is closely related to this reference. The model takes the reflectivities and efficiencies of the optical components into account. For illustration purposes, only the results for the 5 mm diffraction radiator at an electron beam energy of 15 GeV are presented. It should be noted that the DR intensity changes at maximum by 5 % at the high frequency channels within the typical range of beam energies from 11 GeV to 17.5 GeV at FEL user operation. This difference is smaller than the shot-to-shot fluctuations of form factor measurements in this frequency region as well as uncertainties of the spectrometer sensitivity itself. The spectrometer sensitivity obtained at 15 GeV can thus be applied within this beam energy range without restrictions. For a possible future cw operation with lower beam energies, the spectrometer sensitivity will have to be determined in a similar way.

The dispersion at the gratings is modeled in the simulation according to the grating equation

$$\beta = \arcsin \left( \frac{c}{fd} - \sin \alpha \right), \quad (5.3)$$

where  $\beta$  is the angle of dispersion with respect to the grating normal,  $\alpha = 19^\circ$  the angle of the incoming radiation,  $f$  the frequency of the radiation,  $d$  the grating period and  $c$  the speed of light. By explicitly tracking the radiation from screen to detector plane, the profiles and positions on the detector are obtained for 300 frequencies along the spectrometer range. From those simulated radiation profiles, a morphing algorithm interpolates the profiles and positions on the detector array for 500 frequencies at each grating stage. The profiles are integrated over the transverse dimensions of each detector, which results in the spectral energy density on the detector. By multiplying it with the detector sensitivity (Fig. 4.14) and including the pulse shaping electronics, it is converted to an ADC signal per frequency

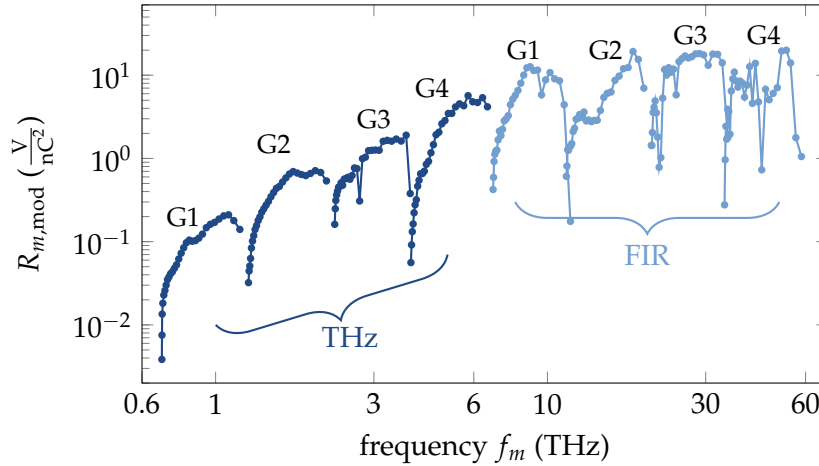


FIGURE 5.1: Modeled sensitivity of the spectrometer for diffraction radiation at the 5 mm aperture and 15 GeV beam energy. For each channel at both grating sets (FIR/THz), the central frequency  $f_m$  and the sensitivity  $R_{m,\text{mod}}$  are obtained by simulations of radiation emission and transport as well as a model for the detector sensitivity.

$dv_{m,1}/df(f)$ . The integration over all frequencies and normalization to the elementary charge yields the modeled spectrometer sensitivity

$$R_{m,\text{mod}} = \frac{1}{e^2} \int_0^\infty \frac{dv_{m,1}}{df}(f) df. \quad (5.4)$$

The central frequency of each detector channel is calculated as the first moment by

$$f_m = \frac{1}{R_{m,\text{mod}}} \frac{1}{e^2} \int_0^\infty f \frac{dv_{m,1}}{df}(f) df. \quad (5.5)$$

The central frequencies obtained hereby agree very well with the frequencies resulting from simple geometric considerations based on the grating equation and deviations, which are mainly present at channels at the edge of each grating stage, are limited to less than 1%.

The modeled spectrometer sensitivity  $R_{m,\text{mod}}$  as function of the central frequency  $f_m$  of the respective channel is shown for the THz and FIR grating set in Fig. 5.1. The spectrometer sensitivity is mostly defined by effects inside the spectrometer, while contributions due to the spectral distribution of DR are not visible on this scale. First of all, the eight grating-stages are clearly distinguishable by a sawtooth-like structure. At each grating stage, the sensitivity increases with dispersion angle and thus frequency. This is due to the non-linearity of the dispersion angle  $\beta$  with frequency (see Eq. (5.3)). At smaller frequencies, the slope of the dispersion angle is steeper such that less frequencies are dispersed in the same dispersion angle interval. In addition, the transverse radiation profile is strongly contracted for large dispersion angles (low frequencies) at the grating – as it is not reflected but diffracted – and is thus not optimally focused in the detector plane. Both effects result in a lower sensitivity. Some channels at the edges of the grating stages experience a large drop in sensitivity due to the limiting aperture of the focusing ring mirror (see Fig. 4.12). The overall decreasing sensitivity towards small frequencies is due to stronger diffraction at low frequencies. Frequencies in the THz regime are not focused down to the detector size of 2 mm. Modulations within the grating stages itself are due to the

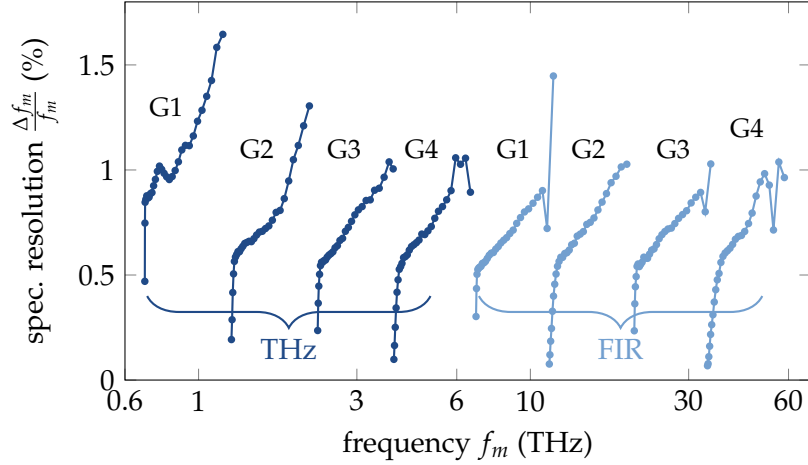


FIGURE 5.2: Resolution of the spectrometer for DR at the 5mm-aperture and 15 GeV electron beam energy. The resolution is determined by the second moments of the modeled ADC signals per frequency  $dv_{m,1}/df(f)$  (see Eq. (5.7)).

response of the pyroelectric detectors (Fig. 4.14) and the polarizer inside the spectrometer [Wes12]. Variations from channel-to-channel are introduced by a system calibration of the CRISP spectrometer carried out at an FEL operating in the IR-regime [Köv16], which is also considered.

The detector noise floor puts a limit to the smallest significant value of measured form factors at channel  $m$  according to Eq. (5.2). This confidence threshold  $\mathcal{L}(f_m)$  is defined by the form factor calculated from the rms detector noise  $\mathcal{S}_m$ . Here, the confidence threshold is set to  $2\sigma$  of the electronic noise. When averaging over  $N$  pulses, the rms signal noise floor decreases such that:

$$\mathcal{L}(f_m) = \sqrt{\frac{2\mathcal{S}_m}{\sqrt{NR_m}} \frac{1}{Q}} = \frac{\sqrt{2}}{\sqrt[4]{N}} \sqrt{\frac{\mathcal{S}_m}{R_m} \frac{1}{Q}}. \quad (5.6)$$

### 5.1.1 Resolution

The spectral resolution of the spectrometer is in analogy to Eq. (5.5) characterized by the second moment

$$\frac{\Delta f_m}{f_m} = \frac{1}{f_m} \sqrt{\frac{1}{R_{m,mod}} \frac{1}{e^2} \int_0^{+\infty} \frac{dv_{m,1}(f)}{df} (f - f_m)^2 df}. \quad (5.7)$$

The resulting simulated resolution is shown in Fig. 5.2. It varies between values smaller than 0.1% up to 1.7% with large variations along each grating stage. The overall increase towards small frequencies is due to increasing beam size at the detector, which also causes the decrease of the spectrometer sensitivity in Fig. 5.1. Within one grating stage, the resolution is – like the sensitivity – dominated by the non-linearity of the dispersion angle  $\beta$  with frequency in Eq. (5.3). The spectral resolution improves within each grating stage towards lower frequencies because the number of frequencies dispersed into a certain angle interval decreases. At low frequency channels and respectively large dispersion angles, the outer edges of the focusing ring mirror clip parts of the transverse profile and limit the spot size on the detector element. As a result the resolution improves artificially.

In order to visualize the effects of the spectral resolution on form factor measurements, the DR of a rectangular bunch with 100 fs duration is explicitly tracked

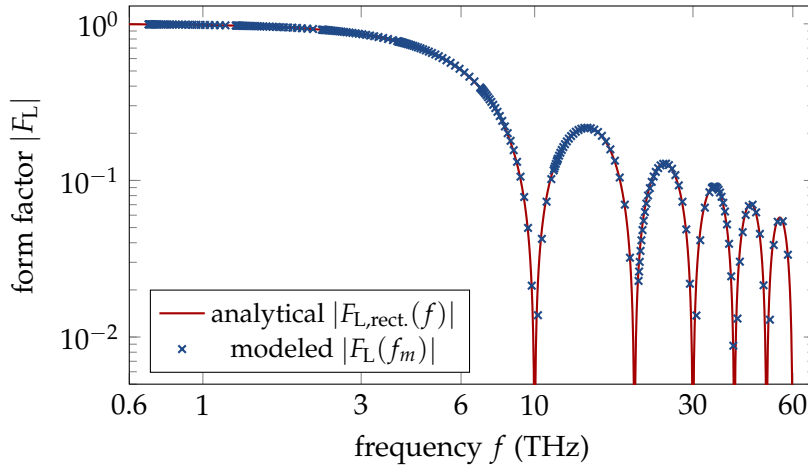


FIGURE 5.3: Simulated influence of the spectrometer resolution on a form factor measurement (blue crosses) of a rectangular current profile with a length of 100 fs, which is compared to its actual form factor (red line). The spectral resolution of the spectrometer allows to resolve fine structures of the form factor up to high frequencies.

through THz beamline and CRISP spectrometer. With this, the influence of overlapping frequencies on the detectors will be accurately modeled. The analytical form factor  $|F_{L,\text{rect.}}(f)|$  of a rectangular bunch with its oscillating behaviour and sharp minima is well suited to demonstrate the capabilities of the spectrometer in terms of spectral resolution. The modeled spectrometer signals  $v_m$  are converted by Eq. (5.2) to yield the simulated form factor measurement  $|F_L(f_m)|$ . The influence of detector noise is here explicitly not considered as the focus lies on the spectral resolution itself (for studies thereof please refer to App. B). In Fig. 5.3, the simulated form factor measurement is compared to the actual form factor of the bunch. Fine structures are correctly reproduced even at high frequency channels of the spectrometer, and the evolution of the form factor is accurately monitored. The spectral resolution of the experimental setup does not influence the quality of form factor measurements for current profile reconstructions.

The result of an actual form factor measurement at European XFEL, which was obtained by converting the spectrometer signals  $v_m$  to a form factor using the modeled sensitivity  $R_{m,\text{mod.}}$  in Eq. (5.2), is shown in Fig. 5.4. The measurement was carried out with a bunch charge of 250 pC and a beam energy of 14 GeV during single bunch operation. The data points are averaged over 100 rf pulses for each grating set, and the error bars mark the rms shot-to-shot fluctuations. The gray area indicates the confidence threshold  $\mathcal{L}(f_m)$  of the spectrometer measurement due to the noise floor as given by Eq. (5.6). The form factor exhibits an overall reasonable evolution: As expected it decreases continuously towards high frequencies, but shows non-physical oscillations and channel-to-channel fluctuations. Especially at the transitions between the individual grating stages, the form factor varies strongly. These are consequences of small misalignment inside the spectrometer and uncertainties – e.g. the sensitivity of the pyroelectric detectors – of the modeled spectrometer sensitivity. This is by no means in contradiction to a well understood radiation emission and transport process. As the spectrometer sensitivity depends strongly on the beam sizes at the detectors, it is also very sensitive to the exact internal alignment. Thus, an in-situ calibration with an independent device is a great advantage as the accuracy of longitudinal form factor measurements is increased.

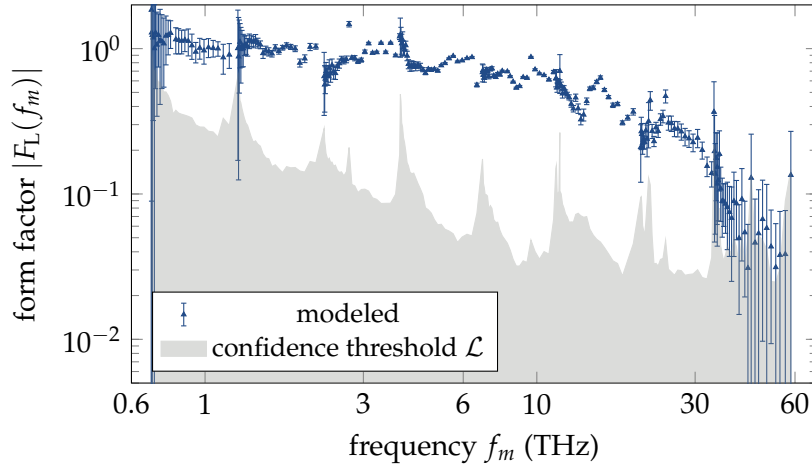


FIGURE 5.4: Form factor measurement based on the CRISP spectrometer and the modeled spectrometer sensitivity using DR at the 5 mm aperture. The overall evolution of the decreasing form factor looks reasonable, but a non-physical oscillatory behaviour and channel-to-channel variations make an in-situ identification (Sec. 5.2) indispensable for current profile reconstructions. The gray area marks the confidence threshold  $\mathcal{L}(f_m)$  due to noise floor, and the error bars represent the rms shot-to-shot fluctuations.

## 5.2 In-Situ Identification

### 5.2.1 Calibration with TDS

The spectrometer sensitivity is calibrated over a wide frequency range of the spectrometer by comparative TDS measurements after the final magnetic bunch compressor BC<sub>3</sub> (Sec. 2.4.1). This can be done because the collimator section of European XFEL is designed to be achromatic and isochronous. As can be seen in Fig. 2.6, there is no significant contribution of the  $R_{56}$ -parameter from the location of the TDS to the spectrometer position, which would influence the electron bunch current profile [Fen+].

The electron bunch current profile measured with the TDS is shown on the left hand side of Fig. 5.5. Hereby, the accelerator is operated with a single bunch (i. e. no MHz bunch train) and special TDS beam optics in the local dump section (see Sec. 2.4.1). With a bunch charge of 150 pC, the average profile of 5 rf pulses at each zero-crossing of the transverse deflecting field is taken. This allows to correct for transverse-longitudinal correlations [Sch+20] and yields a rms bunch duration, which is calculated from the measured current  $I(t)$  as

$$\sigma_m = \sqrt{\frac{\int I(t) \cdot (t - \bar{t})^2 dt}{\int I(t) dt}} \quad \text{with } \bar{t} = \frac{\int I(t) \cdot t dt}{\int I(t) dt}, \quad (5.8)$$

of  $\sigma_m = 14.3$  fs and a peak current close to 5 kA. The correction of transverse-longitudinal correlations are also applied to the unstreaked profile at the observation screen in order to obtain the temporal resolution of the TDS. The result is depicted in Fig. 5.5 and yields a rms resolution of  $\mathcal{R}_t = 5.9$  fs. Subtracting this resolution quadratically results in a rms bunch duration of  $\sigma_t = \sqrt{\sigma_m^2 - \mathcal{R}_t^2} = 13.0$  fs. The TDS profile shape is asymmetric with a slower decrease of the current towards the tail ( $t < 0$ ) of the bunch. The measured bunch properties, like rms duration and peak current, agree with those expected from start-to-end simulations during FEL user operation (see Sec. 2.3). The shot-to-shot fluctuations (see Fig. 5.5) of the rms duration of the TDS

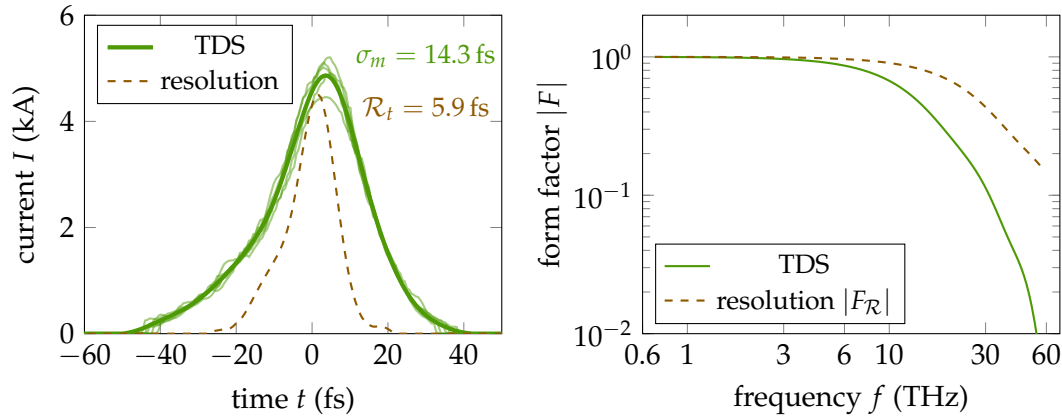


FIGURE 5.5: Electron bunch current profile (left) obtained with the TDS downstream of BC<sub>3</sub> as average of a total of 10 single shot profiles (light green). The average is used to calibrate the spectrometer sensitivity. From the resolution function of 5.9 fs rms duration and the 14.3 fs rms duration of the average profile, the rms bunch duration is calculated. The bunch head corresponds to positive values of  $t$ . The profiles result in the form factors on the right. The resolution function reduces the sensitivity of the TDS towards higher frequencies.

profile as well as the uncertainty on the streak parameter (see Sec. 2.4.1) are small (<5%) and thus not further considered at this point. The spectrometer sensitivity calibration is carried out with respect to the form factor. Therefore, the TDS profile and resolution function are transformed into frequency domain based on Eq. (3.16).

The form factors associated to the measured profiles are presented on the right hand side of Fig. 5.5. The blurring of substructures due to the TDS resolution is expressed in the frequency domain by a decrease of the form factor  $|F_{\mathcal{R}}|$  of the resolution function. A form factor of the resolution function smaller than 1 reduces the sensitivity of the TDS at these frequencies. Consequently, if the resolution form factor  $|F_{\mathcal{R}}|$  is significantly smaller than 1, the TDS is not able to detect any structures in this frequency region.

For the CRISP measurement, the beam optics are switched back to usual FEL operation, and the single bunch is not terminated in the TDS diagnostics dump. The form factor is obtained by the modeled spectrometer sensitivity and averaging over 50 rf pulses for each grating set. The result is depicted in Fig. 5.6 with error bars marking the rms shot-to-shot fluctuations. The gray area marks the confidence threshold  $\mathcal{L}(f_m)$  of the measured form factor signals. For comparison, the form factor of the TDS profile is shown as well. Compared to the spectrometer measurement, which results again in non-physical oscillations and channel-to-channel fluctuations, this is a smooth function of frequency. However, both form factors agree in their slowly and continuously decreasing behaviour. At the grating stage with highest frequencies, the CRISP measurement exhibits large relative shot-to-shot fluctuations due to small signal-to-noise ratio below the confidence threshold.

As mentioned above, the TDS resolution leads to a reduced sensitivity at high frequencies. In this case, a conservative approach ( $|F_{\mathcal{R}}| > 0.4$ ) limits the TDS frequency region to  $f < 30$  THz. Besides, the reduced sensitivity also leads to a steeper decrease of the form factor associated to the measured TDS profile than the form factor of the bunch itself. As this is described by convolution with the resolution function in time domain, it equals multiplication in frequency domain. Inside the sensitive

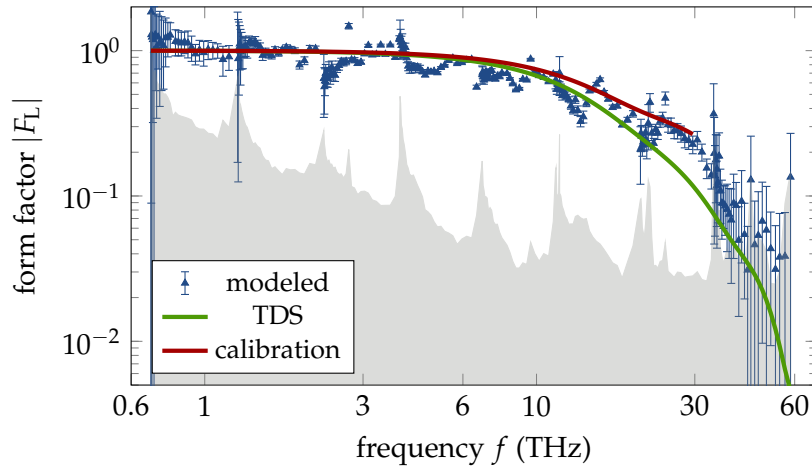


FIGURE 5.6: The form factor of the spectrometer with the modeled sensitivity (blue) follows the overall evolution of the Fourier transform of the TDS current profile (green). The TDS resolution allows a calibration of the spectrometer sensitivity up to frequencies of 30 THz after correcting for the temporal resolution of the TDS (red).

frequency region of the TDS ( $f < 30$  THz), the form factor of the electron bunch can thus be approximated by dividing the measurement with the resolution  $|F_R|$ . The result is illustrated as red line in Fig. 5.6 and the in-situ identified spectrometer sensitivity is set to yield the same results based on Eq. (5.2) in this frequency region.

## 5.2.2 Beam-based methods

### High charge

By increasing the bunch charge to 500 pC, the coherent radiation intensity and thus signal-to-noise ratio increases by more than a factor of 10 compared to the 150 pC bunch charge used in Sec. 5.2.1. This yields a simple way to identify the spectrometer sensitivity at low frequency channels much more precisely. The form factor of such a bunch – TDS calibration already applied – is presented in Fig. 5.7. At the low frequency grating stages, the form factor has almost reached its asymptotic limit of 1. It decreases monotonously into a local minimum at around 12 THz. At low frequencies up to the minimum, the measurement is well approximated by a Gaussian profile. The fit (green) is used to correct the TDS calibration up to 2.3 THz such that the in-situ identified sensitivity leads to the same result.

### Low charge

A calibration of the frequency channels above 30 THz based on TDS measurements is not possible as the TDS is not sensitive to structures at these frequencies (see Sec. 5.2.1). Nevertheless, the in-situ spectrometer sensitivity in this region can be identified using bunches with low charge in combination with the results of the already TDS calibrated region. These bunches with charges of 50 pC or below can be compressed to very short durations of only a few femtoseconds (see Tab. 2.2). In this case, the frequencies of the current profile substructures lie already outside of the frequency range of the CRISP spectrometer. The form factors consequently decrease slowly and monotonously along the entire frequency range (compare also

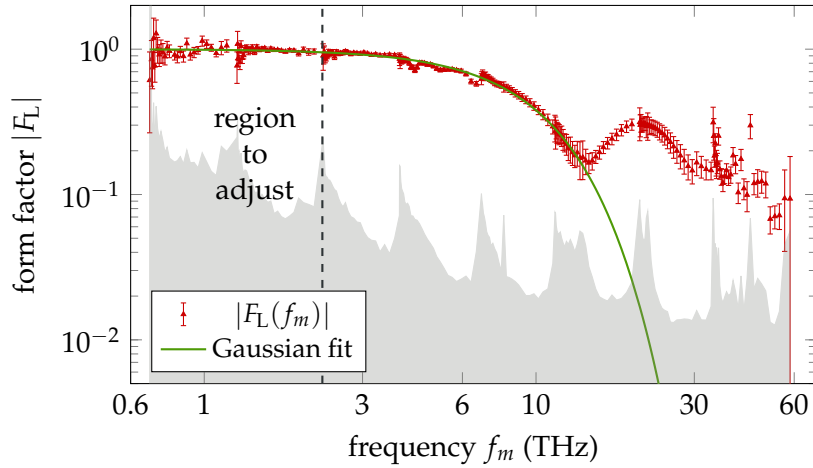


FIGURE 5.7: Measured form factor (red) of a bunch with 500 pC charge based on a combination of the TDS calibrated ( $f_m < 30$  THz) and modeled spectrometer sensitivity. The increased charge and thus more intense DR allows a more precise identification of the spectrometer sensitivity for frequencies below 2.3 THz based on a Gaussian fit after the TDS calibration.

with Fig. 3.4). Thus, the spectrometer sensitivity at high frequencies must yield a homogeneous extrapolation above the TDS calibrated region. This allows to identify the in-situ spectrometer sensitivity.

Figure 5.8 presents the form factor  $|F_L(f_m)|$  obtained with the spectrometer sensitivity of the previous subsection. In the TDS calibrated region, the form factor modulus decreases only down to 0.7 and fulfills the expected behaviour of a slowly and monotonously decreasing form factor. Above this region, the form factor based on the modeled sensitivity shows oscillating behaviour as well as non-physical jumps from channel-to-channel. However, the rms shot-to-shot fluctuations are low and indicate a stable bunch compression. In fact, the form factor in this region follows the form of the modeled sensitivity (Fig. 5.1) in its strong deviations between edge and central channels of the grating stage as well as channel-to-channel fluctuations. The ADC signals  $v_m$  itself behave in comparison rather uniformly at these frequency channels. Therefore, the oscillatory behaviour of the measured form factor is due to the spectrometer sensitivity instead of the electron bunch itself. As the form factor is in this case not sensitive to substructures, spectrometer sensitivity and measured form factor can be flattened by an extrapolation of the calibrated spectrometer region ( $f_m < 30$  THz) using a suitable function describing the current profile envelope.

Modeling is carried out by different analytical functions (e.g. Gaussian, rectangle, sawtooth, composition of two Gaussians) in order to find the best matching form factor in the TDS calibrated frequency range. As illustrated in Fig. 5.8, the different functions lead only to small differences above 30 THz. This confirms that in this case the form factor in the spectrometer frequency region is not sensitive to substructures of bunch shape and the extrapolation based on an envelope function is a well suited approach. However, the best agreement in the TDS calibrated region is obtained with the form factor of a composition at the origin of two Gaussian functions with different durations<sup>1</sup> and 11.8 fs total rms duration. The form factor of this profile is illustrated by the green line. The beam-based identification of the spectrometer

<sup>1</sup> $\exp\left(-\frac{(t-t_0)^2}{2\sigma_1^2}\right)$  for  $t < t_0$  and  $\exp\left(-\frac{(t-t_0)^2}{2\sigma_2^2}\right)$  for  $t \geq t_0$

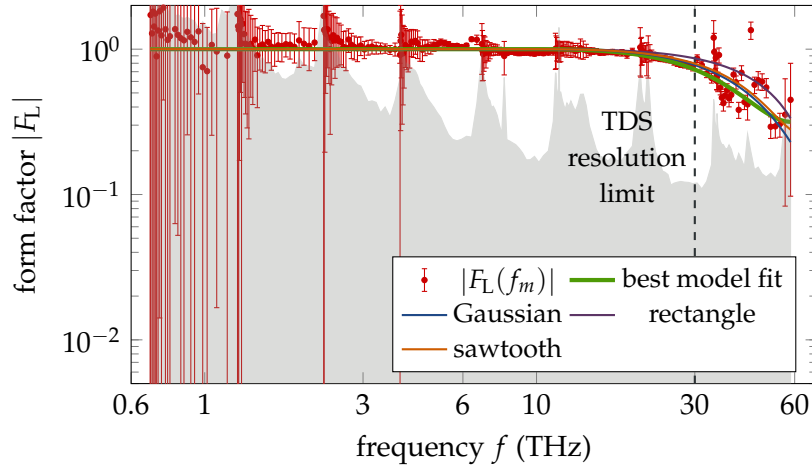


FIGURE 5.8: Measured form factor of a short electron bunch with 50 pC charge (red dots). The underlying spectrometer sensitivity is based on TDS calibration (Sec. 5.2.1) and high bunch charge correction which both exclude the region above 30 THz. In order to identify the in-situ sensitivity in the remaining frequency range several envelope functions are adjusted to fit the TDS calibrated region. The best fit yields a composition at the origin of two Gaussian functions with different durations (green line) and a total rms bunch duration of 11.8 fs. This profile is used for the in-situ sensitivity identification above 30 THz.

sensitivity  $R_m$  above 30 THz is to set in accordance to this extrapolation.

The results in Chap. 6 and 7 will show that the systematic identification of the in-situ sensitivity empowers accurate and absolute current profile measurements of varying bunch shape and durations down to a few femtoseconds. The systematic identification of the in-situ spectrometer sensitivity thus determines the sensitivity sufficiently precise. Minor deviations especially at high frequencies are possible but do not significantly influence current profile reconstructions. This in-situ identified sensitivity of the CRISP spectrometer, which has never before been obtained by such a systematic procedure, is compared to the modeled sensitivity in Fig. 5.9. The differences are small compared to the variation of the sensitivity within each grating stage. To the biggest differences of the identified sensitivity  $R_m$  belong adjustments of edge channels, which are very sensitive to the internal alignment of the spectrometer. Around 10 THz the response of the pyroelectric detectors, which has been considered in the modeled sensitivity, exhibits a region with high sensitivity (see Fig. 4.14). The influence of this increased sensitivity region as well as absorption bands of the polarizer at the two grating stages with highest frequencies (see [Wes12]) are attenuated by the in-situ identification. The remaining differences can be explained by minor misalignment as well as manufacturing tolerances of the pyroelectric detectors.

A comparison of the form factors obtained with the modeled and identified spectrometer sensitivity of the bunch already shown in Fig. 5.4 is given in Fig. 5.10. The modifications due to the in-situ identification are clearly visible in the double-logarithmic illustration of the form factor. The identified sensitivity removes the oscillatory behaviour of the measured form factor and results in smoother transition between the single grating stages. While the overall evolution of the form factor does not change, this uniform behaviour is of extreme importance for the current profile reconstruction. Only with the applied TDS calibration and beam-based methods, the form factor can be sufficiently well characterized along the entire frequency range.

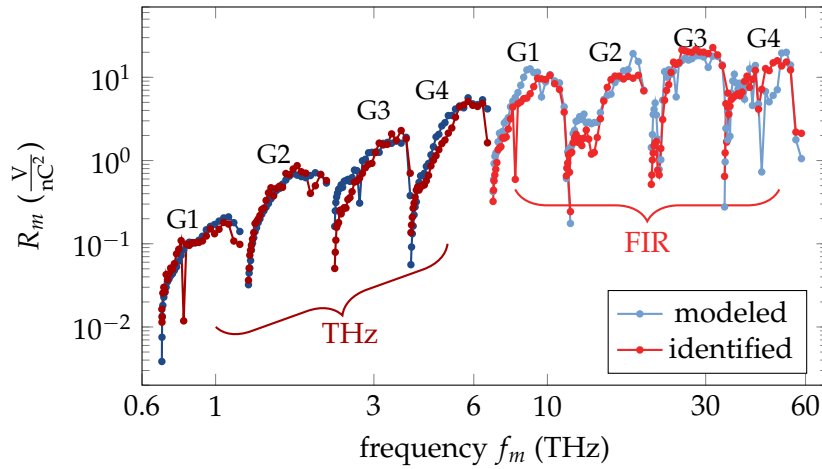


FIGURE 5.9: Comparison of the modeled and the spectrometer sensitivity, which has been identified based on TDS measurements and beam-based methods. Even though the variation of the spectrometer sensitivity within each grating stage is larger than the difference to the modeled sensitivity, the in-situ identification removes the oscillating behaviour and channel-to-channel jumps of the form factor (see Fig. 5.10.)

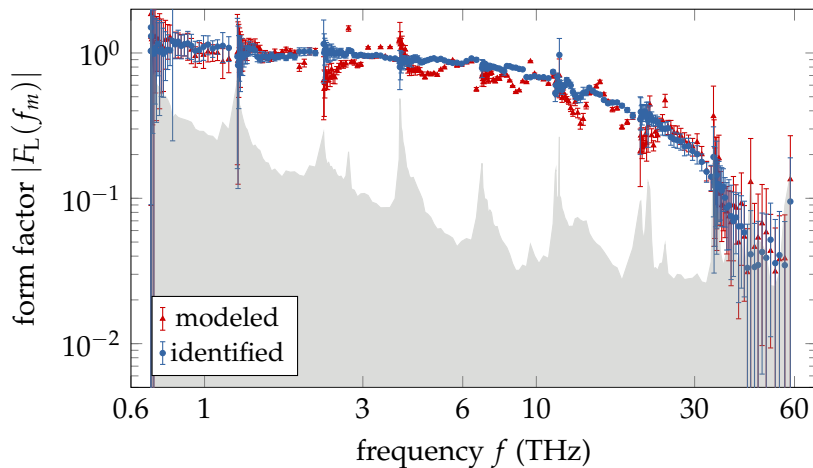


FIGURE 5.10: Form factor of a bunch with 250 pC charge and 14 GeV beam energy measured with the CRISP spectrometer and DR at the 5 mm aperture. From the same spectrometer signals the form factor was obtained once with the modeled (red) and once with the in-situ identified sensitivity (blue). Using the identified sensitivity the oscillating behaviour is removed and the transition between the grating stages is smooth.

Otherwise, jumps and oscillatory behaviour would inevitable lead to current profiles incompatible with electron bunch properties. Before the in-situ spectrometer sensitivity is identified, the TDS is needed for reliable statements about the electron bunch current profile and thus a substantial part of the systematic identification of the in-situ sensitivity. The modeled sensitivity is important for the design of the experimental setup but also of great advantage for the application of beam-based methods to the in-situ sensitivity identification.

The in-situ identified spectrometer sensitivity depicted here is used for all following form factor measurements in this thesis based on DR at the 5 mm aperture. The large variety of bunch shapes and duration as well as the elapsed time between the individual measurements show that the spectrometer sensitivity does not change rapidly. Once determined by the here stated procedures, it can be applied as long as the THz beamline or spectrometer alignment is not modified. This also includes small variation of the electron beam orbit, which will be studied in Sec. 5.5.

### 5.3 Saturation

The in-situ identified spectrometer sensitivity allows to determine the form factor level at which the pulse-shaping and readout components saturate. This is of fundamental importance for the applicability of the spectrometer. For MHz operation, the limiting factor is the RTM's input acceptance range of  $\pm 2.5$  V. The steady state of the superimposing signals at the preamplifier, which reaches roughly 7-times the signal of a single bunch (see Fig. 4.16) must not overcome this voltage level. This limits signals of a single bunch at the RTM input to  $S_{1,\max} = 2.5 \text{ V} / 7 = 0.36 \text{ V}$ . The single bunch signal  $S_1$  at the RTM input is amplified by a factor 4 (see Fig. 4.15) to yield the signal  $v_m$  at the ADC. During single bunch operation, the signals are not superimposed at the RTM input and the limiting factor is the ADC voltage range of 2 V. This however does not influence the saturation at MHz repetition rates, because the saturation limit is higher ( $S_{1,\max} \cdot 4 < 2 \text{ V}$ ) and not further considered at this point. The maximum detectable form factor, which is due to saturation at the RTM, can be estimated in analogy to Eq. (5.2) by

$$|F_L(f_m)|_{\max} = \sqrt{\frac{4 S_{1,\max}}{R_m}} \frac{1}{Q}. \quad (5.9)$$

The resulting limitations for detectable form factors (solid lines) are shown in Fig. 5.11 for the most common charge of 250 pC during FEL operation and the maximum bunch charge of 1 nC. For comparison, the form factors from start-to-end simulations (see Sec. 3.2) at these charges are illustrated. The bunch carrying 1 nC is not compressed to bunch durations as short as in the 250 pC case. Consequently, the form factor drops already at low frequencies. The saturation level  $|F_L(f_m)|_{\max}$  for 250 pC is at all channels above 1 and – as  $|F_L(f)| \leq 1$  – does not limit form factor measurements even for an infinitesimal short bunch. At 1 nC, the DR intensity increases by a factor of 16 (due to the quadratic dependency on bunch charge  $Q$ ) compared to the same form factor at 250 pC. However, as the form factor scales with the square root of DR intensity and respectively signal  $v_m$  (see (Eq. 5.2)) the form factor saturation limit  $|F_L(f_m)|_{\max}$  decreases only by factor 4. This leads to undetectable regions of form factors close to 1. The size of these regions increase with frequency. However, the measurement of a form factor as expected from the start-to-end simulations is not affected.

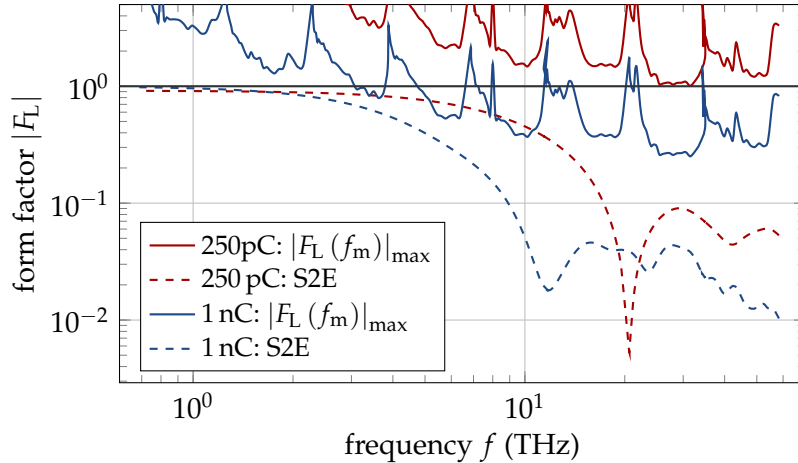


FIGURE 5.11: Form factor saturation limit  $|F_L(f_m)|_{\max}$  due to the pulse-shaping electronics of the CRISP spectrometer at 250 pC and 1 nC bunch charge for multi-bunch operation at 4.5 MHz. For comparison, the corresponding form factors of optimized bunches from start-to-end simulations of European XFEL are illustrated (dashed lines). Only for bunch charges above 250 pC, form factor measurements can be affected ( $|F_L(f_m)|_{\max} \leq 1$ ). However, due to limitations of achievable bunch duration by collective effects, the spectrometer is not expected to saturate even for operation with highest charge (1 nC).

The limitations of the dynamic range of the spectrometer for bunches above 250 pC due to saturation are not an issue for current profile reconstructions. While the saturation limit  $|F_L(f_m)|_{\max}$  decreases with charge, also the form factor at the frequency channels limited by saturation decreases. The minimum achievable bunch durations are dominantly restricted by charge-dependent CSR and space charge effects. Thus, – as shown by the example from start-to-end simulations – the spectrometer signals are not expected to saturate with increasing charge. Due to the sawtooth-like structure of the saturation limit only single channels would start to saturate for bunches with high charge and unexpectedly short durations. The form factor at these channels can however easily be interpolated.

## 5.4 TR/DR Comparison

As described in Sec. 3.4, the intensities and spatial properties of DR and TR are comparable at electron beam energies above several GeV. Therefore, the spectrometer sensitivity of DR promises to be in the vicinity of the TR sensitivity and not to yield any major disadvantages in form factor detection for current profile reconstructions. A measurement of the intensity ratio of DR at the 5 mm aperture to TR using the signals  $v_m$  of the CRISP spectrometer at the same bunch compression setting is shown in Fig. 5.12. A bunch with 250 pC charge ensures sufficient signal along the entire spectrometer range if compressed to adequate bunch durations. The barely visible error bars mark the statistical error on the average of 50 rf pulses while single channels with signals below the confidence threshold are excluded from analysis. For comparison, the ratio of the modeled sensitivities  $R_{\text{mod}}$  for TR and DR are illustrated in the same figure.

As expected from the simulated emission at the screen (see Fig. 4.3), the ratio of TR to DR intensity – and thus spectrometer voltage signal  $v_m$  – does not show a steep drop of DR intensity. The characteristic DR cut-off lies outside of the spectrometer

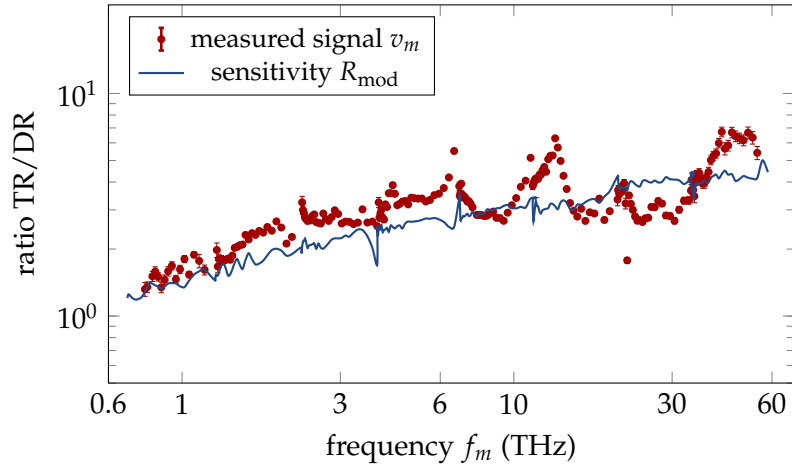


FIGURE 5.12: TR-to-DR ratio of the measured signal  $v_m$  and modeled spectrometer sensitivities  $R_{\text{mod}}$ . Overall the emission process leads to TR between 1.2-times and 4-times more intense than DR.

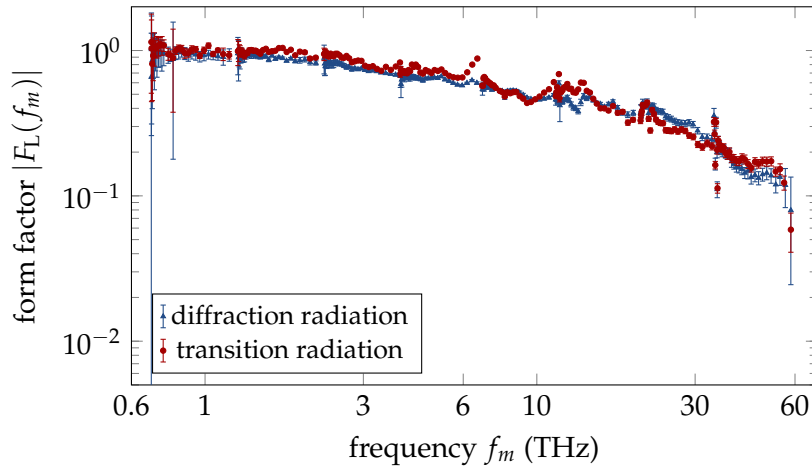


FIGURE 5.13: Form factor measurement with DR and TR at the bunch compression setting used for the comparison in Fig. 5.12. The TR measurement utilizes its modeled spectrometer sensitivity together with the corrections from the DR in-situ identification.

frequency range. Instead the ratio increases continuously with frequency from 1.2 to 4. The TR intensity increases due to the decreasing radiation source size on the finite screen. The DR intensity remains approximately constant because this effect is compensated by the aperture. The experimental observations are in conclusion to the ratio of the modeled spectrometer sensitivities, which is illustrated for comparison and its overall evolution agrees.

The form factors associated to the intensity ratio measurement are illustrated in Fig. 5.13. Using TR and DR, bunches with the same compression settings are characterized. The TR spectrometer sensitivity is modeled – analog to DR – in first place. Afterwards, the TR sensitivity is adjusted using the corrections of the in-situ identification of the DR sensitivity to its model. This TR sensitivity results in almost no non-physical oscillatory behaviour and channel-to-channel fluctuations if compared to form factors obtained with the modeled DR sensitivity (see Fig. 5.4). This demonstrates that differences between the modeled and final sensitivity are mainly due to effects inside the spectrometer (alignment, detector sensitivity,...) which are not

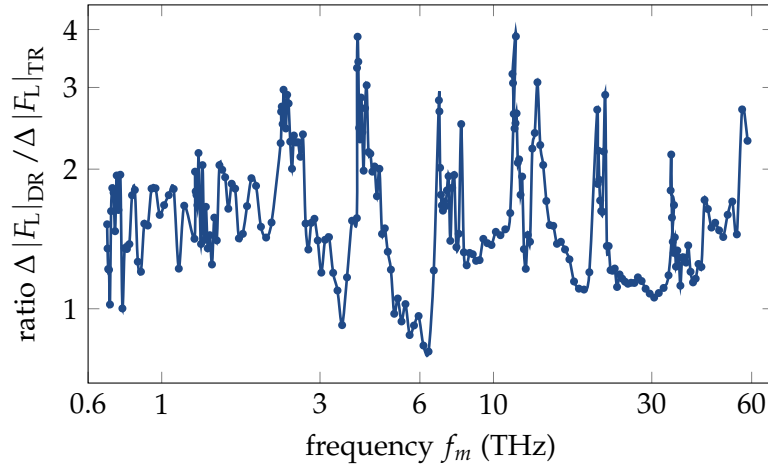


FIGURE 5.14: Ratio of the measured shot-to-shot form factor fluctuations of DR to TR. Compared to TR, the DR fluctuations increase overall by less than a factor of two, and are therefore not causing considerable limitations.

considered by the model and independent of radiation source. The TR sensitivity is finally calibrated by matching the resulting form factor to the DR measurement.

As the form factor scales with the square root of the spectrometer signal  $|F_L(f_m)| \propto \sqrt{v_m}$  (see Eq. (5.2)), the up to five-times increased signal level of TR decreases the confidence threshold  $\mathcal{L}(f_m)$  only by a factor  $\sim 2$ . Also, the measured shot-to-shot fluctuations of the form factor  $\Delta |F_L(f_m)|$  scale by error propagation of intrinsic signal fluctuations  $\Delta v_m$  inversely with the square root of the spectrometer signal  $\Delta |F_L(f_m)| \propto \Delta v_m / \sqrt{v_m}$  and respectively radiation intensity. An increase of shot-to-shot fluctuations  $\Delta |F_L(f_m)|$  by factor  $\sim 2$  when switching from TR to DR would be expected. The ratio of the fluctuations from the above measurement is presented in Fig. 5.14. It shows that – except for some edge channels – even at high frequencies, where the TR signal is overall four-times higher, the rms fluctuations increase on average nevertheless by a factor  $< 2$ . This is because the signal rms fluctuations are also caused by changes of the electron bunch compression itself, and because the intrinsic detector fluctuations  $\Delta v_m$  are increasing with signal amplitude  $v_m$ . As the increased spectrometer sensitivity also reduces the saturation limit, the use of DR at European XFEL does not cause any major disadvantages in accuracy and dynamic range of form factor measurements for current profile reconstructions. However, DR yields the big advantage of being noninvasive and thereby allowing to monitor all bunches inside the train simultaneously.

## 5.5 Orbit Dependencies

The DR screen for the CRISP spectrometer is located downstream of the fast transverse orbit feedback, which ensures a stable orbit along the bunch train. However, the reference electron beam position of the orbit feedback may vary on the day/week time scale due to empirical accelerator optimization. In this section, the consequences of electron beam misalignment with respect to DR screen on the spectrometer sensitivity are studied using simulations. The electron beam may be misaligned with respect to the DR screen and thereby its nominal orbit in two ways: A transverse position offset and an angle with respect to the nominal beam path.

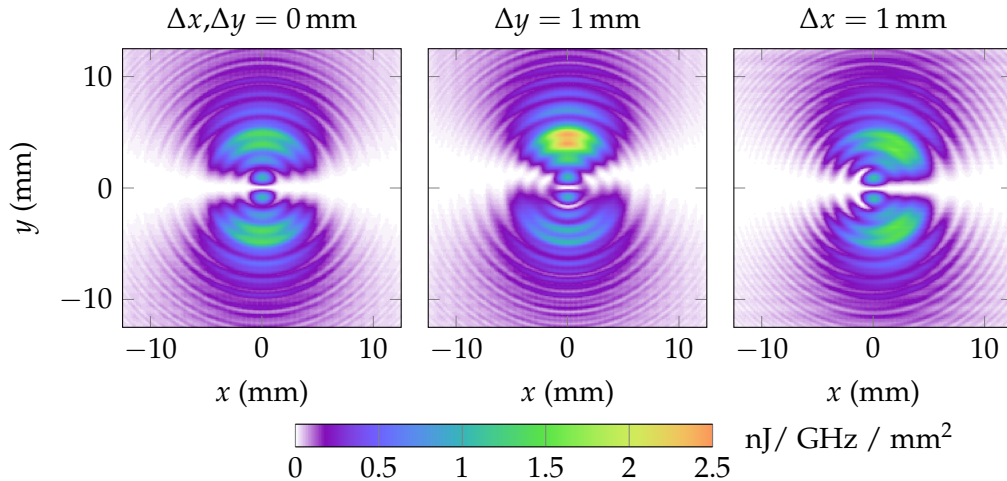


FIGURE 5.15: Simulated radiation profiles for the vertical polarization on the diamond window using the same color scaling with and without vertical  $\Delta y$  and horizontal  $\Delta x$  electron beam displacement at the screen. The offsets modify the transverse radiation properties and lead to an increase of intensity.

An offset of the electron beam with respect to the center of the DR aperture modifies the transverse intensity distribution. This is illustrated by the transverse radiation profiles at 15 GeV beam energy for the vertical polarization in Fig. 5.15. This polarization on the diamond window (see Sec. 4.1) corresponds to the polarization used inside the CRISP spectrometer. While the radiation profile is almost – inclination factor  $\cos \theta$  (see Sec. 3.4) – perfectly symmetric without electron beam offset, the symmetry is broken in the direction parallel to electron beam offset. For a vertical offset, this results in an asymmetry along the polarization axis. The maximum radiation intensity is hereby significantly increased. For an horizontal offset, this leads to an asymmetry perpendicular to the polarization axis, which blurs the characteristic double peaks of DR. The region with radiation close to the maximum intensity is larger in comparison to the case without electron beam offset.

As already indicated, an electron beam offset leads not only to asymmetric radiation profiles, but also effects the totally emitted spectral energy density. This is illustrated in Fig. 5.16. For offsets in any direction (parallel or perpendicular to the polarization axis), the spectral energy density on the diamond window increases. For 0.5 mm offset the intensity increases by little more than 1 %, whereas it is roughly 6 % more intense for 1 mm offset. The spectral energy density thus gets progressively more intense for larger offsets. Both effects are a consequence of the scaling of the Coulomb field with distance  $\rho$  (see Sec. 3.4). An electron bunch centered with respect to the aperture minimizes the radiation intensity, and any offset leads to an increase of the emitted radiation. Hereby, the intensity increases nonlinear with offset. The fact that the spectral energy density grows roughly by the same amount for both directions is caused by the distances of the electron beam to the edges of the screen aperture in the polarization direction. The distance perpendicular can be neglected as almost no radiation is generated there. For a parallel ( $\Delta y$ ) offset, one edge gets closer to the beam while the other moves further away. For a perpendicular beam offset ( $\Delta x$ ), both edges get closer to the beam but are further away than the closest edge for the same parallel offset. The resulting intensity increase by two edges being slightly closer or one edge becoming significantly closer while the other moves further away are almost identical.

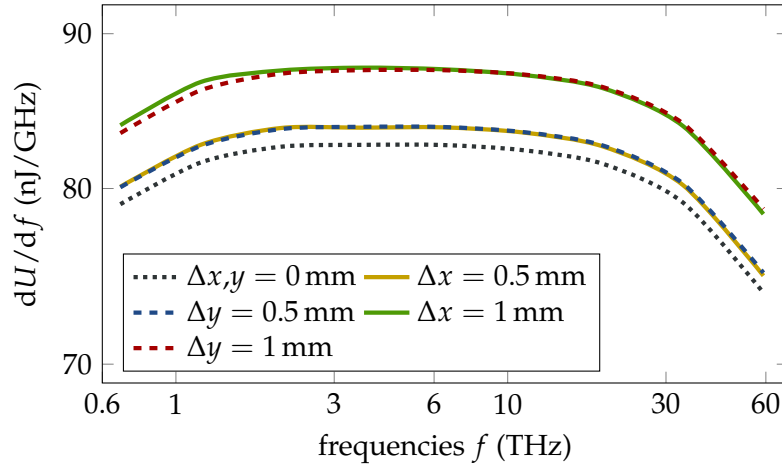


FIGURE 5.16: Simulated spectral energy density on the diamond window of vertically polarized DR for different electron beam displacements with respect to the aperture center. A beam energy of 15 GeV was considered.

The beam offsets in Fig. 5.16 are considered for illustration purposes only, because at the DR screen of European XFEL they are expected to be significantly smaller. The long-term orbit variations due to empiric accelerator optimization are usually limited to few 100  $\mu\text{m}$ . In order to give an upper limit on the influence of the spectrometer sensitivity, an offset of 0.5 mm is assumed in the following. The spectrometer sensitivities have been modeled for vertical and horizontal beam displacement. The ratios of the sensitivities  $R_{m,\text{off}}$  to the modeled sensitivity without offset  $R_{m,\text{mod}}$  are presented in Fig. 5.17. Overall the spectrometer sensitivity increases only by little more than 1 %, which is expected from the spectral energy density on the diamond window (see Fig. 5.16). However, at the edge channels of the individual grating sets the sensitivities deviate by up to 20 % or more. Here, not only the intensity but also modifications of the transverse radiation profile have a strong influence, because the radiation is partly cut by the focusing ring mirrors. The transverse radiation profile is also the reason for a slightly decreased sensitivity at low frequencies with vertical offset. The asymmetry intensifies the radiation loss at vertically limiting apertures. At these frequencies, the beam profiles are comparatively large (see Fig. 4.7).

Variations of angle between electron beam and DR screen do not lead to an increase of intensity. Instead, they only change the path of the radiation inside THz beamline and CRISP spectrometer. However, for reasonable long term variations ( $\Delta x', \Delta y' < 0.1 \text{ mrad}$ ) this has – except from some edge channels at high frequencies – no influence on the spectrometer sensitivity as shown in Fig. 5.17. The inclination factor (see Sec. 3.4) varies so little that there are no effects on the transverse radiation properties. The slightly different path of the radiation does not lead to considerable differences in frequency-channel assignment.

If the measurement of the form factor  $|F_L(f_m)|$  does not account for the spectrometer sensitivity change by orbit offsets the error is given by error propagation of Eq. (5.2) as

$$\Delta |F_L(f_m)| = \frac{1}{2Q} \sqrt{\frac{v_m}{R_m^3}} \Delta R_m, \quad (5.10)$$

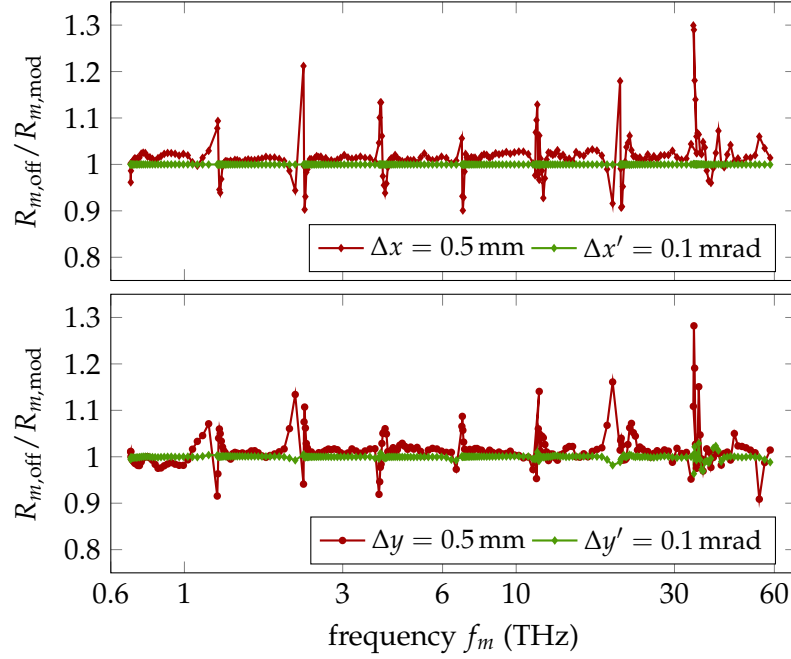


FIGURE 5.17: Ratios of the modeled spectrometer sensitivities  $R_{m,off}$  for different electron beam orbits to the on-axis case  $R_{m,mod}$ . A position offset leads to a slightly increased emission of radiation and affects mainly edge channels due to a modified transverse radiation profile. Variations of the electron beam angle with respect to the DR screen have no considerable consequences.

where  $\Delta R_m$  marks the absolute difference of the actual to the on-axis spectrometer sensitivity  $R_m$ . The relative form factor error is thus

$$\frac{\Delta |F_L(f_m)|}{|F_L(f_m)|} = \frac{1}{2} \frac{\Delta R_m}{R_m}. \quad (5.11)$$

This result demonstrates that there is no need to adjust the spectrometer sensitivity for usual electron beam orbit variations. The errors of the spectrometer sensitivity are further reduced such that the overall form factor error is smaller than 1 %, which is below the shot-to-shot fluctuations caused by electron bunch and detector electronics. At edge channels, where the differences of the spectrometer sensitivities are larger, the uncertainties are in general also larger because of low signal-to-noise ratio. Additionally, form factor variations at edge channels are filtered by data processing (see Sec. 6.1.1). The presented comparison with TDS measurements in Chaps. 6, 7 have been carried out on different dates and are subject to the usual variations of the electron beam orbit. The results confirm that an adjustment of the spectrometer sensitivity due to electron beam orbit variations is not necessary. The orbit variations explain however the small and occasional deviations of the measured form factor  $|F_L(f_m)|$  at spectrometer edge channels.

## Chapter 6

# Benchmarking Based on Complementary Diagnostics

This chapter presents comparative measurements of the CRISP spectrometer and complementary diagnostics at European XFEL. The transverse deflecting structure (TDS) and bunch compression monitor (BCM) downstream of the last bunch compressor (see Sec. 2.3) are used to characterize the current profile at final compression of the electron bunch. The TDS enables a direct comparison of current profiles, while the BCM, which is operated with diffraction radiation, allows comparison of coherent radiation. The measurements have been carried out during beam time dedicated to this thesis. The accelerator has been operated in single bunch mode. Instead of a bunch train filled with MHz repetition rates, only one bunch per rf pulse at 10 Hz repetition rate is generated and accelerated. In this mode, the temporal resolution of the TDS is optimized by special magnetic beam optics inside the diagnostics dump (see Sec. 2.4). If not stated otherwise, all data in the following chapters are obtained using diffraction radiation at the 5 mm aperture.

First, the processing of the spectrometer data is described and the current profile reconstruction is illustrated for a measured data set. A variety of distinct current profiles and the influence of systematic changes of the bunch compression on the current profile properties are characterized with CRISP spectrometer and TDS. Finally, a comparison with the BCM is carried out. Not only is the measured coherent radiation spectrum compared to BCM signals, but one BCM detector is calibrated to yield rms bunch durations.

### 6.1 Data Processing

As detailed in Sec. 3.2, measurements of the coherent radiation spectrum only yield a direct measurement of the form factor modulus. The phase of the complex form factor, which is mandatory for the calculation of the current profile, remains unidentified and must be retrieved by a current profile reconstruction algorithm. The used current profile reconstruction is a further development of the algorithm, that has been applied to CRISP spectrometer data based on transition radiation at FLASH in [Sch+20]. This method combines analytical and iterative phase retrieval. Its principle and some developments carried out within the scope of this work have been described in Sec. 3.3. On the one hand, artifacts with negative currents, that result from minor misconduct in analytical phase retrieval, are removed. On the other hand, ambiguities resulting from arbitrary start phases of the iterative algorithm are avoided. Before the measured spectrometer data can be used for current profile reconstructions however, the data must be processed with respect to the form factor.

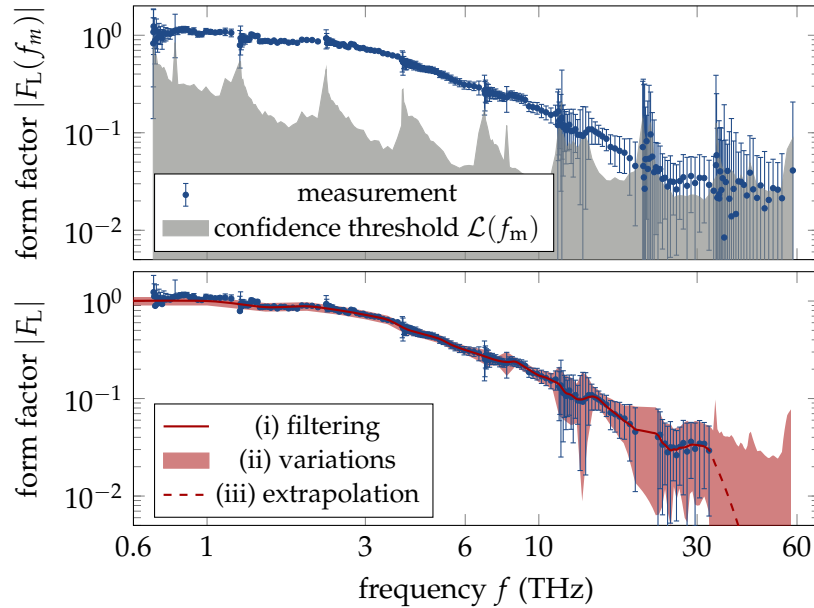


FIGURE 6.1: Measured form factor data of the CRISP spectrometer (top) and the tasks of the data processing (bottom). By filtering (i) the form factor becomes robust against the influence of detector noise. The Gaussian extrapolation (iii) assures proper sampling of the reconstructed current profile. The rms shot-to-shot fluctuations (error bars) and confidence threshold are basis for allowed form factor variations (ii) during the iterative algorithm.

### 6.1.1 Form factor

An example of measured spectrometer data is shown in the top part of Fig. 6.1. The spectrometer signals  $v_m$  are an average of several rf pulses (here  $N = 20$ ) and converted based on Eq. (5.2) as well as charge measurements of a nearby toroid to the form factor modulus  $|F_L(f_m)|$ . The error bars show the corresponding rms shot-to-shot fluctuations. Over a wide frequency range, the form factor data exhibit neither large shot-to-shot nor channel-to-channel fluctuations except from edge channels. But as the form factor modulus decreases, the data points approach the confidence threshold  $\mathcal{L}(f_m)$ , which is given by  $2\sigma$  of the detector noise as defined in Eq. (5.6). Here, the relative shot-to-shot fluctuations increase. If the form factor is below the confidence threshold, the signal is dominated by detector noise. In that case, not only the shot-to-shot fluctuations grow, but the channel-to-channel variations increase as well. These measurement points with large uncertainties require an adequate filtering of the spectrometer data. It is carried out as the first of three tasks of the data processing: (i) filtering, (ii) variations and (iii) extrapolation.

(i) Data points, that do not fulfill the confidence criterion and are below the gray area of  $\mathcal{L}(f_m)$ , are discarded. Additionally, the frequency range is restricted towards high frequencies by the first occurrence of 15 consecutive channels below the confidence threshold. Otherwise, the required interpolation (see (iii)) leads to a considerable bias of the reconstructed current profile depending on the form of interpolation. An example for remaining measurement points is presented by the blue dots in the bottom part of Fig. 6.1. The confidence threshold limits in this case the frequency range of the form factor measurement to  $f_m < 33$  THz. Finally, the data points are linearly interpolated (see (iii)) and smoothed using a Savitzky-Golay filter. The result is shown in the bottom part of Fig. 6.1. The confidence threshold ensures that form

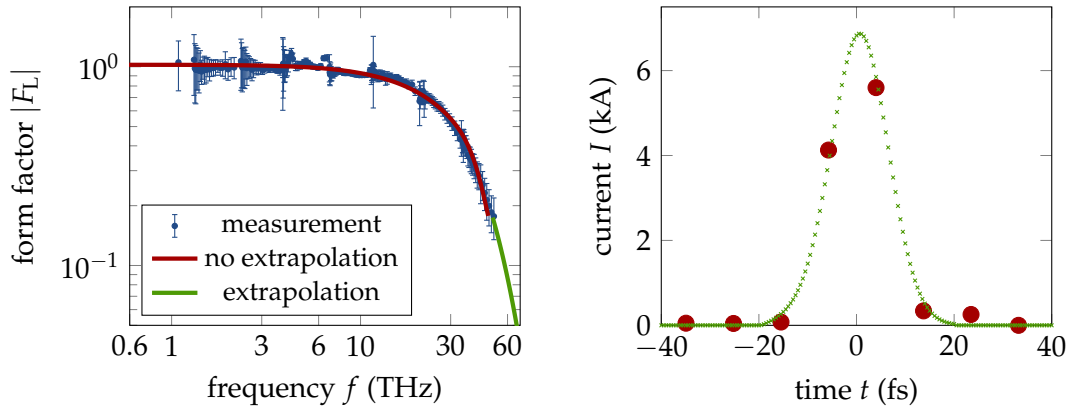


FIGURE 6.2: Visualization of the need for form factor extrapolation to high frequencies. The form factor (left) without extrapolation exhibits only few points along the reconstructed (see Sec. 6.1.2) current profile (right). An extrapolation using a Gaussian function increases the number of points in the time domain without generating additional structure and key parameters (e.g. peak current) can be specified.

factor measurement and current profile reconstruction are not artificially altered by detector noise.

(ii) To ensure a convergence of the iterative Gerchberg-Saxton algorithm towards a physical solution of the current profile, measurement uncertainties have to be considered. This is done by defining a region  $\Delta |F_L(f)|$  in which variations of the form factor are allowed. An example is shown by the red area in Fig. 6.1. If the form factor of the previous iteration lies outside this region, it is replaced by the measured form factor (see Fig. 3.8). Within the scope of this thesis, the performance of the iterative algorithm has been significantly improved by optimizing the allowed variations of the form factor modulus. The filtered form factor data as an average of several rf pulses may not represent the physical properties of one individual current profile due to fluctuations in bunch compression. Therefore, the rms shot-to-shot fluctuations are the basis for allowed form factor variations of the filtered measurement. In regions, where measured data points are below the confidence threshold, all variations of the form factor modulus below the confidence threshold  $\mathcal{L}(f_m)$  are allowed. Uncertainties of the spectrometer sensitivity (e.g. electron beam orbit, beam energy) are considered by granting relative deviations of the form factor by at least 10% even if the shot-to-shot fluctuations are smaller.

(iii) The numerical Fourier transform (FFT) requires a linear grid in frequency domain. The highest frequency of the grid defines the spacing in time domain (see Sec. 3.2). An illustration of the consequences for current profile reconstruction on form factor measurements is given in Fig. 6.2. In this case, the frequency range of the filtered measurement is limited to form factor values above  $|F_L| > 0.1$ . Consequently, the reconstructed current profile (see Sec. 6.1.2) is sampled by only two points with considerable current. Key parameters of the current profile – e.g. peak current – cannot be specified. It is thus mandatory to extrapolate the form factor data to higher frequencies (smaller form factors) in order to properly sample the current profile as shown in Fig. 6.2. A Gaussian extrapolation resembles a limited temporal resolution and minimizes the additionally generated structure on the current profile [Sch+20]. In Fig. 6.2, a Gaussian fit to the few samples of the current profile yields a similar result than the Gaussian extrapolation.

The form factor processing automatically detects the required frequency grid. The grid points  $f_k = kf_g/5$  are generated for  $k = 0, \dots, 1023$  and the spacing  $\Delta f_k = f_g/5$  is determined by the channel at which the filtered form factor (i) has decreased for the first time to  $|F_L(f_g)| < 0.7$ . For typical bunch durations during FEL operation, this results in a corresponding time window of 1 ps with 1 fs spacing. The Gaussian extrapolation above the highest frequency  $f_e$  of the filtered data is carried out by

$$|F_L(f_k > f_e)| = \exp\left(-\frac{f_k^2}{2\sigma_e^2}\right) \text{ with } \sigma_e = \sqrt{-\frac{f_e^2}{2 \ln |F_L(f_e)|}}. \quad (6.1)$$

The transition from measured form factor data to extrapolated region is smooth (see Figs. 6.1, 6.2). The extension of the frequency range is also considered for the form factor variations of task (ii): In the extended frequency range which is in principle still covered by the spectrometer (0.7 THz –58 THz), all variations of the form factor below the confidence threshold are allowed during the current profile iteration. Outside of the spectrometer range, no restrictions on the form factor modulus are applied.

The linear frequency grid may also require an extrapolation to frequencies below the spectrometer range. At European XFEL, this is generally uncritical during FEL user operation as the form factors have reached their asymptotic limit of  $|F_L| \mapsto 1$ . However, to extend the dynamic range of current profile reconstructions, an extrapolation is carried out by a Gaussian curve through  $|F_L(0)| = 1$  and the form factor at the lowest frequencies of the filtered data.

### 6.1.2 Current profile

The form factor modulus  $|F_L(f_k)|$  after the form factor processing (Fig. 6.1 (i) and (iii)), is used to calculate the Kramers-Kronig phase  $\phi_{\text{KK}}$  on the frequency grid according to Eq. (3.17) as

$$\phi_{\text{KK}}(f_k) = \frac{2f_k}{\pi} \sum_{k' \neq k} \frac{\ln |F_L(f_{k'})| - |F_L(f_k)|}{f_k^2 - f_{k'}^2} \Delta f_k. \quad (6.2)$$

The corresponding current profile for the form factor measurement is shown in Fig. 6.3. Its complex form factor  $|F_L(f_k)| \exp(i\phi_{\text{KK}})$  is the input for the Gerchberg-Saxton algorithm together with the allowed form factor variations  $\Delta |F_L(f_k)|$  (Fig. 6.1 (ii)). The negative currents of the Kramers-Kronig profile vanish within the first iterations  $n$  as depicted in Fig. 6.3. The algorithm terminates if the form factor of the adapted current profile is within the allowed variations. Usually, this occurs within the first 1–2 iterations and latest within less than 100 iterations.

In this thesis, the form factor of the reconstructed current profile is always compared to the filtered data of the measurement as done on the right hand side of Fig. 6.3. The comparison demonstrates that with the allowed form factor variations during the reconstruction a solution of the current profile in accordance to the form factor measurement itself is found. The overall computation time including data processing amounts to around 20 ms on an usual office computer and has been significantly improved compared to previous implementations of the Gerchberg-Saxton algorithm for CRISP spectrometer data.

The processing of the form factor measurement leads to a reconstructed current profile, which is robust against spectrometer detector noise. In addition, it ensures

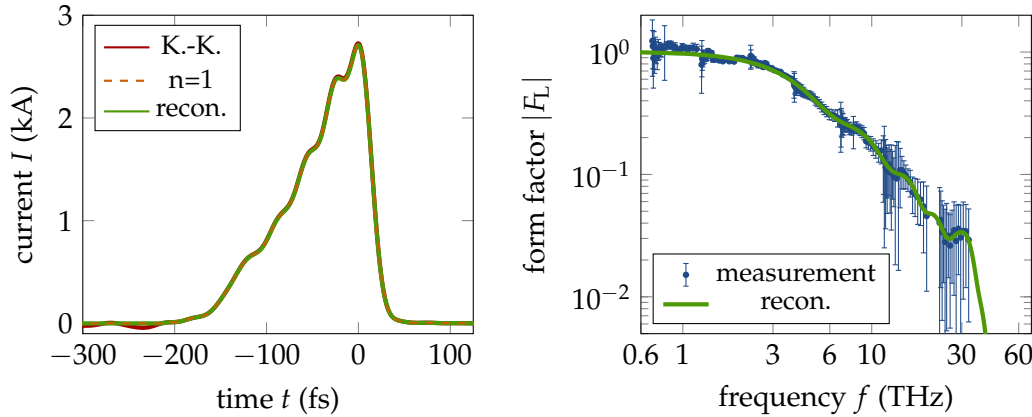


FIGURE 6.3: Results of the Gerchberg-Saxton algorithm. The misconducts on the processed form factor measurements are small such that the current profile (left) of the Kramers-Kronig phase exhibits only small negative current undershoots. They are quickly removed by the iterative algorithm. In this case, the first iteration ( $n = 1$ ) already yields the reconstructed current profile whose form factor modulus agrees with the measurement (right).

the specification of characteristic parameters like e.g. peak current. The current profile of the Kramers-Kronig phase exhibits only small negative current undershoots, which demonstrates the good characterization of the form factor thanks to the identified in-situ sensitivity and data processing. Negative currents are quickly removed by the iterative algorithm under consideration of reasonable measurement uncertainties. The temporal resolution of the combination of CRISP spectrometer and data processing is studied in App. B using simulated form factor measurements of analytical profiles.

## 6.2 Comparative Measurements with TDS

The CRISP spectrometer is operated for the first time with noninvasive diffraction radiation and the implementation of data processing and current profile reconstruction described in Sec. 6.1. In order to benchmark the reconstructed current profiles, comparative measurements with the TDS after the last bunch compressor BC<sub>3</sub> (see Fig. 2.5) in high resolution mode, and thus single bunch operation, have been carried out. First, electron bunches with different current profiles but similar bunch durations are studied. These profiles have been generated using the most common bunch charge (250 pC) during FEL operation and corresponding bunch durations. Bunch duration and charge have also been modified to explore the dynamic range of the CRISP spectrometer afterwards. Finally, both diagnostics are used to characterize the influence of chirp scans in the L<sub>2</sub> and L<sub>3</sub> sections on the electron current profile.

### 6.2.1 Current profiles

A selection of measured form factors from bunches with various compression settings are presented in Fig. 6.4. Only the data points after the filtering (see Sec. 6.1.1), which are used for the current profile reconstruction, are shown. The form factor measurements are an average of 20–50 rf pulses at both grating sets. The charge amounts to 250 pC and the beam energy to 14 GeV. Towards low frequencies, the form factors of all settings asymptotically approach 1. Apart from this, they exhibit

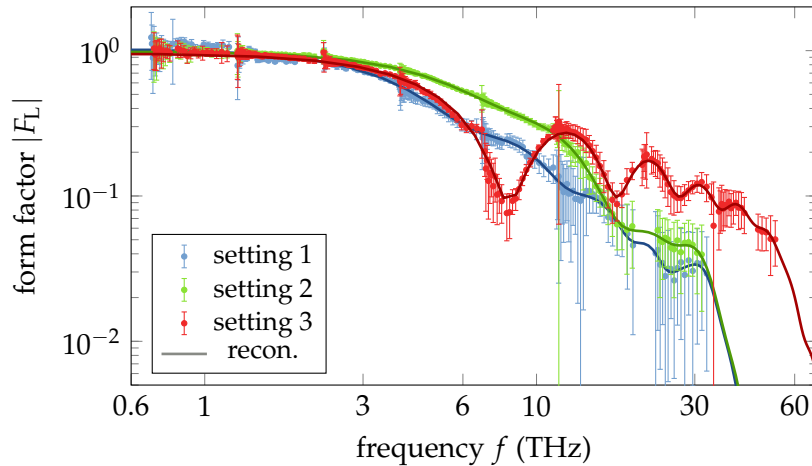


FIGURE 6.4: Form factors measured with the CRISP spectrometer for various settings of bunch compression. The error bars mark the rms shot-to-shot fluctuations and the solid lines the form factor of the reconstructed current profiles.

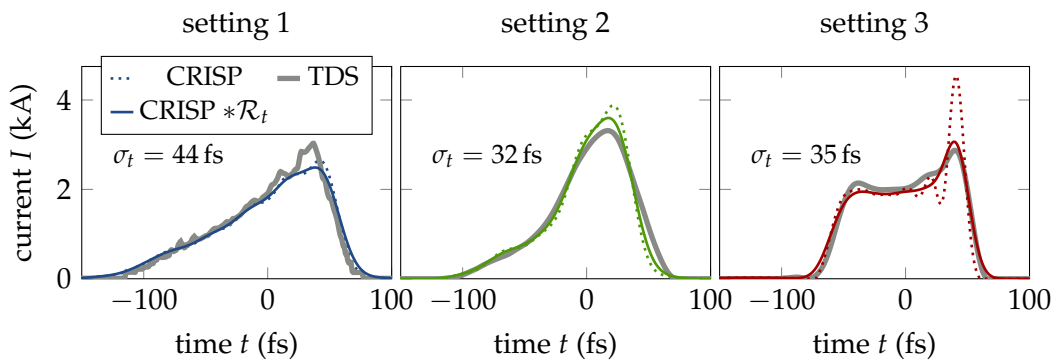


FIGURE 6.5: Comparison of the current profiles reconstructed from form factor measurements (dotted blue, green, red) shown in Fig. 6.4 with current profiles obtained by the TDS (thick gray). For better comparison, the reconstructed current profiles have been convoluted with the TDS resolution of 8 fs (solid lines). Both devices yield conclusive results with striking resemblance. Times with  $t > 0$  mark the head and times with  $t < 0$  the tail of the bunch. The rms bunch durations of the CRISP profiles are stated.

distinct behaviour. While setting 1 is continuously decreasing, the form factor of setting 2 bends towards a steeper slope around 10 THz. The form factor of setting 3 is characterized by an oscillating behaviour. The solid lines show the form factor modulus of the reconstructed current profiles, which are presented in Fig. 6.5.

The different behaviour of the form factors resembles differences in the current profiles. Even though the reconstructed rms bunch durations  $\sigma_t$  – obtained with Eq. (5.8) – are comparable and vary only from 32 fs to 44 fs, the profiles (dotted) exhibit distinct differences in shape: Setting 1 resembles an asymmetric triangular profile, setting 2 has a Gaussian like shape with a slowly decreasing current towards the tail. As expected from the oscillating form factor, the reconstructed current profile of setting 3 offers a rectangular shape with a pronounced leading spike.

The current profiles obtained from TDS measurements are depicted for comparison in Fig. 6.5 as well. Again (see Sec. 5.2.1), the average profile of 5 bunches at each zero-crossing is taken, which allows to correct for transverse-longitudinal correlations by a reconstruction technique [Sch+20]. The special TDS beam optic in the

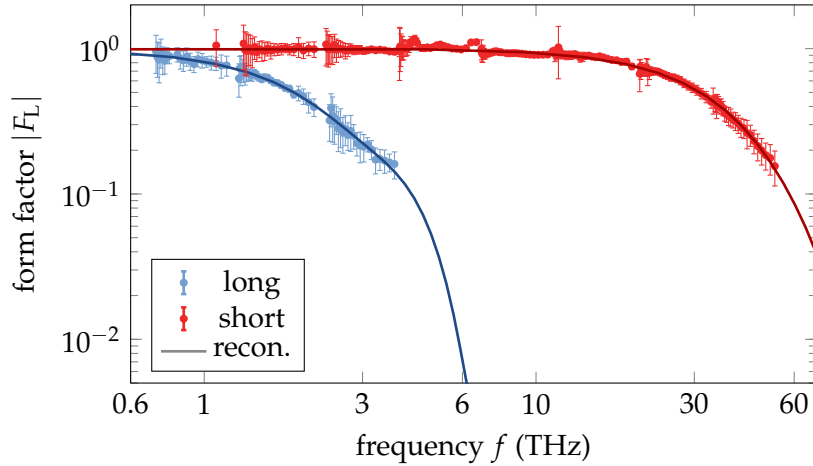


FIGURE 6.6: Measured form factor of a short and long bunch with rms shot-to-shot fluctuations as error bars to demonstrate the dynamic range of current profile reconstruction with the CRISP spectrometer. The solid lines correspond to the form factors of the reconstructed current profiles shown in Fig. 6.7.

local dump section of BC<sub>3</sub> (see Fig. 2.5) enabled TDS resolutions of  $\mathcal{R}_t = 8$  fs during these measurements. The overall shapes and durations of the TDS and CRISP current profiles agree. However, at setting 3, the CRISP profile exhibits more substructure and thereby a higher peak current. These structures cannot be resolved with the TDS resolution. For better comparison, the reconstructed current profiles are convoluted with a Gaussian function representing the TDS time resolution  $\mathcal{R}_t$ . Now (solid lines), the substructures are not resolved, which is in accordance to the TDS measurement. The shot-to-shot fluctuations on the TDS current profile are small (see e.g. Fig. 6.9), and as also the uncertainty of the streak parameter is small (<5%), they are not further considered here.

In order to demonstrate the large dynamic range of the reconstructed current profiles, the measured form factors of a comparably long and short bunch are presented in Fig. 6.6. The measurement of the long bunch with 250 pC charge only yields data points at the low frequency grating set (< 0.6 THz) due to decreased signal-to-noise ratio at high frequencies. For the short bunch with 50 pC, the situation is reversed. The coherent emission at high frequencies yields sufficient signal, but at the lowest frequency grating set the charge generates not enough radiation intensity even for entirely coherent emission. Nevertheless, for both bunches the form factor modulus can be measured down to  $|F_L(f_m)| < 0.2$  and the asymptotic approach towards  $|F_L(0)| = 1$  is well described.

The form factors of the reconstructed current profiles reproduce the measurement points. The corresponding current profile of the long bunch on the left of Fig. 6.7 agrees in overall shape and peak current with the TDS measurement. Due to the reconstructed rms bunch duration of 100 fs, the TDS resolution of 9 fs is negligible for the comparison. The reconstructed current profile of the short bunch is shown on the right. The rms bunch duration results in 6 fs and the peak current exceeds 6 kA. The TDS resolution of this setting is  $\mathcal{R}_t = 12$  fs and dominates the measured current profile of the TDS. Consequently, the CRISP current profile cannot be confirmed. Nevertheless, if the CRISP profile is convoluted with TDS resolution,

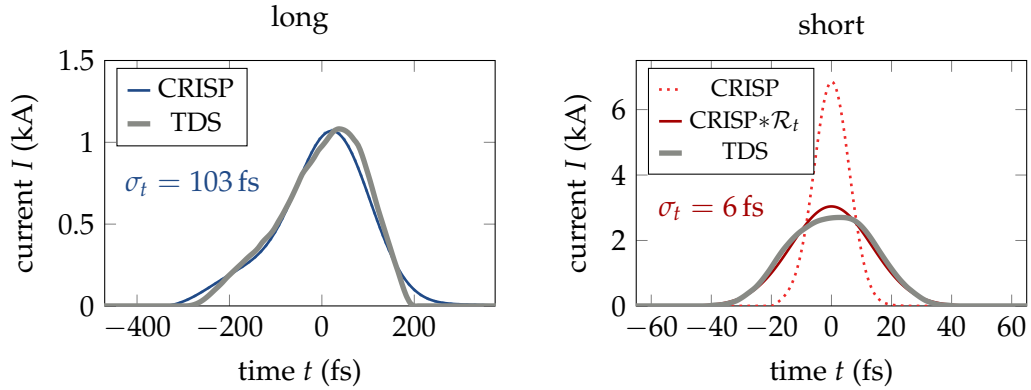


FIGURE 6.7: Comparison of measured current profiles of a long and short bunch by TDS and CRISP spectrometer. The corresponding form factors are shown in Fig. 6.6. Stated are the rms bunch durations of the CRISP spectrometer.

TABLE 6.1: Parameters of the current profiles compared in Figs. 6.5, 6.7. Even though these parameters are very sensitivity to substructure and/or tails with low current, they agree overall within  $\simeq 10\%$  if the TDS resolution  $\mathcal{R}_t$  is considered.

	$\sigma_t$ (fs)		$I_p$ (kA)			$\Delta t_{\text{fwhm}}$ (fs)		
	CRISP	$\sqrt{\text{TDS}^2 - \mathcal{R}_t^2}$	CRISP	TDS	CRISP $\ast \mathcal{R}_t$	CRISP	TDS	CRISP $\ast \mathcal{R}_t$
set. 1	44	43	2.7	3.0	2.5	83	73	89
set. 2	32	32	3.9	3.3	3.6	55	69	59
set. 3	35	33	4.5	2.9	3.1	30	104	105
short	6.0	6.1	6.8	2.7	3.0	14.0	36	31.6
long	103	93	1.07	1.07	1.05	204	216	204

both profiles agree. The CRISP spectrometer is able to characterize the current profile down to shorter bunch durations and more detail than the TDS, even though it is operated with special magnetic beam optics.

Characteristic properties of the current profiles compared in this section are listed in Tab. 6.1. Besides the rms bunch duration  $\sigma_t$ , also peak current  $I_p$  and fwhm bunch duration  $\Delta t_{\text{fwhm}}$  are given. Common practice is to consider the TDS resolution  $\mathcal{R}_t$  on the rms bunch duration by quadratic subtraction as in Sec. 5.2.1. For peak current and fwhm bunch duration, the TDS resolution is taken into account by the convolution of the CRISP profile with the time resolution (CRISP  $\ast \mathcal{R}_t$ ) before the parameters are directly identified from the resulting profile. Without consideration of the TDS resolution, there are partially large ( $> 30\%$ ) deviations of peak current and fwhm duration, which demonstrates the restrictions due to the TDS resolution compared to the CRISP spectrometer. Even though the parameters are very sensitive to substructure and/or low current regions extending at tail or head of the bunch, the parameters agree overall by 10% after considering TDS resolution. Some parameters may deviate stronger even though the profiles itself agree as shown in Figs. 6.5, 6.7.

## 6.2.2 Compression scans

For the results in this section, the bunch compression has been systematically changed by performing chirp scans in the accelerating sections  $L_2$  and  $L_3$  (see Fig. 2.5). The energy dependent path lengths inside the magnetic bunch compressors result in different electron bunch durations (Sec. 2.1), which are detected by TDS and CRISP spectrometer. Each scan has been performed three times. Once the beam has been

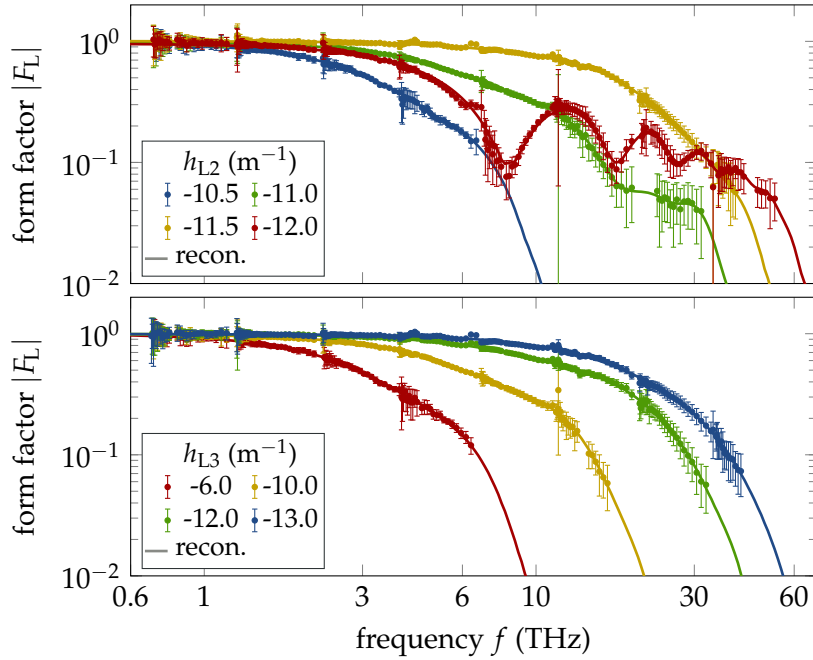


FIGURE 6.8: Selected form factors of the chirp scans in the L<sub>2</sub> (top) and L<sub>3</sub> section (bottom) measured with the CRISP spectrometer.

terminated in the diagnostics dump to apply the special magnetic beam optics for the TDS. The other two scans have been performed individually for FIR and THz grating set of the spectrometer while the beam has been terminated just upstream of the SASE undulators. The form factor at each step is obtained from the average signal of 20 rf pulses. The beam energy amounts to 14 GeV.

A selection of form factors of both compression scans is presented in Fig. 6.8. The top part shows the results of the L<sub>2</sub> and the bottom part of the L<sub>3</sub> scan. A larger negative chirp results in stronger compression and the coherent radiation spectrum extends to higher frequencies. The increased signal also extends the detectable frequency region of the form factor. The L<sub>3</sub> scan covers a larger chirp region while its form factor cut-off shifts by the same frequency interval. The chirp of the L<sub>2</sub> section affects the bunch compression in BC<sub>2</sub> and BC<sub>3</sub>, whereas the chirp of the L<sub>3</sub> section only influences the compression in BC<sub>3</sub>. Starting from moderate compression at  $h_{L2} = -10.5 \text{ m}^{-1}$  and  $h_{L3} = -6.0 \text{ m}^{-1}$ , the form factor begins to extend towards higher frequencies. At  $h_{L2} = -11.5 \text{ m}^{-1}$  and  $h_{L3} = -13.0 \text{ m}^{-1}$ , the form factor extends to highest frequencies and thereby indicates strongest compression. For the L<sub>2</sub> chirp scan, the measurement of an even stronger chirp ( $h_{L2} = -12.0 \text{ m}^{-1}$ ) results in over-compression and a strong oscillatory behaviour of the form factor. In over-compression, the energy dependent path lengths inside the magnetic bunch compressor reverse the direction of the chirp as the electron bunch passes the delicate point of full compression. The resulting current profile is very sensitive to higher orders of the accelerating rf slope (see Sec. 2.1) and is strongly affected by collective effects. Current profile and accordingly form factor are drastically modulated. Even though each form factor measurement is the result of two individual scans for FIR and THz grating set, no transitions between the two grating sets are visible. This demonstrates the stability and reproducibility of bunch compression settings at European XFEL on medium time scales (<days).

As reconstructed current profiles of the CRISP spectrometer have already been compared to TDS results for a large variety of current profile properties in Sec. 6.2.1, these chirp scans are used to study only the characteristic properties of the current profiles continuously over a large range. Rms  $\sigma_t$  and fwhm  $\Delta t_{\text{fwhm}}$  bunch duration as well as peak current  $I_p$  obtained with the TDS and from the reconstructed current profiles of the CRISP spectrometer are compared for both chirp scans in Fig. 6.9. The error bars of the TDS measurements indicate the rms fluctuations of single-shot profiles. As in Tab. 6.1, the TDS resolution  $\mathcal{R}_t = 9$  fs is considered for the rms bunch duration by quadratical subtraction. For the other properties, the TDS resolution is considered by convolution with a Gaussian profile of respective duration.

The rms bunch duration increases from 14 fs at  $h_{L,2} = -11.5 \text{ m}^{-1}$ , and 11 fs at  $h_{L,3} = -13.0 \text{ m}^{-1}$ , to 92 fs, and respectively 103 fs, at the end of the chirp scans. Over-compression leads to an increasing bunch duration at  $h_{L,2} = -12 \text{ m}^{-1}$ , which is not reached in the  $L_3$  scan. Except for the over-compressed region, the rms bunch duration evolves in both cases linearly with imprinted chirp as expected from the analytical treatment in Sec. 2.1. The increasing deviations of the rms bunch duration towards longer bunches are caused by differences in the low current regions at head and tail of the bunch. An example for this behaviour is the long bunch in Fig. 6.7 and the resulting deviations to the CRISP measurement in Tab. 6.1. The low current regions have considerable influence on the rms bunch duration even though the profiles agree overall as indicated by peak current and fwhm bunch duration.

The peak current evolves inversely to the rms bunch duration along both chirp scans. Close to full compression there are large deviations ( $\simeq 30\%$ ) between the peak current detected by TDS and CRISP. They are caused by TDS resolution and agree under the consideration thereof, which denies a detection and thus confirmation of the reconstructed peak currents. The bunch duration  $\Delta t_{\text{fwhm}}$  of the CRISP current profile expressed as fwhm shows partially significant differences to the rms bunch duration. For both scans, the fwhm bunch duration is not decreasing linearly towards full compression. While the rms bunch duration at over-compression of  $L_2$  increases strongly, the effect on the fwhm bunch duration is comparably small. This is caused by a change of the current profile shape, which can be observed at setting 2 and setting 3 of Fig. 6.5. These settings correspond to the measurements at  $h_{L,2} = -11.0 \text{ m}^{-1}$  and  $h_{L,2} = -12.0 \text{ m}^{-1}$  of the presented compression scan. The TDS is unable to resolve such contrasts between rms and fwhm bunch duration close to full compression, because substructures of the current profile are not resolved. To confirm the reliability of the current profile reconstruction, the relative deviations of the characteristic properties to the TDS profiles are given under consideration of the TDS resolution in Fig. 6.15 (see Sec. 6.4).

### 6.3 Comparative Measurements with BCM

The compression scan in Sec. 6.2 is also used for comparative measurements in the frequency domain. The BCM downstream of the last bunch compressor  $BC_3$  detects the coherent diffraction radiation intensity emitted at a 7 mm aperture (see Sec. 2.4.2). The same arguments as for the TDS comparison hold: The collimator of European XFEL is designed to be achromatic and isochronous such that the electron beam optics do not alter the current profile from BCM station to CRISP spectrometer. The BCM hosts two pyroelectric detectors and one of them is operated with a 6 THz

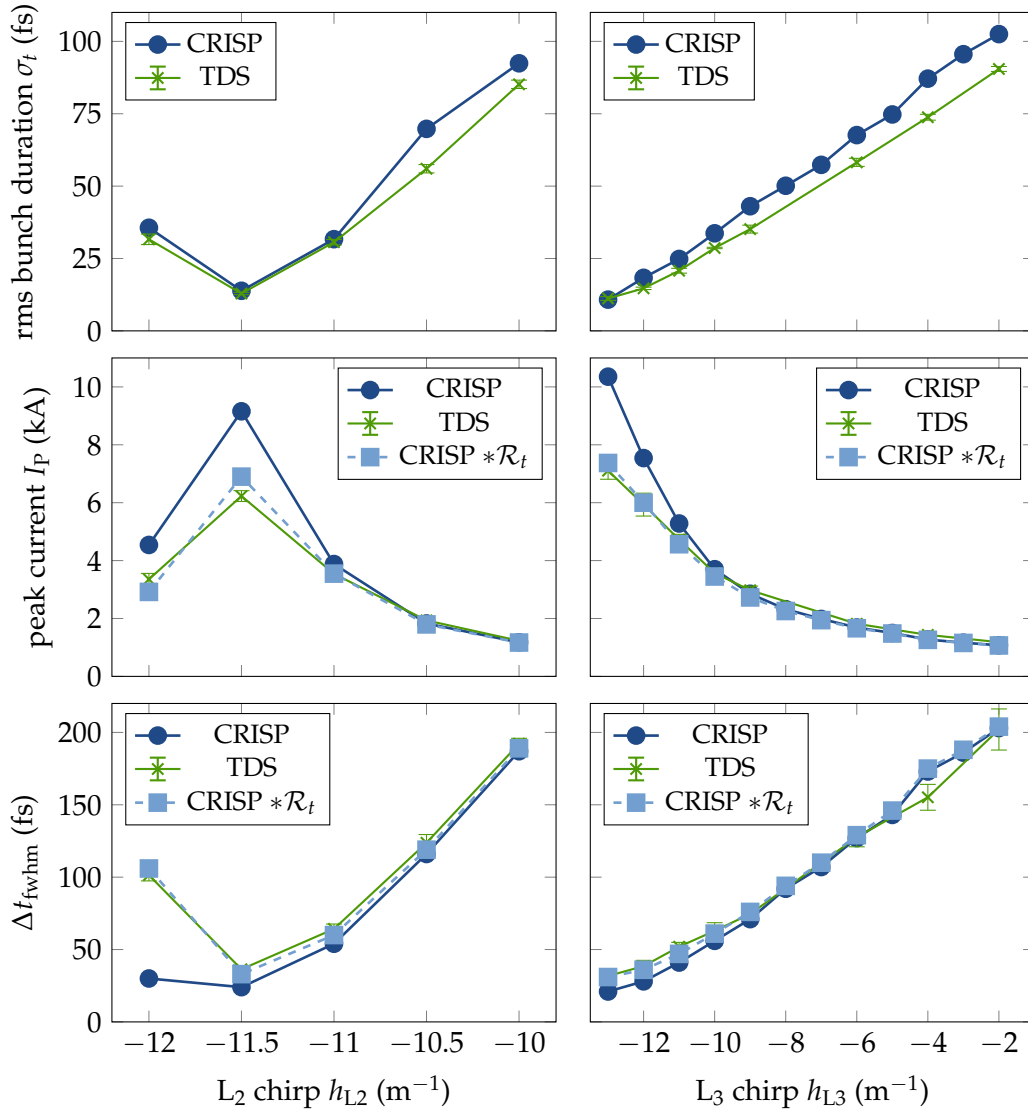


FIGURE 6.9: Behaviour of rms bunch duration, peak current and fwhm bunch duration along the chirp scans in the L<sub>2</sub> and L<sub>3</sub> section. For comparison, the TDS resolution  $\mathcal{R}_t$  has been considered for all parameters. The rms bunch duration of the TDS is obtained after a quadratic subtraction of the resolution, while for peak current and fwhm bunch duration the CRISP current profile is convoluted with the resolution.

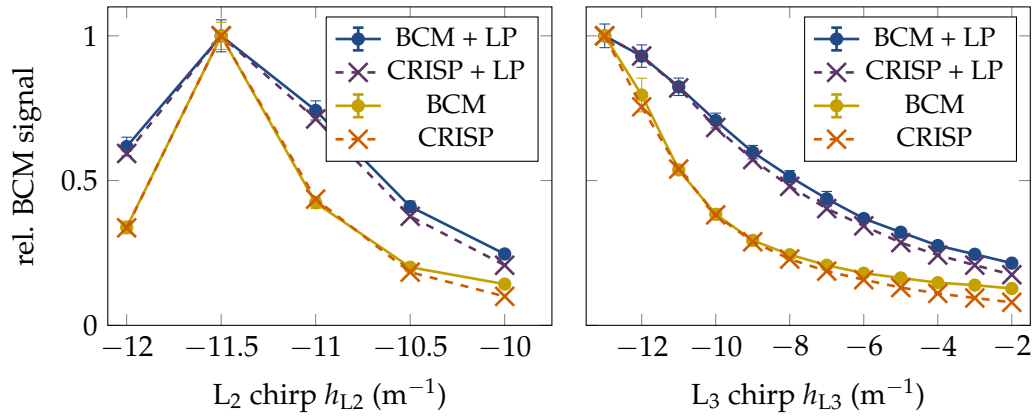


FIGURE 6.10: Comparison of the measured (dots) BCM signals without and with low-pass filter (LP) to simulated (crosses) BCM signals based on the CRISP form factor measurement for chirp scans in the  $L_2$  and  $L_3$  section. In measurement and simulation the low-pass filter leads to a less steep signal slope. The positions of maximum bunch compression are in agreement with the results shown in Fig. 6.9.

low-pass (LP) filter<sup>1</sup>. The purpose of the LP filter will become clear from the results shown in this section.

### 6.3.1 BCM signal

The BCM signals of both chirp scans are normalized to the respective maximum and illustrated in Fig. 6.10. Error bars mark the rms shot-to-shot fluctuations. In order to compare the BCM signal to the form factor measurement of the CRISP spectrometer, the form factors after filtering and extrapolation (see Sec. 6.1.1) are converted to a simulated BCM signal. This simulated – yet CRISP based – signal, which is illustrated by crosses with (LP) and without low-pass filter in Fig. 6.10, is obtained using a modeled BCM sensitivity. The entire BCM setup (screen, beamline, detector) is simulated in a similar way to the spectrometer sensitivity (see Sec. 5.1). The resulting sensitivity can be found in [Din18]. Without low-pass filter, the BCM is roughly sensitive in the frequency range 1 THz – 60 THz. The simulated BCM signal is obtained by multiplication of the sensitivity with the square of the form factor modulus and an integration over the entire frequency range. This simulated signal based on CRISP measurements is illustrated in Fig. 6.10 and agrees in its overall evolution with the BCM measurements.

With and without low-pass filter, the maximum of the signal is located at chirps, which also indicated maximum compression in Fig. 6.9. The signal slopes of the detector operated with low-pass filter are significantly smaller than without low-pass filter. The integrated energy density of the coherent radiation varies strongly above 6 THz (see Fig. 6.8). Even though the form factor is smaller, the large frequency range from 6 THz – 60 THz leads to comparable variations of the area beneath the form factor – and thus total coherent radiation intensity – as for frequencies below 6 THz. Without low-pass filter, the deviations of simulated to measured signal increase with decreasing bunch compression. Caused by reduced signal-to-noise ratio at the CRISP spectrometer, the form factor can only be determined within a smaller frequency range (see Fig. 6.9). Towards higher frequencies, the form factor is extrapolated by a Gaussian function to avoid the generation of additional structure in

<sup>1</sup>multi-mesh filter by QMC Instruments

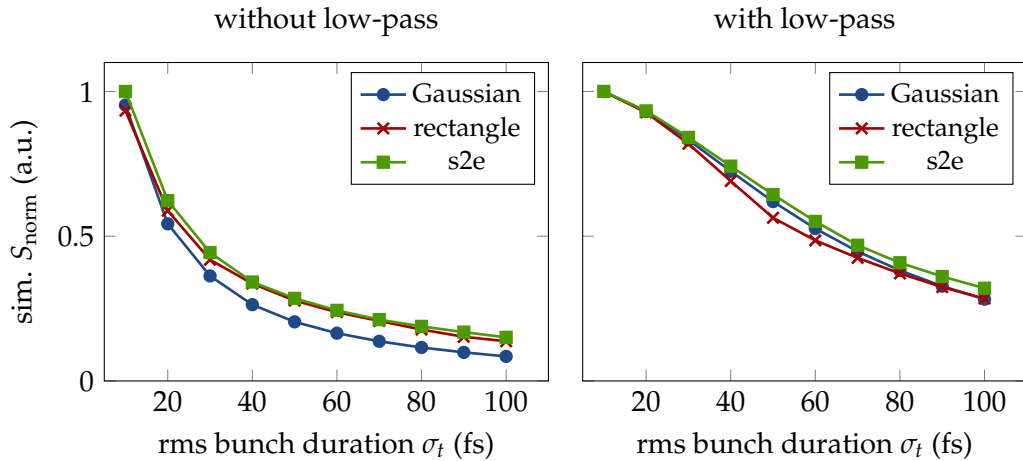


FIGURE 6.11: Simulated BCM signals  $S_{\text{norm}}$  with and without low-pass filter as function of rms bunch duration  $\sigma_t$  for three different current profiles. With low-pass filter the signal slope is smaller for short bunches, but the signals are less sensitive to the actual shape of the current profile.

time domain (see Sec. 6.1.1). However, the Gaussian function most likely decreases steeper than the actual form factor of the bunch. With low-pass filter, the deviations may be caused by the actual position of the detector within the focus of the coherent diffraction radiation. For low frequencies, the transverse beam size of the radiation is larger than the detector itself.

### 6.3.2 BCM bunch duration calibration

For the results shown in Fig. 6.10, the BCM signals are employed as a relative measure of bunch compression at constant bunch charge. In this subsection, it is investigated whether the BCM may also be applicable as an indicator of the absolute rms bunch duration. First, the emitted coherent radiation intensity and thereby the voltage signal  $S_{\text{BCM}}$  scales quadratically with the charge  $Q$  of the electron bunch (see Sec. 3.1). Consequently, comparisons of the emitted coherent radiation and thereby bunch compression at different bunch charges are only possible after normalization

$$S_{\text{norm}} = \frac{S_{\text{BCM}}}{Q^2}. \quad (6.3)$$

The applicability of the two pyroelectric detectors of the BCM as absolute measures of the rms bunch duration after charge normalization are studied in Fig. 6.11. The rms bunch durations  $\sigma_t$  of a Gaussian, rectangular and a current profile from start-to-end (s2e) simulations (see Fig. 3.4) are varied and the corresponding form factors calculated. The simulated BCM signal  $S_{\text{norm}}$  is evaluated in the same way as in Sec. 6.3.1 without (left) and with (right) low-pass filter. For illustration in Fig. 6.11, the signals are normalized to their respective maximum. The signal slope without low-pass filter is steeper for rms bunch durations below 40 fs. As a consequence, the variation of the simulated BCM signal over the same region of rms bunch duration from 10 fs – 100 fs is larger. However, without low-pass filter the relative signal difference of distinct shapes with same rms bunch duration is bigger. In combination with the steeper signal slope below 40 fs rms bunch duration, this leads to a larger range of possible rms bunch durations associated to the same BCM signal  $S_{\text{norm}}$  as

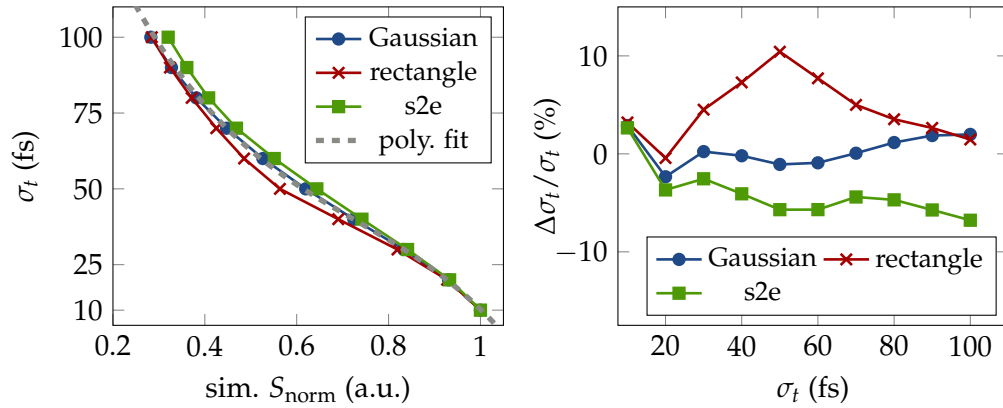


FIGURE 6.12: The rms bunch duration as function of the simulated BCM signal with low-pass filter (left) can be estimated by a third order polynomial in the range 10 fs–100 fs. A fit to the entire data yields deviations less than  $\approx 10\%$  (right).

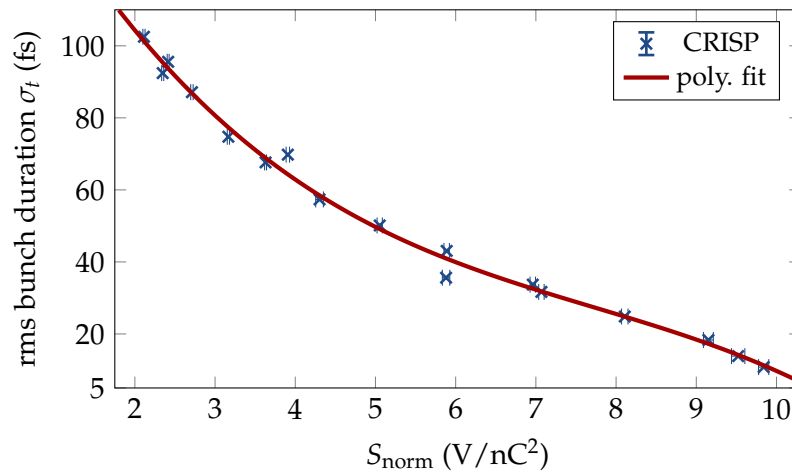


FIGURE 6.13: Rms bunch duration of the current profiles reconstructed from CRISP spectrometer measurements depicted as function of the charge normalized BCM signal  $S_{\text{norm}}$  with low-pass filter obtained during  $L_2$  and  $L_3$  chirp scans. The horizontal error bars mark the error of the mean BCM signal as an average of 20 rf pulses. As expected from simulations (Fig. 6.12), a third order polynomial approximates the data and represents the rms bunch duration calibration of the BCM detector.

compared to an operation with low-pass filter. Because at typical rms bunch durations of 250 pC FEL user operation the signal slope at the expected rms bunch durations 25 fs–35 fs is not drastically decreased, the pyroelectric detector with low-pass filter is better suited for an absolute characterization of the rms bunch duration.

The inverse functions yielding the rms bunch duration from the charge normalized BCM signal with low-pass filter are illustrated on the left of Fig. 6.12. The overall shape is comparable for all three current profiles and can be approximated by a third order polynomial in the range from 10 fs – 100 fs. A fit to the data of all current profiles is illustrated by the dashed curve. The resulting deviations of the rms bunch duration from the individual current profiles are shown on right of Fig. 6.12. The polynomial approximation does not deviate by more than  $\approx 10\%$  from the actual rms duration of the current profiles.

Experimental results from the  $L_2$  and  $L_3$  chirp scans are shown in Fig. 6.13. The rms bunch duration of the current profiles reconstructed from CRISP measurements are displayed against the charge normalized BCM signal  $S_{\text{norm}}$  at the same chirp

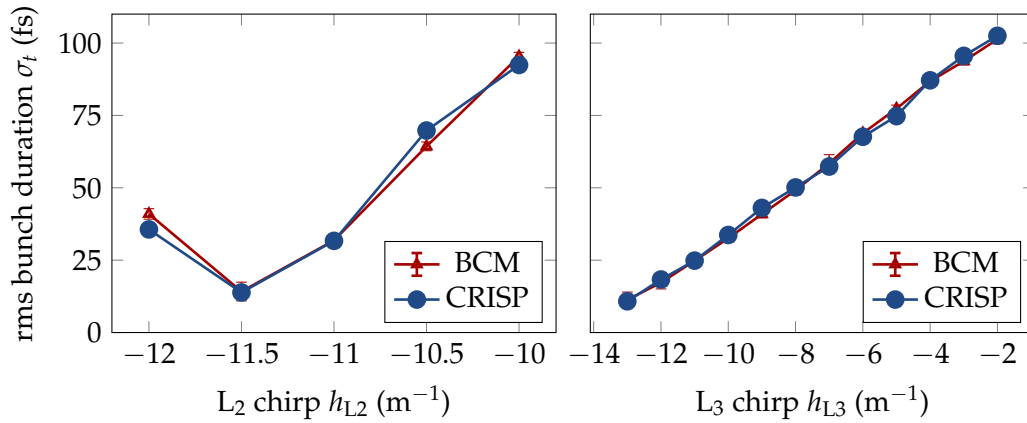


FIGURE 6.14: Bunch lengths during the L<sub>2</sub> and L<sub>3</sub> chirp scan obtained with the BCM calibration compared to the results of the CRISP spectrometer.

setting. The error bars on the horizontal axis mark the error on the mean BCM signal as an average of 20 rf pulses. The measured data points exhibit a similar behaviour as the simulations in Fig. 6.12 and are well approximated by a fit of a third order polynomial. This fit represents the calibration of the BCM with low-pass filter and is used to calculate the rms bunch duration from the charge normalized BCM signal.

Figure 6.14 presents the bunch durations obtained by the BCM calibration. They are compared to the reconstructed current profiles from the CRISP spectrometer for the L<sub>2</sub> and L<sub>3</sub> chirp scan. The behaviour and absolute values of the rms bunch durations agree. Only at over-compression of the L<sub>2</sub> chirp ( $h_{L2} = -12 m^{-1}$ ), there is a fair deviation between both obtained bunch durations. The over-compression leads to strong modulations of current profile and form factor (see Fig. 6.8). Over-compression is anyway not foreseen for FEL user operation.

## 6.4 Conclusion

The results of the CRISP spectrometer have been confirmed by two independent diagnostics in frequency and time domain for the range of bunch durations during FEL user operation. The change of BCM signals under systematic changes of bunch compression have been reproduced based on the measured form factor of the CRISP spectrometer. As the further developed current profile reconstruction from CRISP spectrometer data is robust and fast, it is ideally suited for online monitoring. The reconstructed current profiles have been confirmed by comparative TDS measurements within the expected range of rms bunch durations (6 fs – 100 fs) during FEL operation (see Tab. 2.2). The form factors have been recorded using the in-situ sensitivity identified in Chap. 5 and under influence of usual long term variations of electron beam orbit. Issues caused by the ambiguity of the Kramers-Kronig phase (see Sec. 3.3) have not been observed and the current profiles agree within the TDS resolution. A calibration of the BCM as a measure for the absolute rms bunch duration has been investigated and carried out using a low-pass filter.

The relative deviations between the properties of the CRISP current profile and the results of BCM and TDS along the L<sub>2</sub> and L<sub>3</sub> chirp scan are presented in Fig. 6.15. The error bars mark the rms shot-to-shot fluctuations of the TDS profile and BCM signal. The relative shot-to-shot fluctuations of the BCM bunch duration are large for the shortest bunches ( $h_{L2} = 11.5 m^{-1}$ ,  $h_{L3} = 13.0 m^{-1}$ ). This is caused by the

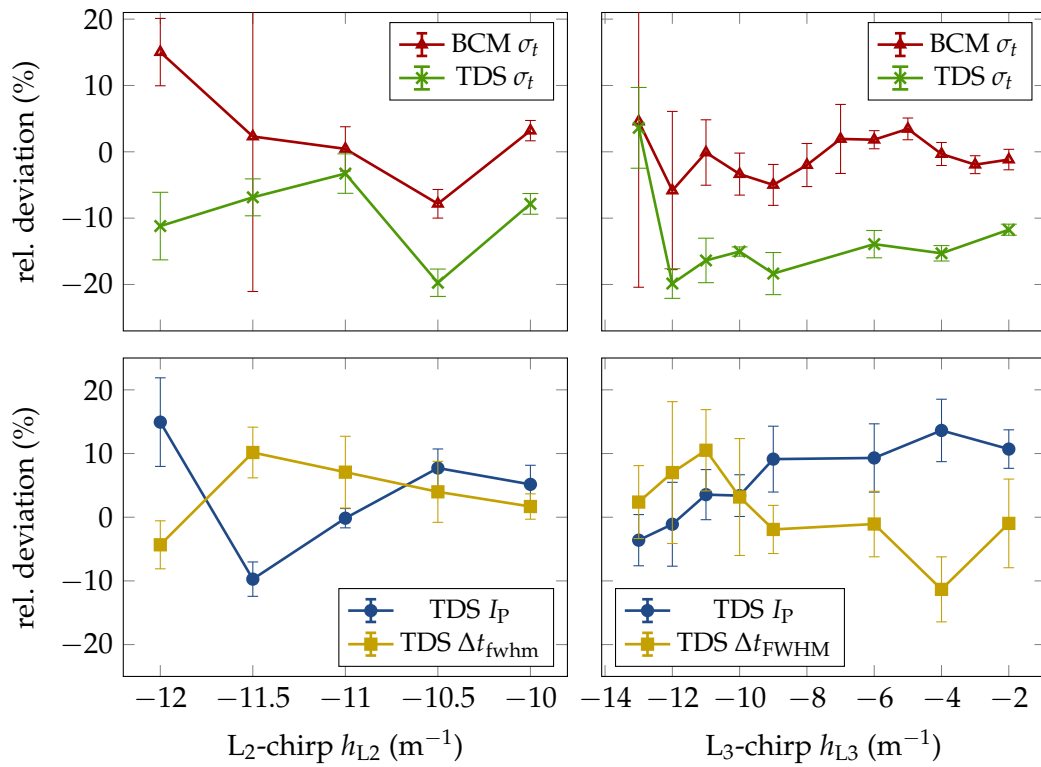


FIGURE 6.15: Relative deviation of the rms bunch duration obtained with BCM and TDS to the rms bunch duration of the CRISP profile along the chirp scans in the L<sub>2</sub> and L<sub>3</sub> section (top). The same for peak current and fwhm bunch duration of the TDS to those of the CRISP profile (bottom). For better comparison, the TDS resolution has been considered in the calculation of these parameters. The error bars mark the corresponding rms shot-to-shot fluctuations of BCM signal and TDS profile.

low-pass filter which leads to a decreased sensitivity on the bunch duration in this region (see Fig. 6.11). For FEL operation with low bunch charge and short bunch durations, the BCM detector without low-pass filter is required to detect changes of the bunch duration. Apart from over-compression at  $h_{L2} = -12 \text{ m}^{-1}$ , the deviations of the BCM are below 10%. The characteristic properties of the TDS current profiles agree overall within  $\simeq 15\%$  considering TDS resolution. Only the rms bunch duration shows at some chirps larger deviations due to its sensitivity on low current regions at head and tail of the bunch. These low currents regions however are of little interest for FEL operation and optimization. TDS and CRISP spectrometer complement each other. While the profile shape of long bunches ( $>100 \text{ fs}$ ) without increased charge ( $\leq 250 \text{ pC}$ ) cannot be reconstructed due to low signal-to-noise ratio at the CRISP spectrometer, it exhibits higher temporal resolution for short bunches. Due to missing comparative diagnostics with sufficient resolution and the complex dependency on bunch charge and shape itself, the temporal resolution of current profile reconstruction can only be studied based on simulations. These studies are carried out in App. B. Form factor measurements in single bunch operation, but also the current profile reconstruction itself, have been established within this thesis as a diagnostics with few-femtosecond resolution for bunches with properties that are foreseen for user operation of European XFEL.



## Chapter 7

# Megahertz Operation

The main motivation for the installation of the CRISP spectrometer at European XFEL is the capability to characterize every bunch inside the bunch train at its final compression and beam energy. Noninvasive diffraction radiation and fast detector electronics allow form factor measurements simultaneously to FEL operation of bunch trains with MHz bunch repetition rates. For an optimized operation of multiple FEL undulator beamlines, the accelerating rf pulse and thereby bunch compression is modified along the bunch train (see Sec. 2.3.1). In this operation mode with two rf flat-tops, the full potential of the CRISP spectrometer can be employed to monitor and optimize bunch compression. The current profile reconstruction from CRISP spectrometer data has already been confirmed by high-resolution TDS measurements in the Chap. 6 and is the basis for the results obtained during MHz operation in this chapter.

In order to operate the CRISP spectrometer with MHz repetition rates, first signal modulations (pileup) due to signal oscillations of the pyroelectric detectors have to be corrected. The pulse-stealing mode of the TDS in the BC<sub>3</sub>-section allows to confirm the absence of artificial modulations on reconstructed current profiles after pileup removal. Afterwards, results obtained parallel to FEL operation with different rf flat-tops are presented and changes of electron bunch compression within the rf flat-tops identified.

### 7.1 Pileup

The custom made pyroelectric detectors allow a compact realization of the spectrometer, exhibit sufficient sensitivity along the required frequency range and can be operated at room temperature in an evacuated environment. However, as was already mentioned in Sec. 4.3.1, post-signal oscillations (ringing) distort the measured spectrometer signal of following bunches. The reason are the piezoelectric properties of the pyroelectric crystals. The heat input to the crystal by the THz/FIR radiation induces mechanical oscillations, which again lead to surface charges caused by the piezoelectric effect and thereby a voltage signal after the pulse shaping electronics. The characteristic frequencies of these oscillations depend on the geometrical dimensions of the crystal. For crystals with thicknesses of a few ten micrometers and transverse dimensions around 1 mm, these frequencies lie in the MHz and kHz range [GA70].

An example for the ringing after the single bunch signal is shown in Fig. 7.1, where the normalized ADC signal with a sampling rate of 54 MHz is depicted. The oscillation amplitude decays slowly over several tens of microseconds while its frequency spectrum lies around 1 MHz (see Fig. 7.4 right). To cope with the bunch

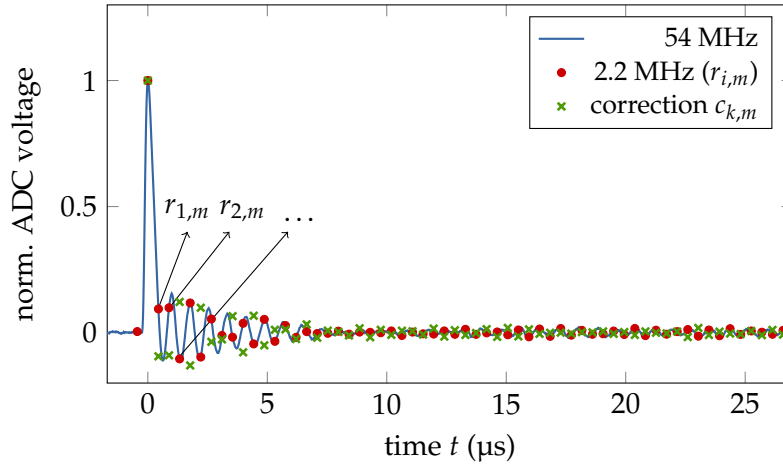


FIGURE 7.1: Post-signal oscillations after the induced signal of a single bunch ( $t = 0$ ) sampled with the ADC rate of 54 MHz (blue line) and the bunch repetition rate of 2.2 MHz (red dots). The green crosses mark the entries of the resulting correction vector  $c_{k,m}$ .

repetition rates of European XFEL (<4.5 MHz), the pulse-shaping electronics are designed to provide a few MHz bandwidth and consequently do not filter these oscillations. The remaining fractions  $r_{i,m}$  (red dots) of the single bunch signal at the position of the  $i$ -th following bunch – in this case on a 2.2 MHz pattern – will superimpose with the bunch induced signal of this following  $i$ -th bunch. A signal pileup occurs. As each bunch leads to a ringing that distorts the signals of the following bunches, the superposition of the measured signal  $v_{n,m}^*$  of the  $n$ -th sample at the bunch repetition rate is (with  $r_{0,m} = 1$ ) described by

$$v_{n,m}^* = v_{n,m} + r_{1,m} v_{n-1,m} + r_{2,m} v_{n-2,m} + \dots + r_{n,m} v_{0,m} = \sum_{i=0}^n r_{i,m} v_{n-i,m}. \quad (7.1)$$

Here,  $v_{i,m}$  are the actual bunch induced signals of the previous samples without distortion by pileup at spectrometer channel  $m$ . This description assumes the same ringing for each bunch inside the bunch train and thus no modification of the mechanical crystal properties.

The effects of the piezoelectric oscillations on the signal of a bunch train with 2.2 MHz repetition rate are simulated in the top part of Fig. 7.2. The bunch train starts at sample  $n_0$  (bunch #1) and the bunch induced signals  $v_{n,m}$  are modeled to be generated by two rf flat-tops. The second rf flat-top exhibits slightly more compression and starts at bunch #450. The experimentally determined fractions  $r_{i,m}$  (see Sec. 7.1.1) are used to simulate the measured signals  $v_{n,m}^*$  under influence of pileup using Eq. (7.1). The pileup leads to an artificial increase of the signal along the first  $\simeq 100$  bunches. Afterwards a steady-state is reached as the ringing of the first bunch has decayed to negligibly small values. A striking consequence of the signal pileup is that the measured signals  $v_{n,m}^*$  are non-zero after the bunch train at bunch #1085 (vertical line), i.e. the signal baseline is not recovered. The experimentally measured signals  $v_{n,m}^*$  of such a bunch train with two rf flat-tops are shown in the bottom part of Fig. 7.2. For comparison with the simulated signal, the trace is normalized to the signal of the first bunch. As in the simulation, the signal increases along the first few bunches followed by a steady state. After the bunch train, the measured signals deviate strongly from zero and the baseline is not recovered. The behaviour of the measured signal agrees very well with the expectations from the simulation and confirms that the pileup effect is well described by the considered model.

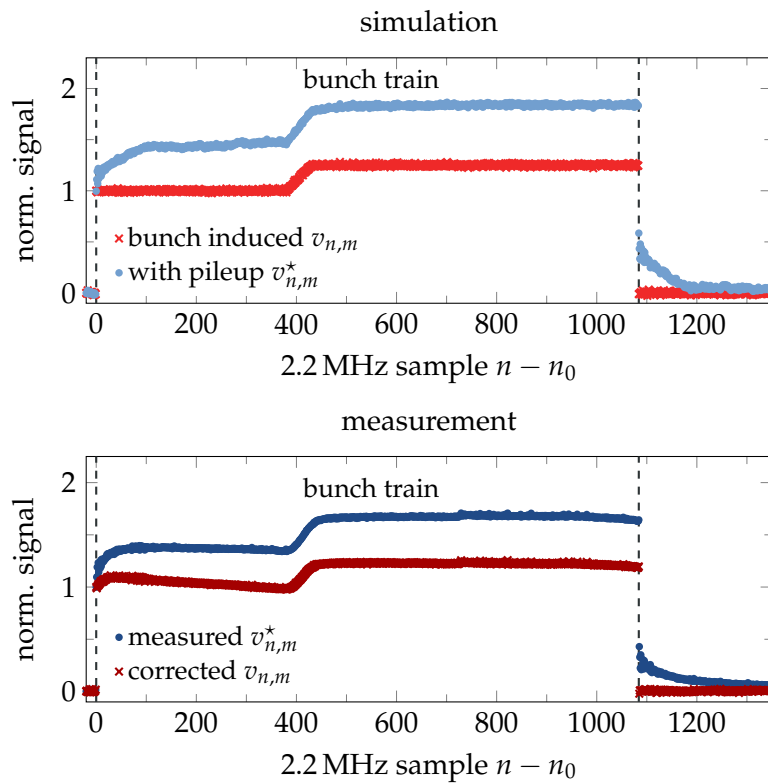


FIGURE 7.2: Top: Simulation of pileup influence on the bunch induced signals of a bunch train with 2.2MHz repetition rate and two rf flat-tops. The vertical lines mark the beginning and end of the bunch train. Due to the pileup the signal baseline after the bunch train is not recovered. Bottom: Measured signal and corresponding signal after pileup correction at 2.2MHz bunch repetition rate. If pileup is corrected, the baseline is successfully recovered. In the measurement, the bunch compression – and thus the corrected signal – exhibits a slight decrease along the first rf flat-top.

By introducing the response vector consisting of the fractions normalized to the bunch induced signal  $\vec{r}_m = (1, r_{1,m}, r_{2,m}, \dots, r_{N,m})$ , Eq. (7.1) can be reformulated to describe an entire bunch train with  $N + 1$  signal samples at the bunch repetition rate using matrix formalism. With the vectors  $\vec{v}_m^*$  for the measured and  $\vec{v}_m$  for the bunch induced signals along the bunch train, this is expressed by

$$\vec{v}_m^* = \mathbf{D}_m \vec{v}_m = \begin{pmatrix} 1 & 0 & \dots & 0 \\ r_{1,m} & 1 & \dots & 0 \\ \vdots & \vdots & \ddots & \\ r_{N,m} & r_{N-1,m} & & 1 \end{pmatrix} \vec{v}_m. \quad (7.2)$$

The response matrix  $\mathbf{D}_m$  is a lower triangular Toeplitz matrix, with its columns determined by the entries  $r_{i,m}$  of the response vector. The zeros in the upper triangular half-space indicate that the signal oscillations do not influence the measured signals of previous bunches. For the setup at European XFEL, this is the case for repetition rates of 2.2 MHz and below. At 4.5 MHz repetition rate, the width of the bunch induced signals is too large and disturbs the signal of the previous bunch. Therefore, Eq. (7.1) is not applicable at this repetition rate with the current electronic pulse shaping (see Sec. 4.3.1).

The matrix formalism allows to retrieve the undisturbed signals  $\vec{v}_m$  by inverting the response matrix  $\mathbf{D}_m$  to the correction matrix  $\mathbf{C}_m$ :

$$\vec{v}_m = \mathbf{D}_m^{-1} \vec{v}_m^* = \mathbf{C}_m \vec{v}_m^*. \quad (7.3)$$

The response matrix can be inverted by either numerical algorithms or by exploiting iteratively the properties of the lower triangular Toeplitz matrix. The inverse matrix will also be a lower triangular Toeplitz matrix with its column entries described by the correction vector  $\vec{c}_m$ . The iterative procedure for the entries  $c_{k,m}$  of the correction vector is [FSZ13]

$$c_{0,m} = 1, \quad c_{k,m} = - \sum_{j=0}^{k-1} r_{k-j,m} c_{j,m} \quad (k = 1, \dots, N). \quad (7.4)$$

An example of the correction vector at 2.2 MHz is shown in Fig. 7.1. Its overall behaviour and decay is similar to the response vector. The results of applying Eqs. (7.3), (7.4) to a pileup distorted measurement are presented by the red dots in the bottom part of Fig. 7.2. Now, the signal increase along the first bunches induced by the pileup is removed and also the baseline after the bunch train is recovered. As will also be confirmed by the following results in this thesis, the pileup is sufficiently characterized by determining the signals fractions  $r_{i,m}$  using a single bunch measurement and the presented procedure allows to remove the influence of signal pileup.

### 7.1.1 Signal processing

The ADC sampling is synchronized to the accelerator timing system and is set to a multiple of the injector laser system, which is also a multiple of all possible bunch repetition rates. As illustrated in Fig. 7.3, it is then possible to extract the signals  $\vec{v}_m^*$  covering all bunches inside the bunch train by simply further reducing the sampling rate in the signal processing. The electronical detector noise floor  $\mathcal{S}_m$ , which defines the confidence threshold  $\mathcal{L}(f_m)$  (see Eq. (5.6)) of the spectrometer, is obtained by the standard deviation of the samples in front of the bunch train. The fixed spacing between the measured signals of the bunches ensures the applicability of the pileup

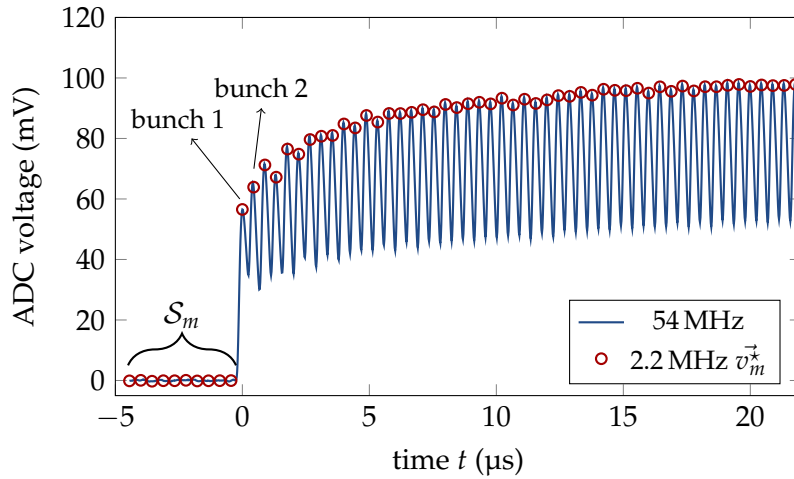


FIGURE 7.3: The measured signals  $v_m^{\vec{x}}$  of the bunches inside a bunch train are obtained by simple division of the ADC sampling rate, which is a multiple of every possible bunch repetition rate. For a bunch repetition rate of 2.2 MHz, every 12th sample (red circles) of the ADC is further processed. The confidence threshold  $\mathcal{L}(f_m)$  (see Eq. (5.6)) is defined by the noise floor  $\mathcal{S}_m$ , which is calculated by the standard deviation of the samples prior to the bunch train.

removal routine as otherwise – e.g. peak detection schemes – the signal fractions  $r_{i,m}$  cannot be considered the same for every bunch.

The response vector  $\vec{r}_m$  for a certain bunch repetition rate is determined by a single bunch measurement with the sampling rate reduced to the respective bunch repetition rate and normalizing it to the signal at the sample of the bunch. However, as shown in Fig. 7.4, decay and frequency spectrum of the ringing are slightly different for each channel  $m$  of the spectrometer. This is due to fabrication tolerances of the pyroelectric detectors but also depends on the currently inserted grating set of the CRISP spectrometer. Frequencies are absorbed differently by the pyroelectric detector with its complex structure consisting of multiple layers (see Fig. 4.13), which leads to a slightly modified ringing at the same channel. The response vector  $\vec{r}_m$  must be determined for each of the 240 central frequencies individually. Thus, it is very important to carry out the response vector measurements with highly compressed bunches of increased charge in order to generate sufficient signal. However, a successful pileup correction requires good knowledge of the response vector down to small values and at some channels the response vector cannot be determined precisely enough due to signal noise. In this case, the measured response vector, or a similar response vector of another channel, may be optimized by an empirical method.

An example for corrected signals along the bunch train prior and after optimization of the response vector  $\vec{r}_m$  is given in Fig. 7.5. The criterion for the quality of the pileup removal is the restoration of the baseline after the bunch train. For this purpose, the parameter

$$\chi_m = \frac{1}{(N_t - N_b)} \sum_{n=N_b+1}^{N_t} \left( \frac{v_{n,m}}{\mathcal{S}_m} \right)^2, \quad (7.5)$$

which sets the corrected signal  $v_{n,m}$  after the bunch train ending at sample  $N_b$  in relation to the intrinsic detector noise  $\mathcal{S}_m$ , is introduced. Hereby,  $N_t$  denotes the total number of samples. Without any influence of pileup on the signals, the parameter

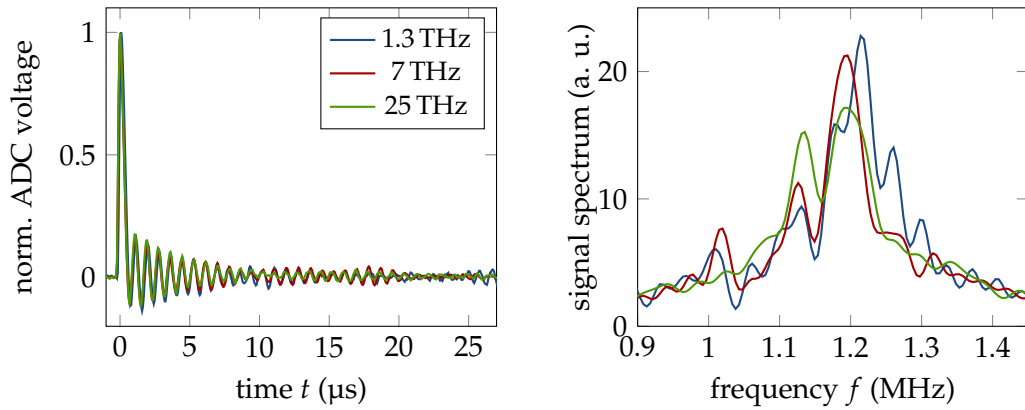


FIGURE 7.4: Left: Ringing at the ADCs after a single bunch signal due to vibrations of the pyroelectric crystal detected with a sampling rate of 54 MHz. Right: Frequency spectrum of the ringing. Each channel with the stated central frequencies  $f_m$  exhibits a slightly different decay and frequency spectrum. The response vector  $\vec{r}_m$  must thus be determined for every channel  $m$  individually.

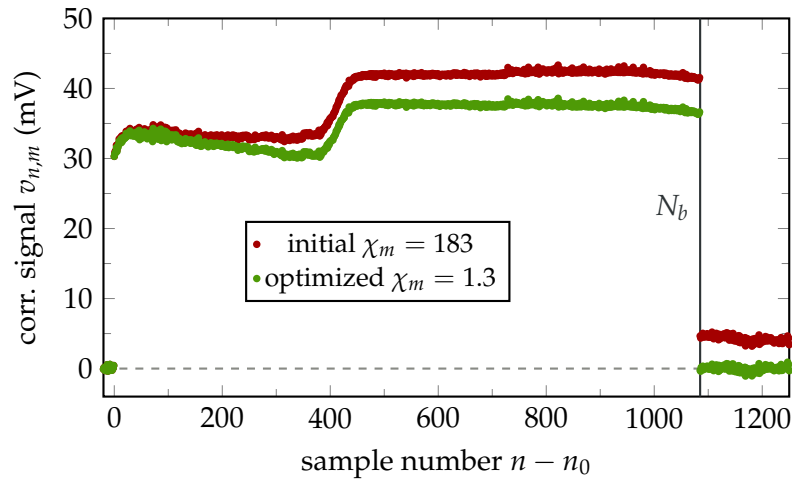


FIGURE 7.5: Pileup corrected signal of one spectrometer channel sampled at the bunch repetition rate of 2.2 MHz. Using the initial correction matrix based on the recorded response vector, the baseline is not perfectly restored. After slight numerical optimizations of the response vector the baseline is much better restored as indicated by the decreasing parameter  $\chi_m$ .

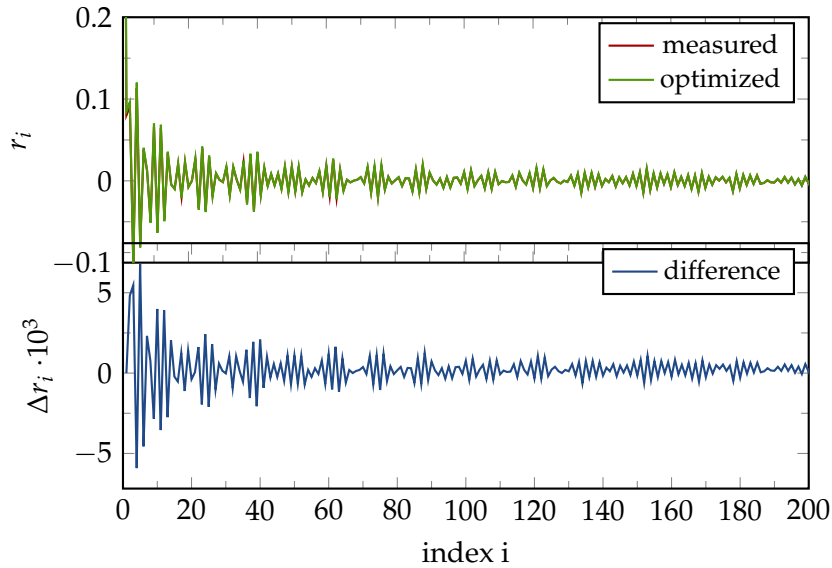


FIGURE 7.6: Top: Measured response vector (red, barely visible) in comparison to the response optimized with an empirical method using a simplex algorithm (green). Bottom: Difference between both response vectors. Even though the differences are in the order  $10^{-3}$ , they have a significant influence on the pileup removal itself (see Fig. 7.5).

$\chi_m$  is near 1. For the response optimization, a simplex algorithm empirically reduces the  $\chi$ -parameter by adding a sixth order polynomial and an exponential decay with varying coefficients to the initial response. This way, the influence of background and noise distortions on the measured response vector can be removed. As can be seen in Fig. 7.5, the initial deviation of the baseline after the bunch train from zero vanishes and thereby also influences of the pileup along the bunch train are corrected. The changes of the response vector itself are marginal and almost not visible in Fig. 7.6. Practical experience has shown that the responses provide stable results over long periods of time (>months) and are not affected by changes of the accelerator settings.

For some channels, the fluctuations of the corrected signal after the bunch train can be a few times higher than the fluctuations before the bunch train, which indicates some residual pileup on the corrected signals. It is hard to classify the exact effects of residual pileup on the corrected signals  $\vec{v}_m$ . Thus, the influence of remaining pileup effects is conservatively estimated for each channel by the maximum deviation  $\mathcal{P}_m$  from zero of the corrected signal after the bunch train. If the estimated pileup error  $\mathcal{P}_m$  of a corrected signal averaged over several (>10) rf pulses is larger than the shot-to-shot signal fluctuations, the pileup removal of this channel is considered not trustworthy and consequently removed before further analysis. Otherwise, the estimated pileup error  $\mathcal{P}_m$  replaces – if larger – the detector noise floor  $2\mathcal{S}_m$  in Eq. (5.6) and yields a new confidence threshold  $\mathcal{L}(f_m)$  for bunch train measurements. The estimated pileup error  $\mathcal{P}_m$  is also considered in the measurement uncertainties by quadratical addition to the rms shot-to-shot fluctuations for the iterative current profile reconstruction.

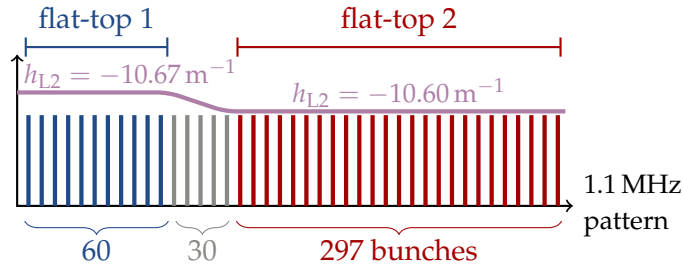


FIGURE 7.7: Schematic of rf pulse and bunch pattern for the comparative measurements at 1.1 MHz bunch repetition rate. Two rf flat-tops with different bunch compression are established by changing the chirp in the  $L_2$  section. 387 bunches are generated and accelerated in total.

## 7.2 Comparative Measurements

In this thesis, current profile measurements have been realized for the first time at MHz bunch repetition rates with the CRISP spectrometer by using noninvasive DR and successful pileup removal as introduced in Sec. 7.1. In order to confirm that the reconstructed current profiles are not influenced by remaining pileup effects, comparative measurements at MHz bunch repetition rates are studied in this chapter. The TDS after the last bunch compressor  $BC_3$  can be operated in pulse-stealing mode (see Sec. 2.4.1), which allows to monitor the current profile of a single bunch inside the train. The bunch is streaked by the TDS and downstream deflected by a fast magnetic kicker onto an off-axis screen (see Fig. 2.8). Timing of TDS and kicker are scanned to select the bunches of the bunch train one after the other. This TDS mode is compatible with FEL electron beam optics however, it results in a worse design resolution ( $\simeq 15$  fs) compared to the one in the local diagnostics dump ( $\simeq 5$  fs) [Yan15]. The bunch compression monitor (BCM) after  $BC_3$  is as well capable of MHz operation and has been calibrated in Sec. 6.3.2 to yield absolute rms bunch durations. In contrast to the TDS, the BCM is – like the CRISP spectrometer – noninvasive to the electron beam such that a scanning procedure along the bunch train is not required.

For the comparative measurements, which have been carried out during dedicated beam time, electron bunches have been accelerated to 14 GeV beam energy at a repetition rate of 1.1 MHz. Thereby, the electron beam has not been sent to the FEL undulator beamlines, but has been terminated in the dump just upstream of the undulators (see Fig. 2.5). As illustrated in Fig. 7.7, the accelerating rf pulse in the  $L_2$  section has been operated with two flat-tops in order to generate detectable changes of the current profile properties along the bunch train. The chirp has been set to  $h_{L2} = -10.67 \text{ m}^{-1}$  inside the first and to  $h_{L2} = -10.60 \text{ m}^{-1}$  inside the second rf flat-top. Thus, the 60 bunches of the first rf flat-top experience a stronger compression inside the bunch compressors  $BC_2$  and  $BC_3$  than the 297 bunches of the second rf flat-top (see Sec. 2.1). Both compression settings are within the typical range of FEL user operation. The total bunch train carries 387 bunches with 30 bunches inside the rf transition region between both rf flat-tops.

The bunch charge is set to 250 pC, but exhibits variations along the bunch train as shown in Fig. 7.8. The charge averaged over 20 rf pulses increases from 0.25 nC at the beginning to more than 0.27 nC at the end of the bunch train. The error band marks the rms shot-to-shot fluctuations. The charge remains constant along the first approximately 10 bunches before it strongly increases within rf flat-top FT 1. Afterwards it approaches its asymptotic limit such that there are less variations along rf

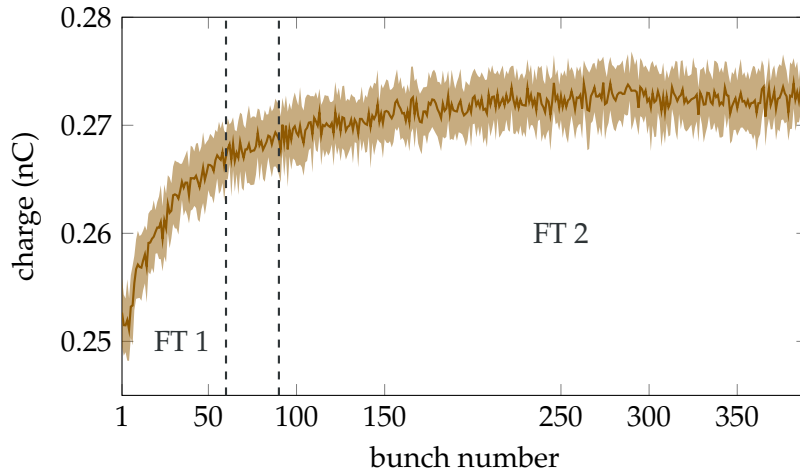


FIGURE 7.8: Charge along the bunch train for comparative measurements at 1.1 MHz repetition rate. The error band represents the rms shot-to-shot fluctuations. The charge increases within rf flat-top FT 1 and exhibits a sudden increase around bunch #10. In rf flat-top FT 2, the charge variations are much smaller.

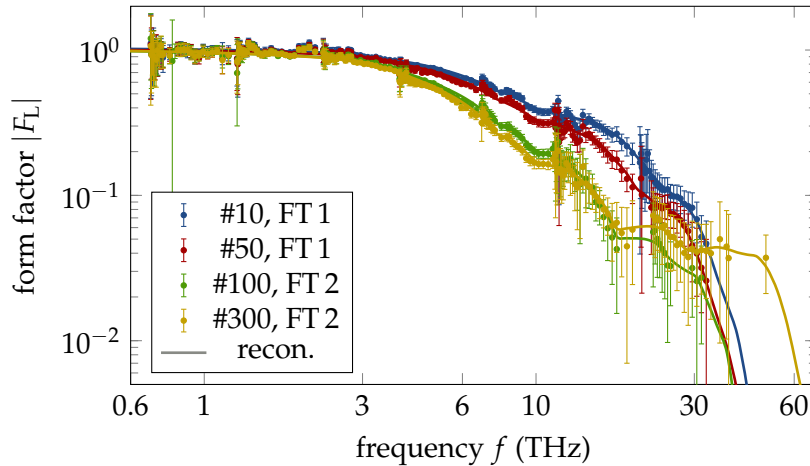


FIGURE 7.9: Measured form factors of two bunches from each rf flat-top during bunch train operation with 1.1 MHz repetition rate. The solid lines mark the form factor of the reconstructed current profiles, which are presented in Fig. 7.10.

flat-top FT2. These variations are caused by the injector laser. During FEL user operation, the injector laser intensity and thus charge is optimized and flattened along the bunch train. However, for the comparative measurements in this section, the charge variations are intentionally not removed. The charge affects the bunch compression by e.g. collective effects, such that variations potentially have an influence on the shape of the current profile. Such characteristic variations of the current profile within the rf flat-tops consequently allow for a more comprehensive comparison of CRISP with BCM and TDS than using rf flat-tops alone.

The form factors of two bunches from each rf flat-top recorded with the CRISP spectrometer are presented in Fig. 7.9. They are an average of 50 rf pulses at each grating set, and the error bars mark the combination of rms shot-to-shot fluctuations and estimated pileup error (see Sec. 7.1.1). The frequency range and uncertainties of the processed form factor data are comparable to single bunch operation (see e.g. Fig. 6.4). The estimated pileup error has no considerable influence on form factor

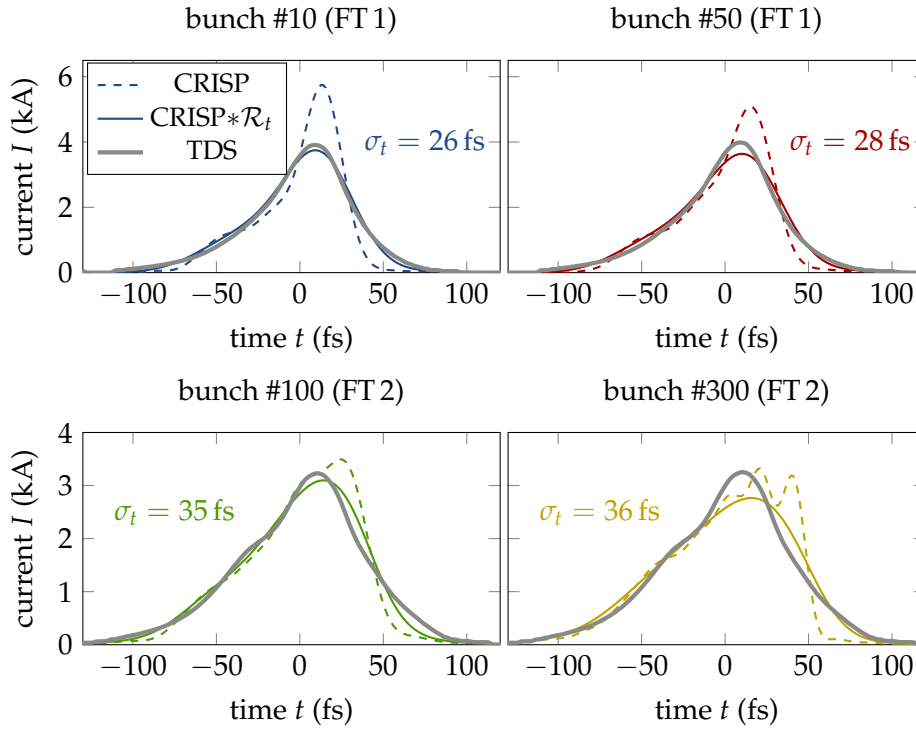


FIGURE 7.10: Current profiles of two bunches from each rf flat-top obtained with CRISP spectrometer and TDS. The rms bunch duration  $\sigma_t$  of the CRISP profile is stated for each bunch. For better comparison, the spectrometer results have been convoluted with the respective TDS resolution  $\mathcal{R}_t$ . Times with  $t < 0$  indicate the tail of the bunch.

measurements, as the signal baselines after the bunch train are well restored. The form factor of the reconstructed current profiles, that are presented as dashed lines in Fig. 7.10, are in agreement with the measurements as shown by the solid lines.

Form factor and current profile exhibit distinct properties for both rf flat-tops. The reconstructed rms bunch duration  $\sigma_t$ , which is noted in Fig. 7.10, increases by more than 5 fs between both rf flat-tops, while the peak current decreases from more than 5 kA in rf flat-top FT 1 to just more than 3 kA in rf flat-top FT 2. These observations are in agreement with the discussed expectations on the bunch compression caused by different chirps imprinted in the  $L_2$  section. Nonetheless, current profile and form factor indicate not only differences between both rf flat-tops, but also within the rf flat-tops. The peak current for example decreases by almost 1 kA from bunch #10 to bunch #50 in rf flat-top FT 1. Inside rf flat-top FT 2, the reconstructed current profile of bunch #300 exhibits significantly more substructure than bunch #100, which reflects in stronger form factor modulations above 20 THz (see Fig. 7.9). The current profile shape of bunch #100 is similar to the current profiles in FT 1. They are described by a Gaussian-like peak with slowly decaying current towards the bunch tail.

As already mentioned, the CRISP spectrometer records the form factor of all bunches within the train. The properties of all current profiles along the train are thus available from the reconstructions of a single data set. Hereby, the frequency grid of the reconstruction algorithm (see Sec. 6.1.2) is kept constant to avoid numerical fluctuations of key parameters like e.g. rms bunch duration. The resulting rms bunch durations are presented in Fig. 7.11. Along the first rf flat-top, it increases continuously from 25 fs to 28 fs with a steep increase after the first ten bunches. In the transition region between bunch #61 and bunch #91, the bunch duration grows

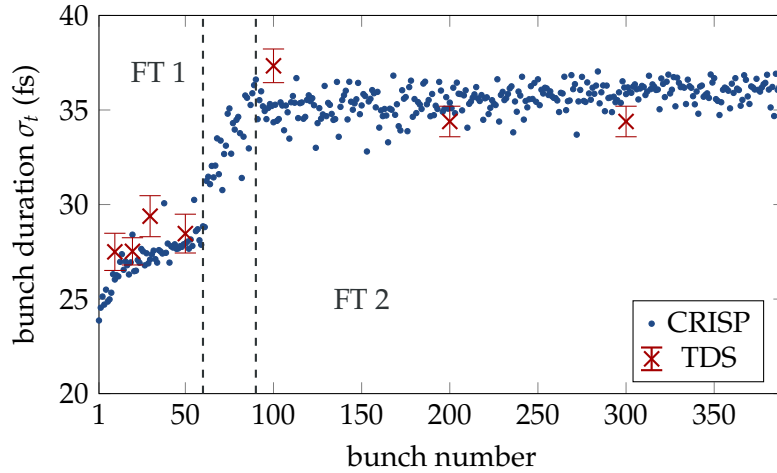


FIGURE 7.11: Comparison of rms bunch durations  $\sigma_t$  obtained with TDS and CRISP spectrometer along the bunch train with two rf flat-tops FT 1 and FT 2 at 1.1 MHz repetition rate. The error bars of the TDS measurement mark the shot-to-shot fluctuations of the measured TDS profile.

rapidly within 30 bunches to 35 fs. Along the second rf flat-top FT 2, the bunch duration increases only slightly. At the end of the bunch train, the rms bunch duration amounts to roughly 36 fs.

As a first comparison, the results of the TDS at the same accelerator settings are investigated. The TDS profiles are obtained by the reconstruction of the average profiles of 10 rf pulses at both zero-crossings (see Secs. 5.2.1, 6.2). The temporal resolution determined from the unstreaked profile varies between 14 fs and 17 fs. The resulting current profiles are compared to the reconstructed profiles of the CRISP spectrometer in Fig. 7.10. Again, the TDS resolution denies a confirmation of substructures and corresponding peak current. Instead, the CRISP profiles must be convoluted (see Sec. 6.2) with the resolution  $\mathcal{R}_t$  to allow comparison. After the convolution, all current profiles agree in overall shape and duration. At bunch #300, the peak current of the reconstructed current profile varies by more than 10% due to the dominant substructure.

The TDS is only capable of monitoring single bunches of the bunch train and not all current profiles of the bunch train are recorded. Instead selected bunch numbers (10, 20, 30, 50, 100, 200, 300) are one after the other characterized. The rms bunch durations of these profiles are compared to the CRISP results in Fig. 7.11. Hereby, the TDS resolution has been considered by quadratical subtraction, and the error bars mark the shot-to-shot fluctuations. Overall, the bunch durations of both devices agree within 10% under consideration of the bunch-to-bunch fluctuations. Both devices detect a rms bunch duration increase of almost 10 fs between both rf flat-tops.

Using the calibration for an absolute rms bunch duration carried out in Sec. 6.3.2, the BCM detector after the last bunch compressor with a 6 THz low-pass filter is utilized as a second comparative diagnostic. The rms bunch durations obtained from the average signal of 20 rf pulses and the corresponding shot-to-shot fluctuations are compared to the results of the CRISP spectrometer in Fig. 7.12. The evolution of the rms bunch duration of the BCM agrees with the results of the CRISP spectrometer. The overall offset of around 1 fs –2 fs ( $\sim 5\%$ ) is within the typical deviations caused by different bunch shapes (see Fig. 6.12). The BCM measurement confirms the steep increase of the rms bunch duration around bunch #10 for which no TDS data is available. The shot-to-shot fluctuations of the BCM bunch duration are smaller than

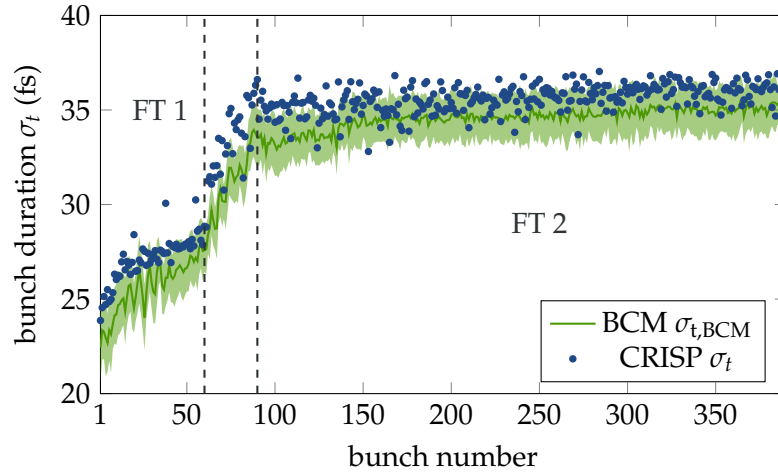


FIGURE 7.12: Rms bunch duration obtained with the BCM based on the calibration carried out in Sec. 6.3.2. Except from an overall offset of around 1 fs, the bunch durations and its evolution along the bunch train agree with the results of the CRISP spectrometer. The BCM also detects a strong increase of the bunch duration around bunch #10.

the overall variations along the bunch train. This indicates that the BCM detector with low-pass filter exhibits enough sensitivity to detect unintentional changes of the rms bunch duration on the femtosecond scale for FEL user operation with 250 pC bunch charge even on a single-shot basis.

The comparison with two independent diagnostics shows no indications for signal pileup effects on the properties of the reconstructed current profiles after the pileup removal. Even though the TDS resolution hampers a comparison of substructures inside the current profiles, the evolution of the bunch durations along the bunch train are consistent. The substructure on the reconstructed current profiles at the end of rf flat-top FT 2 (see bunch #300 in Fig. 7.10) is caused by an increasing form factor at frequencies above 20 THz. However, this cannot be caused artificially by the signal pileup effect, as this far inside the bunch train the pileup has reached an almost steady state (see Fig. 7.2). The steep increase of the rms bunch duration around bunch #10 of the CRISP current profiles correlates with the observations on charge and BCM signal. The BCM detector is a pyroelectric detector as well, which thus requires the same pileup removal method, but detector layout and readout electronics are fundamentally different. A similar behaviour of the signal pileup can therefore be excluded. The rms bunch duration evolves in a similar way as the bunch charge along the rf flat-tops even for the dynamic changes along rf flat-top FT 1. Furthermore, it should be noted that the bunches along the first 50  $\mu\text{s}$  – 100  $\mu\text{s}$  are not sent to the FEL undulator beamlines during FEL user operation to avoid possible variations of the FEL pulse. Wakefields caused by cavity misalignment – for example – lead to orbit variations which reach a steady-state after  $\sim 50 \mu\text{s}$  [Abe+06]. In summary, the results of this section show that the CRISP spectrometer – with its modification carried out within this thesis – is well suited for current profile measurements by noninvasive operation with MHz bunch repetition rates simultaneously to FEL user operation.

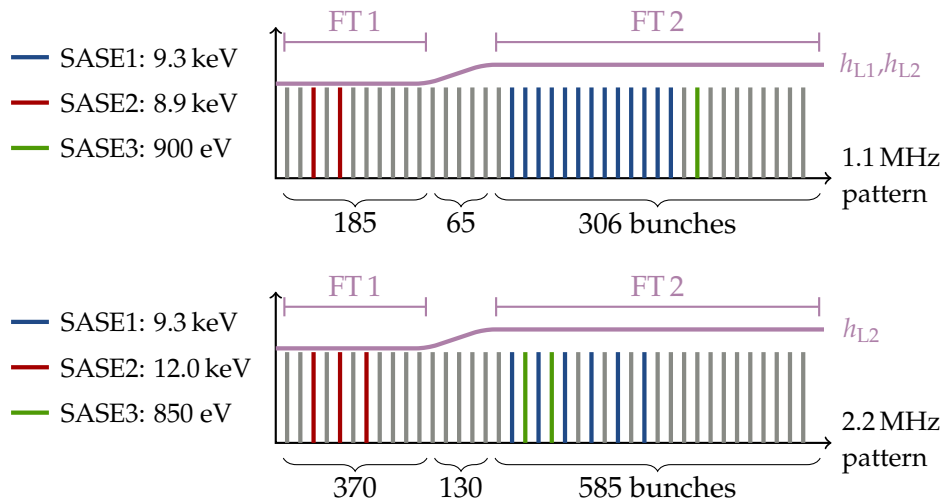


FIGURE 7.13: Schematic of rf pulse structure, bunch pattern and SASE beamline settings for the presented measurements at 1.1 MHz (top) and 2.2 MHz (bottom) bunch repetition rate. During the 1.1 MHz measurement, the chirps in the  $L_1$  and  $L_2$  sections are modified between the rf flat-tops. At the 2.2 MHz measurement, only the  $L_2$  chirp is adapted for the second rf flat-top FT2. The bunch structure inside the rf flat-tops is only given for illustration purposes and may not agree with the actual bunch patterns at the SASE beamlines.

### 7.3 Results during FEL Operation

As the final step of a successful spectrometer commissioning carried out in this thesis, this section presents results obtained during FEL user operation. The insertion of the 5 mm diffraction radiator aperture (see Sec. 4.1) does not lead to any observed consequences on electron bunch or FEL pulse quality. The current profiles inside the bunch train can thus be monitored simultaneously to FEL operation with MHz repetition rates and without any disturbances of the XFEL photon pulses. In order to illustrate results, which are subject to long term variations and different FEL operation modes, a measurement at 1.1 MHz and 2.2 MHz bunch repetition rate is presented. Around 6 months passed between both measurements.

A schematic overview of the rf pulse structures and SASE beamline operations is given in Fig. 7.13. A detailed explanation of the MHz operation mode of European XFEL can be found in Sec. 2.3.1. In both cases, the beam energy amounts to 14 GeV and the bunch charge to 250 pC. The rf pulse is divided in two rf flat-tops FT 1 and FT 2. While at 1.1 MHz, the flat-tops differ by the imprinted chirps in the  $L_1$  and  $L_2$  sections, only the chirp in the  $L_2$  section is adapted for the 2.2 MHz operation. The chirp settings itself are results of empiric optimization of the SASE FEL intensity at the respective FEL undulator beamlines. The photon energy of SASE1 is the same for both measurements, but at the 2.2 MHz measurement SASE2 generates X-ray pulses with higher photon energy. In total, 556 and respectively 1085 bunches are accelerated. In both cases, rf flat-top FT 1 contains the bunches for the SASE2 undulator beamline and FT 2 the bunches for the SASE1 and SASE3 undulator beamlines. However, only a fraction of the bunches inside the individual rf flat-tops are generating SASE radiation inside the undulators. The remaining bunches are terminated, like the bunches inside the transition region between both rf flat-tops, at the dump upstream of the undulator beamlines (see Fig. 2.5).

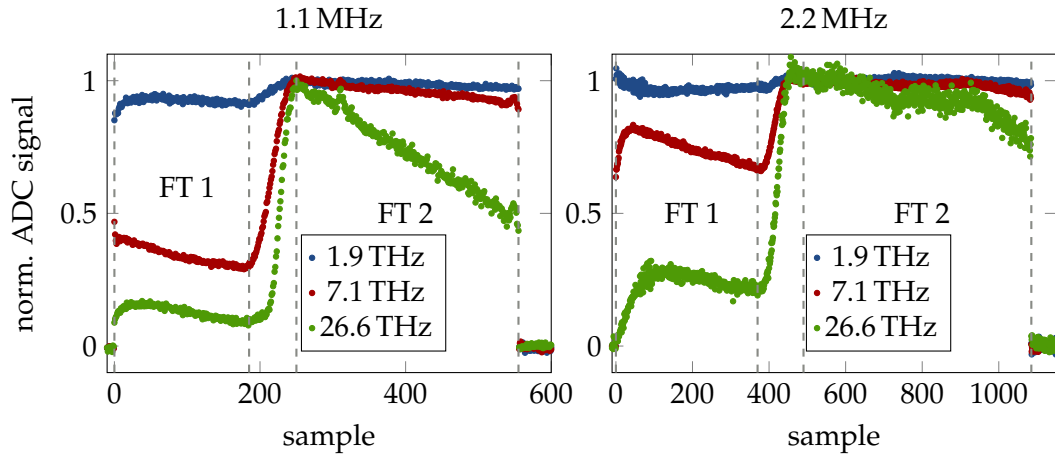


FIGURE 7.14: Normalized and pileup corrected ADC signals of three spectrometer channels for both data sets, which are sampled at the respective bunch repetition rate. The channels represent a moderate low, central and moderate high radiation frequency along the spectrometer range. The baseline after the bunch train is well restored, and the compression settings of FT 2 lead in all cases to an increased CDR intensity.

The pileup corrected signals  $\vec{v}_m$  already allow an insight into the behaviour of longitudinal bunch properties along the bunch train. They are presented for three channels of the spectrometer in Fig. 7.14. The three channels represent lower, central and high frequency region of the spectrometer. The baseline after the bunch train is well restored for both repetition rates, which indicates a successful pileup removal (see Sec. 7.1). For both measurements, the signals clearly exhibit differences between the rf flat-tops. Hereby, the second rf flat-top yields more CDR intensity at all frequencies. Especially, at high frequencies (see 26.6 THz) the signal differences between the rf flat-tops are large with FT 2 yielding more than 4-times higher signal than FT 1. At low frequencies, the differences are much smaller. The reason is clear: At low frequencies, the form factor is close to its asymptotic limit of 1 and its relative changes depending on bunch compression are small. In contrast, the relative changes of the form factor – and thus radiation intensity – at high frequencies are more pronounced.

The spectrometer signals do not only show a difference between both rf flat-tops but also modulations within the individual rf flat-tops. Especially along the first approximately 50 and respectively 100 bunches ( $\sim 50 \mu\text{s}$ ), the spectrometer signals evolve differently depending on the measurement set and frequency. Along the rf flat-tops itself, the signals are in all cases continuously decreasing. Thus, the spectrometer sensitivity is not only sufficient to detect changes of the bunch compression between the rf flat-tops, which are a result of empiric SASE optimization, but also unintentional variations inside the individual rf flat-tops.

The resulting form factors of selected bunches along the bunch train are presented in Fig. 7.15. These bunches represent the beginning of rf flat-top FT 1, center of FT 1, transition region and center of FT 2. After the data processing, the measured form factors cover frequencies up to at least  $f \approx 20 \text{ THz}$  and values down to  $|F_L(f_m)| \approx 0.1$  and smaller. Thus also at 2.2 MHz operation, the bunch repetition rate does not lead to considerable limitations of form factor measurements caused by the pileup effect. For both data sets, the previous observation of an increased CDR intensity in the second rf flat-top FT 2 is reflected in a form factor extending

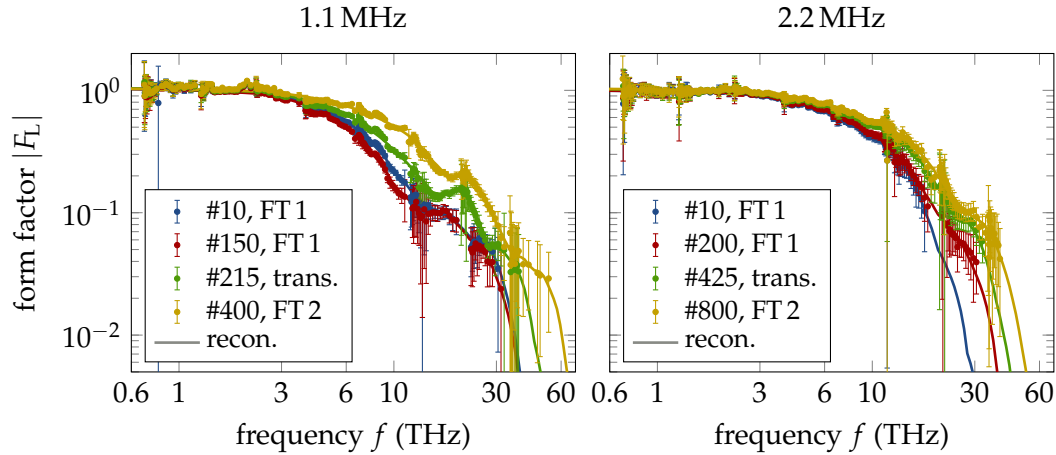


FIGURE 7.15: Measured form factors of selected bunches of the bunch train for both measurements. In both cases, the form factors extend to higher frequencies in the second rf flat-top FT 2. The form factors of the reconstructed current profiles are illustrated by the solid lines.

to higher frequencies. Hereby, the 1.1 MHz measurement shows stronger variations between the two rf flat-tops than the 2.2 MHz measurement. In addition, the form factors of the 1.1 MHz measurement exhibit modulations. Especially in FT 2, there is a pronounced substructure in the frequency range 10 THz – 30 THz. The form factors of the 2.2 MHz measurement are in contrast uniformly decreasing.

The reconstructed current profiles for the selected bunches are presented in Fig. 7.16. Their form factors agree with the measurements as shown in Fig. 7.15. The current profiles of both measurements and rf flat-tops exhibit the characteristic asymmetric shape with a shoulder towards one site, which has also been observed for several current profiles in Chap. 6. As mentioned in Sec. 3.2, the direction of the current profile cannot be determined from form factor measurements alone. Nonetheless, from simulations (see e.g. Fig. 3.4) and experiences of comparative measurements with the TDS (Secs. 6.2, 7.2), the shoulder is assumed to be at the tail of the bunch. The overall bunch durations of the current profiles from both measurements are comparable (20 fs – 35 fs, see also Fig. 7.17) and in agreement with the expectations from simulations of 250 pC FEL operation in Tab. 2.2. The extension of the form factor at rf flat-top FT 2 to higher frequencies reflects itself in a more compressed region containing the high current. The peak current increases by 3 kA for the 1.1 MHz measurement and almost 2 kA for the 2.2 MHz measurement. The 1.1 MHz measurements exhibits more substructure on the current profile, which also results in a reduced peak current at rf flat-top FT 1.

The rms bunch durations of the reconstructed current profiles of all bunches inside the bunch trains are depicted in Fig. 7.17. For both operation modes, the difference in bunch compression of the two rf flat-tops can be well observed in the behaviour of the reconstructed bunch durations. For the 1.1 MHz measurement, the rms bunch duration decreases by almost 10 fs from 33 fs to 24 fs. For the 2.2 MHz measurement, the difference amounts to roughly 5 fs, while the rms bunch duration is at both rf flat-tops shorter than in the 1.1 MHz case. The first 50 and respectively 100 bunches exhibit in both cases a strong dynamic with rapidly changing bunch durations. Whereas the bunch duration is increasing for the 1.1 MHz measurement, it decreases for the 2.2 MHz measurement. Afterwards, the rms bunch duration increases in both cases continuously along rf flat-top FT 1. At FT 2, the bunch duration

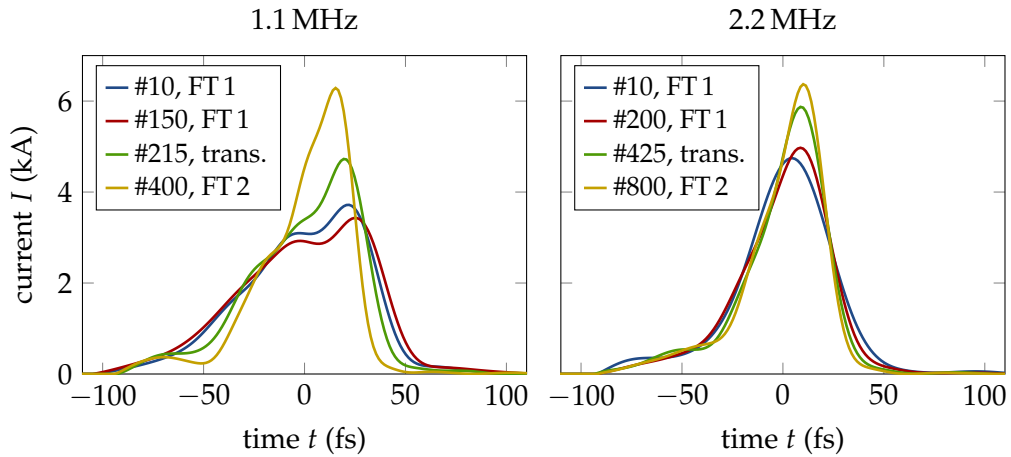


FIGURE 7.16: Reconstructed current profiles based on measurements recorded simultaneously to FEL operation with 1.1 MHz and 2.2 MHz bunch repetition rate. Shown are representative bunches from the beginning of the bunch train, FT 1, transition region and FT 2. The bunch head is most-likely at times  $t > 0$ .

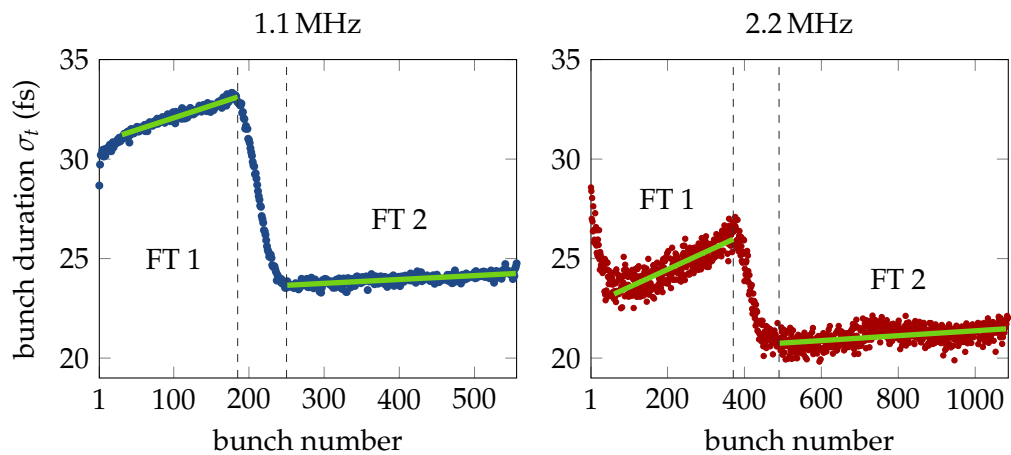


FIGURE 7.17: Rms bunch durations along the bunch train for both measurements. The different bunch compression between the two rf flat-tops is well distinguishable. The first bunches exhibit in both cases strong variations. The solid lines mark the result of a linear fit for the bunch duration within each rf flat-top.

TABLE 7.1: Standard deviation of the reconstructed rms bunch duration from the linear fit along each rf flat-top (see Fig. 7.17), which gives an estimate of the relative rms bunch duration uncertainty. The sensitivity of reconstruction and rms parameter itself depend on the current profile shape, which leads to different values for the rf flat-tops and measurements.

	FT 1	FT 2
1.1 MHz	0.2 fs	0.2 fs
2.2 MHz	0.5 fs	0.4 fs

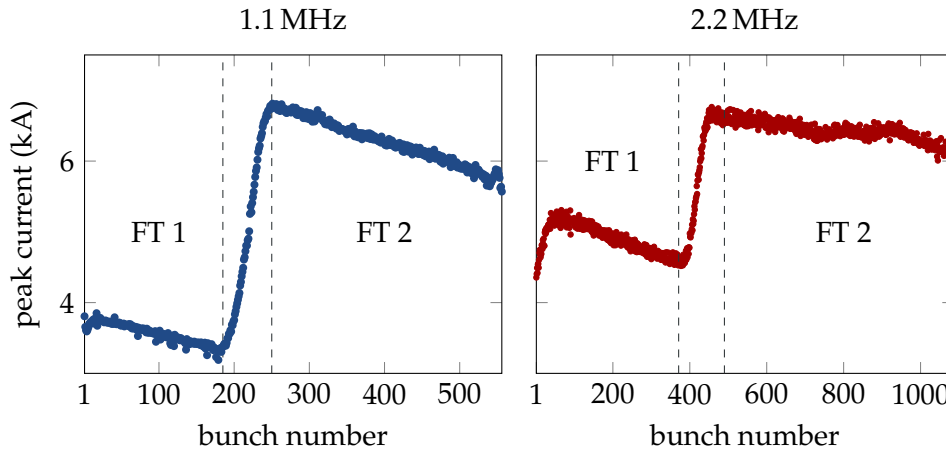


FIGURE 7.18: Peak currents of the reconstructed current profiles along the bunch train for the measurements at 1.1 MHz and 2.2 MHz bunch repetition rate.

remains constant within 1 fs. The CDR intensity at high frequencies, which is presented in Fig. 7.14, exhibits a decrease along FT 2 of the 1.1 MHz measurement. It does not result in a stronger increasing rms bunch duration, but in a suppression of substructure in the high current region (see Fig. 7.16).

The almost loss-free superconducting cavities are resonators of very high  $Q$ , which allow only slow changes of the rf parameters along the bunch train [Aun+00]. It is thus reasonable to assume no short time (bunch-to-bunch) variations of the actual rms bunch duration caused by the accelerating rf. In this case, an upper limit for the uncertainty of the reconstructed rms bunch duration can be identified by estimating a linear increase of the actual rms bunch duration along each flat-top. A linear fit to the reconstructed rms bunch duration along each rf flat-top is presented in Fig. 7.17. The uncertainty of the reconstructed rms bunch duration is estimated by the standard deviation from these fits. The results are listed in Tab. 7.1. In all cases, the estimated uncertainty of the rms bunch duration is below 1 fs. Consequently, small changes of the bunch duration along the train can be accurately detected on the 1 fs scale. The uncertainty of the reconstructed rms bunch duration depends however on the current profile itself. For different bunch shapes, the sensitivity of the current profile reconstruction on the form factor measurement varies. In addition, also the sensitivity of the rms parameter itself depends on bunch shape. These effects lead to an uncertainty that is roughly two-times larger for the 2.2 MHz measurement.

The peak current is less sensitive to small variations at the low current regions of the longitudinal profile compared to the rms bunch duration and is shown in Fig. 7.18. The bunch-to-bunch fluctuations of the 2.2 MHz measurement are strongly reduced. Between the rf flat-tops, the peak current increases by more than 3 kA at the

1.1 MHz and around 2 kA at the 2.2 MHz measurement. This behaviour is consistent with the the rms bunch duration in Fig. 7.17. However, the peak current decreases by 1 kA along FT 2 of the 1.1 MHz measurement while the rms bunch duration shows much less variation. This is a simple demonstration showing that a single parameter of the current profile is not sufficient to describe the complex longitudinal electron beam dynamics at XFELs.

The CRISP spectrometer in combination with noninvasive diffraction radiation and the fast current profile reconstruction algorithm is a very powerful diagnostic for the electron bunch current profile at FELs operating in the hard X-ray regime. Within this thesis, the current profiles of all bunches inside the bunch train have been measured for the first time simultaneously to FEL user operation at European XFEL. As demonstrated, the spectrometer sensitivity and frequency range is well suited to resolve variations of the electron bunch compression not only between but also within the individual rf flat-tops. Using a single CRISP spectrometer measurement, the current profiles of all bunches can be reconstructed. The reconstruction requires only a few seconds to less than a minute on an usual office computer even for longest possible bunch trains. The result is impressively visualized in Fig. 7.19, where the form factors and current profiles of the 1.1 MHz and 2.2 MHz measurement along the bunch train are presented. The current profile reconstruction is robust and yields an unique insight into current profile evolution along the bunch train. For both measurements, the increasing bunch compression in the transition region between both rf flat-tops is well visible. The bunch duration decreases while the peak current increases. At the same time, the form factor extends to higher frequencies. Because the longitudinal current profile varies along the first  $\sim 50 \mu\text{s}$  of the bunch train, these bunches are not used for the generation of XFEL pulses during user operation. It is striking that the bunches inside rf flat-top FT 2, which are used for the SASE1/3 FEL undulator beamline, exhibit in both cases a higher peak current independently of the photon energy at the SASE2 FEL undulator beamline. This is the result of empiric SASE optimization. It is well imaginable that the kicker-septum arrangement for the SASE2 FEL undulator beamline further modifies the electron bunch properties even though it is designed to avoid further compression by its  $R_{56} = 0 \text{ mm}$  parameter [Abe+06].

## 7.4 Outlook

Current profile measurements during FEL user operation with femtosecond resolution for all bunches inside the bunch train, open up many possible applications for the CRISP spectrometer. The identified changes of the electron bunch compression within the rf flat-tops proof that the spectrometer is an ideal candidate for longitudinal – and especially intra bunch-train – feedbacks. Currently, bunch compression feedbacks utilize noninvasive beam energy measurements as a monitor for the rf amplitude and the bunch compression monitors (BCM, see Sec. 2.4.2) for the rf phase [Din18]. However, the single signal of a BCM does not give sufficient insight into the longitudinal beam dynamics to stabilize also the higher order parameters (curvature  $h'$ , third derivative  $h''$ ) besides the chirp  $h$  (see Eq. (2.10)) of the accelerating rf. Here, the spectrometer signals could help to identify proper feedback loops maybe even without the need for current profile reconstructions. Furthermore, the temporal structure of the FEL X-ray pulse is to a great part defined by the current profile [Beh+12]. For the analysis of experiments carried out with the X-ray FEL pulse,

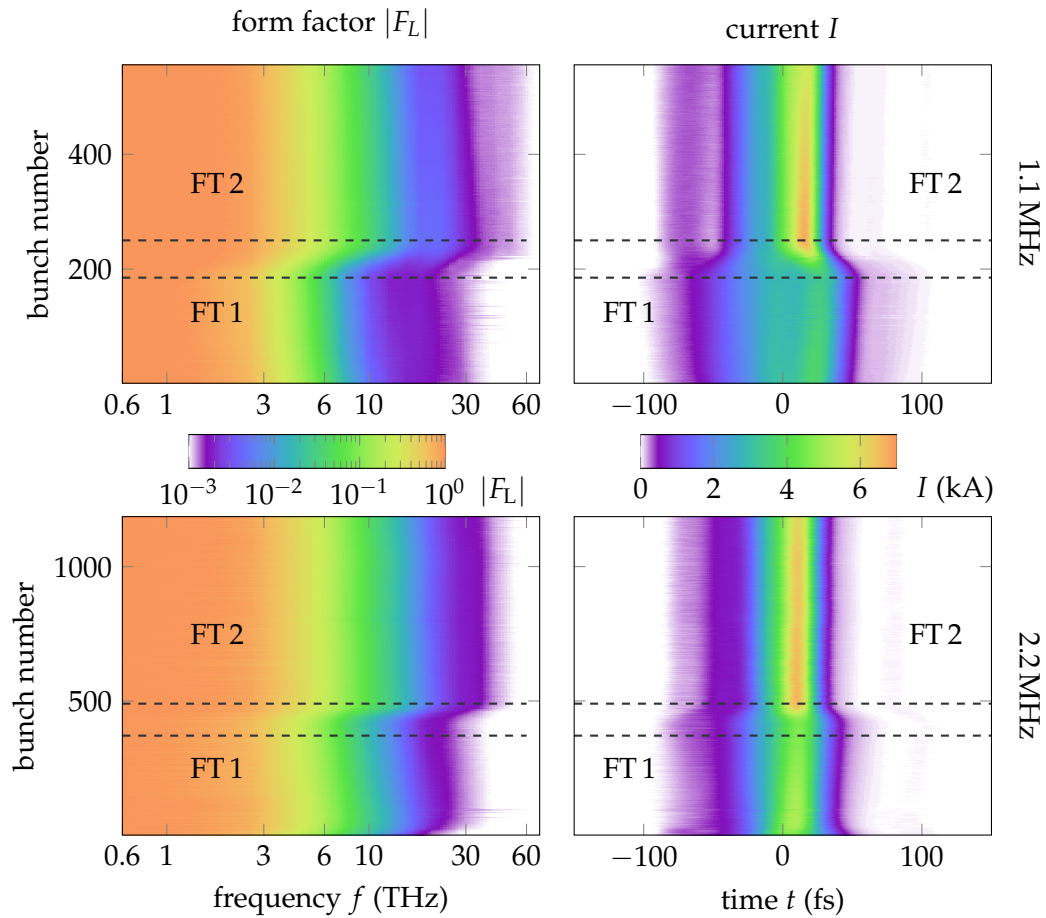


FIGURE 7.19: Form factors (left) and current profiles (right) of the reconstruction from CRISP measurements at 1.1 MHz and 2.2 MHz bunch repetition rate color-coded along the bunch trains. The combination of noninvasive diffraction radiation and CRISP spectrometer gains an unique insight into the evolution of the current profile along the bunch train during FEL user operation.

the reconstructed current profiles could thus be an important information [Düs+14]. The spectrometer data can also support the optimization and generation of shortest possible FEL pulses.

Currently, the pulse-shaping electronics allow the spectrometer to operate only with bunch repetition rates of up to 2.2 MHz. Nonetheless, it is promising that the readout electronics can be modified to operate also with 4.5 MHz repetition rate by exchanging the Gaussian shaping amplifiers (see Fig. 4.15) while maintaining sufficient sensitivity. Additionally, the pyroelectric detector may be replaced by a similar type<sup>1</sup> without polymer coating. This leads to a reduced sensitivity but at the same time shorter signals at the charge sensitive preamplifier [Beh08; Wes12]. This way, the pileup effect may be further reduced. In general, the spectrometer and pileup removal procedure can also be applied for continuous-wave (cw) operation. First studies using an infinite impulse response filter have shown promising results and allow very fast implementations of the pileup correction for intra bunch-train feedbacks [Dur20].

For a measurement of the form factor at both grating sets, the CRISP spectrometer requires roughly one minute because of the time needed to interchange the grating sets. The current profile reconstruction and data preparation are fast and require together roughly 20 ms on an usual office computer for each bunch. Consequently, the reconstruction of an entire bunch train takes less than one minute. However, for online current profile measurements while optimizing and/or changing the accelerator settings it would be desirable to carry out current profile reconstructions with the data from a single grating set while immediately displaying the results. Current profile reconstructions from the data of a single grating set and even single rf pulses are studied in App. C. The current profile reconstruction in its current – not yet explicitly for online measurements optimized – implementation as a Python module is in single-shot operation able to reconstruct five current profiles for each rf pulse on its 10 Hz pattern. Another approach would be to gather the data along a few rf pulses as a floating average and then update the current profile (or key parameters) of representative bunches along the rf pulse on a 10 Hz basis. Optimizing the current profile reconstruction routine for online measurements and distributing the numerical calculations on several CPUs/GPUs is a promising outlook for actual online current profile measurements on a single-shot basis for every bunch inside the rf pulse.

---

<sup>1</sup>based on Infratec LIE-301-X004

## Chapter 8

# Summary

The electron bunch current profile at European XFEL [Dec+20] is of fundamental importance for the FEL process and the required peak currents, but also the demand for ever shorter X-ray pulses, make diagnostics for the current profile inevitable to ensure a successful operation and optimization of the FEL facility. Far-infrared and THz spectroscopy of invasive transition radiation using the CRISP spectrometer [Wes+11] has demonstrated – also based on work carried out within the scope of this thesis – to be a powerful diagnostic for this application [Sch+20]. At European XFEL, the CRISP spectrometer is for the first time operated with noninvasive coherent diffraction radiation (CDR) in order to characterize the form factor of all bunches inside the bunch train, which is generated by a superconducting accelerator and exhibits megahertz (MHz) bunch repetition rates. Current profile measurements of these bunches have been realized in this thesis as follows:

The experimental setup consisting of DR screen, THz beamline and CRISP spectrometer has been installed, modeled and successfully commissioned. It has been shown that the spectral radiation intensity emitted at the diffraction radiation screen suits operation of the CRISP spectrometer. The DR screen does not influence accelerator or FEL performance while beam energies above 11 GeV do not lead to a frequency cut-off at the 5 mm aperture within the frequency range of the spectrometer (0.7 THz – 58 THz). The spectrometer's pulse-shaping electronics have been adapted for MHz bunch repetition rates.

The in-situ sensitivity of the CRISP spectrometer has been identified for the first time based on a systematic procedure. The procedure has utilized a transverse deflecting structure (TDS) and beam-based methods for adjustments of a modeled sensitivity. Nonetheless, the modeled sensitivity deviates only within the single grating stages from the experimentally identified sensitivity, while the overall evolution agrees. This underlines a good understanding of radiation emission, transport and detection.

A fast and reliable current profile reconstruction from the measured form factor modulus has been implemented, which is perfectly suited for online current profile monitoring. Its results for the CRISP spectrometer at European XFEL have been benchmarked with comparative measurements of a transverse deflecting structure (TDS) and a bunch compression monitor (BCM). Hereby, a calibration of the BCM signal with respect to the rms bunch duration has been investigated and carried out. Current profile reconstructions of bunches with rms durations of 6 fs to 100 fs have shown that CRISP at European XFEL covers the entire range of FEL user operation with bunch charges from 50 pC to 1 nC. The reconstructed current profiles exhibit features that could not be resolved with the TDS resolutions (>5 fs) even though it has been operated in a special high-resolution mode. The BCM only yields the overall bunch duration and not the current profile shape. In the regime of FEL user

operation, the key parameters (i.e. rms bunch duration, peak current) of all three diagnostics agree overall within  $\sim 15\%$  if the temporal resolution of the TDS is considered.

In order to realize current profile reconstructions of bunches with MHz repetition rates, the influence of signal pileup has to be removed. The pileup is caused by mechanical oscillations of the pyroelectric crystals, which themselves lead to characteristic frequencies in the MHz regime. A procedure to identify and eliminate the signal pileup for all channels of the spectrometer has been introduced. Comparative measurements along the bunch train with TDS and BCM have confirmed that the spectrometer in its current implementation is capable of form factor measurements up to bunch repetition rates of 2.2 MHz. Finally, the spectrometer has been used to identify variations of electron bunch compression along the bunch train during FEL user operation. Intentional variations introduced by different rf flat-tops for the individual FEL SASE beamlines but also unintentional variations of the bunch duration have been identified with a relative resolution below 1 fs along the bunch train during different operation modes of European XFEL.

In this thesis, noninvasive current profile measurements of electron bunches with MHz repetition rates and rms bunch durations down to a few femtoseconds ( $\sim 6$  fs) have been carried out for the first time at European XFEL. The CRISP spectrometer has been successfully adapted for MHz bunch repetition rates, before it has been installed and commissioned. In combination with further developments of a fast and reliable current profile reconstruction, it now becomes a standard tool for the operation and control of the FEL facility, which allows to characterize the current profile of more than 10 000 electron bunches per second. This thesis proves that CDR spectroscopy is a promising diagnostic for current profile measurements at the upcoming generation of hard X-ray FELs [Gal18; YD19]. The operation of XFELs in 'continuous-wave' (cw) mode with MHz bunch repetition rates benefits greatly from continuous and noninvasive monitoring.

## Appendix A

# Radiation Propagation Based on Fourier Transform

### A.1 Principle of Radiation Propagation

A method for fast numerical propagation of THz radiation for arbitrary non-cylindrical symmetries is presented in [CSS05]. It is based on two dimensional Fourier transform, which can be efficiently calculated by numerical methods. Starting point is the Huygens principle as in Eq. (3.21), but in Cartesian coordinates and without restriction to the x-axis

$$E_x(P, \omega) = -\frac{ik}{2\pi} \iint_{\text{source}} E_x(Q, \omega) \frac{e^{ikR'}}{R'} d\zeta d\eta. \quad (\text{A.1})$$

Hereby  $Q = (\zeta, \eta, 0)$  denotes the location on the source and  $P = (x, y, D)$  the point on the target, i.e. the location at which the electric field shall be calculated. For sake of compactness, only the horizontal field component will be explicitly derived. The vertical field component follows in a corresponding manner. The distance from source point to target point

$$R' = \sqrt{D^2 + (x - \zeta)^2 + (y - \eta)^2} = D \sqrt{1 + \frac{(x - \zeta)^2}{D^2} + \frac{(y - \eta)^2}{D^2}} \quad (\text{A.2})$$

is approximated using the binomial approximation  $(1 + x)^\alpha \approx 1 + \alpha x$  for small  $x$ . In our case, this represents the legitimate assumption that the transverse source and target dimensions are small compared to the distance between source and target. The resulting replacement

$$R' \approx D + \frac{x^2 + y^2}{2D} - \frac{x\zeta + y\eta}{D} + \frac{\zeta^2 + \eta^2}{2D} \quad (\text{A.3})$$

is inserted in Eq. (A.1) for the phase term only as the influence of the transverse displacement is negligible for the amplitude:

$$E_x(P, \omega) = -\frac{ik}{2\pi} \frac{\exp(ikD)}{D} \exp\left(\frac{ik}{2D}(x^2 + y^2)\right) \iint_{\text{source}} E_x(Q, \omega) \exp\left(ik\frac{\zeta^2 + \eta^2}{2D}\right) \exp\left(-ik\frac{x\zeta + y\eta}{D}\right) d\zeta d\eta. \quad (\text{A.4})$$

By introducing

$$k_x = k\frac{x}{D}, \quad k_y = k\frac{y}{D} \quad (\text{A.5})$$

and

$$G_x(\zeta, \eta) = E_x(\zeta, \eta, \omega) \exp\left(\frac{ik(\zeta^2 + \eta^2)}{2D}\right) \quad (\text{A.6})$$

the integral of Eq. (A.4) can be expressed by a two-dimensional Fourier transform

$$F_x(k_x, k_y) = \frac{1}{2\pi} \iint_{\text{source}} G_x(\zeta, \eta) \exp(-i(k_x\zeta + k_y\eta)) d\zeta d\eta. \quad (\text{A.7})$$

Using the properties of fast numerical Fourier transforms, the electric field at the position  $(Dk_x/k, Dk_y/k)$  on the target can be efficiently calculated while covering far-field and near-field diffraction. The expression for the vertical field component is similar, only  $G_x$  must be replaced by

$$G_y(\zeta, \eta) = E_y(\zeta, \eta, \omega) \exp\left(\frac{ik(\zeta^2 + \eta^2)}{2D}\right). \quad (\text{A.8})$$

## A.2 Optical Elements

This Fourier transform method also allows the implementation of optical elements with non-uniform surfaces for e.g. focusing. Due to the geometry of the focusing elements the electric field experiences a different path length depending on the transverse position. This is easily included by introducing the resulting phase shifts of the electric field at the surface of the focusing element, which depend on the transverse position and lead to focusing. A derivation of the phase shifts for many different elements obtained from their geometrical properties is given in [CSS05] and only the important phase shifts in the scope of this thesis will be stated here.

For the toroidal mirrors in the THz beamline with  $90^\circ$  deflection the phase shift amounts to

$$\Delta\phi_{\text{tor}} = k \left( -2f - \zeta + \sqrt{-\eta^2 - \zeta^2 + 2\sqrt{2}f \left( \sqrt{2f^2 - \eta^2} + \sqrt{2}\zeta \right)} \right) \quad (\text{A.9})$$

and for the ring mirrors inside the spectrometer, which are described by parabolic mirrors with direction away from focus, to

$$\Delta\phi_{\text{par}} = k \left( -f - \zeta + \sqrt{f^2 - \eta^2 + 2f\zeta} \right). \quad (\text{A.10})$$

The diamond window separating the accelerator vacuum from the secondary beamline has a wedge shape in order to minimize the interference of internal reflections. Nonetheless, the wedge shape leads to a deflection of the beam and internal reflections have to be considered. Their individual phase shifts still have to be taken into account as they also lead to some interference effects. In the numerical model, reflections up to the fourth order are considered as described in [Cas+06]. The first order mainly experiences a vertical kick of  $\theta_0 = (n_0 - 1)\alpha \approx 14.7 \text{ mrad}$  due to the wedge angle  $\alpha = 1^\circ$  of the window with an only slightly frequency dependent refraction index  $n_0$ .

Transverse deflections of the beam from the optical axis by – for example – tilted mirrors are introduced by adding a linear phase term in the respective transverse plane. For a horizontal deflection by an angle  $\theta_x$ , the additional phase is given by

$$\Delta\phi_{\text{kick}} = k\zeta \arctan \theta_x. \quad (\text{A.11})$$

### A.3 Numerical Implementation

Based on the mathematical procedure above, a dedicated Python code has been developed which is closely related to the Mathematica code *THz Transport* (see [CSS05]). It is used to compute the electric field of transition as well as diffraction radiation and for their transport through a setup of optical elements. The emitted transition or diffraction radiation of electron bunches with a transverse charge distribution that depends only on the distance to the center can be calculated. According to Gauss' law the electric field at any radial distance equals the electric field of a point-like particle with the enclosed charge. From this, the electric field of the bunch is numerically calculated on a fine grid covering the source coordinates  $(\zeta, \eta)$ . The electric field on the grid is set to zero for positions outside of the arbitrary TR/DR screen geometry. Finally, the horizontal and vertical electric field components at the target are calculated using two-dimensional Fourier transforms as in Eq. (A.7). Care must be taken in choosing the right span and step size of the source grid in order to cover the required target size with appropriate resolution. Especially for diffraction radiation in the IR region, many grid points are required. These high frequencies require a fine step size due to the small effective source size (Eq. (3.20)), but the grid span must still cover a sufficient part of the screen outside of the aperture.

The approach is similar for transport of radiation along the THz beamline or inside the CRISP spectrometer. The electric fields on the grid outside of the optical elements are set to zero, and the element specific phase shift is added at the source.



## Appendix B

# Resolution

As a fundamental consequence of the Fourier transform, the temporal resolution of the reconstructed current profile is closely linked to the frequency range of the measured form factor. For this reason, the appendix studies the temporal resolution of the reconstructed current profiles from CRISP spectrometer data based on the form factor processing illustrated in Sec. 6.1.1. The frequency range of the processed form factor depends on the overall sensitivity – thus also on radiation source and transport – but also on the current profile itself. External studies of the temporal resolution of CRISP (e.g. at FLASH) are not applicable at European XFEL. As demonstrated in Sec. 6.2, the transverse deflecting structure after the last bunch compressor does not yield sufficient temporal resolution to characterize the resolution limit of the CRISP spectrometer. The bunch compression monitors yield no information about the structure and shape of the current profile. Studies of the temporal resolution of the reconstructed current profiles at European XFEL can consequently only be carried out based on simulations. It should be noted again that the temporal resolution and accuracy of form factor measurements depend strongly on bunch charge and shape itself. The studied cases of this appendix are only examples to illustrate the origin of limitations. The sole purpose is to give a rough estimate for measurements with the CRISP spectrometer during European XFEL user operation. Nonetheless, it will be shown that the highest frequency of the measured form factor corresponds to an upper limit for resolvable current profile structures even though the detection of shorter bunches is possible.

In the first section, the reconstruction of overall bunch shapes and their key parameters are investigated in the simulation as the bunch duration decreases. In the second section, only a substructure with high peak current is varied while the overall bunch duration remains constant.

### B.1 Overall Bunch Shape

Three examples are used to represent different shapes of current profiles, which are illustrated on the left of Fig. B.1 for a rms bunch duration (see Eq. (5.8)) of  $\sigma_t = 20$  fs. These profiles are defined by a (a) Gaussian function, (b) a composition at the origin of two Gaussian functions with different durations<sup>1</sup> and (c) a result from a start-to-end simulation with prominent substructures (see Fig. 3.4). While the Gaussian profile represents an idealized case, the function of combined Gaussians resembles the typical asymmetry of bunch shapes recorded during FEL operation (see Chaps. 6, 7). The corresponding form factor moduli are depicted on the right of Fig. B.1. Of course, the emphasized features of the profiles are clearly encoded in the frequency

---

<sup>1</sup> $\exp\left(-\frac{(t-t_0)^2}{2\sigma_1^2}\right)$  for  $t < t_0$  and  $\exp\left(-\frac{(t-t_0)^2}{2\sigma_2^2}\right)$  for  $t \geq t_0$

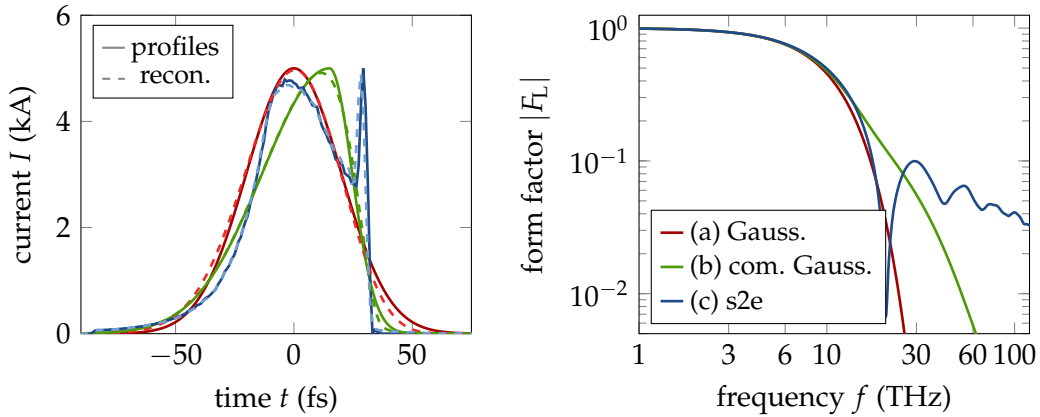


FIGURE B.1: Gaussian (a), composition of two Gaussian functions (b) and a current profile from start-to-end simulations (c) to study the spectrometer resolution. Current profiles as solid lines on the left and corresponding form factors on the right. The dashed lines on the left show the reconstructions from the calculated form factors.

domain. The form factor of the Gaussian profile is steeply and uniformly decreasing. While the profile of combined Gaussians is less steeply but still continuously decreasing, the form factor of the start-to-end simulation exhibits significant modulations above  $\sim 20$  THz. The current profiles reconstructed from the calculated form factors along the frequency range (1 THz – 250 THz) are illustrated as dashed lines on the left. The reconstruction method itself retrieves the current profiles to great level of detail if the form factor modulus is known over the entire frequency range and is not limited by the ambiguities associated to the Kramers-Kronig phase (see Sec. 3.3).

The rms bunch durations of the three profiles are successively decreased by rescaling the time axis, while the peak current remains at 5 kA – a typical design parameter for FEL user operation [Fen+]. The spectrometer measurement for these profiles are simulated using the in-situ sensitivity for DR at 15 GeV beam energy (see Fig. 5.9). The intrinsic detector noise is considered for the calculation of the confidence threshold and the shot-to-shot fluctuations. Variations of the current profile itself, which lead to larger shot-to-shot fluctuations in actual measurements, are not taken into account. The form factor processing and current profile reconstruction is carried out in the same way as for actual measurements (see Sec. 6.1.1). The resulting processed form factors as a simulated average of 50 rf pulses at both grating sets are presented in Fig. B.2 for 20 fs, 10 fs and 5 fs rms bunch duration. With decreasing bunch duration, the form factor measurement is limited to higher values of  $|F_L|$  itself. For one thing, the bunch charge decreases which leads to an increase of the confidence threshold. Secondly, the form factor cut-off shifts to higher frequencies and thus outside of the spectrometer frequency range. Information about high frequency components of the current profile are lost. A striking example are the oscillations of the form factor from the start-to-end simulation, which are not detected by the spectrometer for 5 fs rms bunch duration.

The reconstructed current profiles are compared to the input profile (dashed) in the right column of Fig. B.2. For 20 fs rms bunch duration, all profiles show a good agreement with the input profiles. Even though they are some differences, like the very short feature at the bunch head of the start-to-end profile, the overall shapes (i.e. duration, peak current, asymmetry) are retrieved. This short-time feature is encoded in the high frequencies of the form factor, which lie also for an overall rms

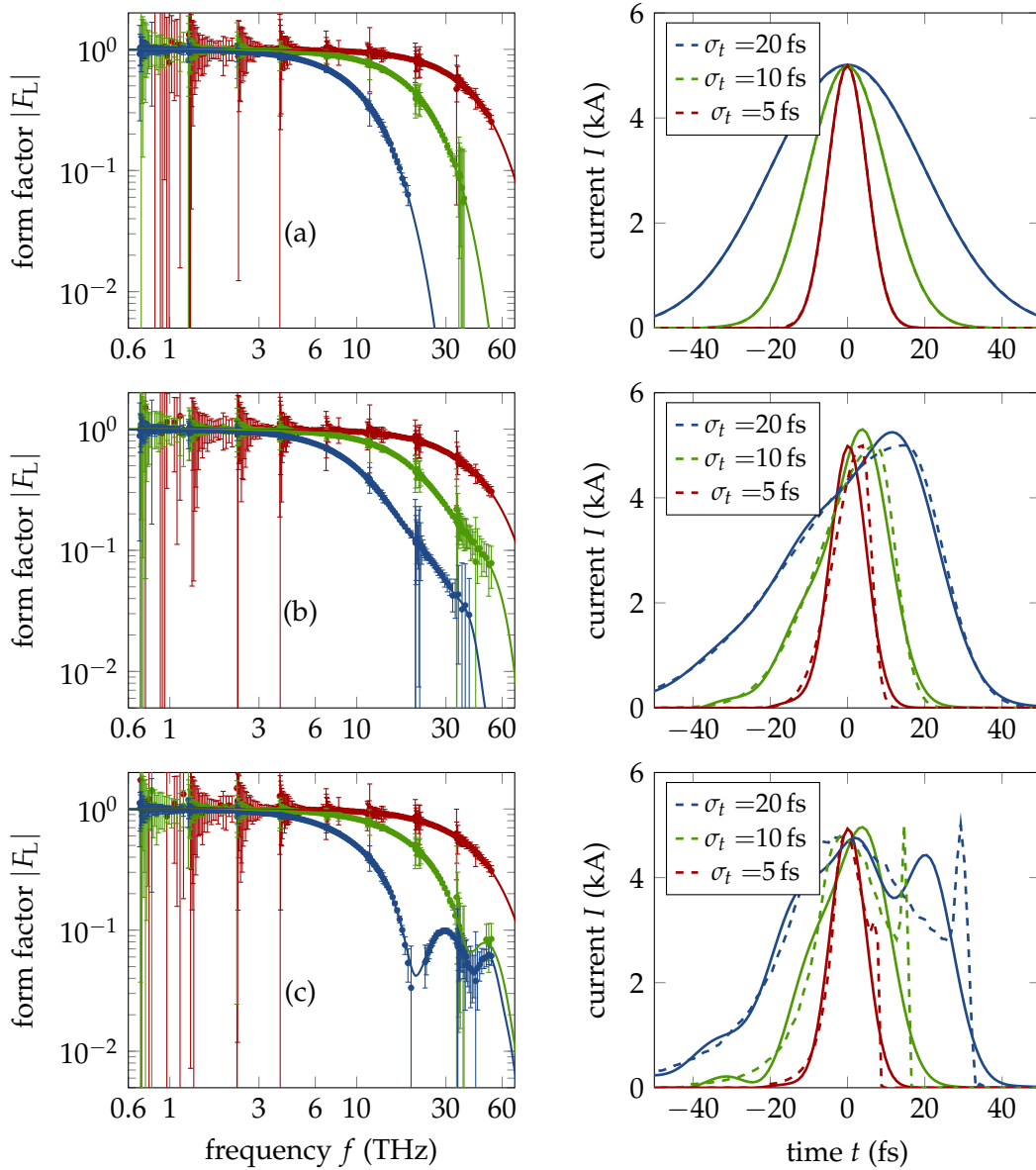


FIGURE B.2: Simulation of form factor measurements and current profile reconstructions for Gaussian (a, top), composition of Gaussian with different widths (b, center) and start-to-end simulation (c, bottom) current profiles. The dashed lines on the right illustrated the input current profiles and the solid lines the reconstructions. For Gaussian profiles (a), the reconstructions overlap perfectly with the input profiles. The form factors of the reconstructions are compared to the simulated form factor measurement and depicted as solid lines as well.

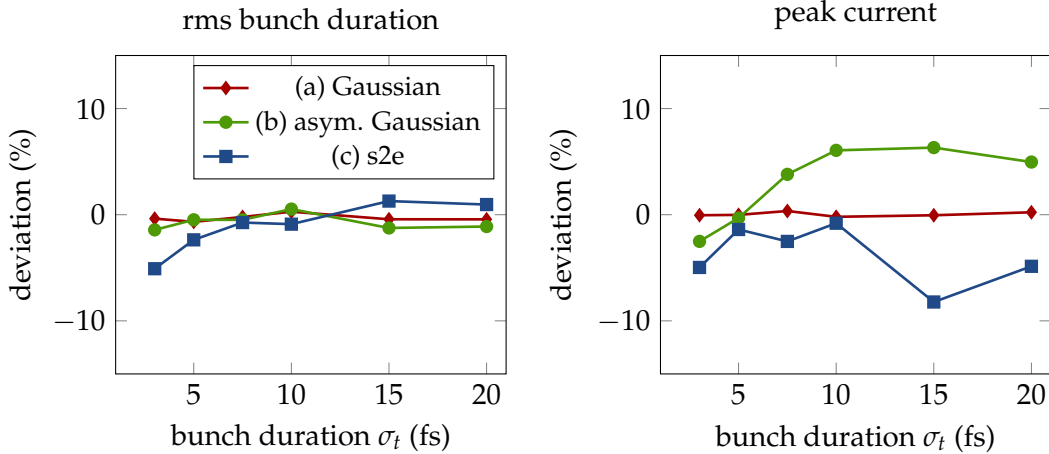


FIGURE B.3: Relative deviation of reconstructed rms bunch duration (left) and peak current to the input as function of rms bunch duration. Down to bunch duration of 3 fs, the key parameters rms bunch duration and peak current are determined with less than 10% deviation. Smaller bunch durations can due to dominating detector noise of these profiles at 5 kA peak current not be reconstructed.

bunch duration of 20 fs outside of the form factor measurement. If the form factor would have been measured up to higher frequencies, the feature would have been correctly retrieved (see Fig. B.1). Comparable features are studied in detail in the second section of this appendix. The shorter the profiles get, the more frequency components of their characteristic features shift outside of the spectrometer range. As a consequence, the reconstructed profile can be understood as the input missing short time scale features. At 5 fs rms bunch duration, the form factors can only be measured down to  $|F_L| \approx 0.3$  and are thus mainly described by the Gaussian extrapolation (see Sec. 6.1.1). Consequently, also the current profile reconstructions only yield Gaussian profiles. Judging from Fig. B.2, the correct reconstruction of the overall shape and asymmetry is limited to roughly 10 fs rms bunch duration at 5 kA peak current. Nonetheless, peak current and overall duration are well retrieved even for shorter bunch duration.

Figure B.3 shows the relative deviation of the reconstructed rms bunch duration and peak current to the input profiles along an even wider range of input rms bunch durations. In contrast to the resolution of time domain measurements – like e.g. a transverse deflecting structure –, the limited frequency region does not change these parameters. For these bunch shapes without high current substructures, rms bunch duration and peak current are correctly ( $< 10\%$ ) retrieved down to 3 fs. However, the reconstruction of such short bunches always yields a Gaussian profile and the overall bunch shape cannot be retrieved. As the measured form factor region (not only the frequency region) is affected by the charge dependent confidence threshold and bunch duration, the deviations of the reconstructed profile are not constant along the range of simulated bunch durations. Also at longer bunch duration ( $\sigma_t \approx 20$  fs), the form factor shift to lower frequencies in combination with the complex frequency dependency of the confidence threshold does not necessarily lead to a form factor measurement range sufficient to reconstruct every detail of the current profile.

The limitation for reconstructions of shortest rms bunch durations is given by the accuracy of form factor measurements. As the reconstruction is dominated by the Gaussian form factor extrapolation, it requires an accurate fit to the marginally

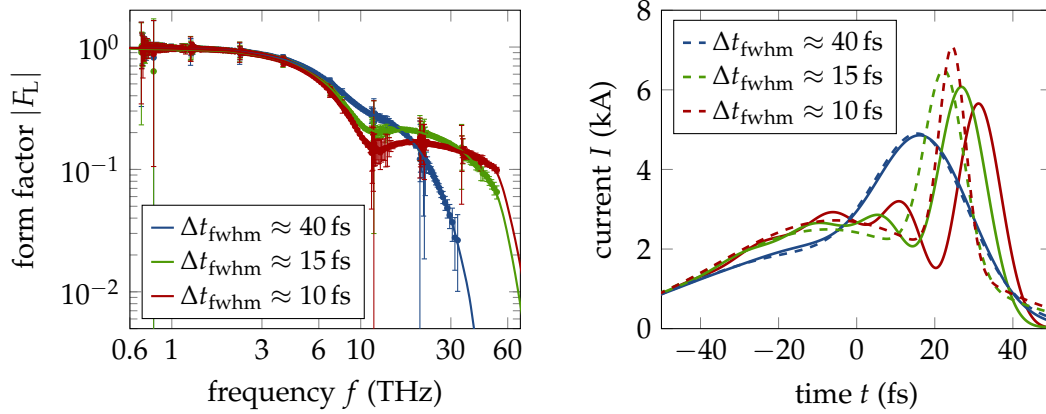


FIGURE B.4: Simulation of form factor measurements and current profile reconstructions for current profiles with a pronounced peak of high current ('spike') described by the fwhm duration  $\Delta t_{\text{fwhm}}$ . The profile has been modeled based on a superposition of two Gaussian functions. The dashed lines on the right show the input functions and the solid lines the reconstructions.

changing form factor along the spectrometer range. At a peak current of 5 kA, the detector noise is too dominant to allow a fit for bunches with less than 3 fs rms bunch duration (bunch charge  $Q < 30$  pC). For actual measurements this limit might be slightly larger due to additional fluctuations caused by the bunches themselves.

## B.2 Pronounced Peaks with High Current

While in the first section, overall shapes have been studied, the focus lies now on substructures with high current. They are especially important as high currents are not only fundamentally affecting the FEL process (see Chap. 1) but also have severe influence on collective effects and thus the overall stability of accelerator and FEL operation.

Here, a high current substructure is modeled by the superposition of two Gaussian functions

$$I(t) = a_1 \cdot \exp\left(\frac{-t^2}{2\sigma_{t,1}^2}\right) + 2a_1 \cdot \exp\left(\frac{-(t - t_2)^2}{2\sigma_{t,2}^2}\right). \quad (\text{B.1})$$

The amplitude  $2a_1$  of the second Gaussian is two times higher, which leads to the profiles presented by the dashed lines on the right of Fig. B.4. This time, the bunch charge of 250 pC and the duration  $\sigma_{t,1} = 30$  fs of the Gaussian profile with less amplitude remains constant, while the duration  $\sigma_{t,2}$  of the second Gaussian is progressively decreased. The separation  $t_2 = 30$  fs is fixed. The resulting substructure ('spike') of the current profile is defined by the fwhm bunch duration  $\Delta t_{\text{fwhm}}$ . The simulated form factor measurements of these current profiles are depicted on the left of Fig. B.4. In comparison to the previous section, the overall form factor does not only shift to higher frequencies. Instead, the spike with high current additionally modifies the form factor, which becomes more pronounced at short spike durations.

The current profiles reconstructed from the simulated measurement are depicted as solid lines on the right of Fig. B.4 and their form factors compared to the simulated measurement by the solid lines on the left. The overall shape (duration, asymmetry) of the reconstructed current profiles agrees with the analytical functions and also the

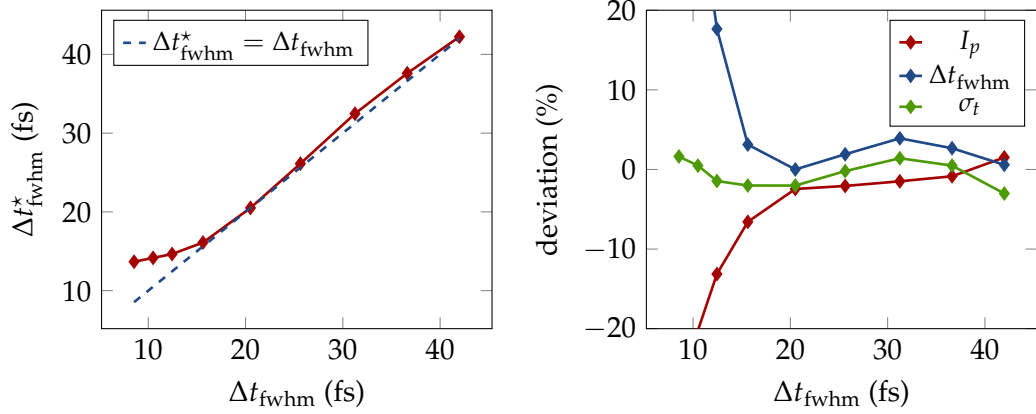


FIGURE B.5: Correlation of spike duration  $\Delta t_{fwhm}^*$  of the reconstruction to spike duration  $\Delta t_{fwhm}$  of the input function (left, red). Relative deviations of key parameters from the reconstructed to the input current profile with high current spike (right).

presence of a high current spike is retrieved. The temporal offsets of the spike position are caused by the Kramers-Kronig phase as input to the iterative current profile reconstruction (see Sec. 3.3) and also occur when the form factor is exactly known along its entire frequency range. In this section however, the focus lies on spike duration and peak current: As the input spike duration decreases, the deviations of the reconstructed spike increase.

The reconstructed fwhm spike duration  $\Delta t_{fwhm}^*$  as function of the actual spike duration  $\Delta t_{fwhm}$  is shown on the left of Fig. B.5. Down to peak spike durations of roughly 15 fs ( $\sim 6.5$  fs rms), the reconstructed spike duration follows the input function illustrated by the dashed line. At shorter durations, the high frequency limit of the spectrometer is not sufficient anymore to cover the spike's spectral shape. As a consequence, the spike width, but also the peak current as demonstrated on the right of Fig. B.5, remains approximately constant. Nonetheless, the overall rms bunch duration  $\sigma_t$  is still correctly ( $< 10\%$ ) retrieved.

The results of this appendix indicate that the overall shape of current profiles is well retrieved down to rms bunch durations of roughly 10 fs during FEL operation with 5 kA peak current. Nonetheless, the rms bunch duration can be monitored to even smaller values around 3 fs. The same holds for the peak current if the profiles do not contain pronounced structures with high peak current. Otherwise, these regions can be resolved down to roughly 6.5 fs rms duration if the form factor has been identified along the entire spectrometer range. The highest spectrometer frequency of  $f_{\max} \approx 60$  THz translates to a sampling of  $\Delta t = 1/2f_{\max} = 8$  fs in time domain and is in accordance with the duration of the resolved spike: The highest frequency of the form factor measurement yields an estimation for the upper limit of resolvable current profile features as expected from the sampling theorem.

## Appendix C

# Online Measurements

As mentioned in the outlook (Sec. 7.4), it would be desirable for many applications, but also for a machine optimization and tuning, to reconstruct the current profile from one grating set alone. This would allow a constant monitoring of the current profile without the waiting time of roughly one minute, which is needed to interchange the grating set. A single grating set operation would potentially also allow single shot operation of the spectrometer without averaging the signals. The knowledge of the current profile of every lasing bunch (i.e. within bunch train and each rf pulse), is of great advantage for the analysis of experiments with XFEL pulses on ultrashort time scales (fs) [Düs+14]. Possible correlations between experimental FEL data and electron bunch current profile could help to characterize the underlying ultra-fast processes.

In this appendix, both possibilities for the CRISP spectrometer at European XFEL utilizing DR at FEL user operation are investigated.

### C.1 Single Grating Set Operation

In order to study the single grating operation of the CRISP spectrometer, form factor measurements from the TDS comparison in Fig. 6.2 are investigated. Two of these form factor measurements at 250 pC bunch charge, which exhibit typical durations for FEL user operation but distinct profiles (see Sec. 6.2), are presented in Fig. C.1. The dashed line marks the separation of THz and FIR spectrometer grating set at  $\sim 6.6$  THz. The presented form factors are an average of 20 rf pulses and the error bars mark the corresponding rms shot-to-shot fluctuations. Using a single grating set, the form factor measurement is significantly restricted. On the one hand, the form factor modulus at the THz grating set does not decrease to values small enough to adequately describe the structure of the current profile. The THz grating set is thus not suited for current profile reconstruction and may only be used to determine the overall bunch duration (see App. B). On the other hand however, the FIR grating set denies a measurement down to the asymptotic limit  $|F_L(0)| = 1$  at low frequencies.

For single grating set operation, the measured form factors of the FIR grating set are extrapolated by a Gaussian function as described in Sec. 6.1.1 to  $|F_L(0)| = 1$  based on a fit to the data points at the lowest frequency channels. This yields a very good approximation of the measured form factor along the THz grating set for both settings as demonstrated by the dashed lines in Fig. C.1. Variations from the measurement at the THz grating set are barely visible.

The current profiles reconstructed only from the extrapolated FIR grating set data are compared for both bunch compression settings to the reconstructions based on the complete data set in Fig. C.2. The form factors of the reconstructed current profiles (solid lines in Fig. C.1) are in good agreement to the measurement using both

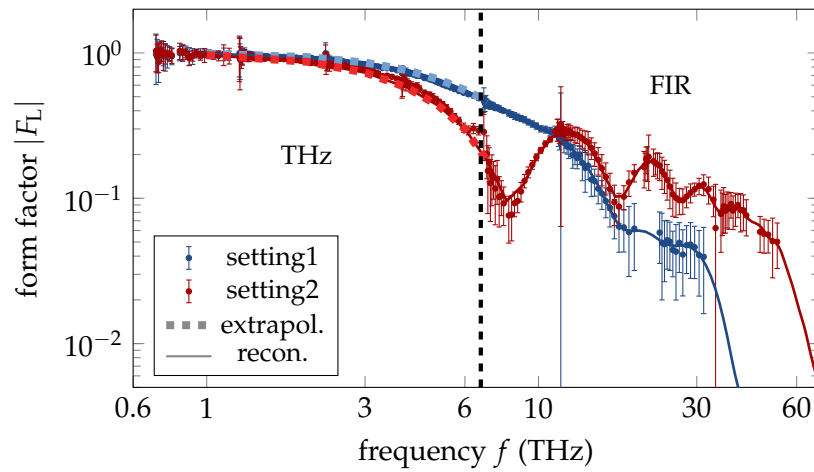


FIGURE C.1: Form factors measured with the CRISP spectrometer using coherent diffraction radiation of bunches with distinct current profiles. The form factors at the THz grating set (divided by the dashed vertical line) can be well approximated by a Gaussian extrapolation. The form factors of the reconstructed current profiles (Fig. C.2) are illustrated by solid lines.

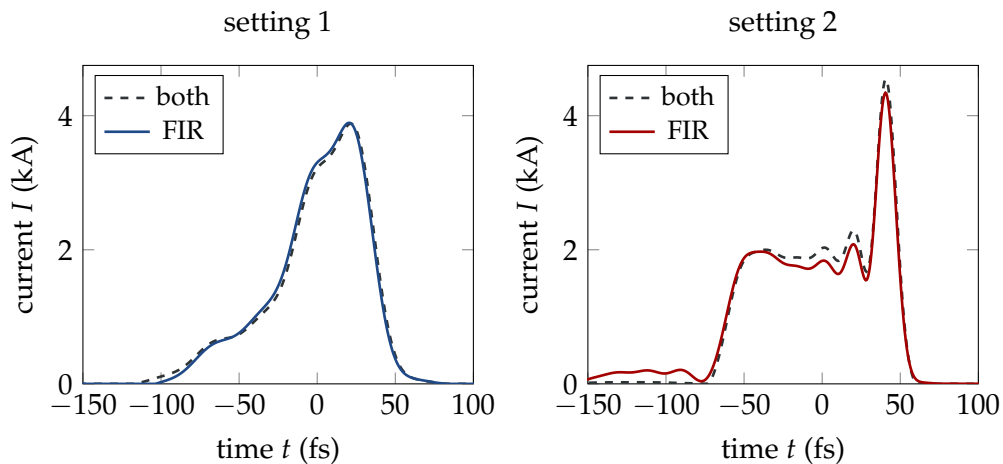


FIGURE C.2: Reconstructed current profile based on data of the FIR grating set compared to reconstruction based on both grating sets. For bunches with around 5 kA peak current – typical for FEL user operation –, the FIR grating set is sufficient to retrieve the structure of current profiles with 250 pC charge.

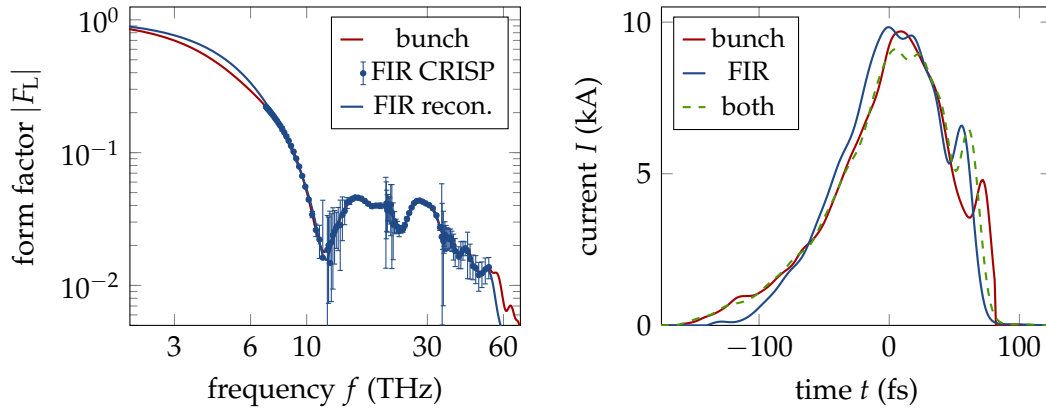


FIGURE C.3: Simulated form factor measurement and current profile reconstruction of a bunch from start-to-end simulations with long bunch durations ( $Q = 1$  nC). The FIR grating set is, even for longest expected bunch duration at XFEL user operation, sufficient to retrieve the current profile with its characteristic features.

grating sets. However, minor misconducts at low frequencies lead to small deviations of the form factor on large time scales for both settings. Large time scales mean that neither shape or peak current are significantly altered but low current regions at head/tail of the bunch are modified. The pedestal of setting 2 is a striking example. Nonetheless, these two distinct profiles – with partially exotic current profiles (setting 2) – demonstrate that single grating operation of the CRISP spectrometer allows an accurate retrieval of the current profile at 250 pC bunch charge during FEL user operation.

Short bunches at the low charge end of the range of European XFEL user operation are even more favorable for measurements with the FIR grating set alone. In this case, the form factor has almost reached its asymptotic limit  $|F_L(0)| = 1$  at the FIR grating set (see Fig. 3.4). A contrary example for long bunches during FEL user operation is the start-to-end simulation for 10 kA peak current at 1 nC bunch charge. The current profile and its form factor are presented by the red curves in Fig. C.3. A CRISP form factor measurement of this current profile is simulated in the same way as in App. B, but this time once for FIR grating set alone and once with both grating sets. The resulting form factor and shot-to-shot fluctuations obtained as the simulated average of 50 rf pulses at the FIR grating set are illustrated on the left of Fig. C.3. The current profile reconstructions based on the simulated form factor measurements for both cases are compared to the bunch's current profile on the right. With and without consideration of the THz grating set, the current profile structure is well retrieved. The minor deviation of the extrapolation from the bunch's form factor at the THz grating set leads again to small differences between both reconstructions on large time scales. The low current tail ( $t < 0$ ) of the bunch decreases slightly faster, which nonetheless has only minor consequences on overall shape and key parameters like peak current.

In the entire range of expected current profiles for FEL user operation, the FIR grating set of the spectrometer is sufficient for current profile reconstructions. As demonstrated with measurements and simulations, the minor deviations of the form factor extrapolation at the THz grating set to the actual form factor have no severe influence on the structure of the reconstructed current profiles.

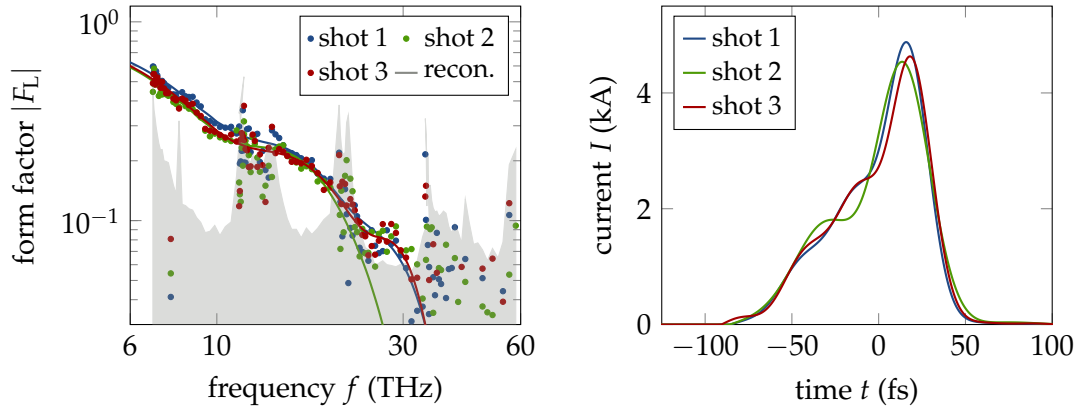


FIGURE C.4: Measured form factor (left) of single shots (rf pulses) at the FIR grating set during FEL operation. The gray area shows the single shot confidence threshold  $\mathcal{L}(f_m)$ . The solid lines mark the form factors of the reconstructed current profiles (right). Duration and overall shape of the reconstructed current profiles are similar and exhibit only small fluctuations.

## C.2 Single Shot Operation

Current profile reconstructions using a single grating set also open up the possibility to reconstruct the current profile from single shots (rf pulses). The left of Fig. C.4 presents the measured form factors of single shots during FEL user operation with 250 pC bunch charge. Hereby, the bunch charge of each rf pulse has been measured to ensure a proper calculation of the form factor for each bunch regardless of charge fluctuations. There are visible shot-to-shot fluctuations of the measured form factors. Adjacent channels show a conclusive increasing or decreasing behaviour. Consequently, the form factor variations are not dominated by detector noise, but by fluctuations of the electron bunch compression itself. Only in regions close to the gray illustrated single shot confidence threshold  $\mathcal{L}(f_m)$  of  $2\sigma$  detector noise (see Eq. (5.6)), the single shot form factors exhibit large deviations. These measurement points are anyhow not considered in the current profile reconstruction (see Sec. 6.1.1) and are only presented here for illustration purposes. Instead of shot-to-shot fluctuations, the allowed variations of the iterative algorithm are limited to 10% of the form factor. The right hand side of Fig. C.4 shows the resulting reconstructions. Overall shape (duration, asymmetry) and peak current of the single shots are similar and show only small fluctuations. The form factors of the reconstructions (left, solid lines) are in good agreement to the respective measurement and conclusive to the measured variations of the individual shots.

The form factor obtained from the mean spectrometer signals measured over  $N = 50$  shots (rf pulses) and the corresponding shot-to-shot fluctuations are compared on the left of Fig. C.5 to the form factors of the reconstructed current profiles of some individual shots. The calculation of the mean reduces the confidence threshold such that the form factor is characterized up to higher frequency than for a part of individual shots. The increasing confidence threshold above 30 THz (see Fig. C.4 left) however is still the limiting factor for the mean spectrometer measurement and the confidence threshold only scales with  $N^{-1/4}$  (see Eq. (5.6)). As a result, the frequency range is only marginal wider than in single shot operation. Apart from shifts of the starting frequency for the Gaussian extrapolation towards higher frequencies

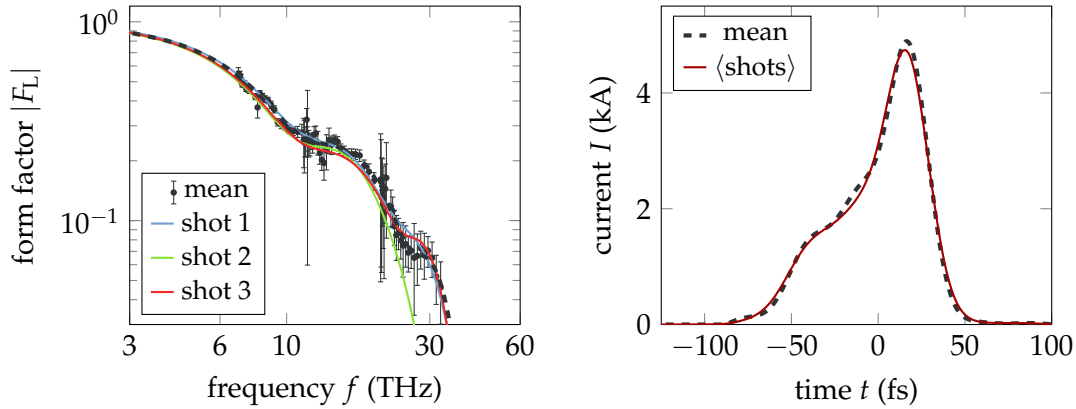


FIGURE C.5: Form factor measurement (left) obtained from the measured mean spectrometer signal over 50 shots (rf pulses) at the FIR grating set compared to the form factors of the single shot reconstructions in Fig. C.4. The average of the reconstructed single shot current profiles (right) yields a similar result than the reconstruction from the mean spectrometer signals. As the level of detail is comparable, single shot operation of the spectrometer does not lead to severe restrictions for current profile reconstruction at 250 pC user operation.

(see Sec. 6.1.1), the reconstructions of the individual rf pulses are within the error bars of the mean measurement.

The right hand side of Fig. C.5 illustrates the current profile of the mean spectrometer signals and the average of the current profiles from each shot. Both averages exhibit a similar current profile with only minor variations and comparable level of detail. Single shot form factor measurements at 250 pC FEL user operation do thus not lead to significant drawbacks in the current profile reconstruction. Peak current and rms bunch duration of the single shots exhibit less than 4% rms fluctuations. In regard of 1.5% shot-to-shot charge fluctuation, these fluctuations demonstrate sufficient robustness and sensitivity of single shot current profile reconstruction using the CRISP spectrometer based on noninvasive DR at European XFEL.



# Bibliography

- [Abe+06] R. Abela et al. *XFEL: The European X-Ray Free-Electron Laser - Technical Design Report*. 2006. DOI: 10.3204/DESY\_06-097.
- [Ack+07] W. Ackermann et al. "Operation of a free-electron laser from the extreme ultraviolet to the water window". In: *Nature Photonics* 1 (2007), pp. 336–342. DOI: 10.1038/nphoton.2007.76.
- [Akr+01] R. Akre et al. "A transverse rf deflecting structure for bunch length and phase space diagnostics". In: *Proceedings of the Particle Accelerator Conference*. 2001, pp. 2353–2355. DOI: 10.1109/PAC.2001.987379.
- [Aku56] E. J. Akutowicz. "On the Determination of the Phase of a Fourier Integral, I". In: *Transactions of the American Mathematical Society* 83.1 (1956), p. 179. DOI: 10.2307/1992910.
- [AM11] J. Als-Nielsen and D. McMorrow. *Elements of Modern X-ray Physics*. Wiley, 2011. DOI: 10.1002/9781119998365.
- [And+09] G. Andonian et al. "Observation of coherent terahertz edge radiation from compressed electron beams". In: *Physical Review Special Topics - Accelerators and Beams* 12.030701 (2009). DOI: 10.1103/PhysRevSTAB.12.030701.
- [And+14] H. L. Andrews et al. "Reconstruction of the time profile of 20.35 GeV, subpicosecond long electron bunches by means of coherent Smith-Purcell radiation". In: *Physical Review Special Topics - Accelerators and Beams* 17.052802 (2014). DOI: 10.1103/PhysRevSTAB.17.052802.
- [Aun+00] B. Aune et al. "Superconducting TESLA cavities". In: *Physical Review Special Topics - Accelerators and Beams* 3.092001 (2000). DOI: 10.1103/PhysRevSTAB.3.092001.
- [Ayv+02] V. Ayvazyan et al. "Generation of GW Radiation Pulses from a VUV Free-Electron Laser Operating in the Femtosecond Regime". In: *Physical Review Letters* 88.104802 (2002). DOI: 10.1103/PhysRevLett.88.104802.
- [Bah11] J. Bahrtdt. "Pushing the limits of short period permanent magnet undulators". In: *Proceedings of the 33rd International Free Electron Laser Conference*. Shanghai, China: THOAI1, 2011, pp. 435–442.
- [Baj+13] S. I. Bajlekov et al. "Longitudinal electron bunch profile reconstruction by performing phase retrieval on coherent transition radiation spectra". In: *Physical Review Special Topics - Accelerators and Beams* 16.040701 (2013). DOI: 10.1103/PhysRevSTAB.16.040701.
- [BN85] R. Barakat and G. Newsam. "Algorithms for reconstruction of partially known, band-limited Fourier-transform pairs from noisy data". In: *Journal of the Optical Society of America A* 2.11 (1985), pp. 2027–2039. DOI: 10.1364/JOSAA.2.002027.

- [Beh08] C. Behrens. "Detection and Spectral Measurements of Coherent Synchrotron Radiation at FLASH". Diploma thesis. Universität Hamburg, 2008.
- [Beh+12] C. Behrens et al. "Constraints on photon pulse duration from longitudinal electron beam diagnostics at a soft x-ray free-electron laser". In: *Physical Review Special Topics - Accelerators and Beams* 15.030707 (2012). DOI: 10.1103/PhysRevSTAB.15.030707.
- [Beu+06] B. Beutner et al. "Beam dynamics experiments and analysis on CSR effects at FLASH". In: *Proceedings of 28th International Free Electron Laser Conference*. Berlin, Germany: MOPPH009, 2006, pp. 56–58.
- [BPN84] R. Bonifacio, C. Pellegrini, and L.M. Narducci. "Collective instabilities and high-gain regime in a free electron laser". In: *Optics Communications* 50.6 (1984), pp. 373–378. DOI: 10.1016/0030-4018(84)90105-6.
- [BFH18] S. Boutet, P. Fromme, and M. Hunter. *X-ray Free Electron Lasers*. Springer, 2018. DOI: 10.1007/978-3-030-00551-1.
- [Bri+14] R. Brinkmann et al. "Prospects for CW and LP operation of the European XFEL in hard X-ray regime". In: *Nuclear Instruments and Methods in Physics Research Section A: Accelerators, Spectrometers, Detectors and Associated Equipment* 768 (2014), pp. 20–25. DOI: 10.1016/j.nima.2014.09.039.
- [CSS05] S. Casalbuoni, B. Schmidt, and P. Schmüser. *Far-infrared transition and diffraction radiation. I : Production, diffraction effects and optical propagation*. TESLA Report 2005-15, 2005.
- [Cas+06] S. Casalbuoni et al. *Far-infrared transition and diffraction radiation. II : The THz beamline at the VUV-FEL linac*. TESLA-FEL 2006-04, 2006.
- [Cas+09] S. Casalbuoni et al. "Ultrabroadband terahertz source and beamline based on coherent transition radiation". In: *Physical Review Special Topics - Accelerators and Beams* 12.030705 (2009). DOI: 10.1103/PhysRevSTAB.12.030705.
- [Cas+01] M. Castellano et al. "Measurements of coherent diffraction radiation and its application for bunch length diagnostics in particle accelerators". In: *Physical Review E* 63.056501 (2001). DOI: 10.1103/PhysRevE.63.056501.
- [Cha93] A. Chao. *Physics of Collective Beam Instabilities in High Energy Accelerators*. Wiley, 1993.
- [CZD20] Y. Chen, I. Zagorodnov, and M. Dohlus. "Beam dynamics of realistic bunches at the injector section of the European X-ray Free-Electron Laser". In: *Physical Review Accelerators and Beams* 23.044201 (2020). DOI: 10.1103/PhysRevAccelBeams.23.044201.
- [CJ18] D. Chenevier and A. Joly. "ESRF: Inside the Extremely Brilliant Source Upgrade". In: *Synchrotron Radiation News* 31.1 (2018), pp. 32–35. DOI: 10.1080/08940886.2018.1409562.
- [Cra+20] P. Craievich et al. "Novel X -band transverse deflection structure with variable polarization". In: *Physical Review Accelerators and Beams* 23.112001 (2020). DOI: 10.1103/PhysRevAccelBeams.23.112001.

- [Cur+20] A. Curcio et al. "Noninvasive bunch length measurements exploiting Cherenkov diffraction radiation". In: *Physical Review Accelerators and Beams* 23.022802 (2020). DOI: 10.1103/PhysRevAccelBeams.23.022802.
- [Cus+20] Tânia F. Custódio et al. "Selection, biophysical and structural analysis of synthetic nanobodies that effectively neutralize SARS-CoV-2". In: *Nature Communications* 11.1 (2020). DOI: 10.1038/s41467-020-19204-y.
- [de 26] R. de L. Kronig. "On the Theory of Dispersion of X-Rays". In: *Journal of the Optical Society of America* 12.6 (1926), p. 547. DOI: 10.1364/JOSA.12.000547.
- [Dec+20] W. Decking et al. "A MHz-repetition-rate hard X-ray free-electron laser driven by a superconducting linear accelerator". In: *Nature Photonics* 14 (2020), pp. 391–397. DOI: 10.1038/s41566-020-0607-z.
- [DW17] Winfried Decking and Hans Weise. "Commissioning of the European XFEL Accelerator". In: *Proceedings of the 8th International Particle Accelerator Conference*. Copenhagen, Denmark: MOXAA1, 2017. DOI: 10.18429/JACoW-IPAC2017-MOXAA1.
- [DH08] H. Delsim-Hashemi. "Infrared Single Shot Diagnostics for the Longitudinal Profile of the Electron Bunches at FLASH". Dissertation. Universität Hamburg, 2008. DOI: 10.3204/DESY-THESIS-2008-024.
- [Der+95] Y. Derbenev et al. *Microbunch radiative tail-head interaction*. TESLA-FEL 95-05, 1995. DOI: 10.3204/PUBDB-2018-04128.
- [Dia] Diamond Materials GmbH Web Page. <https://www.diamond-materials.com/>.
- [Din18] H. Dinter. "Longitudinal Diagnostics for Beam-Based Intra Bunch-Train Feedback at FLASH and the European XFEL". Dissertation. Universität Hamburg, 2018. DOI: 10.3204/PUBDB-2018-03166.
- [DL97] M. Dohlus and T. Limberg. "Emittance growth due to wake fields on curved bunch trajectories". In: *Nuclear Instruments and Methods in Physics Research Section A: Accelerators, Spectrometers, Detectors and Associated Equipment* 393.1-3 (1997), pp. 494–499. DOI: 10.1016/S0168-9002(97)00552-4.
- [DL05] M. Dohlus and T. Limberg. "Bunch compression stability dependence on RF parameters". In: *Proceedings of the 27th International Free Electron Laser Conference*. August. Stanford, USA: TUOB004, 2005, pp. 250–253.
- [DLE05] M. Dohlus, T. Limberg, and P. Emma. "Bunch Compression for Linac-based FELs". In: *ICFA Beam Dynamics Newsletter* 38 (2005), pp. 15–50.
- [Dun18] Mike Dunne. "X-ray free-electron lasers light up materials science". In: *Nature Reviews Materials* 3.9 (2018), pp. 290–292. DOI: 10.1038/s41578-018-0048-1.
- [Dur20] B. Dursun. *Private communication*. 2020.
- [Düs+14] S. Düsterer et al. "Development of experimental techniques for the characterization of ultrashort photon pulses of extreme ultraviolet free-electron lasers". In: *Physical Review Special Topics - Accelerators and Beams* 17.120702 (2014). DOI: 10.1103/PhysRevSTAB.17.120702.
- [Dwe+97] B. Dwersteg et al. "RF gun design for the TESLA VUV Free Electron Laser". In: *Nuclear Instruments and Methods in Physics Research Section A: Accelerators, Spectrometers, Detectors and Associated Equipment* 393.1-3 (1997), pp. 93–95. DOI: 10.1016/S0168-9002(97)00434-8.

- [Eck12] M. Eckert. "Max von Laue and the discovery of X-ray diffraction in 1912". In: *Annalen der Physik* 524.5 (2012), A83–A85. DOI: 10.1002/andp.201200724.
- [Eld+47] F. R. Elder et al. "Radiation from Electrons in a Synchrotron". In: *Physical Review* 71.11 (1947), pp. 829–830. DOI: 10.1103/PhysRev.71.829.5.
- [EFK00] P. Emma, J. Frisch, and P. Krejcik. *A transverse RF deflecting structure for bunch length and phase diagnostic*. Tech. rep. TN-00-12, SLAC, 2000.
- [Eur] European XFEL GmbH Web Page. *www.xfel.eu*.
- [Fen+] G. Feng et al. *Beam Dynamics Simulations for European XFEL*. TESLA-FEL 2013-04. DOI: 10.3204/PUBDB-2018-03653.
- [FMP13] M. Ferrario, M. Migliorati, and L. Palumbo. "Space charge effects". In: *Proceedings of the CAS-CERN Accelerator School: Advanced Accelerator Physics* 009 (2013), pp. 331–356. DOI: 10.5170/CERN-2014-009.331.
- [Fie78] J. R. Fienup. "Reconstruction of an object from the modulus of its Fourier transform". In: *Optics Letters* 3.1 (1978), p. 27. DOI: 10.1364/OL.3.000027.
- [FSZ13] N. Ford, D. V. Savostyanov, and N. L. Zamarashkin. "On the decay of elements of inverse triangular Toeplitz matrix". In: *SIAM Journal on Matrix Analysis and Applications* 35(4): (2013), 35:1288–1302(2014). DOI: 10.1137/130931734.
- [Frö+19] L. Fröhlich et al. "Multi-Beamline Operation at the European XFEL". In: *Proceedings of the 39th Free Electron Laser Conference*. Hamburg, Germany: WEP008, 2019, pp. 335–338. DOI: 10.18429/JACoW-FEL2019-WEP008.
- [Gal18] J.N. Galayda. "The LCLS-II: a high power upgrade to the LCLS". In: *Proceedings of the 9th International Particle Accelerator Conference*. Vancouver, Canada: MOYGB2, 2018, pp. 18–23. DOI: 10.18429/JACoW-IPAC2018-MOYGB2.
- [Gen+14] M. Gensch et al. "THz facility at ELBE: A versatile test facility for electron bunch diagnostics on QUASI-CW electron beams". In: *Proceedings of the 5th International Particle Accelerator Conference*. Dresden, Germany: TUZA02, 2014, pp. 933–934. DOI: 10.18429/JACoW-IPAC2014-TUZA02.
- [GS72] R. Gerchberg and O. Saxton. "A Practical Algorithm for the Determination of Phase from Image and Diffraction Plane Pictures". In: *Optik* 35 (1972).
- [GF45] V. L. Ginzburg and I. M. Frank. "Radiation of a uniformly moving electron due to its transition from one medium into another". In: *J. Phys. (USSR)* 9 (1945), pp. 353–362.
- [GA70] A. M. Glass and R. L. Abrams. "Study of piezoelectric oscillations in wideband pyroelectric LiTaO<sub>3</sub> detectors". In: *Journal of Applied Physics* 41.11 (1970), pp. 4455–4459. DOI: 10.1063/1.1658482.
- [GS06] O. Grimm and P. Schmüser. *Principles of longitudinal beam diagnostics with coherent radiation*. TESLA FEL 2006-03, 2006.
- [Ham+17] M. Hamberg et al. "Electron beam heating with the European XFEL Laser Heater". In: *Proceedings of the 38th International Free-Electron Laser Conference*. Santa Fe, USA: WEP018, 2017, pp. 458–459. DOI: 10.18429/JACoW-FEL2017-WEP018.

- [Has18] E. Hass. “Longitudinal Electron Bunch Shape Reconstruction from Form Factor Modulus based on Spectrally Resolved Measurements of Coherent Transition Radiation”. Dissertation. Universität Hamburg, 2018. DOI: 10.3204/PUBDB-2018-03950.
- [Hei+15] M. Heigoldt et al. “Temporal evolution of longitudinal bunch profile in a laser wakefield accelerator”. In: *Physical Review Special Topics - Accelerators and Beams* 18.121302 (2015). DOI: 10.1103/PhysRevSTAB.18.121302.
- [Hua+10] Z. Huang et al. “Measurements of the linac coherent light source laser heater and its impact on the x-ray free-electron laser performance”. In: *Physical Review Special Topics - Accelerators and Beams* 13.020703 (2010). DOI: 10.1103/PhysRevSTAB.13.020703.
- [Jac03] J. D. Jackson. *Classical Electrodynamics*. Wiley, 2003. DOI: 10.1002/3527600434.eap109.
- [KSR08] K.-J. Kim, Y. Shvyd’ko, and S. Reiche. “A Proposal for an X-Ray Free-Electron Laser Oscillator with an Energy-Recovery Linac”. In: *Physical Review Letters* 100.244802 (2008). DOI: 10.1103/PhysRevLett.100.244802.
- [Kle07] R. Kleiner. “Filling the Terahertz Gap”. In: *Science* 318 (2007), pp. 1254–1255. DOI: 10.1126/science.1151373.
- [Kli06] M. V. Klivanov. “On the recovery of a 2-D function from the modulus of its Fourier transform”. In: *Journal of Mathematical Analysis and Applications* 323 (2006), pp. 818–843. DOI: 10.1016/j.jmaa.2005.10.079.
- [KS80] A. M. Kondratenko and E. L. Saldin. “Generation of Coherent Radiation By a Relativistic Electron Beam in an Ondulator.” In: *Particle Accelerators* 10 (1980), pp. 207–216.
- [Köv16] T. Kövener. *THz Spectrometer Calibration at FELIX*. Master thesis, Universität Hamburg, 2016. DOI: 10.3204/PUBDB-2016-06662.
- [Kra27] H. A. Kramers. “La diffusion de la lumiere par les atomes”. In: *Atti Cong. Intern. Fisica (Transactions of Volta Centenary Congress)*. Como, 1927, pp. 545–557.
- [Kre+13] P. Krejcik et al. “Commissioning the new LCLS X-band transverse deflecting cavity with femtosecond resolution”. In: *Proceedings of the 2nd International Beam Instrumentation Conference*. Oxford, UK: TUAL2, 2013, pp. 308–311.
- [LHS94] R. Lai, U. Happek, and A. J. Sievers. “Measurement of the longitudinal asymmetry of a charged particle bunch from the coherent synchrotron or transition radiation spectrum”. In: *Physical Review E* 50.6 (1994), R4294–R4297. DOI: 10.1103/PhysRevE.50.R4294.
- [Mad71] J. M. J. Madey. “Stimulated Emission of Bremsstrahlung in a Periodic Magnetic Field”. In: *Journal of Applied Physics* 42 (1971), pp. 1906–1913. DOI: 10.1063/1.1660466.
- [Mae+12] H. Maesaka et al. “Electron beam diagnostic system for the Japanese XFEL, SACLA”. In: *Proceedings of the 1st International Beam Instrumentation Conference*. Tsukuba, Japan: MOIC02, 2012, pp. 38–46.
- [MR15] G. Marcus and T. Raubenheimer. *Femtosecond and sub-femtosecond pulses at LCLS-II*. Tech. rep. LCLSII-TN-15-17, SLAC, 2015.

- [Max+13] T. J. Maxwell et al. "Coherent-Radiation Spectroscopy of Few-Femtosecond Electron Bunches Using a Middle-Infrared Prism Spectrometer". In: *Physical Review Letters* 111.184801 (2013). DOI: 10.1103/PhysRevLett.111.184801.
- [Nöl09] D. Nölle. "Electron beam diagnostics for the European XFEL". In: *Proceedings of the 9th European Workshop on Beam Diagnostics and Instrumentation for Particle Accelerators*. Basel, Switzerland: TUOA04, 2009, pp. 158–160.
- [O'S01] P. G. O'Shea. "Free-Electron Lasers: Status and Applications". In: *Science* 292 (2001), pp. 1853–1858. DOI: 10.1126/science.1055718.
- [PDG14] P. Peier, H. Dinter, and C. Gerth. "Coherent Radiation Diagnostics for Longitudinal Bunch Characterization at European XFEL". In: *Proceedings of the 36th International Free Electron Laser Conference*. Basel, Switzerland: THP083, 2014.
- [RG75] L. Rabiner and B. Gold. *Theory and application of digital signal processing*. Prentice-Hall, 1975.
- [Rat+15] D. Ratner et al. "Time-resolved imaging of the microbunching instability and energy spread at the Linac Coherent Light Source". In: *Physical Review Special Topics - Accelerators and Beams* 18.030704 (2015). DOI: 10.1103/PhysRevSTAB.18.030704.
- [Rei13] S. Reiche. "Overview of seeding methods for FELs". In: *Proceedings of the 4th International Particle Accelerator Conference*. Shanghai, China: WEZB102, 2013, pp. 2063–2067.
- [Rön98] W. C. Röntgen. "Über eine neue Art von Strahlen". In: *Annalen der Physik* 300 (1898), pp. 12–17. DOI: 10.1002/andp.18983000103.
- [RB73] C. B. Roundy and R. L. Byer. "Sensitive LiTaO<sub>3</sub> pyroelectric detector". In: *Journal of Applied Physics* 44 (1973), pp. 929–931. DOI: 10.1063/1.1662294.
- [SSY97] E. L. Saldin, E. A. Schneidmiller, and M. V. Yurkov. "On the coherent radiation of an electron bunch moving in an arc of a circle". In: *Nuclear Instruments and Methods in Physics Research Section A: Accelerators, Spectrometers, Detectors and Associated Equipment* 398 (1997), pp. 373–394. DOI: 10.1016/S0168-9002(97)00822-X.
- [SSY04] E. L. Saldin, E. A. Schneidmiller, and M. V. Yurkov. "Longitudinal space charge-driven microbunching instability in the TESLA Test Facility linac". In: *Nuclear Instruments and Methods in Physics Research Section A: Accelerators, Spectrometers, Detectors and Associated Equipment* 528 (2004), pp. 355–359. DOI: 10.1016/j.nima.2004.04.067.
- [Sch16] V. Schlott. "Free-Electron Laser Beam Instrumentation and Diagnostics". In: *Synchrotron Light Sources and Free-Electron Lasers*. Springer, 2016, pp. 701–748. DOI: 10.1007/978-3-319-14394-1\_18.
- [Sch+18] B. Schmidt et al. *Longitudinal Bunch Diagnostics using Coherent Transition Radiation Spectroscopy*. DESY-18-027, DESY, 2018. DOI: 10.3204/PUBDB-2018-01372.

- [Sch+20] B. Schmidt et al. "Benchmarking coherent radiation spectroscopy as a tool for high-resolution bunch shape reconstruction at free-electron lasers". In: *Physical Review Accelerators and Beams* 23.062801 (2020). DOI: 10.1103/PhysRevAccelBeams.23.062801.
- [Sch02] P. Schmüser. "Superconductivity in high energy particle accelerators". In: *Progress in Particle and Nuclear Physics* 49 (2002), pp. 155–244. DOI: 10.1016/S0146-6410(02)00145-X.
- [Sch+14] P. Schmüser et al. *Free-Electron Lasers in the Ultraviolet and X-Ray Regime*. Cham: Springer, 2014. DOI: 10.1007/978-3-319-04081-3.
- [Shi+94] Y. Shibata et al. "Diagnostics of an electron beam of a linear accelerator using coherent transition radiation". In: *Physical Review E* 50.2 (1994), pp. 1479–1484. DOI: 10.1103/PhysRevE.50.1479.
- [Shi07] T. Shintake. "Review of the worldwide SASE FEL development". In: *Proceedings of the 22nd Particle Accelerator Conference*. Albuquerque, USA: MOZBAB01, 2007, pp. 89–93. DOI: 10.1109/PAC.2007.4440331.
- [Sie+20] C. D. Siewert et al. "Hybrid Biopolymer and Lipid Nanoparticles with Improved Transfection Efficacy for mRNA". In: *Cells* 9.2031 (2020). DOI: 10.3390/cells9092034.
- [Tav+18] P. F. Tavares et al. "Commissioning and first-year operational results of the MAX IV 3 GeV ring". In: *Journal of Synchrotron Radiation* 25 (2018), pp. 1291–1316. DOI: 10.1107/S1600577518008111.
- [Wal+16] N. Walker et al. "Performance analysis of the European XFEL SRF cavities, from vertical test to operation in modules". In: *Proceedings of the 28th Linear Accelerator Conference*. East Lansing, USA: WE1A04, 2016, pp. 657–662. DOI: <https://doi.org/10.18429/JACoW-LINAC2016-WE1A04>.
- [WC53] J. D. Watson and F. H. C. Crick. "Molecular Structure of Nucleic Acids: A Structure for Deoxyribose Nucleic Acid". In: *Nature* 171 (1953), pp. 737–738. DOI: 10.1038/171737a0.
- [Wes12] S. Wesch. "Echtzeitbestimmung longitudinaler Elektronenstrahlparameter mittels absoluter Intensitäts- und Spektralmessung einzelner kohärenter THz Strahlungspulse". Dissertation. Universität Hamburg, 2012.
- [Wes+09] S. Wesch et al. "Observation of coherent optical transition radiation and evidence for microbunching in magnetic chicanes". In: *31st International Free Electron Laser Conference*. Liverpool, UK: WEPC50, 2009, pp. 619–622.
- [Wes+11] S. Wesch et al. "A multi-channel THz and infrared spectrometer for femtosecond electron bunch diagnostics by single-shot spectroscopy of coherent radiation". In: *Nuclear Instruments and Methods in Physics Research Section A: Accelerators, Spectrometers, Detectors and Associated Equipment* 665 (2011), pp. 40–47. DOI: 10.1016/j.nima.2011.11.037.
- [Wie15] H. Wiedemann. *Particle Accelerator Physics*. Springer, 2015. DOI: 10.1007/978-3-319-18317-6.
- [Wil00] K. Wille. *The physics of particle accelerators: an introduction*. Oxford University Press, 2000.
- [Woo72] F. Wooten. *Optical properties of solids*. Academic Press, 1972.

- [YD19] J. Yan and H. Deng. "Multi-beam-energy operation for the continuous-wave x-ray free electron laser". In: *Physical Review Accelerators and Beams* 22.090701 (2019). DOI: 10.1103/PhysRevAccelBeams.22.090701.
- [Yan11] M. Yan. "Suppression of COTR in Electron Beam Imaging Diagnosis at FLASH". Diploma thesis. Universität Hamburg, 2011.
- [Yan15] M. Yan. "Online diagnostics of time-resolved electron beam properties with femtosecond resolution for X-ray FELs". Dissertation. Universität Hamburg, 2015.
- [Zag20] I. Zagorodnov. [www.desy.de/fel-beam/s2e/xfel.html](http://www.desy.de/fel-beam/s2e/xfel.html). European XFEL Start-to-End Simulations, 2020.
- [ZDT19] I. Zagorodnov, M. Dohlus, and S. Tomin. "Accelerator beam dynamics at the European X-ray Free Electron Laser". In: *Physical Review Accelerators and Beams* 22.024401 (2019). DOI: 10.1103/PhysRevAccelBeams.22.024401.
- [Zav16] A. A. Zavadtsev. "Three transverse deflecting systems for electron beam diagnostics in the European free-electron laser XFEL". In: *25th Russian Particle Accelerator Conference*. St. Petersburg, Russia: THXSH02, 2016, pp. 196–200. DOI: 10.18429/JACoW-RuPAC2016-THXSH02.
- [Zho+19] F. Zhou et al. "First Commissioning of LCLS-II CW Injector Source". In: *Proceedings of the 10th International Particle Accelerator Conference*. Melbourne, Australia: TUPTS106, 2019, pp. 2171–2173. DOI: 10.18429/JACoW-IPAC2019-TUPTS106.

# List of Publications

- [1] N. M. Lockmann, Ch. Gert, B. Schmidt and S. Wesch. “Noninvasive THz spectroscopy for bunch current profile reconstructions at MHz repetition rates”. In: *Physical Review of Accelerators and Beams* 23.112801 (2020).
- [2] B. Schmidt, N. M. Lockmann, P. Schmüser and S. Wesch. “Benchmarking coherent radiation spectroscopy as a tool for high-resolution bunch shape reconstruction at free-electron lasers”. In: *Physical Review of Accelerators and Beams* 23.062801 (2020).
- [3] N. M. Lockmann, Ch. Gerth, B. Schmidt and S. Wesch. “THz spectroscopy with MHz repetition rates for bunch profile reconstructions at European XFEL”. In: *Proceedings of the 39th International Free-Electron Laser Conference*. Hamburg, Germany: WEP012, 2019, pp. 350–352.
- [4] S. Fahlström, M. Hamberg, Ch. Gerth, N.M. Lockmann, B. Steffen. “NIR spectrometer for bunch-resolved, non-destructive studies of microbunching at European XFEL”. In: *Proceedings of the 39th International Free-Electron Laser Conference*. Hamburg, Germany: WEP035, 2019, pp. 392–395.
- [5] N. M. Lockmann, Ch. Gerth, P. Peier, B. Schmidt and S. Wesch. “A non-invasive THz spectrometer for bunch length characterization at European XFEL”. In: *Proceedings of the 10th International Particle Accelerator Conference*. Melbourne, Australia: WEPGW014, 2019, pp. 2495–2497.



## Acknowledgements/Danksagung

First, I would like to express my gratitude to **Dr. Stephan Wesch**, **Dr. Christopher Gerth** and **Dr. Bernhard Schmidt**. They have been most heavily involved in the work presented in this dissertation and played a fundamental role in its realization. Furthermore, I would like to thank

- the people involved in realizing the experimental setup and the spectrometer readouts: Dr. E. Hass, O. Hensler, K. Ludwig, Dr. P. Peier, L. Petrosyan, J. Roever, A. Schleiermacher and P. Smirnov.
- the people involved in measurements at European XFEL, especially Dr. B. Beutner, Dr. F. Brinker, Dr. S. Tomin and Dr. I. Zagorodnov.
- Dr. Ch. Behrens for introducing me to this very exciting PhD project.
- Prof. Dr. W. Hillert, Dr. T. Limberg and the entire examination board for their commitment.
- the entire groups of FLA and MSK – especially M. K. Czwalińska – at DESY for their support.
- Dr. B. Steffen for many shared rides to and from DESY.
- R. Brabants for his support as a summer student.
- Dr. M. J. Garland and Dr. A. Gottwald for approving important passages.
- Dr. M. Hamberg and S. Fahlström for the exciting project that added a NIR spectrometer to the THz beamline.
- Dr. H. Schlarb for the possibility to realize this project within his group.
- Dr. W. Decking and Dr. D. Nölle for providing beam time at European XFEL.

Schließlich möchte ich mich noch in einem eigenen Absatz bei den Menschen in meinem privaten Umfeld bedanken. Ich danke meiner Familie, dass sie mich über all die Jahre des Studiums, und besonders auch in schwierigen Zeiten, unterstützt hat. Mein Vater Arnulf hat großen Anteil daran, dass ich mich entschieden habe Physik zu studieren und ich bin mir sicher, dass er großen Gefallen an dieser Dissertation gefunden hätte. Ich widme ihm daher diese Dissertation und hoffe so meine Dankbarkeit zum Ausdruck bringen zu können. Meine Freunde und KommilitonenInnen haben für eine tolle und unvergessliche Studienzeit gesorgt. Schließlich möchte ich mich noch bei meiner Frau Margarita bedanken. Danke, dass du mich während des Stress aller Abschlussarbeiten ertragen hast und selbst während des Schreibens zu Zeiten der Corona Lockdowns die Tage abwechslungsreich und erfüllend waren.



## Eidesstattliche Versicherung

Hiermit versichere ich an Eides statt, die vorliegende Dissertationsschrift selbst verfasst und keine anderen als die angegebenen Hilfsmittel und Quellen benutzt zu haben.

Die eingereichte schriftliche Fassung entspricht der auf dem elektronischen Speichermedium.

Die Dissertation wurde in der vorgelegten oder einer ähnlichen Form nicht schon einmal in einem früheren Promotionsverfahren angenommen oder als ungenügend beurteilt.

Hamburg, den 07.04.2021:

---

Unterschrift der Doktorandin / des Doktoranden

